Imperial College London
Department of Electrical and Electronic Engineering

Acoustic Power Distribution Techniques for Wireless Sensor Networks

Akshayaa Pandiyan

January 2022

Supervised by Prof. Eric M. Yeatman

Co-Supervised by Dr Michail E. Kiziroglou

Submitted in partial fulfilment of the requirements for the degree of Doctor of Philosophy in Electrical and Electronic Engineering of Imperial College London and the Diploma of Imperial College London

Statement of Originality

I hereby certify that all material in this dissertation that is not my own work has been appropriately acknowledged.

Akshayaa Pandiyan

Copyright Declaration

Abstract

Recent advancements in wireless power transfer technologies can solve several residual problems concerning the maintenance of wireless sensor networks. Among these, air based acoustic systems are still less exploited with considerable potential for powering sensor nodes. This thesis aims to understand the significant parameters for acoustic power transfer in air, comprehend the losses, and quantify the limitations in terms of distance, alignment, frequency, and power transfer efficiency.

This research outlines the basic concepts and equations overlooking sound wave propagation, system losses, and safety regulations to understand the prospects and limitations of acoustic power transfer. First, a theoretical model was established to define the diffraction and attenuation losses in the system. Different off-the-shelf transducers were experimentally investigated, showing that the FUS-40E transducer is most appropriate for this work. Subsequently, different load-matching techniques are analysed to identify the optimum method to deliver power. The analytical results were experimentally validated, and complex impedance matching increased the bandwidth from 1.5 kHz to 4 kHz and the power transfer efficiency from 0.02% to 0.43%.

Subsequently, a detailed 3D profiling of the acoustic system in the far-field region was provided, analysing the receiver sensitivity to disturbances in separation distance, receiver orientation and alignment. The measured effects of misalignment between the transducers are provided as a design graph, correlating the output power as a function of separation distance, offset, loading methods and operating frequency.

Finally, a two-stage wireless power network is designed, where energy packets are inductively delivered to a cluster of nodes by a recharge vehicle and later acoustically distributed to devices within the cluster. A novel dynamic recharge scheduling algorithm that combines weighted genetic clustering with nearest neighbour search is developed to jointly minimize vehicle travel distance and power transfer losses. The efficacy and performance of the algorithm are evaluated in simulation using experimentally derived traces that presented 90% throughput for large, dense networks.

Acknowledgement

Firstly, my sincere thanks and gratitude to my supervisors, Prof. Eric Yeatman and Dr Michail Kiziroglou, for accepting to oversee my work and their guidance through my PhD journey. It has been a worthwhile journey and an honour to be their student. I genuinely appreciate their patience, support and dedication, which kept me motivated throughout the work period and made this thesis possible.

I would also like to express my heartfelt gratitude to Dr David Boyle and Dr Steven Wright for involving me in their research and spending valuable time with me for discussions and comments about my work. Their valuable feedback on my research progress and results was constructive and inspired me.

I am indebted to the 'Optical and Semiconductor Devices' group for their exciting exchange of ideas and creative discussions, thus creating a positive and productive atmosphere. In addition, the group have been a source of friendship, support, and many valuable memories, extending it far beyond research. My time at Imperial was unforgettable due to them.

I gratefully acknowledge financial support from European Commission H2020 grant and the entire ENHANCE project team for their constant support. I also appreciate the administrative and technical support from Ms Susan Brace, Mr Amine Halimi, Mr Hisham Maarki and Mr Phil Jones, which made my work operative and efficient.

My special thanks to my close friends Kavya, Hakan and Micaela for always being there for me through hardships. Lastly, but most importantly, I would like to thank my parents, brother and grandparents for their endless love, encouragement, and blessings throughout my life. I also admire my patient husband, Mr Yuvaraj Subramanian, for supporting me through rain or shine.

Thank you all for this amazing experience!

Akshayaa Pandiyan

Table Of Contents

List of Figures

List of Tables

List of Variables

A	Area	[m^2]
B	Adiabatic bulk modulus	[-]
C_m	Piezoelectric mechanical compliance	[F]
C_o	Piezoelectric capacitance due to electrodes	[F]
c	Speed of acoustic waves in a medium	[m s^{-1}]
c_{33}^D	Open circuit complex elastic stiffness	[Nm^{-2}]
D	Directivity	[Degrees]
d	Thickness of the piezoelectric disc	[m]
E	Energy Capacity	[J]
F	Force Amplitude	[N]
f	Frequency	[Hz]
f_m	AC Force exerted on the mechanical branch	[N]
$g(f,x)$	Transmission gain of acoustic link	[-]
h_{33}	Piezoelectric pressure constant	[Vm^{-1}]
I_s	Source current	[A]
I_{SPTA}	Sound spatial-peak temporal-average intensity	[Wm^{-2}]
J_1	1st order Bessel function	[-]
K	Number of clusters	[-]
k	Wave number	[-]
k_t	Complex electromechanical coupling	[-]
L_m	Piezoelectric mechanical modal mass	[H]
M_r	Molecular mass	[g mol^{-1}]
N_S	Number of sensors in a network	[-]
N_C	Number of Clusters in a network	[-]
n	Transformer turns ratio	[-]
PDV_{path}	Coordinate locations for the PDV to visit	[-]
$\widehat{P_o}$	Amplitude of sound pressure at equilibrium	[Pa]
$\widehat{P_t}$	Amplitude of sound pressure shift due to source	[Pa]
P	Electrical power	[W]

p	Variation of sound pressure	[Pa]
Q	Harmonic volume velocity	[m^3 s^{-1}]
Q_m	Mechanical quality factor	[-]
R	Molar gas constant	[M m mol^{-1}]
R_m	Piezoelectric mechanical damping	[Ω]
R_o	Piezoelectric dielectric loss	[Ω]
r_{source}	Radius of the piezoelectric disc	[m]
S	Set of sensor nodes	[-]
SPL	Sound Pressure Level	[dB]
SWL	Sound Power Level	[dB]
T	Temperature	[K]
t	Time	[s]
$[U]$	Mutated vector for Genetic algorithm	[-]
$\vec{u}$	Particle flow velocity vector in 3-Dimension	[m s^{-1}]
V	Amplitude of voltage	[V]
$[V]$	Trail vector for Genetic algorithm	[-]
v_x	Particle velocity of wave in 1-Dimension	[m s^{-1}]
X	Reactance	[Ω]
$[X]$	Target vector for Genetic algorithm	[-]
x	Distance between two sensors	[m]
Z	Electrical Impedance	[Ω]
Γ	Reflection coefficient	[-]
ϕ	KLM transformer turns ratio	[-]
α	Absorption coefficient	[-]
β	Phase Speed	[m s^{-1}]
δ	Displacement angle	[Degrees]
ε_{33}^{S}	Clamped complex permittivity	[Fm^{-1}]
η	Efficiency of a system	[%]
θ	Angle from the propagation axis (Directivity Angle)	[Degrees]
λ	Wavelength	[m]
ρ_o	Density of medium at equilibrium	[Kg m^{-3}]
ρ_t	Density shift in medium due to external field	[Kg m^{-3}]

ω	Angular frequency	[radians]
χ_T	Number of nodes in the transmission range	[-]
$Ƶ_o$	Specific acoustic impedance	[Pa s m^{-1}]
$Ƶ$	Acoustic impedance of a medium, $Ƶ = Ƶ_o/A$	[Pa s m^{-1}]
$\Delta\mathbb{Z}$	Distance between standing waves peaks	[m]

SUBSCRIPTS

AC	AC to DC rectifier circuit
In	Inductive Electronics
L	Electrical load
gen	Genetic Clustering generation
max	Maximum
Pi	Piezoelectric property
ref	Reference
rms	Root mean square
RX	Receiver
TX	Transmitter
s	Source
m, n	From sensor node m to sensor node n

SUPERSCRIPTS

BS	Base Station
C	Complex matching
opt	Optimised
R	Resistive matching
S	Attribute of the sensor
SC	Attribute of the storage capacitor
PDV	Attribute of the power delivery vehicle
WSN	Attribute of the power delivery vehicle

List of Abbreviations

1D	1-Dimensional
ADC	Analog-to-Digital Converter
APT	Acoustic Power Transfer
BS	Base Station
cMUT	capacitive Micromachined Ultrasonic Transducers
CN	Centre node
CPT	Capacitively-Coupled Power Transfer
CPU	Control and Processing Unit
EH	Energy Harvesters
EM	Electromagnetic
EN	End nodes
FDA	Food and Drug Administration
FEM	Finite Element Modelling
GA	Genetic Algorithm
GRIN	Gradient Index
IoT	Internet of Things
IPT	Inductive Power Transfer
KLM	Krimholtz, Leedom, and Matthae Model
MRI	Magnetic Resonance Imaging
PCB	Printable Circuit Board
PDV	Power Delivery Vehicle
PLM	Perfectly Matched Layer
pMUT	piezoelectric Micromachined Ultrasonic Transducers
PUEH	Piezoelectric Ultrasonic Energy Harvester
PZT	Lead Zirconate Titanate (Pb(ZrTi))
SONAR	Sound Navigation and Ranging
TSP	Travelling Salesman Problem
WPT	Wireless Power Transfer
WSN	Wireless Sensor Network

1. Introduction

This chapter outlines the scope of this work by describing the main challenges in designing an acoustic power transfer (APT) system for wireless sensor networks. Based on these existing constraints, the goals set for this research are summarised, and the selection of approach is justified. Along with the contributions of this work, this chapter concludes with the overall structure of this thesis.

1.1. Background and Motivation

The rapid growth of embedded and communication electronics has led to evolving Wireless Sensor Network (WSN) research due to its applicability in health, security, robotics, and remote monitoring systems. A WSN of small devices called 'Nodes' collects critical information representing the system status like temperature, strain, humidity, and pressure [1, 2]. Each node consists of an embedded CPU with limited computation power, a smart sensor unit, a transceiver unit and a power unit [3]. Additionally, they communicate with other nodes to transmit data, forming a centralised system to predict and control the network response. Therefore, WSN is a critical enabling technology for the emerging Internet of Things (IoT). Recent and ongoing development projects on this technology include Digital Manufacturing [4], Warehouse Inventory Management [5], Pipeline monitoring [6] and Smart Agriculture [7].

With the desire to make IoT more feasible, a wide range of investigations is ongoing in communication techniques, distributed detection, energy harvesting and rechargeable sensor nodes to improve the energy performance and make them self-reliant for the desired autonomy. For Industrial IoT, a key concern is the wide distribution and access of these nodes. Conventionally, batteries power these nodes but have a limited lifetime. Therefore, a large WSN consisting of thousands of nodes requires high maintenance for accessing, replacing and disposal of the batteries. Integrations of batteries also add substantial space and weight to the node, which bottlenecks the applicability of WSNs. The reliability of WSNs also depends on the successful improvement in the disciplines of energy management for the network. It demands efficient in-situ recharge and storage systems that support the WSNs at all times. The power requirements of a WSN node are analysed in the next section to investigate the potential alternatives for batteries.

1.1.1. Wireless Sensor Nodes

The architecture of a node in WSN consists of four subsystems based on their function: Sensing, Processing, Power Supply and Management, and Communication, as represented in Figure 1.1. Past years have seen an enormous evolution in solid-state electronics and circuit design, which helped improve sensors, controllers, and transmitters' performance and reduce their size and power consumption. It means that the power supply consumes a majority of space inside a WSN node [8]. Therefore, replacing them using inexhaustible energy generators would substantially reduce the size of a node and expand the applicability of WSNs in demanding environments. Analysing each of these units and their power consumption will provide a base specification for the power supply design. In this section, some off-the-shelf devices used for WSNs will be studied to summarise the power consumption of such networks.

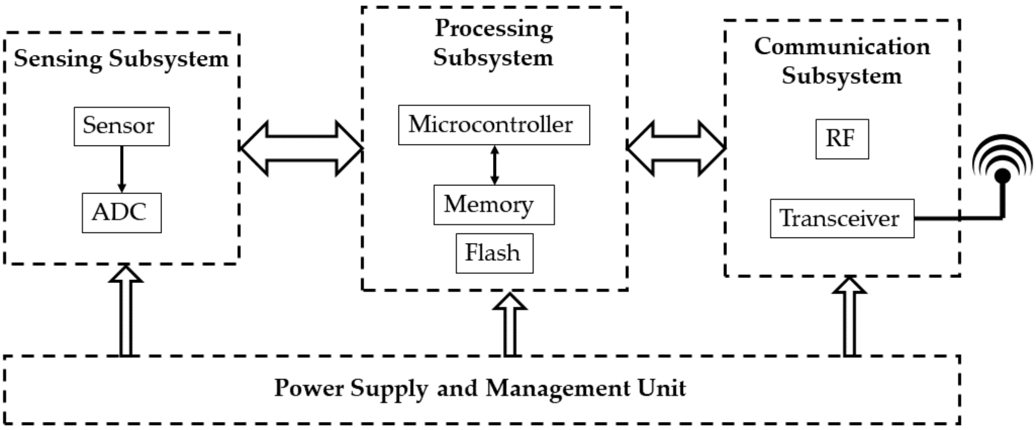

Figure 1.1: Architecture of a Wireless Sensor Node.

The sensing subsystem consists of a transducer that reads physical information from the environment and converts them into current or voltages. The power consumed by a sensor depends on its type, mode of operation and, significantly, its sampling rate. Usually, an Analog-to-Digital Converter (ADC) is connected to these transducers converting them to digital signals processed by a microcontroller. The sensing unit will be active only for a few hundred milliseconds every minute to finish one cycle for most applications. This frequency is application dependant. Therefore, the power consumption per duty cycle can be very low, and Table 1.1 summarises some of the commonly used sensor specifications. The mean power consumption would vary from $5.3\, nJ/Sample$ to $792\ \mu J/Sample$ of 16-bits. Figure 1.2 shows two complete sensing cycles of a wireless sensor from a typical WSN node, where the sensor is active only for short bursts of time.

The processing subsystem of a WSN node consists of a microcontroller along with its internal memory units. The controller functions in driving the sensors in different operation modes and commands the transceiver for data communication. Like the sensing unit, the controller is primarily operated in the idle/sleep mode for the prominent time of the duty cycle. However, its power consumption depends on the controller's operating frequency ranging from $0.71mW$ (ML610Q431) to $67.2mW$ (PIC18F4620).

Table 1.1: Specifications of off-the-shelf sensors (from [9]).

Sensor	Voltage (V)	Current mA ()	Power (mW)	Sampling time (s)	Energy per Sample (μJ)
Temperature (TMP36)	3.3	0.008	0.026	0.0002	0.0053
Light (LM393)	3.3	0.03	0.099	0.0002	0.02
Humidity (HIH-5030-001)	3.3	0.3	0.99	0.8	790
Vibration (SSRSIS181)	3.3	0.6	1.98	0.02	39
Barometric Pressure (MIPAG1XX050BSAAX)	5.0	7.0	35.0	0.02	0.7

The transceiver unit in a sensor node consists of a radio which sends and receives data/signals to communicate among the other nodes in the WSN. The transceiver's power consumption mainly depends on the protocol used for communication within the network and the data logging approach (e.g. real-time data or data flushing). On average, the transceivers consume a few to a hundred milliwatts. It is the highest consumption of a sensor node, which can be realised in Figure 1.2, which depicts the trends of the power consumption in sensor nodes. Table 1.2 summarises the power consumption of different communication protocols.

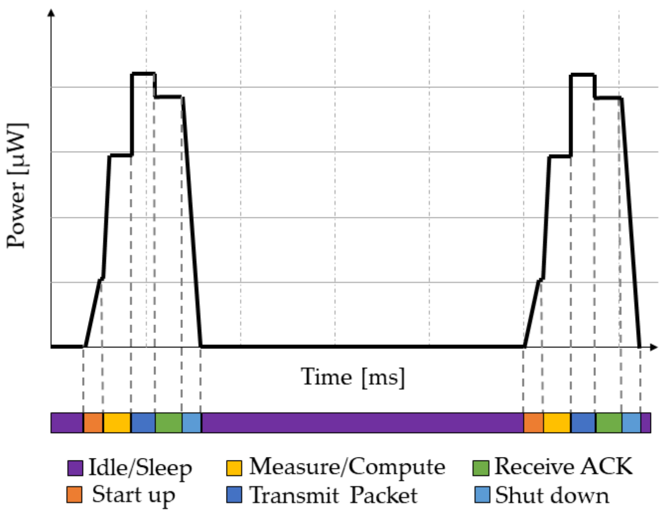

Figure 1.2: Activity profile for a wireless sensor node for two complete cycles exhibiting long sleep periods in-between short wake up cycles.

The choice of technology depends on the typical range of coverage that is convenient for the WSN. As discussed in the previous sections, it is evident that the subsystem's duty cycle should be designed with mindful considerations for an effective low power sensor node. This design specifies the load that is expected from the power supply unit during recharge. Nechibvute et al. in [9] predict that an approximate power generation of a few μW would be sufficient to power the whole system to be autonomous. However, when choosing alternative powering technologies from conventional batteries, it is necessary to have a buffer energy storage such as a supercapacitor to resolve the fluctuations in the available power. This will ensure the proper operation of the WSNs.

Table 1.2: Specifications and comparison of different low power communication modules used in IoT (from [10]).

Type	Module	IEEE Protocol	Voltage (V)	Current (mA)			Power (dBm)		Bit Rate (Kb/s)
				Tx	Rx	Sleep	Tx	Rx	
Wi-Fi-Module	QCA4004	802.11 n	3.3	250	75	0.13	29	24	10
	RS9110-N1102	802.11 b/g/n	3.3	19	17	0.52	13	12.5	11
	RTX41x Series	802.11 b/g/n	3.3	0.76	0.76	0.003	4	4	10
Zigbee Network Protocol	CC2430	802.15.4	3.3	25	27	0.0009	19.5	18.5	250
	ANY900	802.15.4	3.3	33	17	<0.006	20	17.5	250
Zigbee Network Protocol	RC2400	802.15.4	3.3	34	24	0.001	20.5	18	250
	deRFmega128-22M00	802.15.4	3.3	12.7	17.6	<0.001	21	20.5	250

1.1.2. Energy Harvesting

Potential sources that can be converted into usable energy for harvesting are mainly categorised into three types: kinetic, thermal, and radiation. Kinetic energy harvesters utilise the system's acceleration to harness energy [8, 11, 12]. Thermal energy harvesters operate on the thermal gradient between two surfaces within the system with a constant heat supply [13] or a time-varying heat source [14]. In comparison, optical devices use the photoelectric principle to scavenge photons into electrical energy [15]. S. Roundy *et al.* in [16] broadly surveyed these potential sources for WSN and summarised the various sources' power density comparison and lifetime. Similar studies summarising current research on the different classes of energy harvesting can be found in [17-21]. Batteries, the widely used solution for most applications, suffer a short lifetime and are prone to environmental conditions after a few years. In need of a longer lifespan, energy harvesters seem to be a reasonable solution considering their low maintenance cost and independence. However, EH is application-oriented designs, and a single harvester cannot cater to all energy demands. Therefore, comprehensive profiling of the available energy over the frequency spectrum is required to understand the power density of available sources in that environment.

Among them, vibrational energy sources are commonly occurring in most systems. They have attracted ample research in the past decade, motivated by direct integration of the piezoelectric devices (which harvests vibration energy to electric charge) with the electronic circuits and sensor nodes. These vibrations could be from a mechanical or sound source leading to a linear or a rotational vibration.

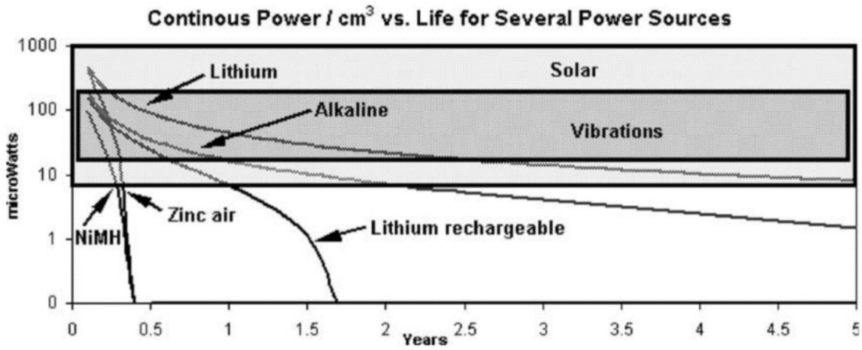

Figure 1.3: Comparisons of power densities of various fixed and parasitic energy sources. (from [16])

Focusing on the research application of industrial WSNs, energy generated from ambient vibrational sources are prone to low and random frequencies, which complicates the harvesting design. As shown in Figure 1.3, solar cells have good power densities and lifespan when excited by direct sunlight. However, given that this work studies the applicability of partial or inaccessible WSN like pipeline monitoring systems or large indoor warehouses, light availability is inadequate for applicable power output.

The availability of a parasitic source vastly depends on the location of the sensor network and tends to change from time to time. This makes it difficult to estimate the output performance of energy harvesters in real-time situations. For instance, the availability of a vibrating source would be distinct in some places far away from the WSN nodes. Wacharasindhu and Kwon demonstrated a creative energy harvesting device by combining electromagnetic transduction (using frequency of typing) and piezoelectric transduction (using force applied on the keys) to harness energy from typing motion from a computer keyboard [22]. This device harnessed $40.8\mu W$ from the piezoelectric component and $1.15\mu W$ from the micro-electromagnetic elements. These micro-harvesters could then be extended into an array capable of producing $3.46mW$ power from a keyboard for recharging a battery while typing. Subsequently, many authors developed hybrid magnetic-piezoelectric devices [14-19], improving their efficiency [23-28]. Recently, many advancements to integrate pyroelectric transduction into Hybrid EHs to develop Pyro-Piezo or Pyro-Photo generators or all three together were proposed [29]. Figure 1.4 shows the different hybrid EHs designs demonstrated by various authors using the various transduction principles.

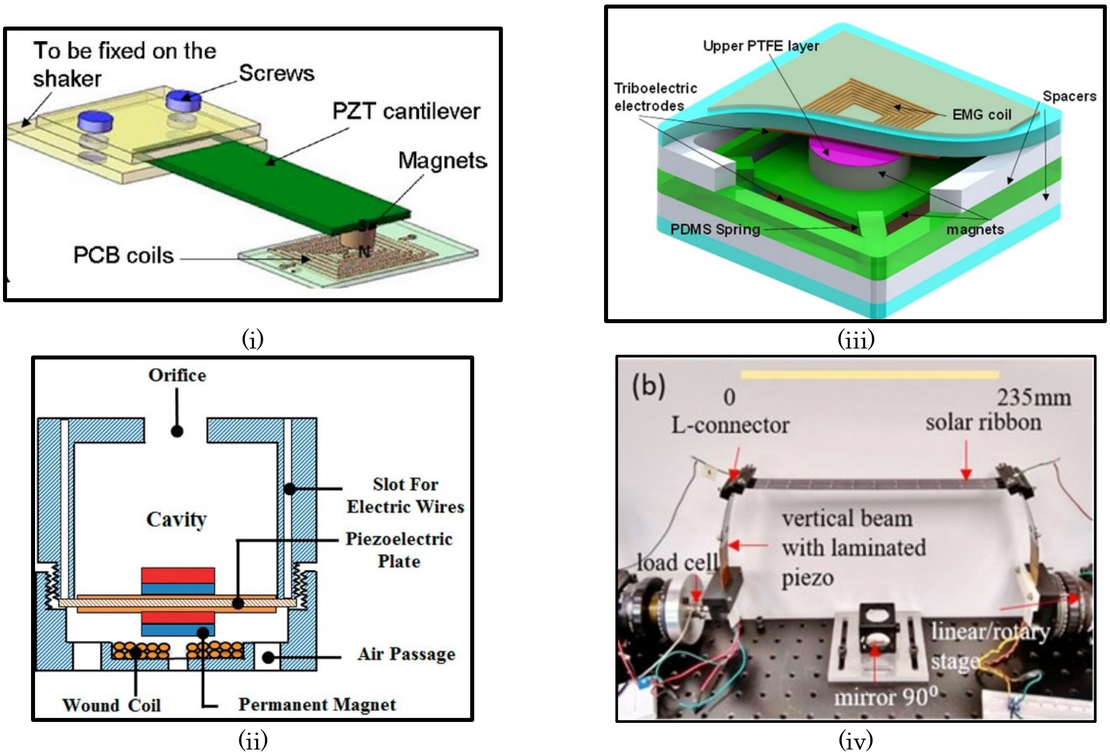

Figure 1.4: Hybrid energy harvesters with multiple energy harvesting principles. (i) Electromagnetic-Piezoelectric system based on beams (from [23]) (ii) Electromagnetic-Piezoelectric system for collecting acoustic energy (from [24]) (iii) Electromagnetic-Triboelectric hybrid system by employing spring-mass(from [25]) (iv) Piezo – Photoelectric hybrid system for integrated wind harvesting (from [30])

The hybrid energy harvester cited above integrates different elements for each source or transduction method. As a result, the number of components increases, enlarging the volume of the final device. Also, most piezoelectric materials inherit pyro and photoelectric properties. Therefore, this setback can be challenged by designing a single transducer exhibiting different characteristics [14]. However, caution must be taken while designing these devices, as some cases observed (pyro-piezo devices) degenerative results while combining the thermal and piezo effects [31]. Therefore, the structure of these devices should utilise the thermal effect profitably to amplify the displacement of the piezoelectric transducer, which consequently increases the generated charges. Moreover, it is crucial in a hybrid EH that the electric interface is compatible with the different DC and AC frequencies of the output voltage from the various transduction methods.

1.1.3. Wireless Power Transfer

Another viable replacement of batteries for WSNs is by employing Wireless Power Transfer (WPT) methods. Unlike energy harvesting techniques, WPT consists of a power receiver instead of harvesting ambient potential energy, driven by a dedicated (or distributive) remote power transmitter operating at a specific frequency. As a result, it benefits higher generated power without direct contact between the transmitter and receiver, potentially driving high demanding WSN nodes. Thus, the development of WPT, which can recharge partially or in-accessible nodes without contact, is potential to provide a more stable power supply for industrial WSN nodes.

A broad spectrum of research has emerged on WPT techniques gaining significant attention due to their connectivity range, portability, and ability to recharge isolated nodes. These methods are commonly classified as near-field or far-field transmission. The near-field methods utilise the inductive or capacitive coupling effect of nonradiative electromagnetic fields. Among these, Inductive Power Transfer (IPT) is most popular, having applied to both commercial and products like wireless mobile [32] and electric vehicles chargers. The far-field WPT techniques adopt acoustic, optical, RF or microwave fields as the energy carrier. An overview of the different WPT methods will be discussed in this section, emphasising acoustic systems.

IPT systems deliver energy by creating alternating magnetic flux by driving the primary coil with sinusoidal current (Figure 1.5 (i)). This flux then penetrates through a medium (air, tissue, metals), delivering energy to the secondary coil to transduce this to electrical power. This alternating current is then rectified and stored in the power supply subsystem of the WSN node. These systems have gained lot of attention, as recent publications demonstrate WPT systems with an efficiency of up to 95 % for distances in the cm range [33-35]. Lawson *et al.* reported a long-range inductive power transfer system using a large planar coil ($1\ m$ by $1\ m$) as a transmitter and planar receiver coils of $170\ mm$ by $170\ mm$ [36]. They experimentally demonstrated a power transfer $> 10\ mW$ for separation distances up to 6 m by maximising the Q factor through novel coil constructions. Although the system can transfer sufficient power to power a sensor node, the transfer efficiency of the system is very low. The team later proposed a high Q coil measurement system for IPT systems in [37] and modelling the link efficiency trend over separation distance for varying Q. It was observed that increasing the Q from 100 to

1000 enables a significant increase in the transfer efficiency for long-distance power transfer. In [38], Park *et al.* improved the transfer distance to 5 m between the primary and secondary coils and managed to experimentally obtain primary coil to load efficiencies of 29%, 16%, and 8% for 3, 4, and 5m distance respectively. Despite promising broad freedom of mobility, the coupling between the primary and secondary coils deteriorates drastically over a large distance and needs large reactive currents in both systems. It consequently generates high eddy currents, conductive losses, and a heating effect.

In IPT systems, precise alignment along with shorter separation distance between the charging devices is crucial to obtain high efficiencies. For instance, Agbinya and Mohamed [39] demonstrated near 100% transfer efficiency by closely placing multiple receiver coils arranged in a hexagonal cell structure at 5 cm. However, the transfer efficiencies reduced to 40% and 10% when the separation distance between the coils increased to 15 cm and 35 cm, respectively.

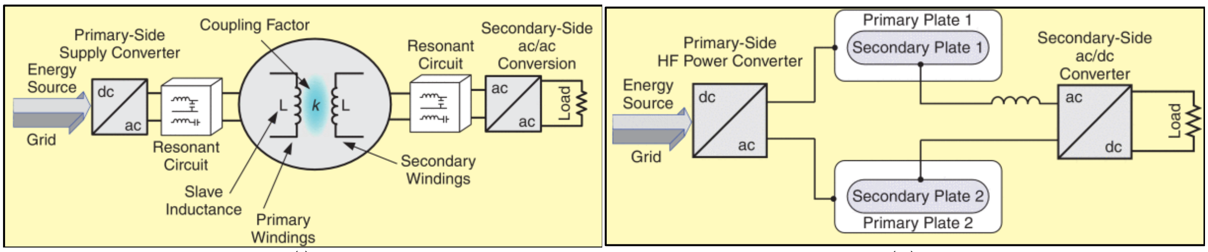

(i) (ii)

Figure 1.5: Block diagram of near-field WPT systems where the primary side is the transmitter and the secondary side is the receiver (i) Inductive WPT system. (ii) Capacitive coupled WPT system. (from [40])

Capacitively-Coupled Power Transfer (CPT) is a technique that utilises alternating electric field between two isolated plates resulting in a displacement current that can flow through a medium (Figure 1.5 (ii)). It is an emerging technology that fewer researchers have explored due to the limited separation distance. As a consequence of the inverse proportionality of the capacitance with the distance, CPT methods require high voltage and frequencies to transfer a reasonable amount of power. This high voltage can lead to electric breakdown during power conditioning. However, CPT is less susceptible to electromagnetic interference due to the constrained nature of the electric field, but the use of high frequencies might negate this effect. CPT systems can reach $50-80\%$ efficiency over a short distance of $0.1-0.5mm$ [40].

Electromagnetic (EM) energy transfer is a far-field WPT technique that utilises EM waves such as microwave (1 GHz to 1000 GHz), RF (20 kHz to 300 GHz) or optical waves (300 GHz to 3000 THz) to deliver energy. The energy flow diagram of an optical WPT system is as shown in Figure 1.6(i). For WPT, optical systems are usually operated in or near-visible region ($700\,nm$ to $400\,nm$) using lasers to generate an optical beam later transduced to electrical power by a photodiode. Current research demonstrates a power generation of $1-12\,W$ with a $20-30\%$ conversion efficiency over meters of distance [41-43]. However, high power laser beams could be highly dangerous and hazardous [44].

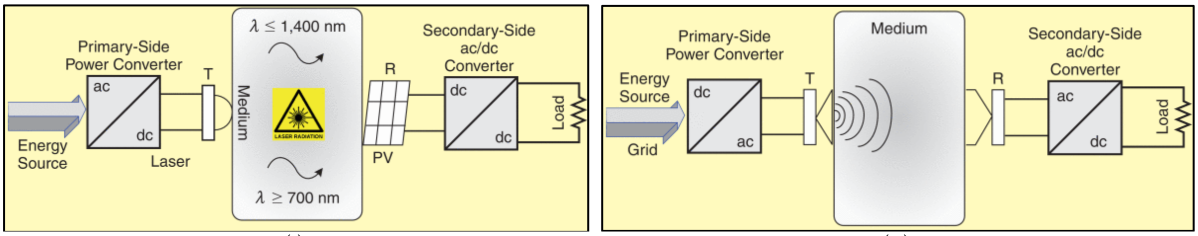

(i) (ii)

Figure 1.6: Block diagram of far-field WPT systems with a transmitting (T) and receiving (R) transducer. (i) Optical WPT system (ii) Acoustic WPT system.(from [40])

RF WPT system, on the other hand, has gained attention in recent years. The transmitter antenna is driven at cellular or Wi-Fi frequency to transmit power to the receiver through the air. However, EM waves decay quickly over short distances[45-48] due to spatial spreading. For example, it was reported in [49] that a $30\,cm$ increase in distance between the antennas reduces the efficiency by 60%. However, EM waves can be directed through beamforming to reduce spatial losses [50]. Beamforming is an algorithmic way of manipulating each antenna transmission such that all of them constructively converge at the receiver antenna. It aids in directing the radiation precisely to the desired location, avoiding any alignment issues [51]. Although this reduces propagation losses and interference, the antenna length of RF waves should be at least an order of the wavelength to be directive and transmit reasonable power.

Acoustic Power Transfer (APT) delivers power via pressure waves through a medium that can propagate pressure (e.g. air, metal, or tissues). Figure 1.6 (ii) shows an APT system block diagram where a power amplifier drives the transmitting transducer converting sinusoidal signals into mechanical vibrations (sound). When a receiver is placed in the path of these sound waves, it can harness electrical power that recharges the power supply subsystem of the WSN node. These transducers are similar to piezoelectric energy harvesters, except in APT systems the receivers are driven by a steady power of a known frequency. APT is commonly employed in biomedical applications and through wall transmissions [52-60]. Bao *et al.* designed a prototype device to transfer 1kW power using 50mm diameter piezoelectric transducers with an 84% efficiency [61].

1.1.4. Air Based Ultrasonic Power Transfer

Among the previously discussed alternatives for battery systems, IPT and APT systems seem promising candidates based on their efficiency and power delivery [62]. Recent publications have shown a total efficiency of 95%, including electronics, for IPT systems. However, when the separation distance between the primary and the secondary coil is much larger than the coil diameter, the efficiency of the IPT system decreases rapidly.

Waffenschmidt and Staring modelled the optimal efficiency for loop inductor coils for the IPT system. They determined that although the system can reach very high efficiency with low quality factors, this only holds up to certain separation distances. Their results presented a relatively flat curve until the maximum distance, after which the efficiency drops sharply (Figure 1.7(i)) [33]. Having this as the reference, Roes [63] compared the theoretical efficiency of the IPT and APT systems of similar dimensions (Figure 1.7(ii)). The theoretical limits of IPT were later confirmed by the measured energy transferred by Kurs *et al.* in [64], represented by black points. This paper analysed the power transfer efficiency of two self-resonant coils of $30\,cm$ radius over differing separation distances. $50\,\%$ efficiency was measured at a $2\,m$ distance when the receiver coil was driven by a $60\,W$ power and sharply decreased to $30\,\%$ at $2.25\,m$, as predicted by Waffenschmidt and Staring. However, the efficiency decreases gradually for the APT systems and outperforms IPT systems after $2\,m$ separation distances. Also, acoustic waves can propagate through metal and soil, providing an economical solution for recharging partial or inaccessible WSN nodes located farther from the transmitter.

Sound has waves propagation properties similar to EM waves. However, acoustic waves have lower speeds than EM waves. This results in a much smaller wavelength for sound waves at any given frequency. Consequently, more directional transmitters and receivers can be fabricated at reasonable sizes and be easily integrated with MEMS devices. Alternatively, for a fixed-sized APT system, the frequency of operation can also be reduced substantially due to the smaller wavelength. Hence, reducing the losses from power conditioning and switching circuits.

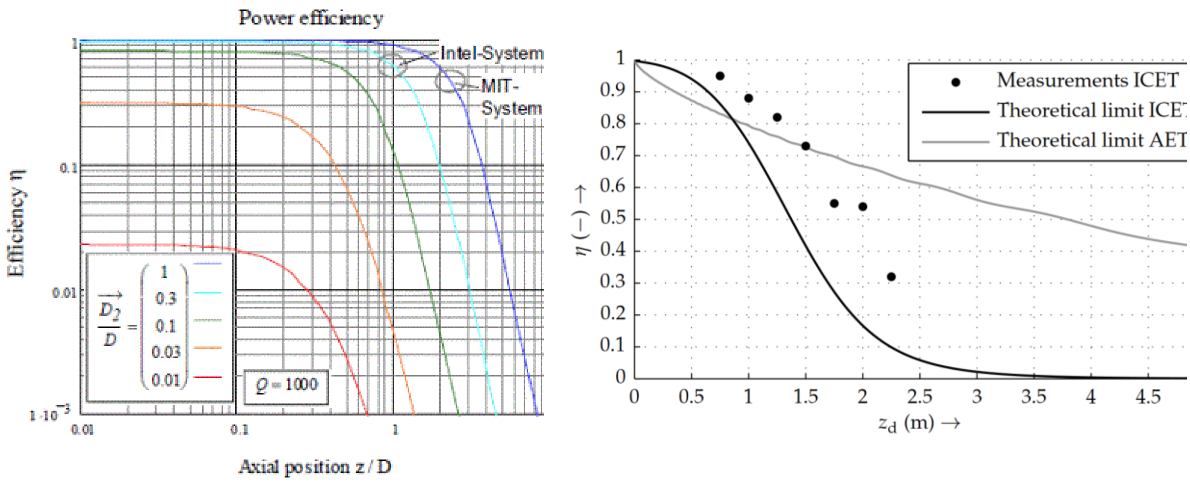

Figure 1.7: Existing comparison between IPT and APT systems (i) Power efficiency analysis of an IPT system using 30 *cm* coils with a measured $Q = 1000$. The performance is analysed with their axial distance z with respective size ratio (from [33]). (ii) Comparative analysis of theoretical limit of Inductively Coupled Energy Transfer (ICET) [33], and Acoustic Energy Transfer (AET) systems [63] along with experimental results from Kurs *et al.* [64] for similar system dimensions (from [63]).

Examining the current literature on APT, biomedical applications and through-wall transmission is widespread. Nevertheless, the number of publications transmission through air is relatively low. A more detailed literature review of the state-of-the-art APT technologies will be discussed in Section 2.2. Considering the broad potential and the passive development of APT techniques through the air, this research aims to provide a detailed analysis of its limitations for recharging extensive WSNs, methods to overcome these challenges and explore strategies for improving the transfer efficiency of the existing APT system. Alternative two-stage WPT techniques combining IPT, and APT methods will also be investigated and examined.

1.2. Research Objectives

1.2.1. Challenges

Thus far, only a handful of research has accomplished experimentally analysing the behaviour of acoustic power transfer in air-based systems. While Roes, in [65], accurately modelled the energy transfer of APT systems to give fundamental insight into the effects in acoustic wave propagation, many factors like the directivity of the transducer were not accounted for in the model. Combining these existing models with finite element analysis and improvising the model through experimental data would allow a more comprehensive view of APT systems. Overall, the power level obtained from air based APT is low when compared to fluid or through-metal transmission. This is mainly due to the acoustic impedance difference between air and the piezoelectric transducer generating the acoustic waves leading to reflection at the transducer-air boundary in both transmitter and receiver. Designing an impedance matching layer in power transducers would surely improve the efficiency of air-based APT systems.

Apart from reflective losses, acoustic waves also suffer from increasing spatial losses when operating in longer travelling distances. Adopting beam directive methods like beam forming or acoustic lenses would reduce these spatial losses. It also makes the APT system versatile to have a single transmitter - multiple receiver architecture. Besides understanding the current limitations of each technology, taking advantage of its benefits to develop a multi-stage power transfer technique could prove an effective method for industrial WSN applications. The efficiency of an APT system is also dependent on its operating frequency. Therefore, higher efficiency can be achieved for air-based APT systems when the frequency is optimised for the separation distance between the transmitter and the receiver.

1.2.2. Research Goals

This research aims to find an effective recharge strategy for partial or inaccessible WSN nodes as an economical substitute for batteries. Wireless power transfer techniques appear to be a viable solution for these applications, among which inductive and acoustic power transfer methods demonstrate potential transfer efficiencies. Also, the power transceivers should be of reasonable size compared to the WSN nodes for practical applicability. Therefore, the core objectives of this thesis can be summarised as:

- Using the existing APT models, understand and characterise critical parameters to identify the limit of attainable transfer efficiency achievable by APT systems.
- Investigate the parameters limiting the power transferred to the receiver and methods to overcome the constraints.
- Identify methods to increase APT systems' range (in terms of separation distance) through directive acoustic beam techniques.
- Developing multi-stage power transfer methods for effective recharging

In essence, this work aims to provide an insight into acoustic power transfer and explore its potential for industrial WSN powering solutions. The goal is to make WSN autonomous by recharging them (lower maintenance) or evaluating power management by scheduling and using standby conditions. Eventually, transferring energy efficiently in the cm or m range would allow considerable freedom for device mobility.

1.2.3. Contributions

The results of this work were presented in various international conferences as listed in Table 1.3, including accepted or submitted peer-reviewed journals. The chapters with which each publication is more closely associated are also listed.

Table 1.3: Conference proceedings and publications of the results of this work

Reference	Publication	Associated Chapter
[66]	A. Y. Pandiyan, M. E. Kiziroglou and E. M. Yeatman, "Complex Impedance Matching for Far-Field Acoustic Wireless Power Transfer," 2021 IEEE 20th International Conference on Micro and Nanotechnology for Power Generation and Energy Conversion Applications (PowerMEMS), 2021, pp. 44-47, DOI: 10.1109/PowerMEMS54003.2021.9658395.	Chapter 3
-	A.Y.S. Pandiyan, M. E. Kiziroglou and E. M. Yeatman, "Broadband Acoustic Power Transfer Using Reflection Characterisation and Impedance Matching", Smart Materials and Structures (PowerMEMS 2021 Special Issue) (Under Preparation)	
[67]	A. Y. S. Pandiyan, R. L. Rosa, M. E. Kiziroglou and E. M. Yeatman, "Understanding Far Field Ultrasonic Power Transmission for Automobile Sensor Networks in Free Space," *2019 19th International Conference on Micro and Nanotechnology for Power Generation and Energy Conversion Applications (PowerMEMS)*, Krakow, Poland, 2019, pp. 1-4.	Chapter 4
-	A.Y.S. Pandiyan, M. E. Kiziroglou and E. M. Yeatman, "3D Profiling of Misalignment and Misoreintation losses in Far-Field Acoustic Power Transfer" (under preparation)	
[68]	A. Y. S. Pandiyan, M. E. Kiziroglou, D. E. Boyle, S. W. Wright and E. M. Yeatman, "Optimal Energy Management of Two Stage Energy Distribution Systems Using Clustering Algorithm," *2019 19th International Conference on Micro and Nanotechnology for Power Generation and Energy Conversion Applications (PowerMEMS),* Krakow, Poland, 2019, pp. 1-4.	Chapter 5
[69]	A. Pandiyan, D. Boyle, M. Kiziroglou, S. Wright and E. Yeatman, "Optimal Dynamic Recharge Scheduling for Two Stage Wireless Power Transfer," in *IEEE Transactions on Industrial Informatics.* DOI: 10.1109/TII.2020.3035645	

1.3. Thesis Structure

This thesis presents the work on air based ultrasonic wireless power transfer for recharging low-power electronics. The thesis is divided into seven chapters as follows:

Chapter 1 briefly introduces the background and the motivation of this work, listing the research objectives and the thesis contents.

Chapter 2 presents the basic principles overseeing acoustic wave propagation through air and presents a comprehensive literature review on the state-of-the-art acoustic energy harvesters and wireless power transfer methods. Challenges of the current technology are identified, and strategies to address these issues are discussed.

Chapter 3 reports the applicability of different off-the-shelf transducers that can be utilized for APT systems, and the choice of transducers for this work is justified based on attenuation, diffraction, power density and safety guidance. The selected transducers' impedance-frequency profile was later measured to investigate the most suitable matching technique for optimum power delivery. Subsequently, the matching load impedance for operating frequencies near resonance was analytically and experimentally determined.

Chapter 4 analyses the sensitivity of the load voltage and power delivered by the APT receiver as a function of its separation distance from the transmitter, orientation, and alignment. The standing waves between the transducers due to reflection is also studied in detail. By utilising the impedance matching techniques from the previous chapter and frequency tuning, approaches to overcome the reflection losses are discussed in this chapter.

Chapter 5 employs the finding of the experimental data to develop a software that evaluates the efficiency of a *Two-stage power transfer system* for large industrial WSNs using power delivery vehicles and genetic clustering algorithms. This chapter describes the system model and presents the pseudocode of the various stages in the algorithm. The efficiency of the proposed wireless two-stage network is compared with the inductive power transfer network based on the network parameters, algorithm parameters, and computational demands.

Chapter 6 summarises the achievements in this thesis and discusses future works.

2. Literature Review

This chapter provides a detailed introduction to the field of acoustics and summarises the state-of-the-art Acoustic Power Transfer (APT) methodologies. The initial objective of this research is to provide an autonomous solution to charge Wireless Sensor Nodes (WSN) by APT with comparable efficiency with IPT systems in the far-field region. To achieve this, it is essential to understand the first principles relating to acoustic waves, particularly travelling through the air. Therefore, the basic concepts and equations overlooking wave propagation and sound pressure are outlined to understand the prospective and technological limitations. Subsequently, existing and emerging acoustic wireless power delivery techniques are reviewed and analysed for their potential application for powering WSNs.

2.1. Acoustic Physics

Acoustic waves are pressure variations or changes in density propagating through a medium by means of compression and rarefaction. This variation is produced through a vibrating source such as strings or electromechanical discs. Depending on the direction of energy transfer with respect to the wave oscillation/vibration direction, they can be classified as longitudinal or transverse waves. The oscillations are parallel to the direction of energy in the former, whereas they have a perpendicular relationship in the latter. Although sound can travel through solids in both modes, sound waves in the air are entirely longitudinal waves. This is due to the rigidity of solids, which makes them capable of resisting change in shape and therefore support transverse waves.

When a source applies a force to the air, the particles in its direct vicinity move in the exerted force's direction, causing a dense site in the medium. A vibrating source, in turn, causes both pushing and pulling forces resulting in areas with fewer and dense particles. These local changes in density correspond to local changes in pressure and particle velocity, which defines the characteristics of acoustic power transfer. In this section, the field of acoustic physics concerning sound propagation through the air will be discussed, summarising the equations for sound pressure distribution and velocity. Therefore, this section primarily depends on acoustic textbooks [70-75], which can be referred to for further knowledge in sound theory.

2.1.1. The Wave Equation

The propagation of an acoustic wave from a source at a finite speed is a function of the medium's elastic properties and density [73]. This function is governed by the wave equation, which can be derived from combining the derivation of the isentropic (adiabatic and reversible) equation of state (Eq. 2.1), linearised continuity equation (Eq. 2.3) and the linear form of Euler's equation (Eq. 2.4) [70, 74, 76].

Consider a system with pressure $\hat{P}_o$ and density ρ_o at equilibrium. Applying an acoustic field to the system would shift the pressure and density to $\hat{P}_t$ and ρ_t respectively, resulting in the isentropic equation of state:

$$\hat{P}_t - \hat{P}_o = \rho_o \frac{\partial \hat{P}_t}{\partial \rho_t} \left(\frac{\rho_t - \rho_o}{\rho_o} \right) = B \frac{\rho_t - \rho_o}{\rho_o} \tag{2.1}$$

where B is the adiabatic bulk modulus for the medium. By introducing a variable for the variation of pressure (acoustic pressure), $p = \hat{P}_t - \hat{P}_o$ and density $\rho = \rho_t - \rho_o$, the equation of state can be linearised as:

$$p = B \frac{\rho}{\rho_o} = c^2 \rho \tag{2.2}$$

where $c = \sqrt{\frac{B}{\rho_o}}$ is the speed of propagation of the acoustic waves in that medium.

The continuity equation defines the conservation of mass for the acoustic field as

$$\frac{\partial \rho}{\partial t} + \rho_o \nabla \cdot \vec{u} = 0 \tag{2.3}$$

where, the vector $\vec{u} = u_x\hat{x} + u_y\hat{y} + u_z\hat{z}$ represents the particle flow velocity in 3-dimensions over time t. Similarly, the conservation of momentum in three-dimensional space is defined by Euler's force equation as follows:

$$\nabla p + \rho_o \frac{\partial \vec{u}}{\partial t} = 0 \tag{2.4}$$

By taking the time derivative of Eq. 2.3 and the spatial derivative of Eq. 2.4, the respective equations Eq. 2.5 and Eq. 2.6 are derived.

$$\frac{\partial^2 \rho}{\partial t^2} + \rho_o \nabla \cdot \frac{\partial \vec{u}}{\partial t} = 0 \tag{2.5}$$

$$\nabla^2 p + \rho_o \nabla \cdot \frac{\partial \vec{u}}{\partial t} = 0 \tag{2.6}$$

By subtracting the above two equations and substituting the linearised equation of state (Eq. 2.2), the linearised lossless wave equation for acoustic propagation in fluids can be derived as:

$$\nabla^2 p - \frac{1}{c^2}\frac{\partial^2 p}{\partial t^2} = 0 \tag{2.7}$$

2.1.2. Acoustic Impedance, Intensity and Power

Intrinsically, sound waves are progressive waves that travel through matter to transfer energy from one place to another, but not matter. For an acoustic wave propagating along the x-axis, the pressure fluctuation ($p(x,t)$) is represented as a function of its particle velocity in phase travelling at the same direction ($u(x,t)$) is interpreted as:

$$p(x,t) = \rho_o c\, u(x,t) \tag{2.8}$$

where $Ƶ_o = \rho_o c$ is the specific acoustic impedance of the medium, that characterises the opposition of a medium to wave propagation. The specific acoustic impedance of air varies with temperature and humidity as it changes the density and speed of sound. For instance, $Ƶ_o = 428\, Pa\, s\, m^{-1}$ in the air at $0°C$ and $Ƶ_o = 409\, Pa\, s\, m^{-1}$ at $25°C$ [77].

$Ƶ_o$, however, depends only on the medium of propagation. When a source transmits sound energy into a medium, the size of the air mass pushed by the source should also be considered. This is defined by the acoustic impedance ($Ƶ$) of the medium to the source as:

$$Ƶ = \frac{Ƶ_o}{A} \tag{2.9}$$

where, A is the surface area of the source.

The acoustic properties of several materials of interest are listed in Table 2.1. As can be observed, the specific impedance of lead zirconate titanate (PZT) and air are very different. When waves propagate between mediums of differing impedance, a fraction of its amplitude is reduced along the boundary and reflected. This reflection loss due to impedance mismatch between mediums is comprehensively reviewed in Section 2.1.4.

As the sound waves propagate in a medium, the pressure variation along the propagation direction suggests the exchange of potential energy within the sound wave particles. Also, the particles vibrate along with their equilibrium, implying that they have kinetic energy. These forms of energy are retrieved to transfer power from the transmitter to the receiver. The instantaneous acoustic intensity ($\vec{I}(x,y,z,t)$) is defined as the power per unit area and can be calculated as the product of the incident acoustic wave pressure ($p(x,y,z,t)$) and acoustic particle velocity ($\vec{u}(x,y,z,t)$) as shown in Eq. 2.10.

$$\vec{I}(x,y,z,t) = \mathrm{p}(x,y,z,t) \cdot \vec{u}(x,y,z,t) \tag{2.10}$$

Correspondingly, the instantaneous acoustic power can be derived by integrating the sound intensity over the surface area in the direction normal to that surface. The sound pressure and power present in nature have a wide range in amplitude. To address this, a logarithmic scale is introduced to represent the root mean square value of the pressure variation relative to a reference value defined as the Sound Pressure Level (SPL).

$$\mathrm{SPL} = 20 \log\left(\frac{\mathrm{p_{rms}}}{\mathrm{p_{ref}}}\right) \mathrm{dB} \tag{2.11}$$

where, $p_{ref} = 20\ \mu Pa$. As the sound power intensity depends on the squared value of the pressure, the effective sound power can similarly be represented as Sound Power Level (SWL) in the logarithmic scale, measured in dB. SWL at a distance d from the source with directivity factor D can be expressed as:

$$\mathrm{SWL} = 20 \log\left(\frac{\mathrm{p_{rms}}}{\mathrm{p_{ref}}}\right) - 10 \log\left(\frac{D}{4\pi d^2}\right) dB \tag{2.12}$$

Table 2.1: Acoustic properties of several materials considered in this work.

Material	Density [$\mathrm{kgm^{-3}}$]	Acoustic Velocity [$\mathrm{ms^{-1}}$]	Acoustic Impedance [MRayls]
Air (25° C)	1.2	346	4.09 x 10^{-3}
Water (20° C)	1000	1480	1.48
PZT	7500 ~ 8000	4000 ~ 5000	30 ~ 40
ABS	1050	2250	2.4
Polystyrene	930	2400	2.2
Acrylic Plastic	1180	1430	1.6

2.1.3. Propagation of Waves

In this section, two simple sound wave types are considered to study the variations of the acoustical variables, such as the sound pressure and particle velocity as a function of their spatial distribution. For this, plane waves and spherical waves are considered due to their simplicity. Understanding wave propagation would be essential to explain phenomena such as attenuation, reflection, and refraction in the next section.

- **Plane Waves**

Plane waves are the sound wave of which the acoustical variables only depend on one spatial coordinate. In any given instant, all variables are constant in the plane perpendicular to that coordinate direction. Assuming a plane wave travelling along the x-axis, the wave equation (Eq. 2.7) can be simplified as:

$$\frac{\partial^2 p}{\partial x^2} - \frac{1}{c^2}\frac{\partial^2 p}{\partial t^2} = 0 \tag{2.13}$$

As illustrated in [72], the general solution for this expression can be derived as:

$$p(x,t) = f(x - ct) + g(x + ct) \tag{2.14}$$

where, the first term of the expression $p(x,t) = f(x - ct)$ represents that an initial disturbance $f(x)$ at time $t = 0$ will be shifted by a distance ct for every increasing t and is resistant to any shape or phase changes. The second term represents the same result but in the opposite x-direction. Thus, parallel surfaces perpendicular to the x-axis (propagation axis) will have the same vibrational state and phase (Figure 2.2 (a)).

The particle velocity associated with this pressure distribution would also have the general solution $u = x - ct$. Therefore, simplifying the Euler's equation (Eq. 2.4) for x-axis propagation and substituting the solution will derive:

$$\frac{\partial p}{\partial u} - \rho_o c \frac{\partial v_x}{\partial u} = 0 \tag{2.15}$$

where, v_x is the velocity of the wave in the x-direction. Implementing indefinite integral and ignoring the constant, the expression can be reduced to:

$$v_x = \frac{p}{\rho_o c} = \frac{p}{Z_o} \tag{2.16}$$

Hence, the particle velocity of a plane wave is proportional to the pressure distribution governed by the specific acoustic impedance of the medium.

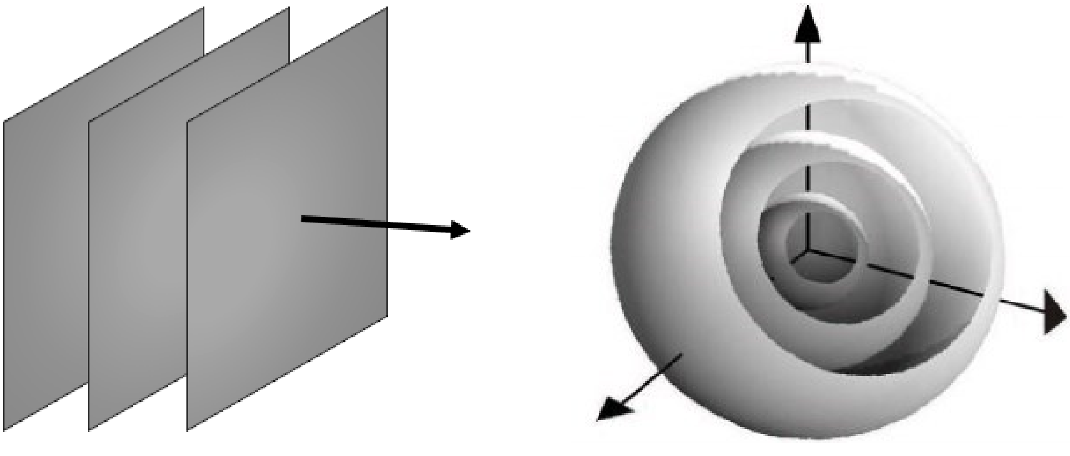

(a) (b)

Figure 2.1: Propagation of simple types of sound waves (a) Plane waves (b) Spherical waves from [78].

Now, going back to Eq. 2.2, the sound velocity for an adiabatic state can be derived as:

$$c = \sqrt{\left(\frac{\partial \hat{P}_t}{\partial \rho_t}\right)_{\rho_o}} \tag{2.17}$$

The equation of state for perfect gas is given as:

$$\frac{\hat{P}_t}{\hat{P}_o} = \left(\frac{\rho_t}{\rho_o}\right)^{\kappa} \tag{2.18}$$

where the constant κ is the adiabatic or isentropic exponent and $\kappa_{air} = 1.4$. By differentiating Eq. 2.18 and substituting in Eq. 2.17:

$$c^2 = \left(\frac{d\hat{P}_t}{d\rho_t}\right)_{\rho_o} = \frac{\kappa\hat{P}_t}{\rho_t} \approx \frac{\kappa\hat{P}_o}{\rho_o} \tag{2.19}$$

Furthermore, the general equation of state for perfect gas is defined as:

$$\frac{\hat{P}_t}{\rho_t} = \frac{RT}{M_r} \tag{2.20}$$

where, T is the absolute temperature, $R = 8.31 N\, m\, mol^{-1}$ is the molar gas constant and M_r is the molecular mass of the gas composition. From combining Eq. 2.19 and Eq. 2.20, the sound velocity of a perfect gas can be concluded as:

$$c = \sqrt{\frac{\kappa RT}{M_r}} \tag{2.21}$$

- **Spherical Waves**

Although more complicated waveforms can be broken down into plane waves as harmonic waves, spherical waves are a more realistic approximation for sound waves from a point source. The propagation of a spherical wave is illustrated in Figure 2.1 (b). Comparing Figure 2.1 (a) and (b), for a distance r from the source while the sound intensity stays constant for plane waves, it decreases for spherical waves as the surface area of the sphere increases.

The pressure distribution of spherical waves can be obtained by simplifying the wave equation and adopting spherical polar coordinates for its quantitative analysis [72].

$$\frac{\partial^2 p}{\partial r^2} + \frac{2}{r}\frac{\partial p}{\partial r} - \frac{1}{c^2}\frac{\partial^2 p}{\partial t^2} = 0 \tag{2.22}$$

Substituting $p(r,t) = f(r,t)/r$ in Eq. 2.22 to obtain the one-dimensional form:

$$\frac{\partial^2 \mathrm{f}}{\partial \mathrm{r}^2} - \frac{1}{\mathrm{c}^2}\frac{\partial^2 \mathrm{f}}{\partial \mathrm{t}^2} = 0 \tag{2.23}$$

Analogous to the solution obtained for plane waves in Eq. 2.14, the pressure distribution of a spherical wave can be represented as:

$$\mathrm{p}(r,t) = \frac{1}{r}\mathrm{f}(r - ct) \tag{2.24}$$

This expression signifies that the pressure wave is radially expanding and is travelling in the direction of increasing r values. This behaviour is reasonable since the intensity of spherical waves becomes weaker during propagation. Similar to Eq. 2.14, the solution $p(r,t) = \frac{1}{r}g(r+ct)$ is also valid, however this implies a contracting spherical wave towards $r\ = 0$ which is not realistic. Therefore, the second term is omitted.

For calculating the particle velocity of the spherical wave, Eq. 2.4 is converted into its radial components and substituting a radial velocity v_r for $\vec{u}$,

$$\frac{\partial p}{\partial r} + \rho_o \frac{\partial v_r}{\partial t} = 0 \tag{2.25}$$

Replacing the time differential with a multiplication factor of $j\omega$ yields,

$$\mathrm{j}\omega\rho_o v_r = -\frac{\partial p}{\partial r} \tag{2.26}$$

where, ω is the angular velocity of the spherical wave.

Consider spherical wave radiation of surface area $4\pi r^2$, the time derivative of its volume velocity $(Q(t))$ is equivalent to $\dot{Q}(t) = \frac{4\pi}{\rho_o} f(-ct)$ for $r\ \to 0$ and neglecting the higher derivatives. Combining $f(t)$ from this and the harmonic volume velocity $Q(t) = \hat{Q}e^{j\omega t}$ with Eq. 2.24, gives:

$$p(r,t) = \frac{j\omega\rho_o\hat{Q}}{4\,\pi r}\ e^{j\,(\omega t\,-\,kr)} \tag{2.27}$$

$$\frac{\partial p}{\partial r} = \frac{j\omega\rho_o\ \hat{Q}}{4\pi r}\left(-\frac{1}{r} - jk\right) e^{j(\omega t\,-\,kr)} = -\left(\frac{1}{r} + jk\right) p(r,t) \tag{2.28}$$

where, $k\ =\ \omega/c$ is the wavenumber. Substituting Eq. 2.28 in Eq. 2.26 leads to,

$$v_r = \frac{p(r,t)}{\rho_o c}\left(1 + \frac{1}{jkr}\right) \tag{2.29}$$

Clearly, the particle velocity and the sound pressure are not in phase. For minimal distances, the imaginary term prevails, causing a 90° phase shift between the particle velocity and the sound pressure. However, for very large distances $(kr \gg 1)$ in far field and therefore $(r \gg \lambda)$, the ratio of v_r and $p(r,t)$ approaches the specific acoustic impedance, $Z_o = \rho_o c$. In physical terms, this can be interpreted as, at farther distances from the centre of the source, the curvature of the spherical waves becomes trivial, and they can be approximated as plane waves. The limit in which this prevails depends on the wavelength and the sound frequency, partitioning the propagation medium into the 'near-field' and 'far-field' regions.

- **Circular Piston Sound Source**

Prior to investigating the near-field and far-field attributes, it is practical to understand the properties of the sound source radiating the pressure field. Abstractly, a sound source is observed as a point source located at the origin of the propagation medium. In this work, the behaviour of sound sources can be treated as a disc-shaped planar source imitating a piston-like action, vibrating with uniform amplitude (Figure 2.2). According to the Huygens principle, the behaviour of such sources can be derived from treating each point on the radiating surface as a point source, and the acoustic field at any point of interest is the vector sum of contributions from all point sources [74].

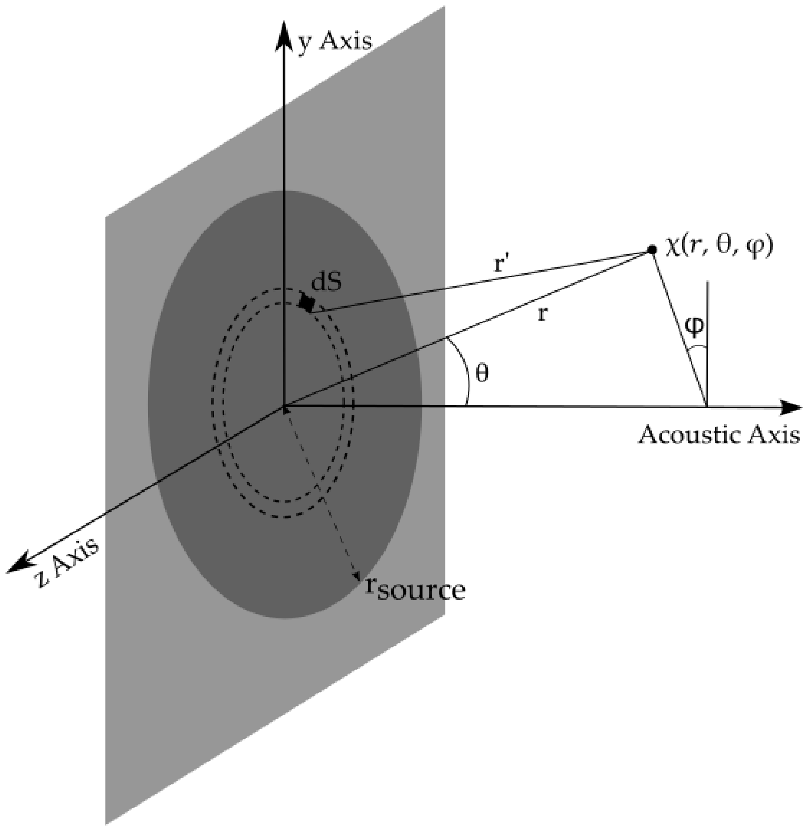

Figure 2.2: Geometry of a circular-piston transducer along with the definition of coordinates.

Consider a symmetric disc source of radius r_{source} and area S with fixed back plate. This radiates sound only in the forward direction (half-sphere) at a harmonic particle velocity of $v_o = \hat{v}_o e^{j\omega t}$ at the surface. Assuming a point $\chi(r, \theta, \varphi)$ at $r \gg r_{source}$, the total sound pressure will be [72]:

$$p(r, \theta, t) = \frac{j\omega\rho_o\hat{v}_oS}{2\pi r} \cdot \frac{2J_1(kr_{source}sin\theta)}{kr_{source}sin\theta} e^{j(\omega t-kr)} \tag{2.30}$$

where, J_1 is the 1st order Bessel function and k is the complex wavenumber, $k = \beta^2 + \alpha^2$ in which $\beta = \omega/c_o$ is the phase speed and α is the attenuation/absorption coefficient of the propagation medium. Hence the directionality factor of the circular piston defined as the ratio between the pressure at any angle θ to the propagation axis is represented by,

$$\mathrm{D}(\theta) = \frac{2J_1(ka\ sin\theta)}{ka\ sin\theta} \tag{2.31}$$

Consequently, the directivity of the transmitting transducer depends on the factor $ka = \frac{2\pi r_{source}}{\lambda}$, which is the ratio of the perimeter of the transducer to the wavelength. On the acoustical axis, Eq. 2.30 can be further simplified as $\theta = 0$.

$$p(r,t) = \rho_o c \hat{v}_o \left(e^{j(\omega t - kr)} - e^{j\left(\omega t - k\sqrt{r^2+a^2}\right)}\right) \tag{2.32}$$

This equation expresses two plane waves with opposite phases, one originating from the centre and the other from the rim of the transducer, and they interfere with each other. In this work, the pressure distribution field and the transducers' directivity will be comprehensively investigated and discussed in Chapter 3.

- **Near- Field and Far-Field**

As already stated, the characteristics of the sound wave change with respect to the distance from the source. The Near Field (NF) is close to the radiating surface where the absolute sound pressure oscillates and has multiple minima and maxima (Figure 2.3). This is mainly due to the pressure wave generated by the piston's centre interfering with that from the rim. When an APT receiver is placed in this region, it makes the transferrable power unpredictable. The boundary of the NF region located L distance away from the source is characterised as:

$$L = \frac{(2a)^2 - \lambda^2}{4\lambda} \tag{2.33}$$

Beyond the NF region is the Far Field (FF), in which the pressure envelope becomes more predictable and smoother. However, the radiation beyond the NF boundary experiences spherical spreading, resulting in intensity decay with increasing distance. In some literature, the small region surrounding L is considered the 'Transition Field' or 'Natural Focus' [56].

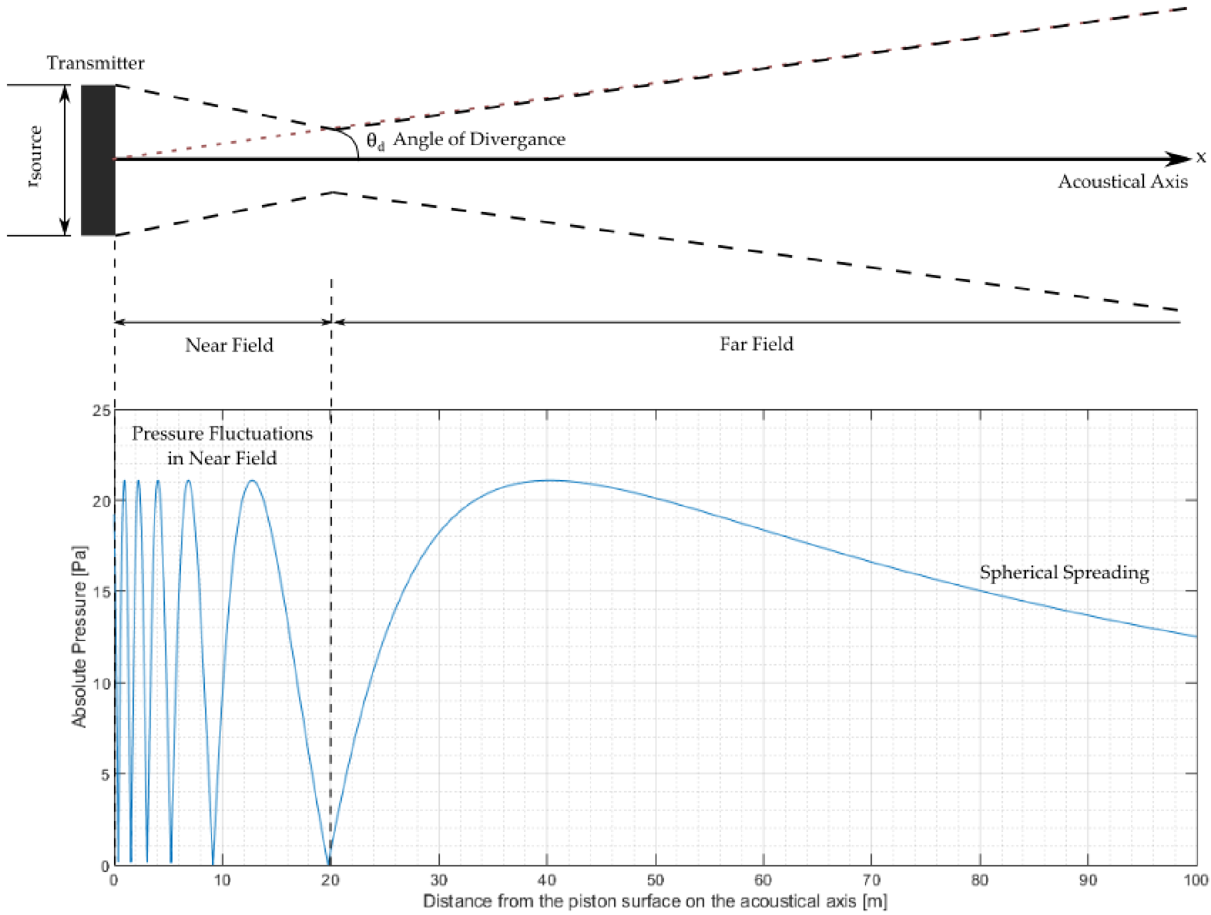

Figure 2.3: Variations in the magnitude of absolute pressure along the acoustical axis of a circular piston transmitter with $kr_{source} = 30$.

2.1.4. Acoustic Propagation Losses

The energy of the sound wave depletes during its propagation through a medium through various dissipative processes. Since discussing the theory of sound dissipation in different mediums and deriving their wave equation is beyond the scope of this thesis, this section aims to provide only a short introduction of such propagation losses focussing on sound waves travelling in a gaseous medium. More comprehensive insight can be found in the standard literature on acoustics, such as [72, 79].

- **Attenuation of Sound**

Until now, the formulations of the acoustic variables are based on the assumption that all changes of state are adiabatic. However, the compressions and the rarefactions of the air particles carrying the sound wave are accompanied by local variations in temperature. This results in a loss of energy in the form of heat as the wave propagates through air. An absorption coefficient (α) is introduced (as briefly described in Eq. 2.30) to the angular wavenumber to account for such losses.

Deriving the value of α is demanding research in itself, as it is a function of the air temperature, relative humidity, atmospheric pressure, frequency and gas composition. Bass *et al.* and his group have accomplished comprehensive research on the analytical model of energy transfer mechanisms in an air mixture and have published experimentally validated values for this attenuation coefficient [80-82]. For this work, the data from the available literature is assumed.

- **Impedance Mismatching and Reflection**

A sound wave arriving at the boundary between two different media is partly thrown back by the extended surface (Reflection), and the remainder changes its direction by an oblique angle when it penetrates the interface (Refraction). The amount of sound pressure reflected at the surface for a sound wave travelling from a medium of acoustic impedance Z_1 to Z_2 at normal incidence is defined by a reflection coefficient related by [83]:

$$\Gamma = \frac{\hat{P}_r}{\hat{P}_i} = \frac{Z_2 - Z_1}{Z_2 + Z_1} \tag{2.34}$$

Expressly, it is defined as the ratio between the amplitude of the incident (P_i) and the reflected (P_r) pressure. As this work focuses on APT in the far-field range, the curvature of the spherical waves from the source is negligible and can be considered as plane waves. For a plane wave approaching the surface at an angle θ_1, a part of the wave is penetrated and reflected at angles θ_2 and θ_3 respectively (Figure 2.4(a)). The refraction is governed by Snell's law defined by [84]:

$$k_1 sin(\theta_1) = k_2 sin(\theta_2) \tag{2.35}$$

where k_1 and k_2 are the wavenumber of the waves in the respective medium.

Then, the reflection coefficient would be a function of the incident and the reflected angle expressed as:

$$\Gamma(\theta) = \frac{Z_2 cos(\theta_1) - Z_1 cos(\theta_2)}{Z_2 cos(\theta_1) + Z_1 cos(\theta_2)} \tag{2.36}$$

and the transmission coefficient (T) is expressed as:

$$T = \frac{2\, Z_2\, cos(\theta_1)}{Z_2 cos(\theta_1) + Z_1 cos(\theta_2)} \tag{2.37}$$

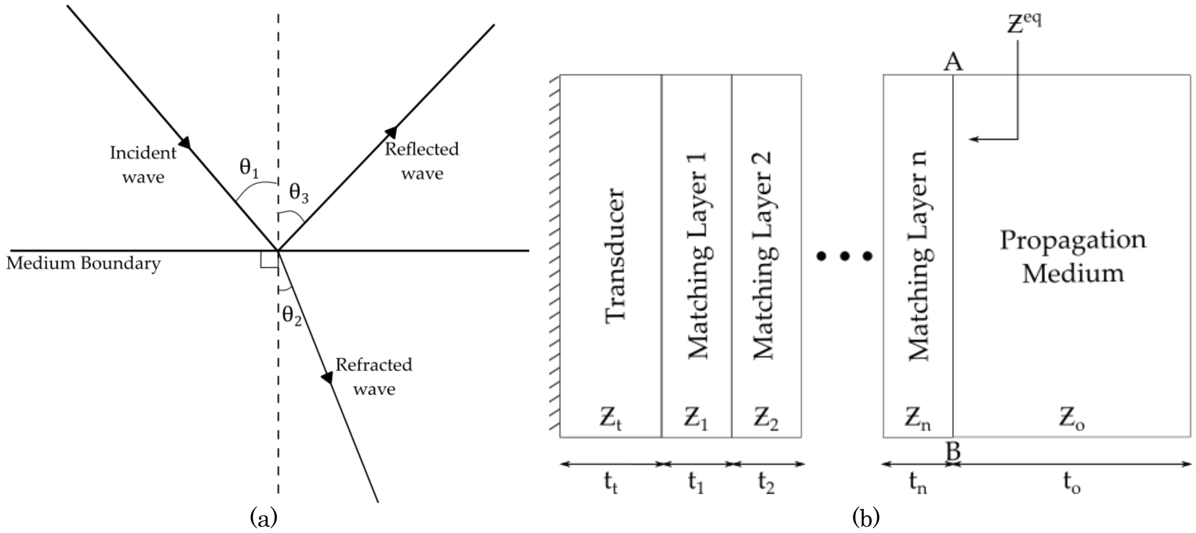

Figure 2.4: Reflection and impedance matching for acoustic wave propagation (a) Parameters defining reflection at a local boundary (b) Schematic description of multilayer impedance matching technique.

Accordingly, the absorption coefficient is related to the sound intensity by:

$$\alpha = \frac{I_i - I_t}{I_i} = 1 - |\Gamma|^2 \tag{2.38}$$

For this reason, if the difference between the impedances and the sound velocity of the travelling medium differs immensely, the reflection coefficient will be more significant, leading to smaller wave penetration and high absorption. For a piezoelectric transducer, the acoustic mismatch between the ceramic and the propagation medium is modelled by a high unloaded mechanical quality factor ($Q_m = 500 - 1800$) [85], which narrows the range of operating frequencies near the series resonant frequency [56]. Therefore, it is essential to tune the frequency of the transmitter-receiver pair and to match the acoustic impedance of the transducer and the medium. In addition, the reflected wave superimposed with the source wave results in local peak pressure recognised as standing waves. The effects of standing waves in the far-field are analysed and experimentally studied in Section 4.1.

Several impedance matching techniques are based on either single layer or multilayer matching [57]. The simplest impedance matching technique applies a thin layer of $\lambda/4$ thickness between the transducer and the propagation medium. For optimal matching, the impedance of the matching layer $Z_{matching}$, should be close to the value [86]:

$$Z_{matching} = \sqrt{Z_{PZT} \cdot Z_{medium}} \tag{2.39}$$

and have low losses at the operating frequency. However, finding material with properties close to this exact value would restrict the system design. Multilayer matching provides freedom to choose the matching material and design the layer profile [87-92]. Figure 2.4(b) shows a multilayer impedance matching with n layers fabricated on the transducer. The specific acoustic impedance of the medium, the matching layers and the transducers are represented as $\mathbb{Z}_o$, $\mathbb{Z}_i$ (where $i = 1,2,\cdots,n$), and $\mathbb{Z}_t$ respectively. Assume the corresponding layers have thickness t_o, t_i and t_t respectively. A transfer matrix is defined for each layer of impedance matching that represents the relation between pressure and normal particle velocity at either boundary, satisfying the continuity of the pressure and the continuity of the normal component of particle velocity [87]. Therefore, the transfer matrix of the nth material layer with impedance $\mathbb{Z}_n$ and thickness t_n is given by:

$$T_n = \begin{bmatrix} cos(k_n t_n) & j\mathbb{Z}sin(k_n t_n) \\ \frac{jsin(k_n t_n)}{\mathbb{Z}_n} & cos(k_n t_n) \end{bmatrix} \tag{2.40}$$

where k_n is the wave number in the nth material. Assuming that the thickness of the transducer, $t_t \gg t_n$, the equivalent transfer matrix is the product of all the layers as,

$$T^{eq} = T_1 T_2 \cdots T_n = \begin{bmatrix} T_{11}^{eq} & T_{12}^{eq} \\ T_{21}^{eq} & T_{22}^{eq} \end{bmatrix} \tag{2.41}$$

and the equivalent impedance $\mathbb{Z}^{eq}$ at the ports of the medium AB (Figure 2.4 (b)) is,

$$\mathbb{Z}^{eq} = \frac{T_{11}^{eq}\mathbb{Z}_p + T^{eq}12}{T_{21}^{eq}\mathbb{Z}_p + T^{eq}22} \tag{2.42}$$

This represents a complex interaction between the transmitted and reflected waves in each boundary of the system. Utilising the transfer function matrix, the boundary transfer function between two media can also be used for focusing acoustic beams by introducing metamaterial ‘acoustic lens’ structures in the propagation medium [93-97]. Currently, these air-borne acoustic lenses are primarily used for focusing acoustic imaging and position sensing systems. Alternatively, the impedance of the source can be reduced by choosing polymer piezoelectrics like Polydimethylsiloxane (PDMS) or porous ceramics. This reduces the intensity of acoustic waves reflected in the source-medium boundary.

2.2. Acoustic Power Transfer

Acoustic energy in its purest form is utilised in many industrial and medical applications like ultrasonic cleaning, Sound Navigation and Ranging (SONAR) systems, ultrasonic imaging, and non-destructive testing techniques. In these applications, the ultrasonic energy is used for detection or converted to heat energy (like ultrasonic welding) without converting back into electrical energy. In APT systems, however, the ultrasonic signal is transmitted as pressure waves from the transmitter and converted from mechanical to electrical energy to power or recharge a sensor node (Figure 2.5). Before reviewing the state-of-the-art APT systems, the functionalities of its components are discussed in detail.

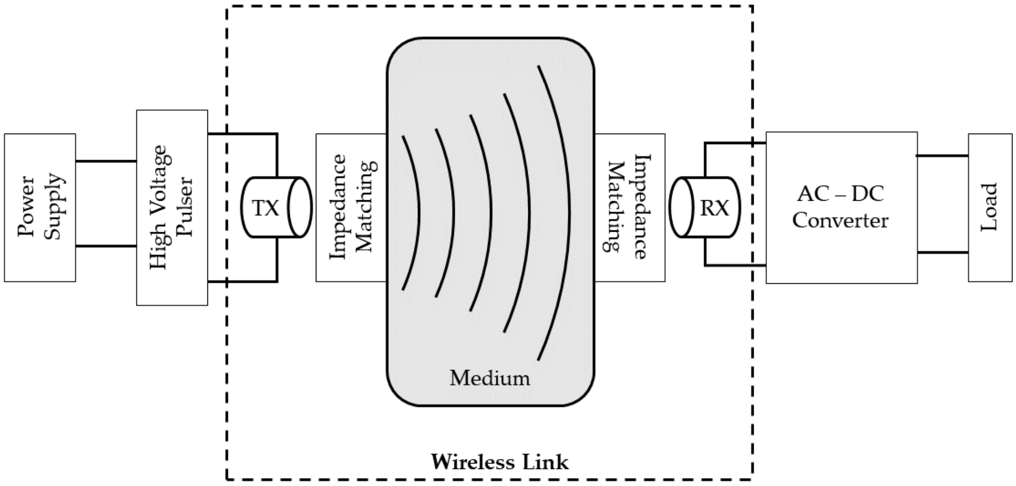

Figure 2.5: Typical schematics of an acoustic power transfer system.

A continuous electric signal is applied to the transmitter through a power amplifier. The transmitter is typically a PZT disk that can convert an electrical signal to mechanical vibrations through the inverse piezoelectric effect. Subsequently, these mechanical vibrations are transmitted to the receiver through a medium as pressure waves. When pressure waves travel between two different materials, a part or whole of the signal could be reflected in the opposite direction due to the acoustic impedance mismatch. Therefore, to effectively transfer the pressure waves between the transducer and the medium, an impedance matching layer can be added to the transmitter and the receiver. Then, the sound energy captured by the receiver is harnessed as electricity via the piezoelectric effect using similar PZT disks. The generated electricity, at this point, is an alternating voltage that needs to be rectified and regulated for charging or powering sensor nodes. However, as the frequency of the received power is known, a simple AC-DC full bridge rectifier in parallel can efficiently convert the voltage into DC form for reasonable receiver voltage.

Besides its frequency, the mechanism used to transmit sound waves depends on the medium between the transmitter and the receiver. Consequently, the current research on acoustic power transfer can be categorised as fluids, metal, and air medium transmission. This section describes the existing and emerging research on these APT systems.

2.2.1. Fluid or Tissue Transmission Medium

Cochran *et al.* [52] first pioneered ultrasonic power transmission in 1985 for electrical augmentation of Osteogenesis, where a current is delivered to the bone fracture site to aid healing. In this work, the authors proposed two configurations using bimorph PZT-5 plates incorporated in a fixation device placed in contact with the bone for transducing mechanical movements into electrical energy, as shown in Figure 2.6(i). Firstly, this implant can generate adequate current to assist Osteogenesis by harvesting the stress due to physiological loading. Alternatively, the device can be externally activated by a direct piezoelectric effect when a non-invasive low-level ultrasonic signal of $2.25\ MHz$ is applied to the skin. *In vivo* experimentation of this ceramic device in canine femur bone produced voltage up to $600\ mV$. After tuning the transmitter frequency for maximised power transfer, an average current of $100\ \mu A$ were recorded after half-wave rectification, providing peak energy of $10\ mWcm^{-2}$.

Batteries take up the most volume in medical implants, making them difficult for integration. For the device mentioned above, where the operating frequency is $2.25\ MHz$, and the speed of sound in human tissue is approximately $1400 - 1600\ ms^{-1}$, the wavelength of sound is in the range of $0.6 - 0.7\ mm$. This reduces the overall dimensions of the APT supported devices drastically, making them an attractive solution for powering implanted devices [62]. Following Cochran *et al.,* many researchers published innovative work dealing with APT systems for powering medical implants [56, 57, 98, 99].

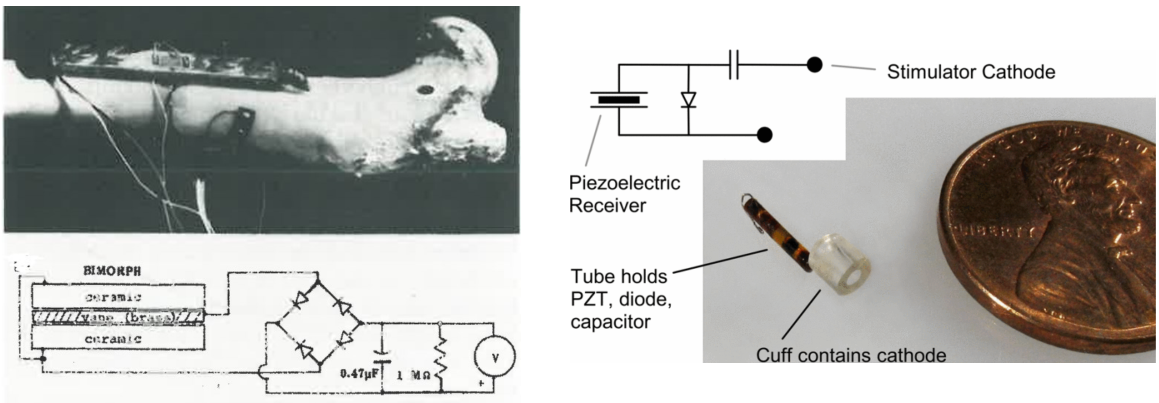

(i) (ii)

Figure 2.6: Biomedical implants powered by wireless acoustic power transfer (i)Laminated bimorph fixture mounted on a canine femur for testing and its corresponding schematics of the measuring circuit used during loading [52]. (ii) Nerve simulator cuff for exciting the sciatic nerve bundle in a limb. The device encloses a PZT receiver, rectifier and cathode coated with epoxy and sealed in a polyimide tube[53].

Larson and Towe [53] demonstrated a miniature nerve cuff stimulator of 8 mm length, 1 mm thickness and 1.13 mm diameter to produce electrical currents for clinical therapy (Figure 2.6(ii)). This device was tested by implanting it in a rat hind limb near the sciatic nerve, providing a separation distance of 12 cm between the transmitter and the receiver to avoid near-field complications. When supplied with a source signal of 1 MHz, the *in vivo* testing generated a 1 mA current with pulse intensities ranging up to $10 - 150\ mWcm^{-2}$.

Charthad *et al.* later in [54] illustrated the possibility of fabricating an mm-sized device for both APT and data transfer. The authors prototyped a device of 4 mm by 7.8 mm in dimension consisting of an ultrasonic transducer working at a frequency of 1 MHz, a CMOS IC and an off-chip antenna. It provides the potential to transduce the ultrasonic waves for power along with a hybrid bi-directional data link consisting of an ultrasonic downlink and RF uplink. The device was implanted 3 cm into chicken meat to resemble human muscle characteristics during testing, which successfully transferred 100 μW power, resulting in a power density of 71 $mWcm^{-3}$. This possibility of transferring power and establishing a data link has been explored by many researchers [100-106]. They all employ piezoelectric ultrasonic transducers for power and data transfer, predominantly at very high frequencies (MHz range) [107].

Meng and Kiani [55] further explored the potential and limitations of mm-sized APT devices for biomedical application by modelling and optimising sound beams for disc-shaped transmitters of 1 mm^3 device operating at 1.1 MHz frequency. They experimentally tested the device with the derived optimised parameters when immersed in a tank of castor oil (emulating blood characteristics). They measured a power transfer efficiency of 0.65 % for a 3 mm separated distance between the transmitter and the receiver, which validated the simulated efficiency of 0.66 % for a 2.5 $k\Omega$ load. However, data on the measurement of output power was not included in the script.

Similarly, Ozeri and Shmilovitz in [56] proposed an APT device to power implanted microdevices. The APT system consists of a piezoelectric receiver (Figure 2.7) 15 mm in diameter and 3 mm in thickness with a graphite impedance matching layer and operating at 673 kHz. The system reached a power transfer efficiency of 27 % when the transducers were separated by 5 mm, delivering 70 mW power to the load. This work also contributed considerably to analysing an APT system's main design parameter in fluids, such as frequency selection, acoustic impedance matching, and power conditioning circuit design for the receiver. Therefore, building a detailed finite element model (FEM) model in order to study the acoustic pressure field generated by the transmitter and analyse the optimised position of the receiver for maximum power transfer.

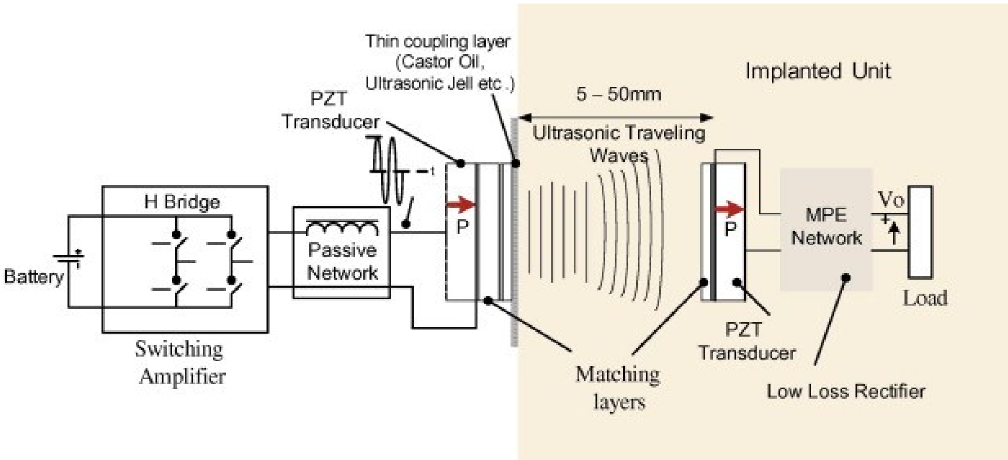

Figure 2.7: Acoustic power transfer system with graphite matching layer for powering biomedical microdevices (from [56]).

The same group later improved the APT setup by exciting the transmitter through gaussian radial distribution instead of a continuous switching signal to reduce the acoustic field-side lobes, resulting in a more focused beam. This was achieved by fabricating the same PZT device patterned with an electrode surface divided into six concentric elements of $23\,mm^2$ area each. The measured power transfer efficiency improved to $39.1\,\%$ at $5\,mm$ separation distance and $650\,kHz$ operating frequency, delivering $100\,mW$ to the load. The authors also stated that this efficiency reduces to $17.6\,\%$ at a $40\,mm$ separation distance, delivering $45\,mW$ power to the load, which is still sufficient for most biomedical implants.

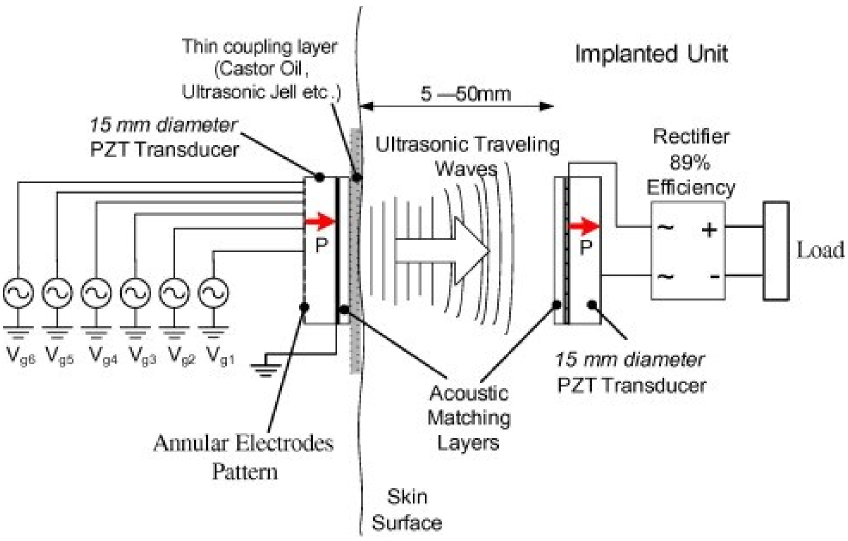

Figure 2.8: Improvised acoustic power transfer system proposed in [57], introducing Gaussian radial distribution excitation for the transmitter. (from [57])

Further to the transmitter design, they later proposed a non-invasive method for measuring the acoustically transferred power through an inductive link and an algorithm to monitor the harvested power [108]. This is achieved by affixing a passive impedance (inductor fabricated by 10 turns of 34 AWG magnet wire) whose electrical characteristics change depending on the level of power captured by the receiver. Therefore, this monitoring device consumes negligible power. The data of the change in impedance is then monitored externally to compute the transferred power.

Most application-focused biomedical APT systems are designed for the biosensor's specific energy needs, and further optimisation is not considered once the specifications are met. However, researchers try to extract as much power as possible from the receiver for general-purpose solutions. For this, essential losses such as attenuation, diffraction and reflection must be considered during the design stage. Among the listed, reflection between the transducer surface and the medium is the leading cause for efficiency losses of an APT system. Shigeta *et al.* [109] proposed a water-based ultrasonic power transmission system coupled with a Cockcroft-Walton circuit to rectify and boost the output voltage. However, due to the high impedance of the rectifier and the lack of acoustic matching between the transducer and water, the authors only managed to achieve a 1% power transfer efficiency. The same group further investigated the impedance mismatch and simulated an ANSYS model to optimise the circuit parameters to maximise the output power from the receiver [100]. The improvised design demonstrated an improved transfer efficiency by around 50 % experimentally for a separation distance of 32.3 mm, delivering 10 mW power to the load [77].

Denisov and Yeatman [110] proposed a novel micro-actuator implant directly powered by ultrasonic waves instead of electrical power conversion for functions such as drug release or mechanical adjustments of prosthetic devices. This is achieved by designing a receiving membrane coupled to a discrete oscillator capable of converting the acoustic energy into motion, as shown in Figure 2.9. The microactuator has an active area of 0.5 mm^2 and 55 μm thick and is fabricated using silicon and silicon dioxide. The coupling elements play a crucial part in translating the vertical motion to lateral oscillation. The device produced 9.6 – 9.9 μm vibration amplitude with an amplification factor between 240 – 250 for separation distance up to 5 mm when tested experimentally.

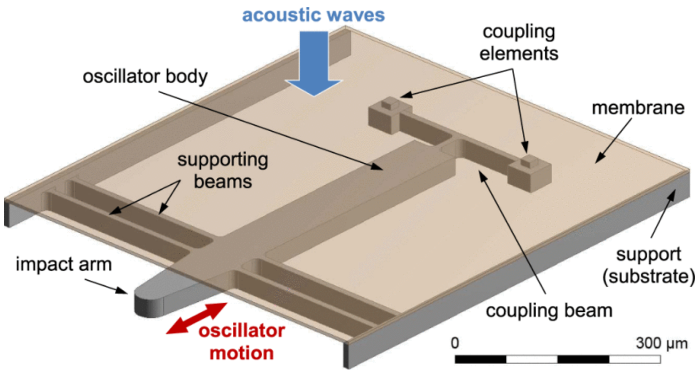

Figure 2.9: Micromachined mechanical oscillator powered by acoustic energy coupling vertical motion into lateral motion [110].

The majority of the publications discussed so far are most efficient in the mm-range of separation distances, and the power transfer efficiency decreases for longer distances. Therefore, to access deeply implanted devices, Sanni *et al.* [103] proposed a multi-tier interface that combines inductive and acoustic transfer methods to transfer sufficient power and collect and transmit data from the implants (Figure 2.10). Initially, an inductively coupled PCB spiral coil transmits $5\,W$ power across $10\,mm$ of air gap with 83 % efficiency using a prototyped CMOS driver. The rectified power from the secondary coil then drives an ultrasonic transmitter at $200\,kHz$ to power an ultrasonic receiver $70\,mm$ away, improving the range of the wireless power link to $80\,mm$. The simulation results demonstrated a power transfer efficiency of 1 %, delivering $8\,mW$ power to the implant. This power can adequately recharge an implant operating at a frequency of $500\,kHz$ to transmit 4 bits of information over an $18\,msec$ time period. Although this is limited by the transfer efficiency of the ultrasonic link, many prospective improvements can improve the efficiency, such as adapting the APT driver circuits or adding an impedance matching layer for the transducers.

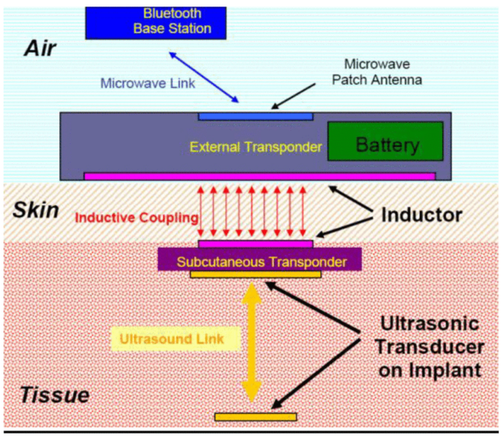

Figure 2.10: System architecture block diagram of a two-tier inductive acoustic power transfer link for deeply implanted devices (from [103]).

Mazzilli *et al.* [111] designed a wireless ultrasonic transcutaneous link for implanted devices located 10.5 cm deep. Considering biological side effects such as cavitation, a 1 MHz source signal is transmitted from a transmitter of active area 2880 mm^2 to a receiver of active area 50 mm^2. *In vivo* testing of the proposed device in a testing water tank showed a power transfer efficiency of 2.3 %. The device was also tested with a phantom material developed by *Institut National de la Santé et de la Recherche Médicale* (INSERM) to mimic human tissue, and the efficiency dropped to 1.6 %. This is because biomedical devices aiming to be implanted in human tissue should not be tested in water as the propagation losses in water (0.002 $dB\ cm^{-1}MHz^{-1}$) are much higher in tissue (0.9 $dB\ cm^{-1}MHz^{-1}$) [112]. Moreover, the correlation between the propagation losses and the power transfer efficiency of the system is non-linear due to factors such as wave spreading and reflection in the medium. Therefore, the difference in the magnitude of the propagation losses in the test and the applied medium should be as negligible as possible.

Apart from reflective and propagation losses, the orientation and alignment of the receiver with respect to the transmitter is also an important design parameter to consider for APT systems. However, publications investigating the power delivered to the load as a function of offset and angle are limited [56, 108, 113-119]. Christensen and Roundy [120] analysed such important misalignment issues comprehensively in an APT system for biomedical implants. The authors inspected the voltage and power sensitivity of circular piezoelectric transducers (with titanium matching layers) to variations in separation distances, operating frequency, receiver diameter and alignment variations. They proposed four design graphs to define the voltage and power of an APT system: depth magnitude (function of separation distance), depth fluctuation (function of fluctuations due to standing waves), half-angle (the angle at which the power is half of its zero-angle-zero-offset value) and half offset (distance at which the power is half of its zero-angle-zero-offset value). These plots aid system designers to compute the range of uncertainty that can be expected from the system.

Misalignment issues, in general, can be addressed by miniaturising the receiver, allowing freedom of movement for the receiver with the main acoustic lobe of large transmitters. It consequently reduces the bulkiness of the APT device, diminishing the effect of voltage fluctuations due to standing waves. However, this will reduce the power generated by the receiver; thus, a balanced system design is essential. To achieve this, Shi *et al.* [121] fabricated a micro-electromechanical system (MEMS) device that consists of PZT diaphragm arrays with broad operational bandwidth. This device was termed a

Piezoelectric Ultrasonic Energy Harvester (PUEH) and acted as the APT receiver, capable of minimising the standing wave effect by tuning the frequency. *In vitro* testing with a water tank showed six times increase in output power (from 0.59 μWcm^{-2} to 3.75 μWcm^{-2}) at 1 cm between the transducers by just tuning the frequency from 250 to 240 kHz for that distance. The separation distance was increased to 2.3 cm, and a 6 mm pork tissue was introduced between the transducers to resemble human tissue. However, when the operating frequency is 370 kHz, only 16.5 nW power delivered to the load. By tuning the PUEH to 330 kHz, the output power increased to 85.2 nW. This device attracted many researchers, given its favourable size for easy chip integration with existing implants. This unwrapped the possibility of using piezoelectric Micromachined Ultrasonic Transducers (pMUT) consisting of an array of small-diaphragm structures using PZT for APT links shown in Figure 2.11 [122].

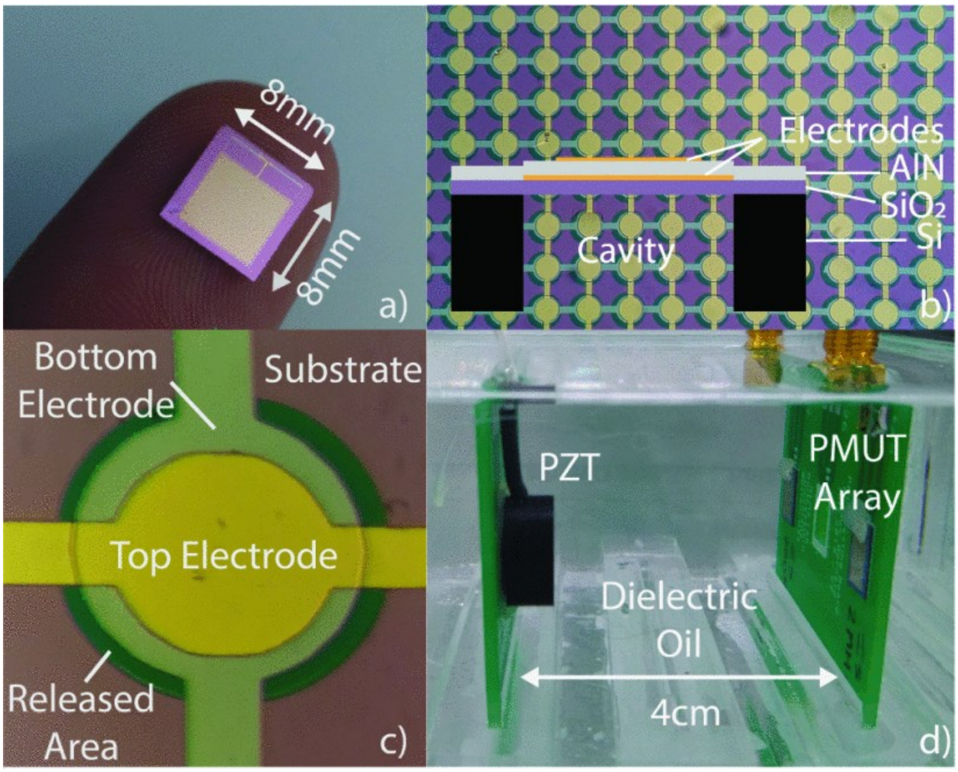

Figure 2.11: pMUT array designed and fabricated by Herrera *et al.* [123], showing the array and the individual array elements. The device was tested in a dielectric oil test tank for *in vivo* testing (from [123]).

Basaeri *et al.* [124] numerically analysed the performance of square ultrasonic PZT receivers and optimised their film thickness for optimum power delivery using COMSOL FEM analysis. The simulated pMUT receiver design was developed and characterised in an acoustically isolated water tank. The device could provide 0.7 mW power to an optimal load of 4.3 $k\Omega$ when energised by an input signal of 322 $mWcm^{-2}$ at 88 kHz with a separation distance of 20 mm. The same group also investigated the performance of pMUT receivers compared to commercial ultrasonic transducers (with similar active area) when subjected to misalignment and disorientation [105]. Through the same experiment setup, the authors measured the pMUT receivers' average performance output of 86 %, 91.7 %, and 111 % to changes in depth, alignment, and orientation, respectively, when compared with commercial transducers. However, the improvement in the performance is mainly due to the small effective surface area ($4\,mm^2$) of the tested transducers and therefore have wider beam. But several researchers have recently proposed the design and application of pMUT devices for implantable medical devices [125-128], showing great potential for non-invasive implant recharge.

2.2.2. Metal Transmission Medium

When compared with other wireless power transfer methods, APT has the advantage of being able to penetrate through enclosed metallic structures, as it is immune to the Faraday cage effect. Therefore, APT becomes an ideal solution to wirelessly transfer energy through metal walls where essential sensor nodes connected by intricate wires or a battery would be cumbersome or hazardous. Examples include pipeline systems [58], gas cylinders, aircraft engines [129] or nuclear waste containers [130].

Similar to APT systems in fluids, through-metal APT have an acoustic transmitter and receiver attached on either side of a metal wall. An acoustic wave propagates through the metal to recharge the nodes on the other side. However, higher power transfer efficiencies can be easily achieved through metal transmission relating to fluid or air medium because of similar acoustic impedance between metal ($45\,MPa\,s\,m^{-1}$ for steel) and piezoelectric ceramics ($30\,MPa\,s\,m^{-1}$ for PZT). A good impedance matching between the transfer medium promotes optimal power throughput.

Various acoustic WPT systems have been designed and modelled using metal transmission media [131-135], and some in combination with through wall data communication [136-139]. These works focus on the physical and mathematical modelling of metal-based APT systems on wave propagation equation and piezoelectric theory. Therefore, they highlighted investigations coupling the APT system performance to the driving frequency, the mechanical properties of PZT, metal properties and electrical loading of transducers. Some of these research groups also studied the sensitivity of the power delivery for different geometric shapes and the exciting vibration modes (thickness-stretch or thickness-twist mode) of the transducers. This assisted in making careful design considerations for optimal power delivery. However, only numerical analysis was presented in the aforementioned literature, and the proposed system was not measured or validated with a test setup.

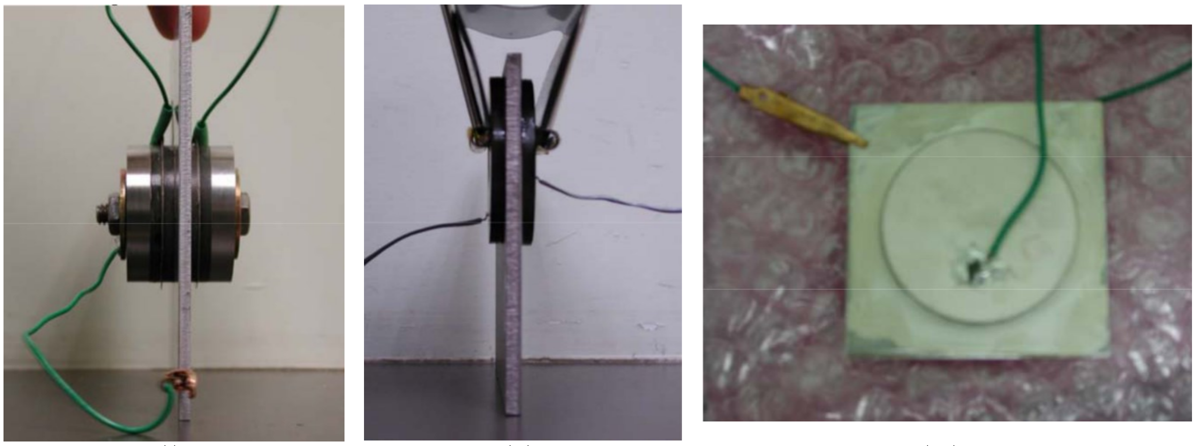

(i) (ii) (iii)

Figure 2.12: Testing configurations used in [140] using two PZT disks across a 2.5mm titanium plate for acoustic WPT. (i) Stress-bolted PZT disks (ii) PZT disks clamped from a mechanical clamp using grease as a matching layer. (iii) PZT disks attached to the metal plate through an epoxy bond. (from [140])

Sherrit *et al.* [141] proposed an alternative network equivalent model to study the sandwiched plate PZT power delivery performance, improving previous numerical models. This model can be easily adapted to account for additional acoustic elements such as impedance matching or back insulation layers. Also, other circuits like transmitter driver, electrical impedance matching, or power conditioning circuits can be appended to this model. The model was later tested using two PZT disks on either side of a 2.5 mm thick titanium plate in three configurations: stress bolted, clamped with grease and attached to the metal slab using conductive epoxy (Figure 2.12)[140]. These configurations showed a power transfer efficiency of 12 %, 53 % and 40 %, respectively. Although the clamped configuration gains the highest efficiency, it is impractical from an application point of view. Subsequently, several papers were published by the same group using FEM for designing sensors enclosed in the sealed metal tank for space applications [142, 143].

They later demonstrated a high-power APT system for through-wall transmission using a pair of 50 mm diameter prestressed PZT four-ring stacks (Figure 2.13) attached to the sides of a 5 mm thick titanium plate using epoxy bond [144]. The experimental results show that high power levels up to 1083 W can be transmitted with 84 % efficiency with a driving frequency of 24.5 kHz. The acoustic energy loss and compensation analysis of the proposed device showed that reflectors could effectively reduce the plate wave energy losses [60]. The authors suggested further thermal analysis to determine the sensitivity of the transducers due to thermal detuning, along with investigations on the vibration modes (sheer or radial) and geometries to improve the transfer efficiency.

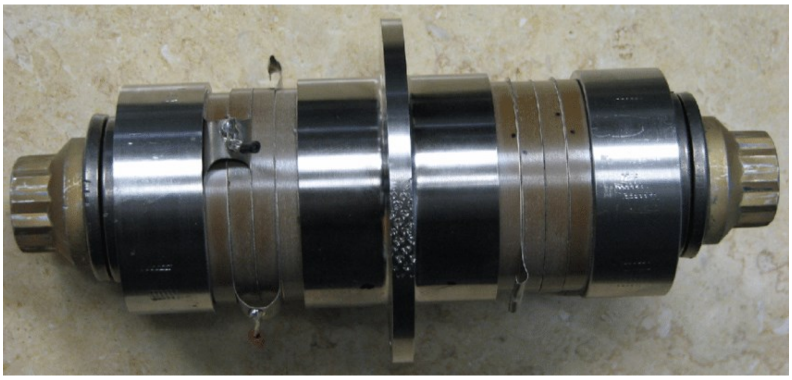

Figure 2.13: High power PZT stack on either side of a 5 mm titanium plate. Each stack of PZT consists of 4 rings [60].

Moss *et al.* [145, 146], a research group at the Australian Defence Science and Technology Organization, published similar findings modelling stacked PZT acoustic systems in LTSpice™ and experimentally validating the results by mounting the designed transducers across aluminium metal walls of 1.6 mm thickness for powering structural health monitoring systems embedded within aircraft and other high-value assets. The PZT disks are bonded to the metal through silver loaded epoxy of 100 μm thickness. When the transmitter was excited in thickness mode at 1 MHz, a rectified output power of 300 mW was measured at the receiver with a 30 % power transfer efficiency. This was later improved to 42 % efficiency and 420 mW output power by changing the piezo material from Pz27 to Pz26, upgraded with a data communication link at 115 $kbps$ data rate [147]. The same system was downsized to 10 mm PZT disks for reducing the footprint by 93 %, achieving the same power transfer efficiency and data rates [148]. The authors later proposed a detachable system using NdFeB magnets and a standard high-Z ultrasonic couplant between the magnet and plate to match the acoustic impedance. The device was driven at 4.2 MHz and 1 VA across a 1.6 mm aluminium plate to transfer 340 mW power at a 34 % power transfer efficiency [149]. Following this, many researchers proposed different configurations (two pairs of PZT configuration [150-153], 3 PZT configuration [150, 151, 154]) and different modes of communication [137, 155] used for dual (power-data) transmission using APT systems. Yang *et al.* [156] has comprehensively summarised the literature of different WPT techniques used in through-metal power delivery.

Kiziroglou *et al.* [58] presented an APT solution for monitoring pipeline structures using acoustic surface waves to transfer power over more considerable distances instead of through-wall power transfer. The system was experimentally studied using two PZT disks of 48 mm diameter and 7.9 mm thickness sandwiched between an aluminium adapter and reflector. These were mounted on a cast-iron tube of 118 mm diameter and 8 mm thickness, 1 m apart, as shown in Figure 2.14(i). The system was tested under multiple scenarios, such as an empty pipe and a water-filled pipe. The results demonstrated a power delivery of 18 mW with approximately 0.1 % power transfer efficiency with an operating frequency of 47.5 kHz. This is the longest separation distance covered by an APT system using metal as the transmission medium (as of March 2021).

Recently, Fu *et al.* [59] presented a system-level study of ultrasonic WPT systems to power embedded sensor nodes enclosed within metallic structures. The setup was demonstrated using two piezoelectric transducers mounted on the sides of an aluminium plate for varying thickness, as shown in Figure 2.14 (ii). The authors also proposed a power management module for the receiver that provides a suitable constant voltage for the sensing unit. Upon testing, an output power of 1.73 mW was delivered onto a load of a 1.5 $k\Omega$ resistor when the transmitter was driven with a continuous 15 V signal at 42.6 kHz through a 6 mm thick aluminium plate.

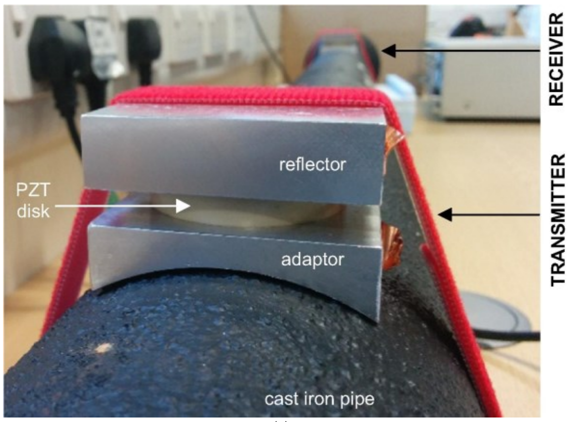

(i)

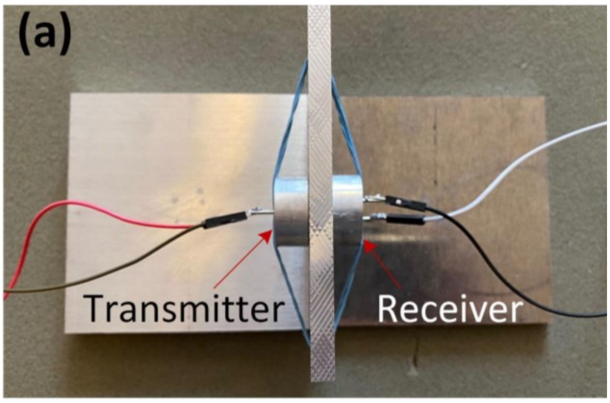

(ii)

Figure 2.14: Experimental setup of acoustic WPT systems (i) surface-wave transmission of acoustic waves in iron cast pipes using PZT disk transducers [58]. (ii) through-metal transmission for powering sensor nodes proposed by Fu *et al.* [59].

2.2.3. Transmission Through Air

As discussed in the previous chapter, transmitting acoustic energy through air is highly challenging due to the attenuation of open-air and the acoustic impedance mismatch between air and piezoelectric ceramics. Therefore, the combination of acoustic WPT with a gaseous medium is less explored by researchers than biomedical or through-metal applications [157]. However, it has constructive and potential applications, especially in powering inaccessible sensor nodes, reducing the weight of cable slabs and long-distance low power sensor recharging.

Ishiyama *et al.* [158] conducted initial experiments for investigating the applicability of acoustic WPT systems in the air for powering low-power mobile applications. The researchers developed a set of 36 mm and 16 mm transducers for transmitter and receiver, respectively operated at 28 kHz. However, as they were unable to transmit high-pressure sound waves, the output power delivered was very low. The authors later updated the system by designing and fabricating plastic horns for the transmitter to improve the transmitted sound pressure. Horns are structures attached to the active surface of the transducer to limit the spreading of the acoustic wave. Therefore, it guides the sound wave to propagate along a path, and it typically has a constantly increasing cross-sectional area. The measured output power was 4 μW, which is yet very low. However, the authors indicated that the measurements were performed with a non-optimised setup and are only indicative.

Roes *et al.* [65], in 2011, after reviewing the developments of acoustic WPT systems [159], instigated investigations for modelling ultrasonic WPT in air. In this work, they modelled the system dimensions through FEM and calculated the effect of attenuation along with its power transfer efficiency. As a result, a theoretical efficiency limit on achievable efficiency of 53 % was calculated for the acoustic WPT system considering 10 % losses due to mechanical and electrical characteristics of the transducer. This is much higher than the 2% efficiency that would be attained by using inductive WPT for the same system dimensions [33]. The model was experimentally tested using an open-back PX051 transducer with a unimorph piezoelectric disc attached to a 12 mm aluminium diaphragm, as shown in Figure 2.15 (i). For a separation distance up to 10 cm, a peak power transfer efficiency of 16% was achieved with 37 μW power delivered to the load at 17 kHz. To improve this, the authors examined the effect of reflections through FEM modelling [160] and affixed stepped exponential horns to the transducers to reduce resonances due to impedance mismatch [161] (Figure 2.15 (ii)). Through experiments, they observed that even though the horns did not reduce the reflections, they significantly improved the performance of the WPT for longer separation distances (Figure 2.15 (iii)).

SonicEnergy™ (previously known as uBeam) [162] is a recently established company that capitalises on acoustic WPT technologies for wirelessly powering high-power electronics such as mobile phones. The company proceeded by designing ultrasonic transmitter transducer, controller, and communication modules for power and data transfer through acoustic waves [163-168]. Although the working efficiency of these power transfer systems has not been officially reported by the company [169], lately, many patents on the ultrasonic beamforming techniques using transducer arrays have been registered [170-172].

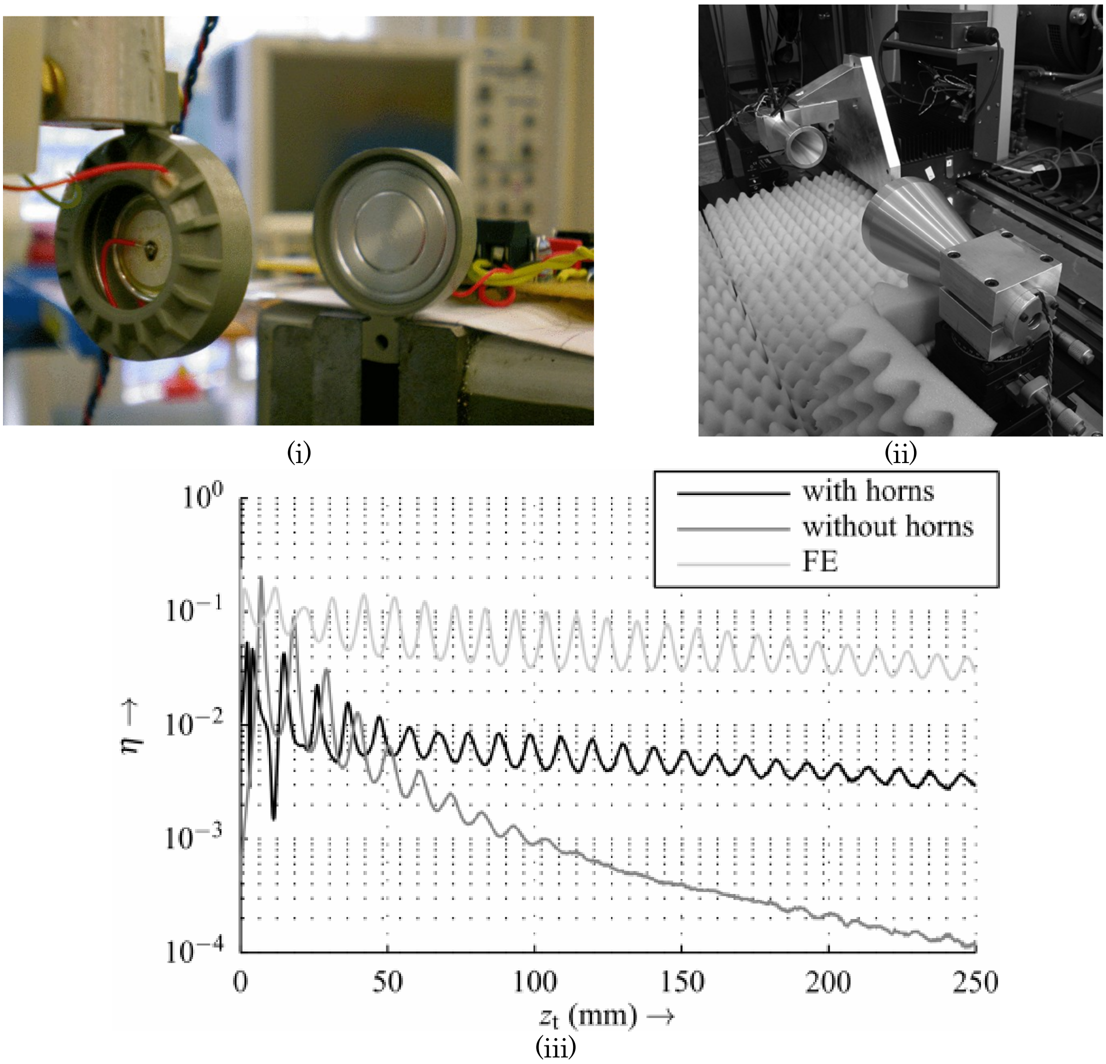

Figure 2.15: Acoustic transmission through the air. (i) Experimental setup from Roes *et al.* with open-backed transducers (from [65]). (ii) Updated transducers affixed with stepped exponential horns to improve the reach (from [161]). (iii) Comparison of the power transfer efficiency of the two experimental setups and the FEM simulations (from [161]).

Klymko *et al.* [173] studied the behaviour of phased transducer arrays for powering sensors inside a Magnetic Resonance Interferometer (MRI) machine through acoustic WPT transmission in the air. They designed an array of piezoelectric speakers along with the MRI interior in a curved manner (as shown in Figure 2.16), forming a parabolic transducer. Through experiments, the authors demonstrated the possibility to transmit a focused acoustic beam of 4% accuracy to the receiver. This system delivers 1 μW power to the load when excited with 10 mW at 16 kHz. While this shows a power transfer efficiency of 10^{-4}, the authors indicate that this is the prototype of the system. Further improvements in efficiency can be achieved by optimising the transducer geometry.

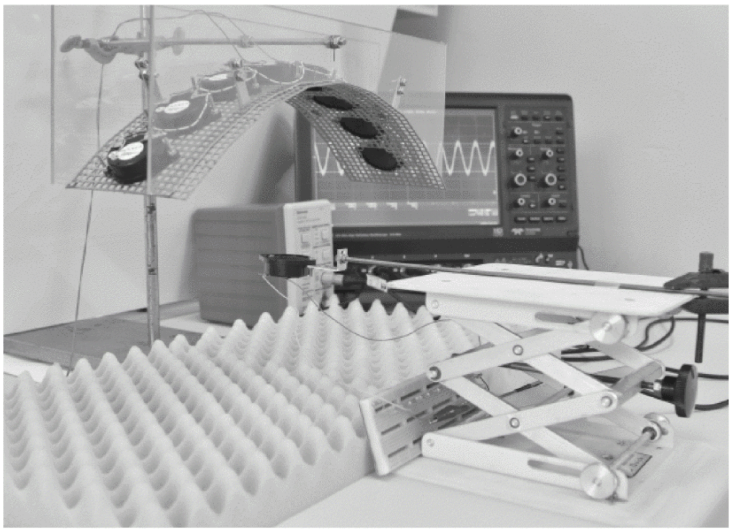

Figure 2.16: Experimental setup shows the arched parabolic phased array transmitter with the single receiver transducer to harness the focused acoustic beam [173].

Surappa and Degertekin recently characterised a parametric model for capacitive Micromachined Ultrasonic Transducers (cMUT) for acoustic power transmission through the air [174]. The authors used 1D lumped parameter modelling to optimise the cMUT device's system dimension and fabricated it with a resonance frequency of 24.22 kHz. The device was then tested using a piezoelectric transducer, as shown in Figure 2.17. The novel device was reported to harness an output power of 40.5 μW across a load resistor of 100 Ω at a power transfer efficiency of 0.32 %. However, the authors indicated that the device efficiency could be significantly improved by designing an impedance matching circuit for the receiver.

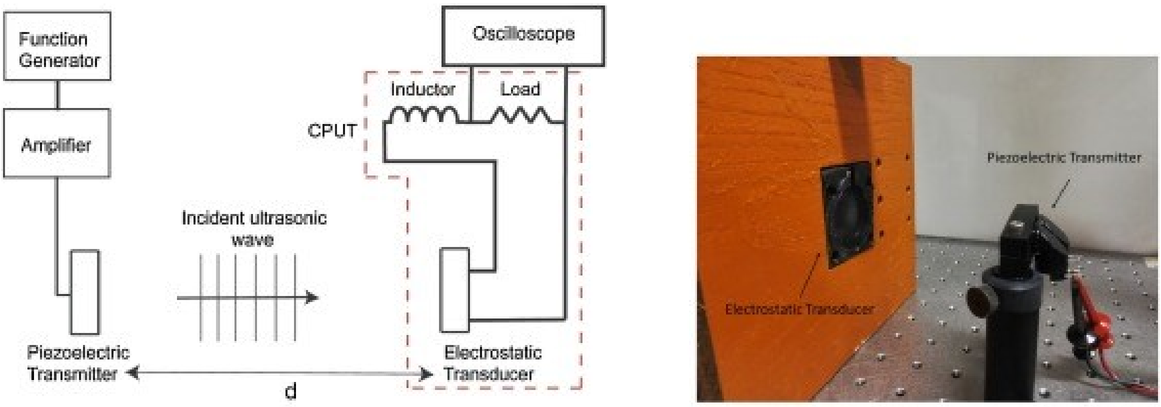

Figure 2.17: The experimental setup and schematics showing the piezoelectric transmitter and a cMUT receiver for ultrasonic WPT [174].

2.3. Conclusion

This chapter highlights the underlying physics of acoustic wave behaviour and its propagation losses. The theoretical limit of the energy transfer efficiency of an APT system when propagating in the air is derived based on diffraction, attenuation and transducer losses. Acoustic losses due to reflection at the transducer-medium boundary are briefly discussed, emphasising the importance of the difference in material acoustic impedance non-linearly affecting the efficiency of the APT system. Therefore, the materials' density and sound speed are important design parameters for airborne APT systems. Finally, a review of the recent progress in APT systems for biomedical, through-metal, and through-air systems is provided afterwards. The advantages and limitations of using acoustic waves for far-field power transfer are analysed, showing the bottlenecks and potential imminent acoustic wireless power transfer solutions. This chapter provides guidelines and the basic concepts overlooking the APT system designed in this work.

3. Transducer Efficiency and Impedance Matching Techniques

The purpose of this chapter is to investigate the performance of acoustic transducer for APT through air and different load matching techniques to identify the optimum method to deliver power to the APT receiver. First, piezoelectric transducers operating as transmitters and receivers were modelled using equivalent circuit modelling. Their matching load impedance was calculated preceding impedance frequency analysis. Subsequently, the output impedance of the receiver was experimentally studied to find the maximum power point. In addition, the effect of impedance matching for different frequencies near the transducer's resonance frequency was studied, demonstrating that increased power can be delivered to the receiver by controlling the frequency. This is because frequency variation changes the ratio between transmitter-receiver distance and wavelength, allowing shifting from standing wave intensity valleys to peaks. The ability of a tuneable receiver can therefore allow dynamically selecting the transmitter frequency to ensure that the receiver lies at a standing wave peak position. Finally, a summary of the power experimentally extracted for the different loading techniques is discussed to validate the analytical results.

3.1. Transducer Modelling

An essential challenge in quantifying the performance of an APT is understanding the significant parameters governing the losses in the system. For an air based APT system, the chief loss mechanisms limiting power transfer efficiency are attenuation through the medium, wave spreading, reflection and transduction losses. Therefore, modelling these effects is mandatory to understand the limitations of the technology in terms of distance, frequency, transfer efficiency, and transmission power (ISO226).

As discussed in Chapter 2, acoustic transduction devices convert electrical energy into mechanical vibrations and vice versa. These devices include piezoelectric, electrostatic, and electromagnetic transduction devices. Their transduction efficiency accounts for the losses in converting electrical to mechanical energy in transmitters and conversely mechanical to electrical energy in receivers, relying on the transduction method. For instance, strong mechanical stability under cyclic stress, high electromechanical coupling factor and low dielectric loss are necessary for efficient acoustic piezoelectric transducers. As optimising the transducer design is an intricate field of research by itself, this falls out of the scope of this thesis. Instead, different off-the-shelf airborne piezoelectric transducers were assessed and selected for APT application to function as transmitters and receivers.

The power supply units of microelectronic devices and rechargeable batteries generally require a DC supply. Therefore, a power conditioning circuit is essential to rectify the acoustic receiver's AC power, typically consisting of an AC-DC rectifier and a DC-DC converter to achieve optimum power extraction. This section presents the different modelling techniques and the assessment of the different ultrasonic transducers considered for APT application and their selection criteria. Following this, the transducer efficiency is modelled for transmitter and receiver operation to study the impedance-frequency characteristics.

3.1.1. Piezoelectric Transducer Modelling

A piezoelectric transducer has different modes of operation, dependent on the directions of vibration and electric field. Therefore, multi-dimensional tensors are defined for the piezoelectric stress, strain, and electric field components to characterise the dynamic behaviour of the transducer for a spectrum of frequencies. However, near the transducer's fundamental resonant frequency, it is assumed that the ultrasound wave generated is predominantly by one active surface in contact with the medium directly or through a matching layer. This is especially true when the width-to-thickness ratio of the piezoelectric layer operating in thickness-extension mode is greater than 10 (Eq. 2.30).

Detailed literature can be found on piezoelectric transducer models for energy harvesters, which can be adapted for an APT receiver. Many researchers employed mathematical modelling to model these harvesters [175]. Although this provided an efficient way to estimate and optimise the electrical output of the harvesters, the inverse-piezoelectric effect was not taken into consideration because coupling in the mechanical equation is oversimplified or ignored [176]. Further modelling techniques include approximate distributed parameter modelling, distributed parameter modelling and lumped parameter modelling for energy harvesters. In these one-dimensional (1D) models, the dynamic behaviour of a piezoelectric transducer can be depicted as an equivalent electrical circuit for a limited range of frequency bordering the resonance. Furthermore, representing the system parameters as equivalent circuits aids to implement and adapt using circuit simulation software [60, 77].

- **Lumped Parameter Model**

The fundamental way to define the piezoelectric behaviour is by approximating the system elements into lumped components using Rayleigh-Ritz formulation, representing the transducer's spatially distributed behaviour [177-179]. This approach considers the transducer as a mass-spring-damper system for decoupling the mechanical and electrical behaviour of the transducer.

The lumped parameter model of a piezoelectric transducer is as depicted in Figure 3.1. This simplified model consists of an electrical branch interlinked to the mechanical branch through a transformer with n turns ratio representing the piezoelectric coupling vector. The electrical branch consists of the inherent capacitance of the electrodes, C_o and the dielectric loss R_o. However, R_o is typically very large and has a negligible effect on the system behaviour at the acoustic frequency range. The mechanical resonance of the transducer can be modelled by the series RLC circuit of the modal mass (L_m), mechanical damping (R_m), and compliance (C_m) of the transducer.

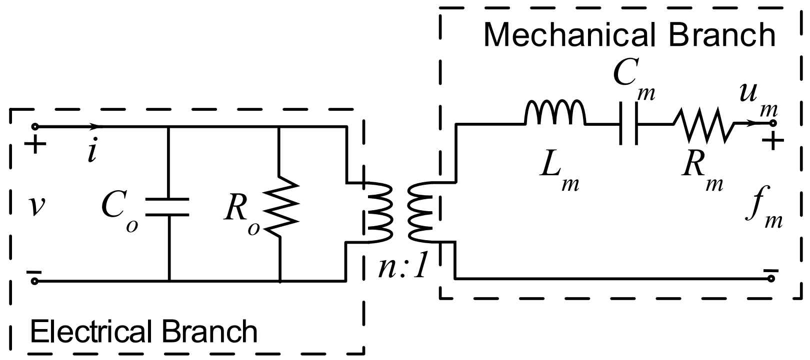

Figure 3.1:Equivalent circuit of a piezoelectric transducer using lumped parameter modelling.

The electrical branch is governed by the voltage v across the transducer electrodes with a current i flowing through the piezoelectric material. Therefore, when an APT transmitter is powered by an AC source (I_s), the electrical power is converted to mechanical vibrations exerting a force $f_m = m * a$ on the medium with velocity u_m by the base vibration, where m is the effective mass of the piezoelectric element and a being its acceleration due to the electrical source. Decoupling the electrical and mechanical systems helps analyse the characteristics of the transmitter and the receiver independently. Although this model gives an initial insight on the dynamic behaviour of piezoelectric transducers, the approximations applied in the model limits it to a single vibration mode of cantilever piezoelectric beam. Many researchers have adapted this for specific piezoelectric architectures for modelling energy harvesters.

- **Mason and KLM Model**

To define the highly complex electromechanical behaviour of acoustic piezoelectric transducers, Mason in [180] modelled the thickness mode piezoelectric plate transducers by combining electrical network theory and the constitutive equations defining the underlying physics of electromechanical systems. Researchers widely use this model to represent the piezoelectric transducers [100, 120, 181] by treating its architecture as a capacitor network.

Additionally, the Mason equivalent circuit model does not have additional assumptions or approximations beyond the governing equations of the piezoelectric layer and acoustic propagation[182]. Therefore, the circuit is interchangeable with the direct solution to represent both the transmitter and the receiver. Figure 3.2a represents the final form of the Mason model for acoustic parallel-plate piezoelectric transducers.

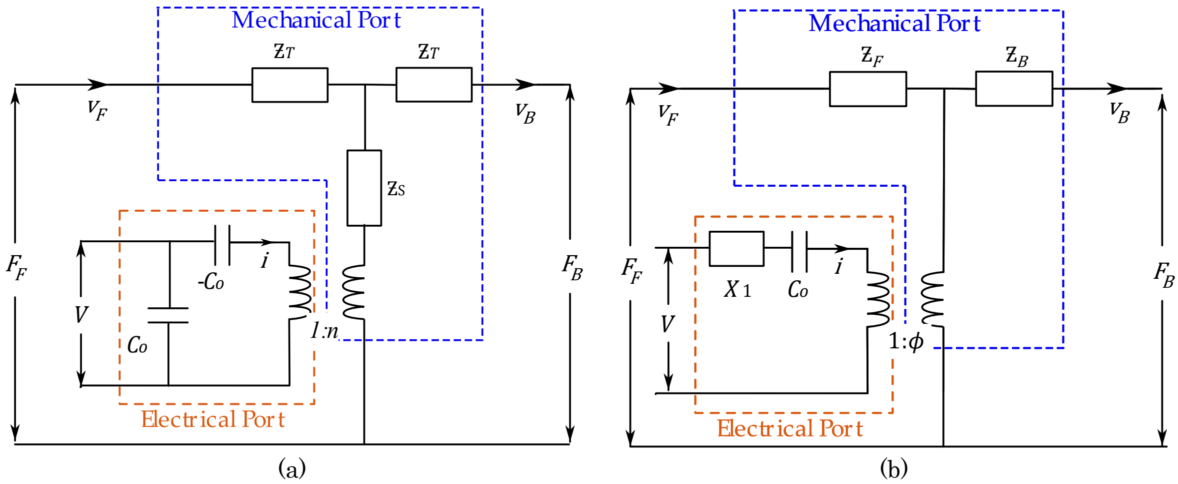

Figure 3.2: Equivalent circuit models for parallel plate piezoelectric transducers. (a) The final form of the Mason model. (b) The adapted KLM model (figure referred from [182]).

The mechanical branch is divided into the transducer's front face and the back face represented by suffices F and B, respectively. Similar to the lumped parameter model, the voltage (V) and the current (i) in the electrical ports are converted into forces (F) and velocities (v) in the mechanical branch by an ideal electromechanical transformer with n turns ratio. Therefore, the free or clamped condition of the piezoelectric surfaces can be represented as a short circuit or open circuit conditions in the mechanical port correspondingly.

Krimholtz, Leedom, and Matthae later altered the Mason Model to replace the negative capacitance and reduce the calculation complexity when multiple piezoelectric layers are combined to form the KLM model [183] (Figure 3.2b). The acoustic impedanc of the front and back plates are represented by Z_F and Z_B respectively. However, it has been shown that the models are interchangeable as they produce similar results [184]. The modelling parameters of both are summarised in Table 3.1. Although both equivalent circuit models consider thickness-mode operation, alternative formulations for other modes and architectures are also researched and established [177, 185-188].

Table 3.1: Summary of the Mason and KLM equivalent circuit system modelling parameters for a parallel plate piezoelectric transducer.

<table>
<tr><th></th><th>Mason Model [180]</th><th>KLM Model [183]</th></tr>
<tr><td>From Manufacturer</td><td colspan="2">Thickness of the piezoelectric disc, d$[m]$
Radius of the piezoelectric disc, $r_{source}[m]$
Density of material, ρ$[kgm^{-3}]$
Resonance frequency, f$[Hz]$
Open circuit complex elastic stiffness, $c_{33}^{D}[N/m^2]$
Clamped permittivity, $\varepsilon_{33}^{S}[F/m] = \varepsilon_o\varepsilon_r$
Complex electromechanical coupling, k_t</td></tr>
<tr><td>From System Design</td><td>-</td><td>Impedance at the left acoustic port, $\mathbb{Z}_L[\Omega]$
Impedance at the right acoustic port, $\mathbb{Z}_R[\Omega]$</td></tr>
<tr><td>From Calculation</td><td colspan="2">Surface area of the piezoelectric disc, $A[m^2] = \pi r_{source}^2$
Angular frequency, $\omega = 2\pi f$
Speed of sound, $c_{piezo}[m/s] = \sqrt{c_{33}^{D}/\rho}$
Acoustic impedance, $\mathbb{Z}_o\ [\Omega] = \rho A c_{piezo}$
Piezoelectric pressure constant, $h_{33}[V/m] = k_t\sqrt{c_{33}^{D}/\varepsilon_{33}^{S}}$
Wave number, $k = \omega/c_{piezo}$
Parallel plate capacitance,
$C_o[F] = \frac{\varepsilon_{33}^{S}A}{d}$</td></tr>
<tr><td></td><td>Transformer turns ratio, $N = C_o h_{33}$
$\mathbb{Z}_T[\Omega] = i\mathbb{Z}_o tan\left(\frac{kd}{2}\right)$
$\mathbb{Z}_S[\Omega] = -i\mathbb{Z}_o csc(kd)$</td><td>$M = \frac{h_{33}}{\omega\mathbb{Z}_o}$
Transformer turns ratio,
$\phi = \frac{1}{2M}\csc(kd/2)$
$X_1[\Omega] = i\mathbb{Z}_o M^2 sin(kd/2)$
$\mathbb{Z}_F[\Omega] = \mathbb{Z}_o\frac{\mathbb{Z}_L cos(kd/2) + i\mathbb{Z}_o sin(kd/2)}{\mathbb{Z}_o cos(kd/2) + i\mathbb{Z}_L sin(kd/2)}$
$\mathbb{Z}_B[\Omega] = \mathbb{Z}_o\frac{\mathbb{Z}_R cos(kd/2) + i\mathbb{Z}_o sin(kd/2)}{\mathbb{Z}_o cos(kd/2) + i\mathbb{Z}_R sin(kd/2)}$</td></tr>
</table>

When an electrical source of V_S is applied to the equivalent circuit, the electromechanical transformer produces a corresponding force in the mechanical branch. As a result, the active surface perceives an opposing force from the transmission medium modelled by the acoustic impedance of the medium $Z_a = R_a + jX_a$. Figure 3.3a represents the equivalent network of an APT transmitter. Since the back face of the transducer is clamped, the loading nodes of the back face is open-circuited. Therefore, $v_B = 0$ and F_B is the open circuit voltage for clamped surfaces.

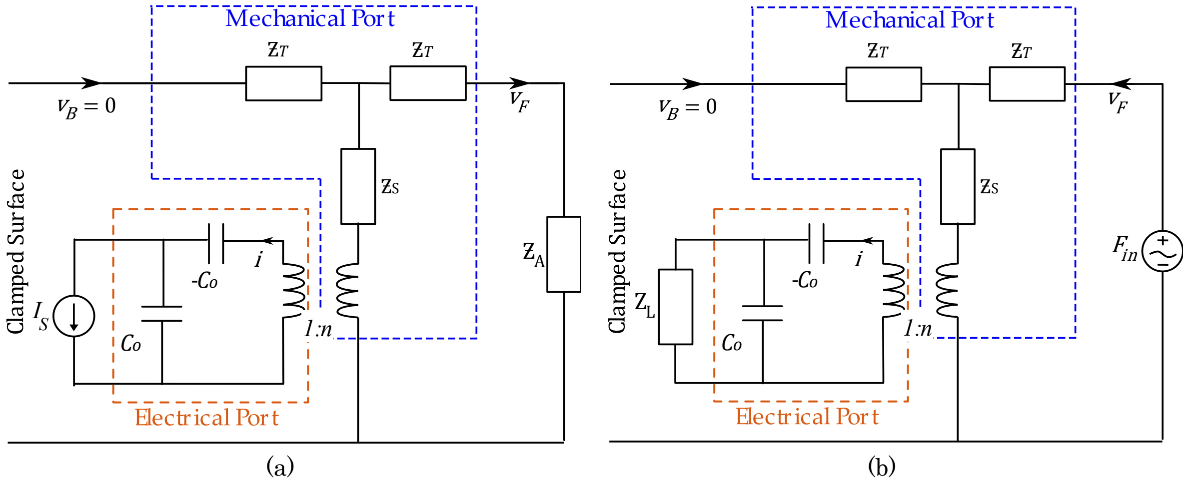

Figure 3.3: Mason model with source and load for (a) APT transmitter (b) APT Receiver.

As equivalent circuit models are reversible in principle, the receiver can be modelled as a voltage source F_{in} (analogous to the force of the received sound waves) powering the mechanical branch, and the electrical power from the receiver is delivered to a load impedance Z_L (Figure 3.3b). The load impedance must be matched with the transducer for optimum power delivery.

- **Finite Element Modelling**

The discussed equivalent circuit models are 1-Dimensional models in which the piezoelectric behaviour is depicted for an active surface in one axis. These modelling methods can fulfil functional roles to design simple piezoelectric transducers and evaluate their electrical efficiency. However, ultrasonic piezoelectric transducers are complicated devices where multidisciplinary understanding in mechanical engineering, electrical engineering, materials chemistry and wave physics is preferable. Accordingly, finite element modelling (FEM) has been gaining popularity due to its 3-Dimensional modelling and ability to link multiple physics into the model.

FEM analysis is predominantly a software aided tool that solves a physical model by discretising the system into a finite number of elements. The equations stated by the governing physics are evaluated for each element's boundary conditions using partial differential equations and approximations. The solution for each element is successively assembled to form the global solution that defines the system behaviour. Therefore, FEM modelling can solve physical systems of immense complexity through the quantisation of complicated geometries. Furthermore, modelling different geometries of the piezoelectric element reduces resources in transducer design and selection.

In this work, a hybrid modelling method is followed where both the equivalent circuit and FEM modelling methods are used. Modelling appertaining to the electrical optimisation of the transducers are modelled using the Mason model, whereas the attenuation and efficiency of the acoustic power link between the transmitter and the receiver are modelled using FEM analysis in COMSOL software.

3.1.2. Impedance Matching

Impedance matching in APT systems typically consists of matching the real impedance of the transmitter circuit and electrical load to those of the corresponding transducers. When operated at their resonance frequencies, the transducers have real impedance with no reactive component to tune out. Therefore, employing a resistive load to the transducer is sufficient to extract the maximum power from the APT receiver. However, there will be circumstances where operation off-resonance is desirable or necessary. For instance, having different models, manufacturers or operating at varying ambient conditions may cause the transmitter and receiver resonances to differ.

Also, reflection between the transducers can prompt standing waves in the far-field region, causing nodes and antinodes that affect the power levels at the receiver. To evade this problem, the transmitter frequency can be detuned to alter the wavelength of the standing waves to place the receiver near a positive antinode. This can be experimentally measured and is discussed in detail in section 4.1. Consequently, the load on the APT receiver should be matched to tune out the reactance corresponding to its operating frequency. In this section, the optimum load obtained for the Thevenin and Norton equivalent circuit is analytically evaluated.

- **Norton Equivalent Circuit**

The transducer's equivalent circuit model (Figure 3.3) can be further simplified to its Norton equivalent, as shown in Figure 3.4. Consider an AC source powering the APT transmitter, $i_S(t) = \sqrt{2}I_S sin(\omega t)$ and an internal impedance of $Z_S = R_S + iX_S$. The current passing through the load is given by:

$$i_L = \left|\frac{Z_S}{Z_L + Z_S}\right| \cdot i_S \tag{3.1}$$

The average power (P_L) delivered to the load impedance $Z_L = R_L + iX_L$ can be calculated as[66, 189]:

$$P_{R_L} = I_{L,rms}^2 R_L = \left|\frac{Z_S}{Z_S + Z_L}\right|^2 I_S^2 R_L \tag{3.2}$$

$$= \left|\frac{R_S + jX_S}{R_S + jX_S + R_L + jX_L}\right|^2 \cdot i_S^2 \cdot R_L \tag{3.3}$$

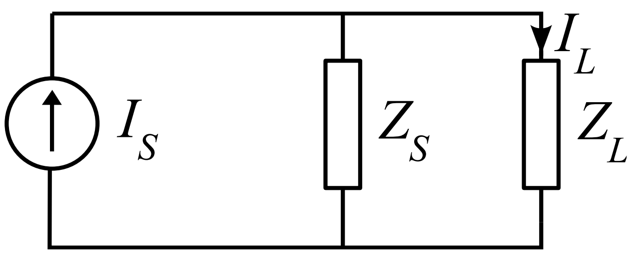

Figure 3.4: Norton Equivalent of the piezoelectric equivalent circuit.

To maximise the delivered power, the denominator of Eq. 3.3 should be minimum. The effective reactance of the denominator can be cancelled when $X_L = -X_S$, which will reduce Eq. 3.3 to:

$$P_{R_L} = \left|\frac{R_S + jX_S}{R_S + jX_S + R_L - jX_S}\right|^2 \cdot i_S^2 \cdot R_L \tag{3.4}$$

$$= \left|\frac{R_S + jX_S}{R_S + R_L}\right|^2 \cdot i_S^2 \cdot R_L \tag{3.5}$$

$$= \left(\frac{\sqrt{R_S^2 + X_S^2}}{\sqrt{(R_S + R_L)^2}}\right)^2 \cdot i_S^2 \cdot R_L \tag{3.6}$$

$$= \frac{R_S^2 + X_S^2}{(R_S + R_L)^2} \cdot i_S^2 \cdot R_L \tag{3.7}$$

The resistive load value (R_L) for which the power would be maximum is obtained by calculating the derivative of Eq. 3.7 with respect to R_L and equating it to zero as follows:

$$\frac{\mathrm{d}P_{R_L}}{\mathrm{d}R_L} = (R_S^2 + X_S^2) \cdot i_S^2 \cdot \frac{\mathrm{d}}{\mathrm{d}R_L}\frac{R_L}{(R_S + R_L)^2} \tag{3.8}$$

$$0 = (R_S^2 + X_S^2) \cdot i_S^2 \cdot \left(\frac{(R_S + R_L)^2 - 2R_L(R_S + R_L)}{(R_S + R_L)^4}\right) \tag{3.9}$$

$$0 = \frac{(R_S + R_L)(R_S + R_L - 2R_L)}{(R_S + R_L)^4} \tag{3.10}$$

$$0 = \frac{R_S - R_L}{(R_S + R_L)^3} \tag{3.11}$$

$$0 = R_S - R_L \tag{3.12}$$

$$R_S = R_L \tag{3.13}$$

Therefore, the maximum power output occurs when the load resistance is equivalent to the source resistance. Consequently, when the load is a complex conjugate of the source impedance $Z_L = R_S - iX_S$, then the maximum power delivered to the load is:

$$P_{L,opt}^{C} = \frac{R_S^2 + X_S^2}{4R_S} I_S^2 \tag{3.14}$$

$$V_{L,opt}^{C} = \frac{\sqrt{R_S^2 + X_S^2}}{2} I_S \tag{3.15}$$

where, the output power depends only on the source properties and the load resistance. This type of loading will be referred to as 'Complex loading' further in this work.

Alternatively, in some cases where reactive impedance matching is impractical. For example, due to very low operating frequency, large inductive components will be required to compensate for the transducer capacitance. In such instances, a resistive load must match the total complex output impedance. This type of loading will be referred to as 'Resistive loading' in this script. To derive the optimum load resistance, the load reactance X_L is set to zero in Eq. 3.3. Subsequently, taking the derivative with respect to R_L yields:

$$\frac{dP_{R_L}}{dR_L} = \sqrt{(R_S^2 + X_S^2)} \cdot i_S^2 \cdot \frac{d}{dR_L} \frac{R_L}{(R_S + R_L)^2 + X_S^2} \tag{3.16}$$

$$0 = \frac{((R_S + R_L)^2 + X_S^2) - 2R_L(R_S + R_L)}{((R_S + R_L)^2 + X_S^2)^2} \tag{3.17}$$

$$0 = R_S^2 + R_L^2 + 2R_S R_L + X_S^2 - 2R_L R_S - 2R_L^2 \tag{3.18}$$

$$0 = R_S^2 + X_S^2 - R_L^2 \tag{3.19}$$

$$R_L = \sqrt{R_S^2 + X_S^2} \tag{3.20}$$

As for Eq.3.14, the maximum power for a purely resistive load can be derived as:

$$P_{L,opt}^{R} = \left| \frac{R_S + jX_S}{\sqrt{R_S^2 + X_S^2} + R_S + jX_S} \right|^2 \cdot i_S^2 \cdot \sqrt{R_S^2 + X_S^2} \tag{3.21}$$

or,

$$P_{L,opt}^{R} = \frac{|Z_S|^2}{|Z_S| + R_S} \cdot \frac{i_S^2}{2} = \frac{R_S^2 + X_S^2}{\sqrt{R_S^2 + X_S^2} + R_S} \cdot \frac{i_S^2}{2} \tag{3.22}$$

and the voltage across the load can be derived as:

$$V_{L,opt}^{R} = \left| \frac{(R_S + iX_S) \cdot R_L}{R_S + iX_S + R_L} \right| I_S R_L \tag{3.23}$$

- **Thevenin Equivalent Circuit**

The Thevenin equivalent circuit of a system is represented as a voltage source (V_S) in series with its impedance ($Z_S = R_S + jX_S$) as shown inFigure 3.5. A series complex load of Z_L is connected to this circuit. The optimum load for such load in different configurations is discussed in this section.

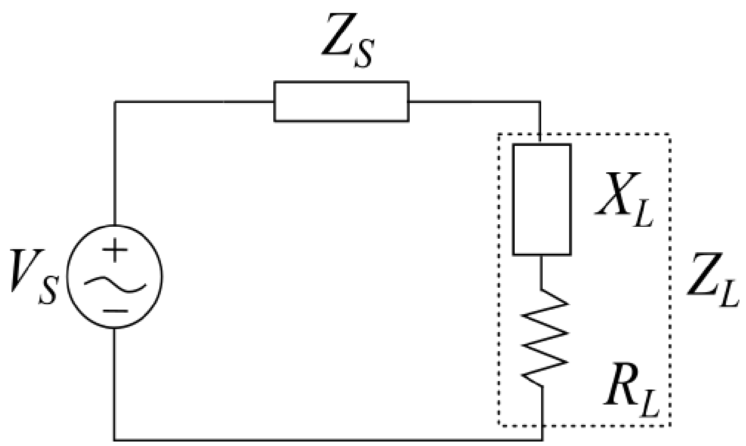

Figure 3.5: Thevenin equivalent circuit with a series of load resistance and reactance.

The voltage across the load resistance can be obtained from the voltage division rule as,

$$V_{R_L} = \frac{R_L}{(Z_S + Z_L)} \cdot V_S \tag{3.24}$$

and the power delivered to the load resistance is calculated as,

$$P_{R_L} = V_{R_L}^2 / R_L \tag{3.25}$$

Substituting Eq. 3.24 in Eq. 3.25,

$$P_{R_L} = \frac{R_L^2}{(Z_S + Z_L)^2} \cdot \frac{V_S^2}{R_L} \tag{3.26}$$

$$= \frac{R_L}{(Z_S + Z_L)^2} \cdot V_S^2 \tag{3.27}$$

Similar to the Norton equivalent derivation, the load reactance should be the conjugate of source reactance for the denominator term to be minimal, maximising the delivered power. Under this condition, the value of R_L that maximises P_L^C can be found by calculating the derivative of 3. and finding its roots. The result is $R_L = R_S$, yielding the typical impedance matching condition as in the case of a Norton model: $Z_L = Z_S^*$. Therefore, the maximum power delivered for complex matched load will then be:

$$P_{L,opt}^C = \frac{R_S}{(R_S + jX_S + R_S - jX_S)^2} \cdot V_S^2 \tag{3.28}$$

$$= \frac{R_S}{4R_S^2} \cdot V_S^2 = \frac{V_S^2}{4R_S} \tag{3.29}$$

It can be noted that in the case of the Thevenin equivalent circuit, the delivered power is completely independent of the reactance of the circuit. This difference in comparison with the Norton model is due to the difference in the physical significance of the assumptions for a constant current with a complex impedance in parallel in the Norton model and the assumption for a constant voltage with a complex impedance in series in the Thevenin model.

If complex impedance matching is not practically possible, the optimal resistive load can be calculated in the same way as in the Norton model, giving an optimal load of $R\_L = \sqrt{R_S^2 + X_S^2}$. In this case $X_L = 0$ and the maximum power becomes:

$$P_{R_L}^{MAX} = \frac{R_L}{(R_L + R_S)^2 + X_S^2} \cdot V_S^2 = \frac{1}{Z_S + R_S} \cdot \frac{V_S^2}{2} \tag{3.30}$$

In conclusion, the power delivered to a complex load impedance is higher (Eq.3.14) when compared to a purely resistive load (Eq.3.22), especially for transducers operating at lower frequencies or with high reactive impedance. Since the reactance of the transducer is a function of frequency, it is essential to evaluate the impedance of the transducer at its operating frequency for selecting the optimal load. For this reason, the transducer impedance is studied for a spectrum of frequencies in the next section to calculate the load impedance required to moderate the reactive impedance in both the transmitter and receiver circuit.

3.2. Transducer Selection

Limitations of an APT system are determined by losses in the APT link between the transducers and the energy conversion efficiency of the transducers. Although unavoidable losses like attenuation, diffraction and geometric spreading of the waves affect the APT link efficiency, these losses depend on the frequency of the acoustic waves. Therefore, studying the effect of frequency on wave attenuation would narrow the transducer specifications to minimise geometric losses.

Additionally, the transduction efficiency depends on the transducer case geometry, material, and the mode of piezoelectric vibration. These different aspects of the transducer which influence its APT system efficiency are analysed in this section. Different off-the-shelf transducers are experimentally evaluated to determine the most suitable model to analyse and optimise the APT system. Transducers from the same manufacturer with various frequencies and designs were employed to avoid anomalies due to different piezo-element properties. The transducers are manufactured from Fuji Ceramics using C-6 class piezoelectric material for the active layer. The essential parameters of the transducer are listed in Table 3.2. Figure 3.6 presents the different transducers used in this work.

Table 3.2: Specifications of transducers from Fuji Ceramics selected for evaluation.

Parameter [Unit]		FUS-40E	FUS-110A	FUS-40BT	FUS-40BR
Piezoelectric layer properties	ρ $[kgm^{-3}]$	7650			
	c_{33}^{D} $[N/m^2]$	15.91e10			
	ε_{33}^{S} $[F/m]$	7.809e-9			
	k_t $[-]$	0.52			
Transducer properties	Type*	T/R	T/R	T	R
	Nominal frequency, f $[kHz]$	40	110	40	40
	Sensitivity $[dB]$	43 (at 30 cm)	54(at 40 cm)	105	57
	Capacitance $[nF]$	2	0.6	2.6	2.6
	Directionality $[deg]$	40	7	80	-
	Max. Input Voltage $[V]$	50 (Peak)	40 (Peak)	15 (RMS)	15(RMS)
	Case Design	Open type	Matching layer	Drip-proof	Drip-Proof
	Outer Diameter $[mm]$	16	37	17.8	17.8
	Height $[mm]$	12	17.2	11	11
	Optimum Resistive Load $[k\Omega]$ (measured)	10	0.8	-	2.7

*T- for transmitter; R- for receiver; T/R – for dual purpose

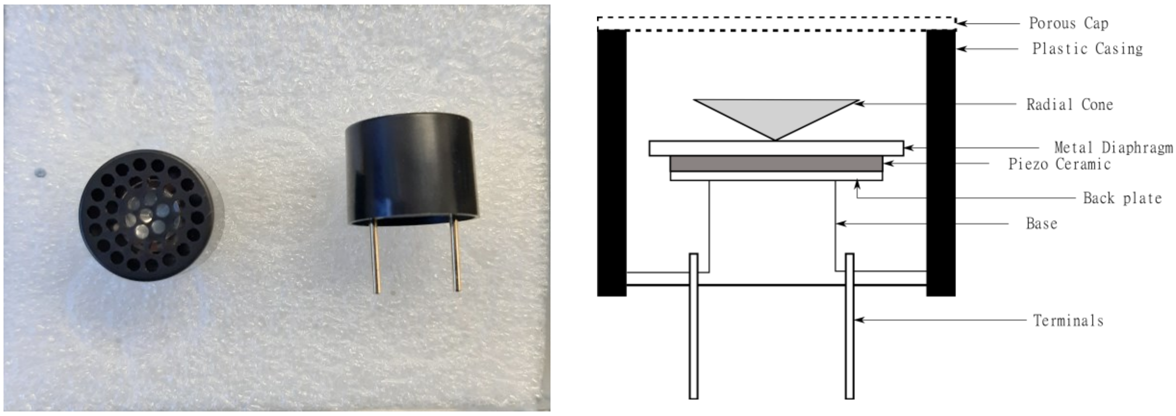

(a)

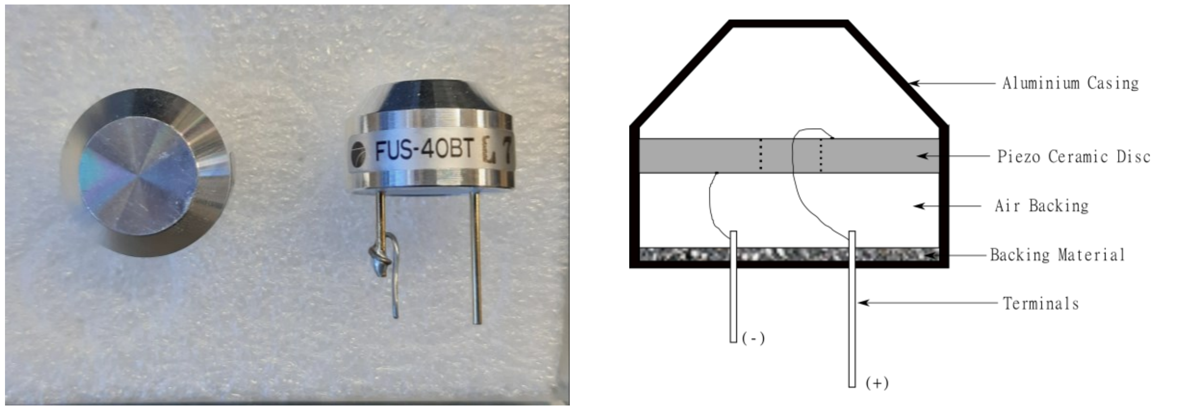

(b)

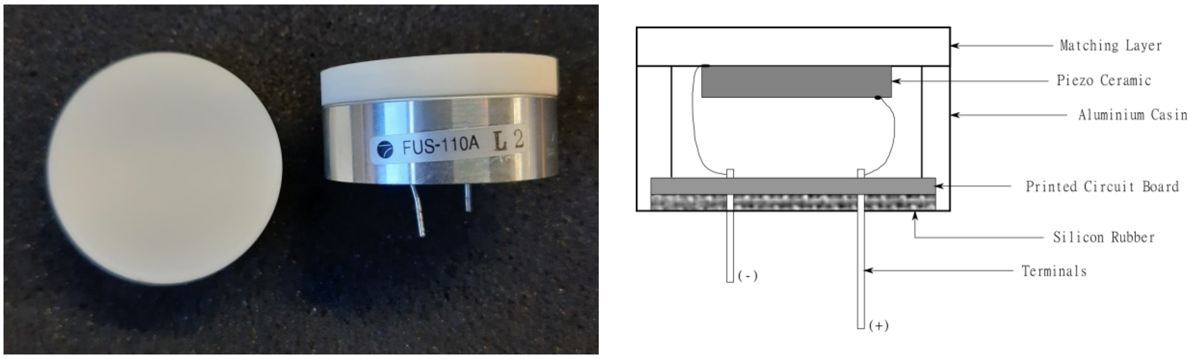

(c)

Figure 3.6: Off-the-shelf piezoelectric airborne ultrasonic transducers from Fuji Ceramics that will be investigated in this work (a) FUS-40E and its schematics (b) FUS-40B series (c) FUS-110A and its schematics.

3.2.1. Safety Standards

Unlike biomedical APT systems, standards for delivering power to wireless devices by transmitting high SPL acoustic waves through the air is not strictly defined. However, the ISO 620:2003 [190] (soon to be updated by ISO/CD 226) states safety specifications to evaluate the physical limitations of the generated acoustic field in the presence and absence of a listener. This can be used as general guidance for limiting the spatial-peak temporal-average intensity (I_{SPTA}) of the continuous acoustic field.

The two governed exposure parameters defined in most safety standards for continuous exposure are the frequency of operation and the average intensity of the acoustic field. It is essential to avoid high-intensity acoustic waves between 2 Hz and 20 kHz for wireless power transfer, which could cause noise irritation to humans and animals. Therefore, a transducer with its natural frequency in the ultrasonic range is selected for this work. The Food and Drug Administration (FDA) address to limit the I_{SPTA} to $7200\ \mu Wmm^{-2}$ to avoid thermal damage to tissues for diagnostic and power delivery devices [191]. The maximum transmitting SPL of all the sample transducers listed in Table 3.2 is well below this range. Also, prominent absorption losses in air and vast acoustic impedance difference between biological tissue and air reduce thermal heating risk due to continuous exposure to the acoustic field.

3.2.2. Frequency Selection

Other parameters that can be affected by the operating frequency are the attenuation and diffraction coefficients which directly affect the pressure amplitude and the APT link efficiency. This is analytically and experimentally investigated using FUS-40E and FUS-110A transducers operating at the resonance frequency of $40\,kHz$ and $110\,kHz$ respectively.

- **Diffraction**

The power harvested from the APT receiver is directly proportional to its surface area, and the acoustic waves that failed to be captured by the receiver are reflected into or absorbed by the medium. Therefore, the energy transfer will be optimal when the transmitted acoustic field is a narrow beam. However, diffraction occurs in the edges of the transmitter surface, causing side lobes of acoustic fields that prevent focused beams. A 2-Dimensional axisymmetric model is simulated in COMSOL using the pressure acoustics model, where a normal acceleration with dimension specified in Table 3.2 positioned at the origin transmits spherical acoustic wave radiation into the air medium of 1 m by 1 m area. The resulting SPL is shown in Figure 3.7.

The acoustic wave transmitted from FUS-110A is substantially focused than in FUS-40E and creates a higher number of side lobes in the former. The difference in the transmitted acoustic field can be explained by analysing the ratio between the transmitter radius and the wavelength. When this ratio increases, i.e., as the frequency increases, the transmitter surface changes from a point source to a large plate with a discrete array of acceleration points compared to its wavelength. Consequently, this creates a collimated beam of acoustic pressure between the APT transducers with high directionality. In other words, the FUS-40E has a $r_{source}(8\,mm) \approx \lambda(8.5\,mm)$ will act as a point source producing spherical acoustic radiation. Therefore, the wave is inclined to wave spreading and have significant geometric losses. On the other hand, the FUS-110A have a $r_{source}(18.5\,mm) \gg \lambda(3\,mm)$, so acts a piston source transmitting plane waves into the medium. Therefore, the acoustic beam has higher SPL in the near field, but the wave spreading losses in the 40kHz transducer is consistent throughout the field.

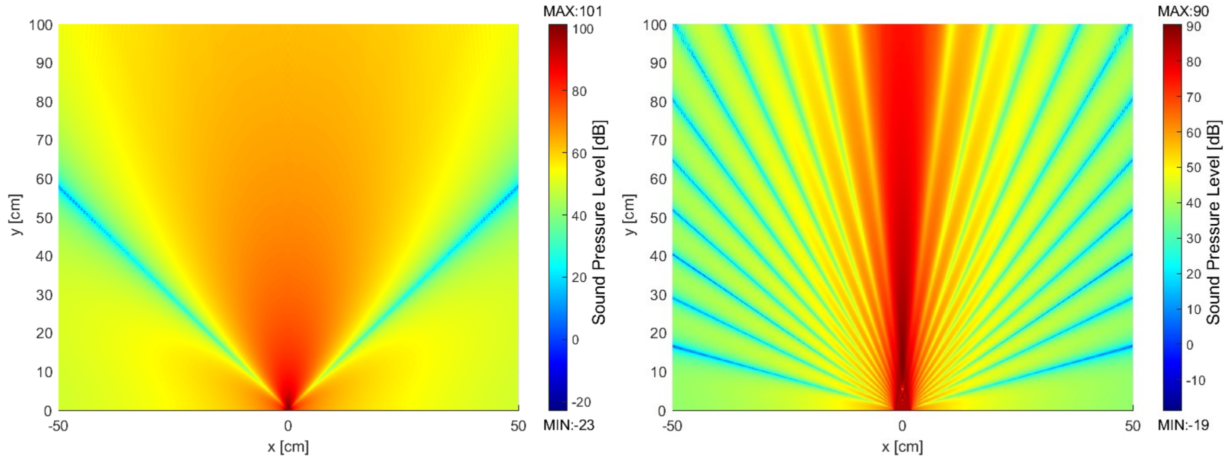

(a) (b)

Figure 3.7: COMSOL simulation for studying the diffraction profile of (a) FUS-40E and (b) FUS-110A transducers operating at their respective resonance frequencies.

The diffraction pattern for both transducers is simulated in COMSOL to study the relationship between the received power, receiver area and the operating frequency. A transmitter of varying frequency and dimensions presented in Table 3.2 is simulated to accelerate $1000\,m/s^2$ to tranmit power to a receiver of identical dimensions $35\,cm$ away. The computed received pressure integrated over the area of the receiver is plotted in Figure 3.8. Noticeably, the pressure exerted on the FUS-40E receiver is less compared to FUS-110A. The main contributing factor is the contrast in surface area of the transducers, where the active area of the FUS-40E and FUS-110A is $2\,cm^2$ and $10\,cm^2$ respectively. Further, the geometric losses in the FUS-40E receiver are significant due to spherical wave spreading. However, for the FUS-110A, the transmitted acoustic beam is more intense and focused targeted at the receiver location; therefore, the received pressure is tenfold higher than the FUS-40E receiver.

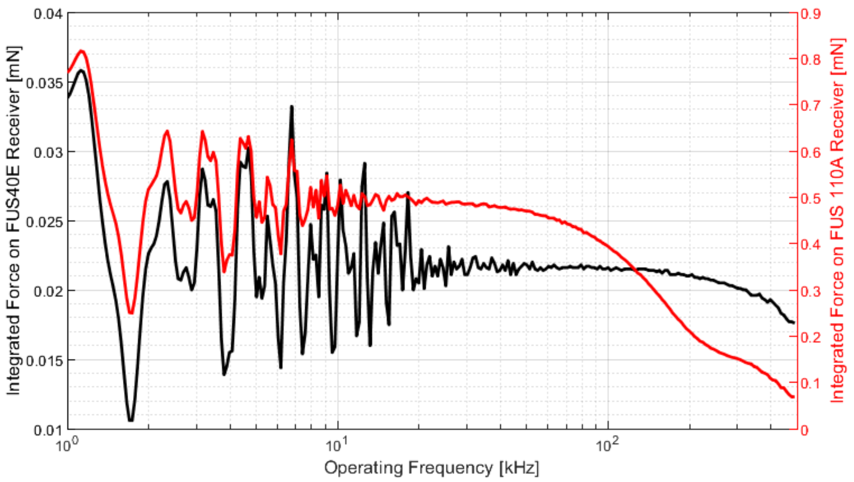

Figure 3.8: Integrated force exerted on the receiver 35 cm away from the transmitter operating at varying frequency.

For low operating frequencies, the transmitter radius is much smaller than the wavelength ($r_{source} \gg \lambda$). This creates multiple spherical lobes of acoustic waves that interfere with one another, resulting in valleys and peaks of acoustic pressure. Therefore, the pressure on the receiver surface differs for small changes in frequency. Additionally, although higher frequencies have lower diffraction losses, the attenuation and absorption losses increase with higher frequencies. This is evident from Figure 3.8, where the received pressure decays sharply for frequencies higher than 50 kHz. This is examined experimentally in the next paragraph by measuring the attenuation of the voltage across the receiver for increasing separation distance.

- **Attenuation**

Sound waves are subject to substantial absorption and attenuation loss as they propagate through a medium. The attenuation coefficient, as explained in Eq. 2.30, is a function of the operating frequency that will impact the decay of acoustic wave pressure over its travelling distance.

To experimentally determine the impact of attenuation, the selected transducers (used as both transmitter and receiver) powered by a STEVAL-IME011V2 high-voltage ultrasonic pulser board from STMicroelectronics is installed on a mounting bracket with precise position control. The pulser board requires a 3 V power supply, as shown in Figure 3.9a and generates a continuous square wave of the resonance frequencies with a voltage of $44V_{p-p}$ using two other power supplies. The whole setup is later lined with acoustic foam to reduce reflections and isolate the transducers from external noise, as shown in

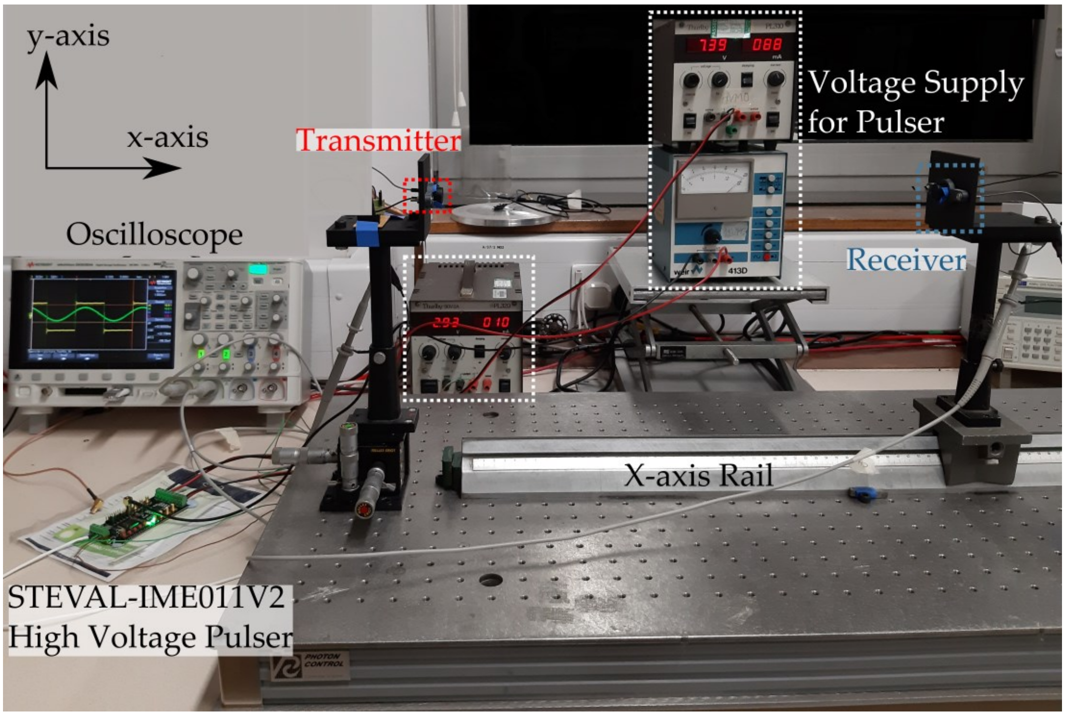

(a)

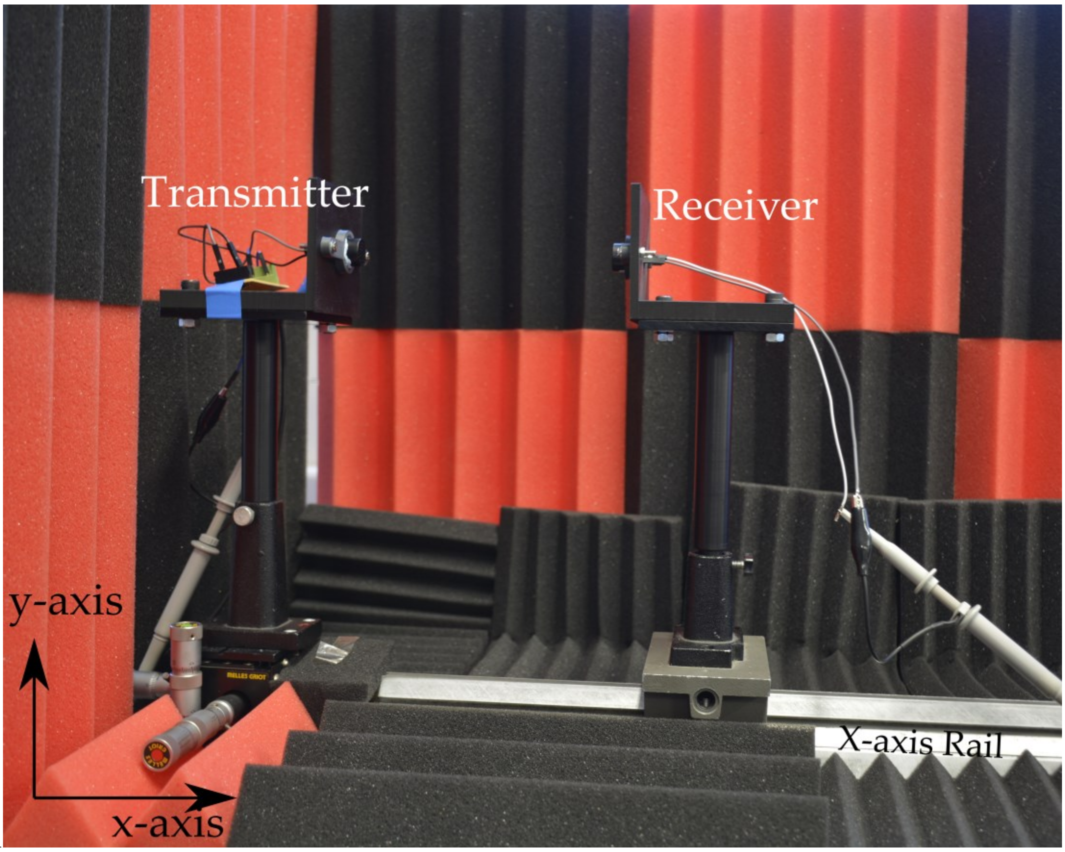

(b)

Figure 3.9: Experimental setup for analysing the APT transducers. (a) Displayed without acoustic foam to view the powering and measuring equipment. (b) Actual setup lined with acoustic foam to reduce reflections.

Figure 3.9b. Finally, the receiver is accurately aligned such that both transducers coaxially overlap and is moved along the x-axis rail for varying the separation distance between the transducers from 0 to 95 cm.

The open-circuit (OC) voltage across the receiver terminals is measured at $200\,\mu m$ increments in separation distance between the transmitter and the receiver. The results from the distance sweep for both the transducers are plotted in Figure 3.10a. The acoustic field in the near field region is unpredictable, and therefore significant fluctuations in the received voltage are observed for the FUS-110A until $33\,cm$. Also, the FUS-110A transducer is a matching-layer type with a $2\,mm$ thick plastic layer between the active surface and air to match the acoustic impedance. However, the oscillation in the receiver voltage is noticed well into the far-field region. This also applies to the FUS-40E transducer. Since both the transmitter and receiver faces are perfectly aligned, reflected acoustic waves due to impedance mismatch alternate between the transducers, causing reflections. These reflections cause sharp positive and negative peaks in the energy transfer efficiency due to superposition. The influence of reflections in energy transfer is investigated in detail in chapter 4.

For estimating the attenuation coefficient of the frequencies, the moving average of the data for every 10 data points is calculated and fitted for an exponential model. This moderates the nodes and antinode of the received voltage and acheives a better exponential fit of the curve. The results for FUS-40E and FUS-110A transducers are displayed in Figure 3.10b and Figure 3.10c, along with the corresponding fitted parameters. The attenuation of the voltage increases for higher frequencies, which is apparent from the attenuation coefficient that increases from -0.16 for the FUS-40E transducer operating at $40\,kHz$ to -1.54 for the FUS-110A transducer operating at $110\,kHz$. Further, for similar electrical input power for the transmitter, the FUS-110A transmitting SPL is significantly less than FUS-40E. For instance, an optimum resistive load of $0.8\,k\Omega$ was measured for the FUS-110A at its resonance frequency which yielded $12.2\,\mu W$ when the receiver was placed at $35\,cm$ separation distance (far-field limit). For similar circumstances, the FUS-40E transducer yielded $96\,\mu W$ at $35\,cm$ for an optimum resistive load of $10\,k\Omega$ at $40\,kHz$ frequency. In conclusion, the 40 kHz operating frequency was selected for this work attributable to its low attenuation and fitting the safety guidelines for wireless power transfer.

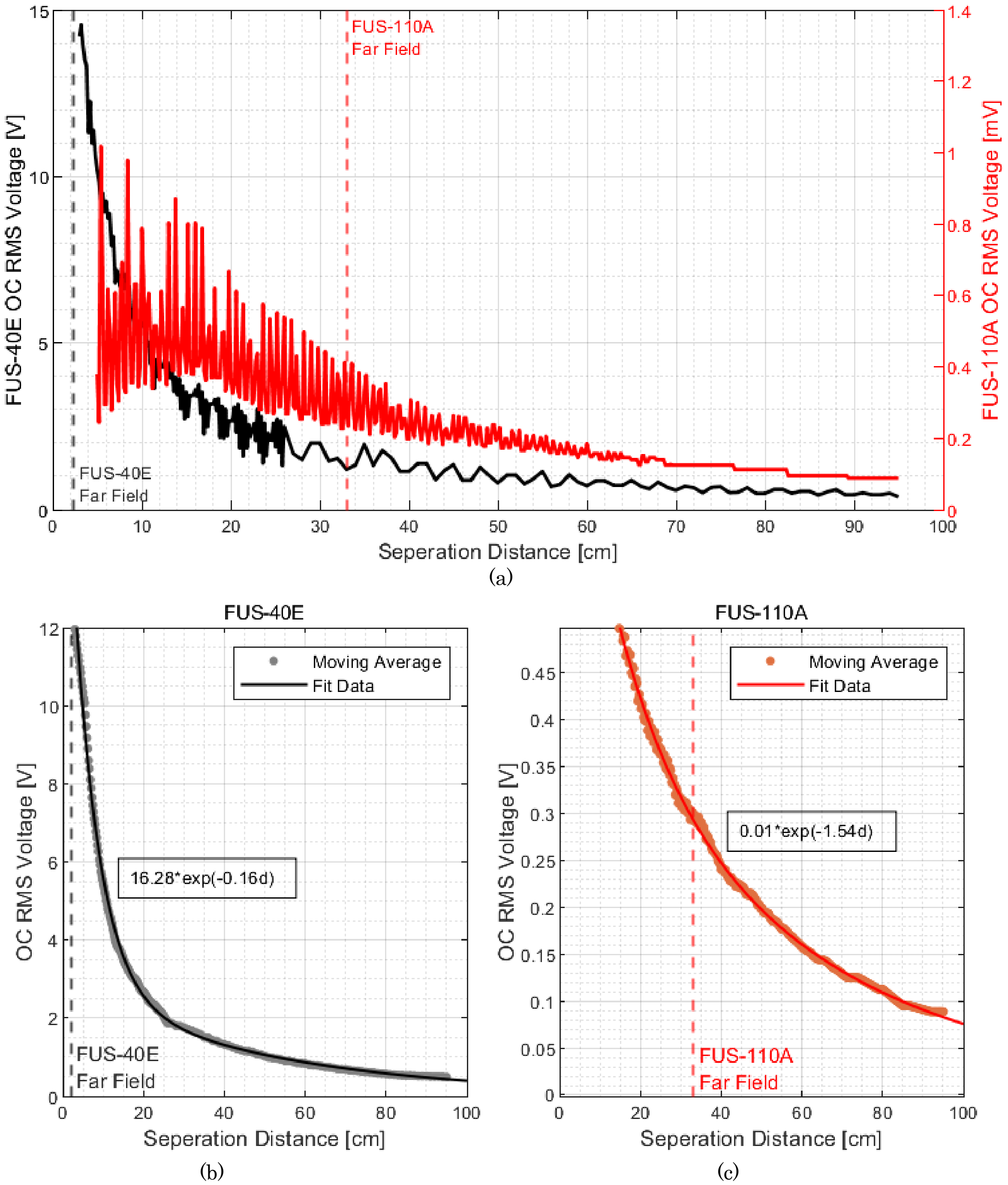

Figure 3.10: (a) Measured open circuit (OC) voltage across a set of FUS-40E operating at 40 kHz and FUS-110A transducer operating at 110 kHz receivers for varying separation distance between the transducers. The measured data is processed for moving average for every 10 data points and fitted to an exponential function to compute the attenuation coefficient for (b) FUS-40E and (c)FUS-110A transducer.

3.2.3. Transducer Structure

Piezoelectric transducers are used in different architectures, out of which the bulk mode and the flexural mode are standard for ultrasonic transducers. This section investigates the FUS-40E and FUS-40B series operating at a nominal frequency of 40 kHz, but with different structural configurations. The FUS-40E transducers are circular soft ceramic PZT plates glued to a metal diaphragm (unimorph) operating in flexural vibration mode enclosed in a plastic case. The active side of the plastic case has circular holes for an open-type tube (Figure 3.6). These are dual-purpose transducers and therefore can be used as both the transmitter and receiver.

The FUS-40B series transducers are closed type transducers with a metal case enclosing the piezo element. The active element is a circular piezoelectric disc operating in radial mode vibration. As these are single-purpose transducers, FUS-40BT is used as a transmitter, and the FUS-40BR is used as an APT receiver. Using the setup illustrated in Figure 3.9, different combinations of the transducers were examined for transmitting SPL, receiver sensitivity and power output. Since the input voltage for FUS-40BT is restricted to 15 V, the STEVAL-IME011V2 voltage pulser excites the transmitter with 15 V_{p-p}. The receiver's corresponding optimum resistive load is connected in series, and its voltage was recorded for varying separation distance from 3 cm to 26 cm for every 200 μm. the piezoelectric material used in both designs is the same C-6 class PZT from Fuji ceramics. The results of three transducer combinations: FUS-40E to FUS-40E, FUS-40BT to FUS-40E, and FUS-40BT to FUS-40BR, are plotted in Figure 3.11.

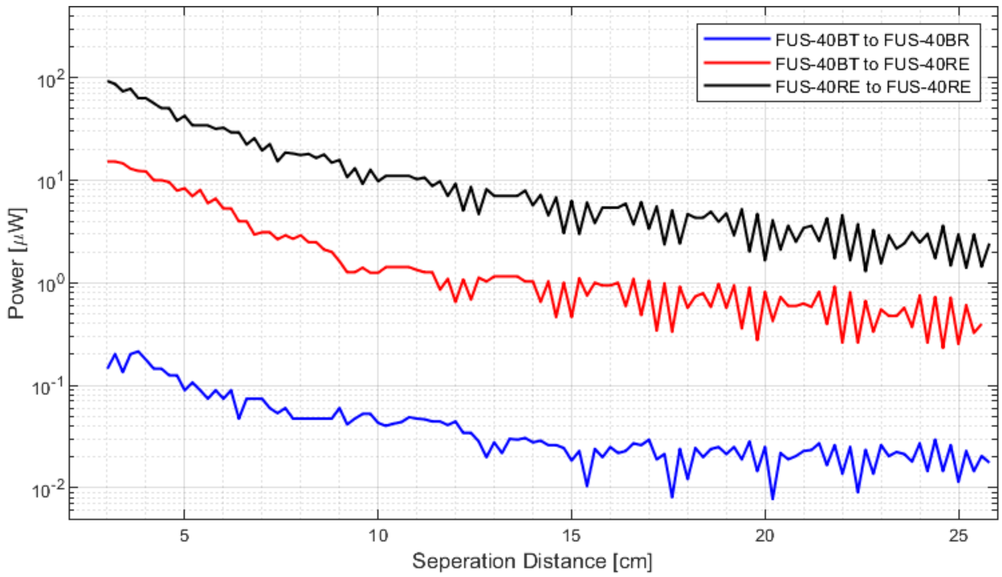

Figure 3.11: Measured received power for different transducer types operating at 40 kHz for a distance sweep between 3 cm to 26 cm.

Regardless of the transducer model, the attenuation of the acoustic wave appears to be constant in all cases, as it is principally a function of the operating frequency and the ambient conditions. The reflection for the FUS-40B series is marginally less than the FUS-40E, which is perceptible from the reduced power fluctuations in FUS-40B for separation distance less than 15 cm. This might be a consequence of the chamfered edges of the transducer that deviates the reflected acoustic waves from the path of the transmitted waves. However, the power density of the FUS-40S series is lower than the FUS-40E. This is evident from the power yield difference for the combinations FUS-40E to FUS-40E and FUS-40BT to FUS-40E, as the FUS-40RE receiver delivers more power to the load for the same transmitted power. Furthermore, the FUS-40E transmitter has a higher transmitting SPL, given that the FUS-40E to FUS-40E has the highest power yield. For this reason, the FUS-40E airborne ultrasonic transducer from Fuji Ceramics was selected for this work and will be used as both transmitter and receiver.

3.3. Experimental Validation

The frequency responses of the FUS-40E transducers under various conditions are experimentally examined in this section. Methods to improve the transmitted power are later presented to analyse the effects of different loading techniques.

3.3.1. Impedance Frequency Analysis

The transducer impedance was measured as a function of frequency using Precision Component Analysers 6440B. Four samples of the same model were measured to judge their variance, although they showed the same results. The average equivalent resistance and reactance, including air resistance on the membrane, are plotted in Figure 3.12. The impedance measurements revealed three resonance frequencies for the transducers at 39.5 kHz, 61 kHz and 333 kHz. The higher harmonics are far from the fundamental resonance. Hence, it is relatively inconsequential for this work. The inset graph focuses on the impedance trend around 40 kHz, which is the nominal frequency of the transducer.

However, the behaviour of a piezoelectric resonator is usually sensitive to ambient conditions such as temperature, humidity and pressure. The transducer mechanical parameters might significantly change if the ambient condition essentially modifies. Therefore, in this section, the impedance was analysed in varying temperatures and pressure to identify any parameters that would impact the transducer resonance frequency.

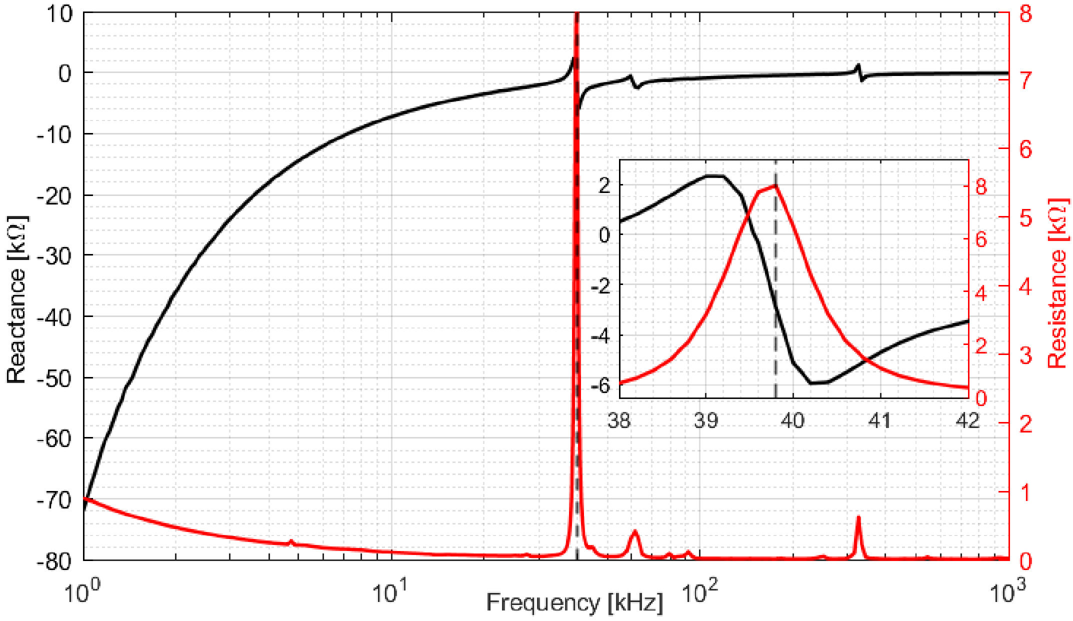

Figure 3.12: Equivalent reactance and resistance of FUS-40E piezoelectric resonator measured at $25.6^{\circ}C$ and 20% R.H. dry air.

- **Change in Temperature**

In this study, the FUS-40E transducers were placed in an automated desiccator chamber, where the chamber temperature can be controlled between $20^{\circ}C$ to $45^{\circ}C$. The impedance was measured at varying temperatures by keeping the relative humidity constant at 20% dry. Figure 3.13 shows the impedance measured for varying temperatures from the ambient temperature $25.6^{\circ}C$ to $40^{\circ}C$. It is evident from the results that, although there is slight impedance variation near the resonance peaks for different temperatures, this is negligible.

Also, a detailed inspection identified that the transducer resonance frequency remained constant, and only the magnitude of impedance changed around the harmonic frequencies. For all temperatures, the fundamental series resonance occurs at 39.5 kHz when the impedance is minimum, and the circuit current is maximum. Similarly, 40.5 kHz is the fundamental parallel resonance when the impedance is maximum and the circuit current is minimum. Therefore, this may be attributed to a change in the transmission medium properties instead of the piezoelectric element.

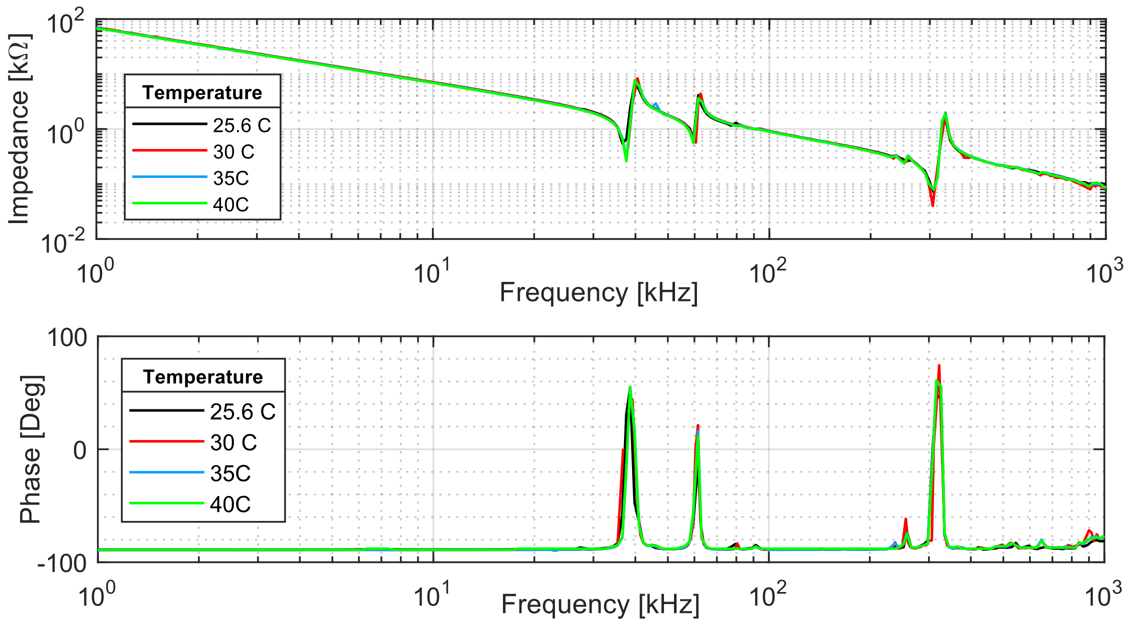

Figure 3.13: Impedance profile of FUS-40E transducers showing impedance (top) and phase (bottom) for varying temperature and 20% R.H. dry air.

- **Change in Pressure**

When an AC electrical source powers the transmitter, the active membrane will apply a pulsating pressure into the transmitting medium resulting in acoustic waves. As a result, the membrane will also experience an opposing force, which was modelled as Z_a in Figure 3.3a. In order to distinguish between the transducer's mechanical impedance and the medium resistance (Z_a), the opposing force should be eliminated or reduced to a minimum. This can be achieved by measuring the reactance and resistance of the transducer in a vacuum where the medium resistance, $Z_a \approx 0\Omega$. Consequently, by comparing the measurements in air and vacuum, $Z_a = R_a + jX_a$ for air can be evaluated. Also, it is noteworthy that the back surface of the transducer is clamped. Therefore, the measured Z_a will include the resistance of air only on the front surface.

The transducer is placed in a small vacuum chamber, as shown in Figure 3.14, which is externally connected to the impedance analyser. The measured equivalent resistance and reactance under different pressure is plotted in Figure 3.15 with the surrounding conditions at 25.6°C and 20 % RH dry air. The dashed box surrounding the fundamental frequency is focused on the inset graph in Figure 3.15.

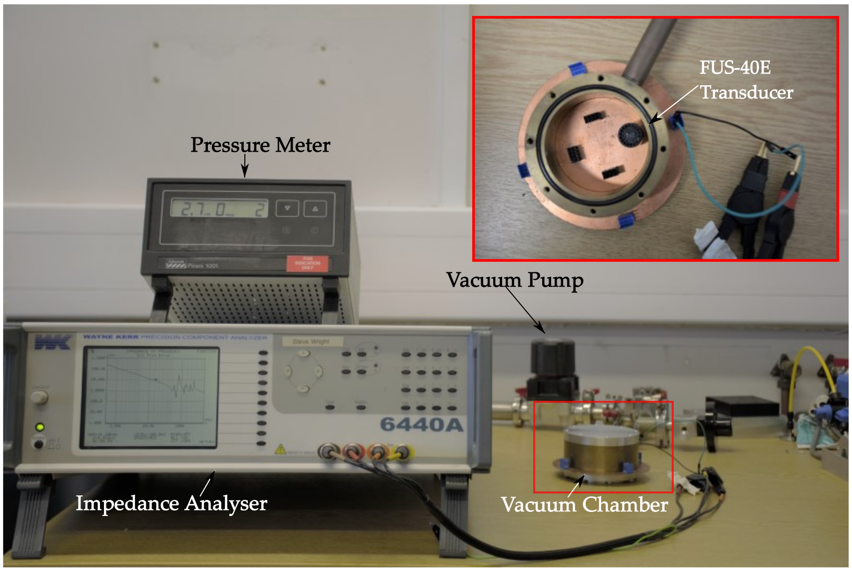

Figure 3.14: Experimental setup for measuring the impedance of FUS-40E transducer in air and vacuum. The inset picture shows the inside of the small vacuum chamber.

The reactance trend of the transmitter in a vacuum is similar to that in atmospheric pressure (meaning, X_a is small). Therefore, the resonance frequency will not be impacted by the transducer's mode of operation (transmitter or receiver). However, resistance in vacuum is much higher than in atmospheric pressure. The measured difference was 8.3 $k\Omega$, possibly due to the higher radiation absorption between the membrane and the medium at lower pressure.

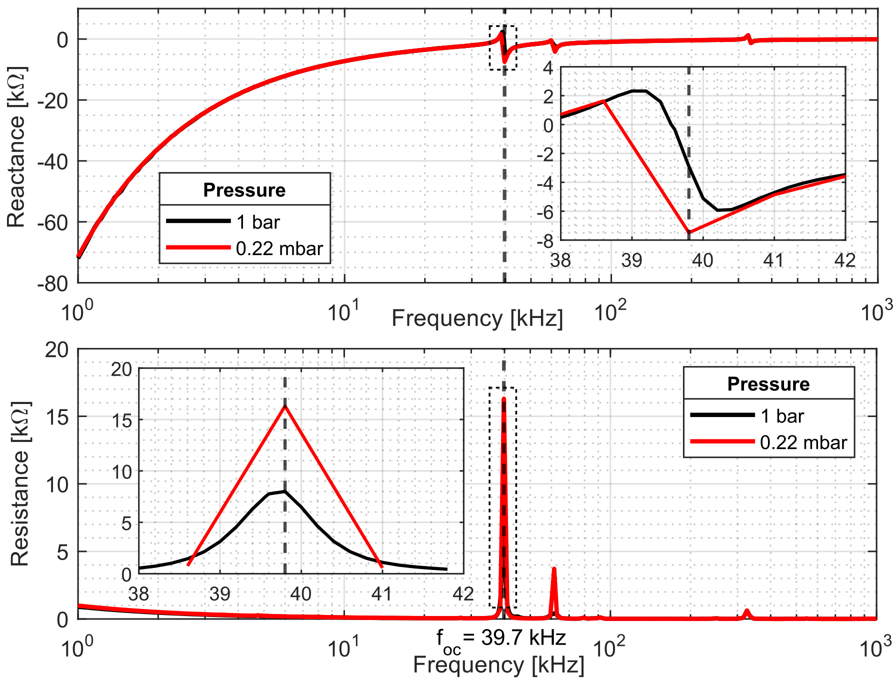

Figure 3.15: Measured reactance (top) and resistance (bottom) of a FUS-40E transducer in atmospheric pressure and vacuum (0.22 $mbar$) to calculate Z_a.

From Figure 3.15 (bottom), the source impedance measured in air is purely resistive at $f = 39.7\ kHz$, which is the measured fundamental resonance frequency of the transducer. The transducer provides the maximum output voltage obtained for a given incident wave at this frequency, signifying the open-circuit condition. Therefore, using a resistive load to match the impedance at this frequency would be sufficient to deliver maximum power. Considering Figure 3.4, the Z_S of a piezoelectric transducer can be approximated as a capacitor and resistor in series, which can be matched by a load Z_L consisting of an inductor and resistor in series. Table 3.3 summarises the required load impedance for both resistive and inductive load matching for different transmitter frequencies.

It is also evident from Figure 3.15 (top, inset) that from $38\,kHz$ to $39.5\,kHz$, the equivalent reactance of the transducer is positive. This implies that the modal mass overcomes the capacitance of the transducers at this frequency range. Consequently, the transducer has an inductive behaviour in this range, and a capacitor in series with a resistor is needed for load matching.

Table 3.3: Measured transducer impedance and equivalent calculated values for complex and resistive loading.

Frequency $[kHz]$	Source Impedance		Load Matching		
			Resistive	Complex	
	$X_S[\Omega]$	$R_S[\Omega]$	$R_L^R[\Omega]$	$L_L[mH]$	$R_L[\Omega]$
37	-500	190	540	2	190
37.5	-100	300	320	0.5	300
38	500	550	750	$(8.4\,nF)$	550
39	2300	3130	4000	$(1.8\,nF)$	3130
39.5	0	7500	7500	0	7500
40	-5100	6500	8250	20	6500
40.4	-5900	3200	6700	23	3200
41	-4700	1100	5000	18	1100
41.4	-4000	660	4000	15	660
42	-3500	360	3500	13	360

3.3.2. Load Impedance Matching Techniques

To verify the calculated matched impedance values, a FUS-40E transmitter is powered by a STEVAL-IME011V2 in the same setup as shown in Figure 3.9. The pulser board generates a continuous square wave of pre-programmed frequencies surrounding the resonance with a voltage of $44V_{p-p}$. The receiver is fixed at 10 cm separation distance away from the transmitter, accurately aligned to overlap coaxially. A series network of an inductive (ELC DL07) and a resistive decade box (RS PRO R-100) is connected

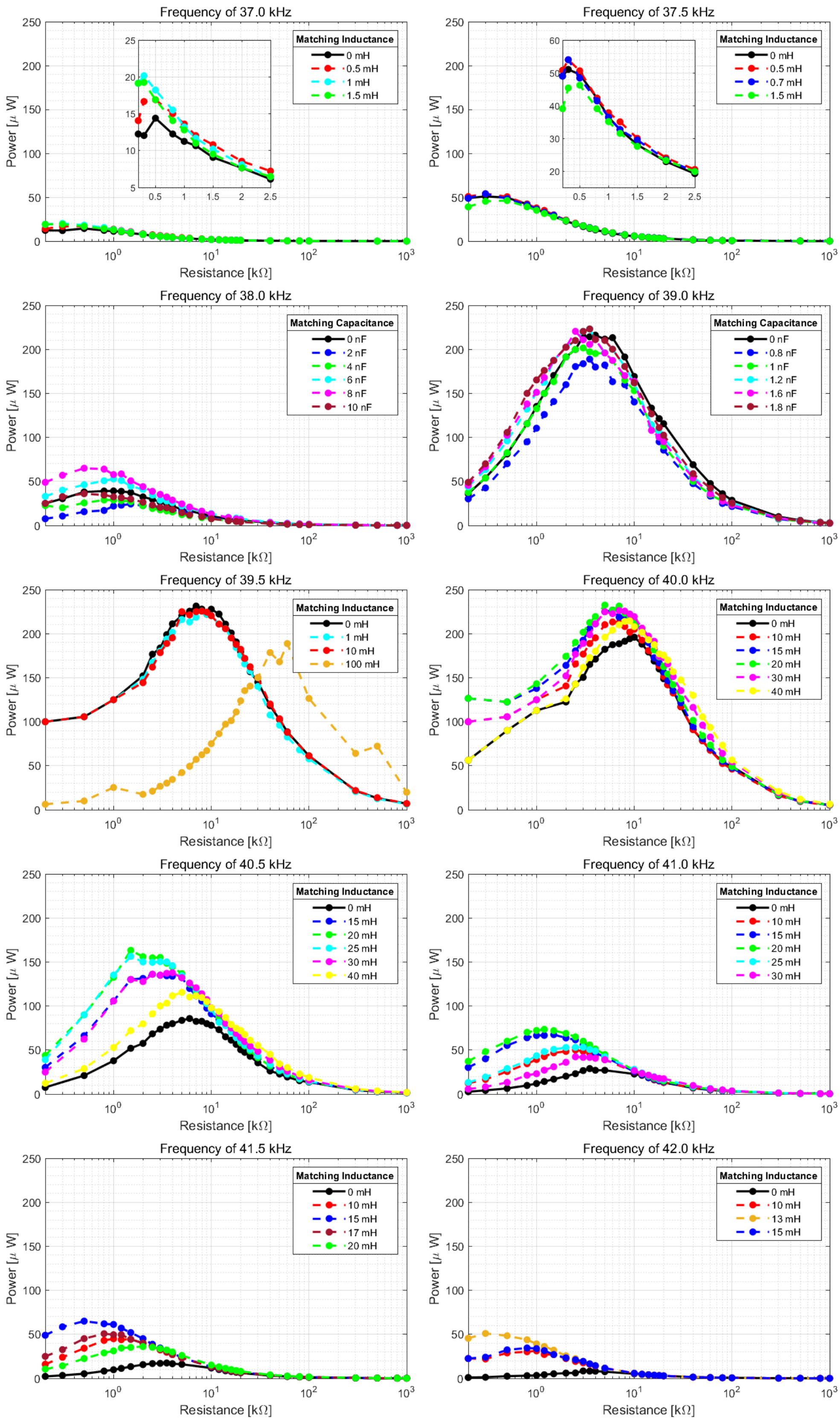

Figure 3.16:Resistance sweep of the APT receiver for complex and resistive matched loading techniques to find the optimum load for maximum power.

across the receiver ports to measure the power delivered to the load. The inductance is replaced by a capacitance decade box (TENMA 72-7265) for frequencies between 38 kHz and 39.5 kHz. Similar arrangements are adopted for tuning the reactance of the transmitter.

Figure 3.16 shows the output power measured delivered to the load resistor operating at different frequencies. The measurements were taken at ambient conditions of $25.5(\pm 0.5)^{\circ}C$ temperature and 20% R.H. dry air. The measured power is plotted as a solid black line for resistive loading and dashed colour lines for complex (inductive or capacitive) loading. Also, the power axis in all plots is kept identical to correlate the power trends in varying frequencies. Since the power yield at $37\ kHz$ and $37.5\ kHz$ is low, an inset graph is added to focus on the power trend neighbouring the maximum power point. It is also worth noting that only the receiver is load matched for these measurements.

At $39.5\ kHz$, resistive loading generates the optimum power as the reactance of the transducer tends to zero approaching the resonance frequency. It is observable from Figure 3.16 that when a $1\ mH$ inductive load is introduced to the receiver, the power delivered to the load is reduced from $230\ \mu W$ to $225\ \mu W$. The power was further reduced by $52\ \mu W$ when connecting a $100\ mH$ inductance to the load that introduces high reactive power in the circuit. However, significant power improvements can be seen in other operating frequencies when changing from resistive to inductive loading. Nevertheless, all the graphs demonstrate a reduction in power yield once the load reactance is more than the optimum reactive load.

Consider the increase in delivered power, $\Delta P_L = P_L^C - P_L^R$ where, P_L^C and P_L^R is the power delivered to the load in complex loading and resistive loading, respectively. The graphs of off-resonance frequencies show a trend of increasing ΔP_L when the operating frequency moves away from resonance. Additionally, ΔP_L near the parallel resonance ($40.5\ kHz$) is higher than at series resonance frequency ($37.5\ kHz$), which could be attributed to the higher impedance at the former ($Z_{parallel} = 8.35k\Omega$) than later ($Z_{series} = 0.26k\Omega$). Therefore, tuning out a higher reactive power using complex loading boosts the power delivered to the load. For instance, the power yielded at both $38\ kHz$, and $41\ kHz$ operating frequency ($1.5\ kHz$ away from the resonance frequency) under resistive loading is similar. However, the ΔP_L achieved by complex loading in $41\ kHz$ is $20\ \mu W$ higher than in $38\ kHz$.

To experimentally determine the optimum complex and resistive load for the receiver, comprehensive investigations were implemented with reactive load incremented in minor steps. The results for the centre frequencies are shown in Figure 3.17. The measured optimum load impedance for both resistive and reactive loading is summarised in Table 3.4, which agree with the theoretical calculations.

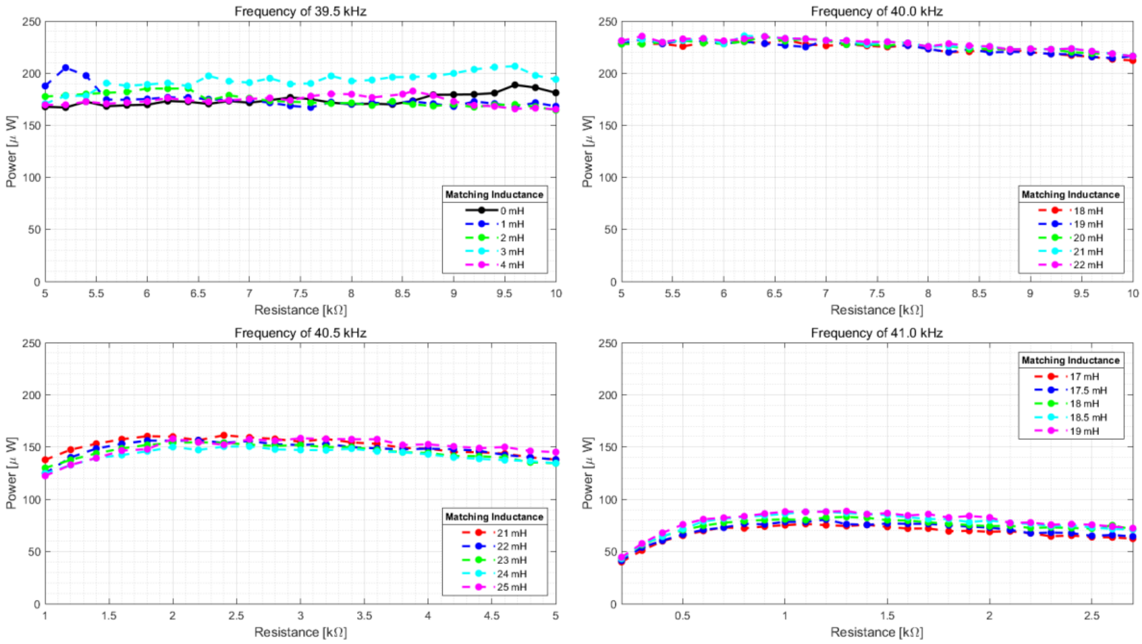

Figure 3.17: Thorough investigation to experimentally determine the optimum load for complex loading.

Furthermore, it is evident from Figure 3.16 and Figure 3.17 that power delivered to the receiver decreases irrespective of the load matching as the operating frequency deviates from resonance. This is due to the mismatch between the transmitter and the receiver tuning. Considering that the transmitter reactance is also significant at non-resonance frequencies, considerable power is lost as reactive power. To remedy this, an inductor is connected to the transmitter to electrically resonate with the capacitance of the transducer at its operating frequency. By fixing the calculated reactive load matching values for the receiver, the optimal matching inductor for the transmitter is experimentally determined and is summarised in Table 3.4.

For low frequencies such as $37\,kHz$ and $37.5\,kHz$, the tuning inductance for the transmitter is very low ($< 1\,mH$) and the ΔP_L due to transmitter matching is trivial. Therefore, the transmitter is not tuned for these frequencies. The power transfer efficiency for different combinations of the load techniques is studied in the next section.

Table 3.4: Measured optimum load for tuning the transmitter and receiver for both resistive and complex loading techniques.

Frequency $[kHz]$	Transmitter	Receiver		
		Resistive	Complex	
	$L_S[\Omega]$	$R_L^R[\Omega]$	$L_L[mH]$	$R_L[\Omega]$
37	0	500	1	300
37.5	0	300	0.7	300
38	(8.4 nF)	800	(8.4 nF)	500
39	(2 nF)	4000	(1.8 nF)	3500
39.5	0	7500	0	7500
40	20	10000	20	6500
40.4	18	6000	23	2400
41	17	3500	20	1500
41.4	11	3500	15	500
42	10	3000	13	300

3.3.3. APT System Transfer Efficiency

The same experimental setup as shown in Figure 3.9b is use

Th d to analyse four different impedance matching techniques: (1) Resistive loading at receiver and no transmitter tuning (R- Resistive Matched) (2) Complex loading at receiver and no transmitter tuning (R-Complex Matched) (3) Complex transmitter tuning and resistive loading at receiver (T- Complex Matched) (4) Complex loading at receiver and complex transmitter tuning (Both Complex Matched). Figure 3.18 summarises the power delivered to the receiver at varying frequencies for these mentioned techniques.

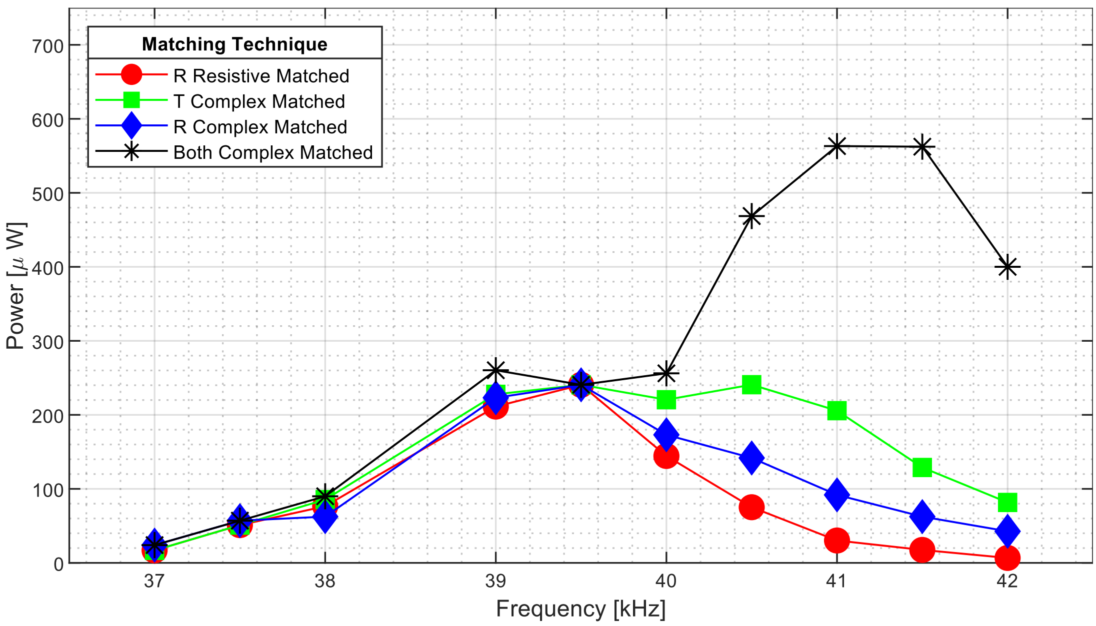

Figure 3.18: Power delivered to the load at the receiver for different impedance matching techniques for a transmitter powered by a $44V_{p-p}$ source voltage.

Evidently, the power yield for all the impedance matching techniques at the resonant frequency is indifferent, as the resistive and complex loading condition is unvaried. Also, the power yield of the APT system is minimum at the R- resistive matched condition for non-resonance frequencies. This is in agreement with the analytical results from Eq. 3.22 and Eq.3.14, where considerable power is dissipated by the transducer reactance as reactive power. By introducing a reactive component to the load in the R-complex matching, the power is improved in off-resonant frequencies. Namely, a maximum of 88% increase was observed at 40.5 kHz operating frequency when the power delivered to the load was improved from $75\mu W$ to $142\mu W$. The calculated voltages across the load resistor and the calculated power are tabulated in Table 3.5.

Table 3.5: Measured RMS voltage and the calculated power delivered across the load resistor for the various load matching techniques.

Frequency	R- Resistive Matched			R-Complex Matched			T- Complex Matched			Both Complex Matched		
$[kHz]$	R_L^R $[k\Omega]$	V_L^R $[mV]$	P_L^R $[\mu W]$	R_L^C $[k\Omega]$	V_L^C $[mV]$	P_L^C $[\mu W]$	R_L^R $[k\Omega]$	V_L^R $[mV]$	P_L^R $[\mu W]$	R_L^C $[k\Omega]$	V_L^C $[mV]$	P_L^C $[\mu W]$
37	0.5	260	17	0.3	240	24	0.5	260	17	0.3	240	24
37.5	0.3	350	51	0.3	370	57	0.3	350	51	0.3	370	57
38	0.8	700	77	0.5	500	62	0.8	740	85	0.5	600	90
39	4	2600	211	3.5	2500	223	4	2700	228	3.5	2700	260
39.5	7.5	3800	241	7.5	3800	241	7.5	3800	241	7.5	3800	241
40	10	3400	144	6.5	3000	173	10	4200	220	6.5	3650	256
40.5	6	1900	75	2.4	1650	142	6	3400	241	2.4	3000	469
41	3.5	920	30	1.5	1050	92	3.5	2400	206	1.5	2600	563
41.5	3.5	700	17.5	0.5	500	62	3.5	1900	129	0.5	1500	562
42	3	400	6.5	0.3	320	42	3	1400	82	0.3	980	400

Comparing the R-resistive matched and the R-complex matched approaches, ΔP_L and the transducer reactance in that operating frequency appears to be directly related. This is sensible since the matched load tunes out the transducer reactance to "rectify" the lost reactive power. Moreover, the decay in power when the operating frequency moves away from the resonance is low in R-complex matching. However, improving the system efficiency solely using this method becomes limited or negligible for operating frequencies between 37 kHz to 39 kHz as the reactance of the transducer is low. Therefore, tuning the transmitter according to the operating frequency would improve the power transfer efficiency by increasing the SPL of the transmitted acoustic waves.

The transmitter's reactive power was evaluated using a small resistor of 280 Ω to its ground terminal. The voltage and the phase difference between the source voltage and the resistor were measured to get the transmitter current and phase. Table 3.6 summarises the trends in real and reactive power dissipated by the transmitter as a function of its operating frequency. When the transmitter reactance X_S is not tuned, the source current is observed to be out phase. Consequently, a fraction of the power is lost as reactive power, resulting in low SPL for the transmitted sound waves. For example, operating at 41 kHz, the current is 77° out of phase with transmitter voltage. Consequently, more than 97 % of the power delivered to the transmitter is lost as reactive power. By introducing an inductor, the phase difference was reduced to 10°, boosting the delivered real power and subsequently increasing the SPL. This is apparent from Figure 3.18 as both 'T complex matched' and 'Both complex matched' consistently have higher power throughput than the other techniques.

Since the transmitter is not tuned for 37 kHz, 37.5 kHz, and 39.5 kHz, the results for R-resistive and T-complex, R-complex and Both complex is indifferent. However, significant improvement is observed for transmitter frequencies when the capacitance of the transmitter is tuned with an inductance (40 kHz to 42 kHz). For instance, at 41 kHz, the received power with and without transmitter tuning is 206 μW and 30 μW. This is further boosted by a factor of 17 when both the transmitter and receiver is tuned. However, the conditioning circuits for high frequency should be designed with caution as the load resistance is very low ($< 1k\Omega$), leading to large circuit currents.

Table 3.6: Evaluation of the transmitter reactive power for off-resonance frequencies.

Frequency $[kHz]$	RMS Voltage $[V]$	RMS Current $[mA]$	Phase $[Deg]$	Real power $[mW]$	Reactive Power $[mVAR]$
37	13	10	-67	50	120
37.5	13	10	-31.5	110	68
38	13	10	42	96	87
39	13	10	36.5	104	77
39.5	13	10	0	130	0
40	13	10	-38	102	80
40.5	13	10	-62	60	115
41	13	10	-77	29	127
41.5	13	10	-81	20	128
42	13	10	-84	13	129

Matching the inductive reactance of the transmitter for the operating frequencies 38 kHz and 39 kHz yielded scarce improvement in power yield due to the low reactance of the transducer at these frequencies. Table 3.7 summarises the power transfer efficiency of the APT system for the different loading conditions when the receiver is placed 10 cm away from the transmitter with accurate coaxial alignment. The efficiency is calculated as the ratio of the RMS real power delivered to the receiver's load to the RMS apparent power fed to the transmitter. In most cases, the power transfer efficiency is favourable at the 'Both complex matched' method for operating frequencies where the reactance of the transducer is capacitive. Maximum efficiency of 0.43% was achieved in this work when the transmitter was powered with 130 mW at 41 kHz.

Table 3.7: Power transfer efficiency of the different load matching methods.

Frequency [kHz]	Power Transfer Efficiency [%]			
	R- Resistive Matching	R-Complex Matching	T-Complex Matching	Both Complex Matching
37	0.013	0.018	0.013	0.018
37.5	0.04	0.04	0.04	0.04
38	0.06	0.05	0.07	0.07
39	0.17	0.17	0.18	0.2
39.5	0.18	0.18	0.18	0.18
40	0.11	0.13	0.17	0.2
40.5	0.06	0.11	0.19	0.36
41	0.02	0.07	0.16	0.43
41.5	0.013	0.04	0.1	0.43
42	0.005	0.03	0.07	0.31

3.4. Conclusion

A study on transducer selection and optimum load matching techniques dedicated to acoustic wireless power transfer through air is presented. A hybrid modelling approach using both equivalent circuit modelling (for electronic conditioning circuit optimisation) and finite element modelling (for APT link optimisation) was applied to examine off-the-shelf airborne ultrasonic transducers. The 40 kHz operating frequency is selected for remote powering considering the safety guidance, diffraction, attenuation, and transducer design losses.

Subsequently, the transducers' impedance frequency response was measured to calculate the equivalent matching impedance and the analytical solutions were validated experimentally by determining the matching inductance and load resistance value at the maximum power point. Experimental results show that resistive matching is an acceptable solution at resonance frequency as the transducer reactance is negligible. However, for operating frequencies off-resonance, the power yield substantially increases when both transducers are correctly tuned. For instance, the power increased from $240\ \mu W$ to $563\ \mu W$ when shifting from $39.5\ kHz$ to $41\ kHz$, as both transducers are tuned for optimum power transfer.

Additionally, reactance cancellation broadens the operational bandwidth of the APT system by up to $4\ kHz$ where power greater than $240\ \mu W$ can be achieved. However, the power improvement for operating frequencies less than $39\ kHz$ is negligible, which needs further investigation. This is especially true when the transducer reactance is inductive.

The contributions of this chapter are to provide a strategy for APT transducer selection and evidence the complex load matching technique to improve the power yielded by an

APT receiver. Future work will apply the findings to design a self-tuneable impedance matching circuit for varying frequencies to control the losses due to reflection and standing waves between the transducers.

4. Acoustic Power Transfer Link

The power generated by an acoustic receiver is a function of its position relative to the transmitter in terms of depth, orientation, and alignment. Furthermore, acoustic waves incident on the surface of the receiver will partially reflect into the propagation medium, altering the APT link's behaviour. In this chapter, the acoustic wave behaviour in the medium and the transducer power sensitivity is studied for changes in their location and alignment. This analysis provides insight into the FUS-40E transducer employed in an APT system, which facilitates designing a robust APT system with low power sensitivity for fluctuations in receiver position and alignment with reference to the transmitter. In particular, the system performance is defined for varying frequencies and methods to develop a robust APT system using auto-tuning and impedance matching.

4.1. Reflections

Like electromagnetic waves in transmission lines, a fraction of the sound wave will be reflected when a mismatch between the transducer and propagation medium impedance occurs. The amplitude of the reflected wave is proportional to the impedance difference. Therefore, as the acoustic impedance between PZT and air differs vastly, a significant fraction of the acoustic energy is reflected into the air at the transducer-medium boundary for both the transmitter and the receiver. Consequently, sound waves are continually reflected between the transducers until the power of the acoustic waves is dissipated as absorption. In addition, the reflected wave has a phase difference with reference to the transmitted wave which depends on the position of the transducers and the acoustic wave properties. Consequently, the two counter propagating waves of the same frequency interferes, leading to peaks and valleys of acoustic power in the medium. This forms a standing wave in the propagation medium, altering the output power profile of the APT link.

At positions where the phase difference is a multiple of 2π, the reflected and the transmitted wave will be in phase and interfere constructively. Therefore, the transmitted and the reflected wave resonate, in the medium amplifying the pressure amplitude of the transmitted wave. Contrastingly, in positions where the reflected wave has as $(2n + 1)\pi$ phase difference, the waves will interfere destructively, reducing the transmitted wave amplitude. The location of these positions depends on the transducer separation distance, frequency of the transmitted wave and medium sound velocity. In this section, the reflection between two piezoelectric transducers is modelled using finite element modelling in COMSOL Multiphysics, and the results are then experimentally validated to study the standing wave behaviour in air medium.

4.1.1. FEM Analysis

The APT system is simulated in COMSOL Multiphysics by adopting piezoelectric and acoustic physics coupled through boundary conditions between the transducers and air medium. The simulation is expected to present a comprehensive model describing the coupling between the transducers and the transmission medium, wave propagation and the occurrence of reflections at boundaries. The system model was designed as a symmetric 2-D model as shown in Figure 4.1, consisting of two piezoelectric membranes with the piezo dimensions summarised in Table 3.2, operating at 40 kHz. The transducers were placed in a dome of air medium of 50 cm radius including a 5 cm perfectly matched layer (PLM). In addition, a mesh with subdivisions of size $\lambda/5$ is created to compute the acoustic behaviour.

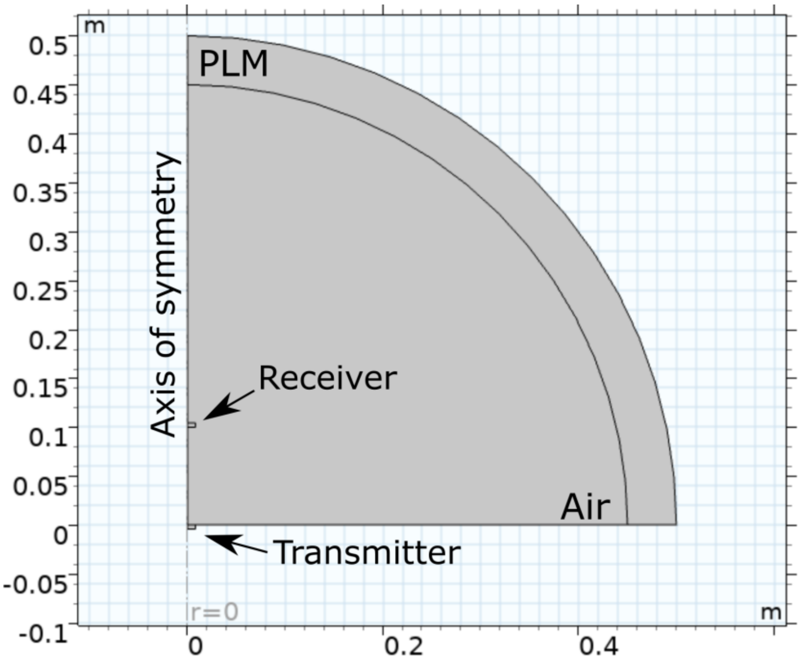

Figure 4.1: 2-Dimensional symmetric model implemented in COMSOL for FEM analysis of standing waves in an air-based APT system.

A parametric sweep by increasing axial distance between the transmitter and the receiver is performed for the shown system. The integrated acoustic pressure across the receiver surface facing the transmitter was evaluated, and the results are plotted in Figure 4.2. Analysing the results in MATLAB, the received power can be interpreted as a superpositioned wave consisting of a deteriorating signal representing a mean RMS value of the received sound pressure (Exponential component) with a dynamic component due to reflection (Sinusoidal Component) (Figure 4.2b). The source of the modulating amplitude of 30 mm wavelength is explained later in this section. Christensen and Roundy in [120] formulated the distance between the standing wave peaks ($\Delta\mathbb{Z}$) as shown in Eq. 4.1 and this can be defined as the half wavelength of the transmitted sound. This is because the standing waves interfere constructively when the reflected wave is 180^o phase difference from the transmitted wave. The distance between the peaks of the simulated sinusoidal component was measured as 4 mm, agreeing with Eq. 4.1.

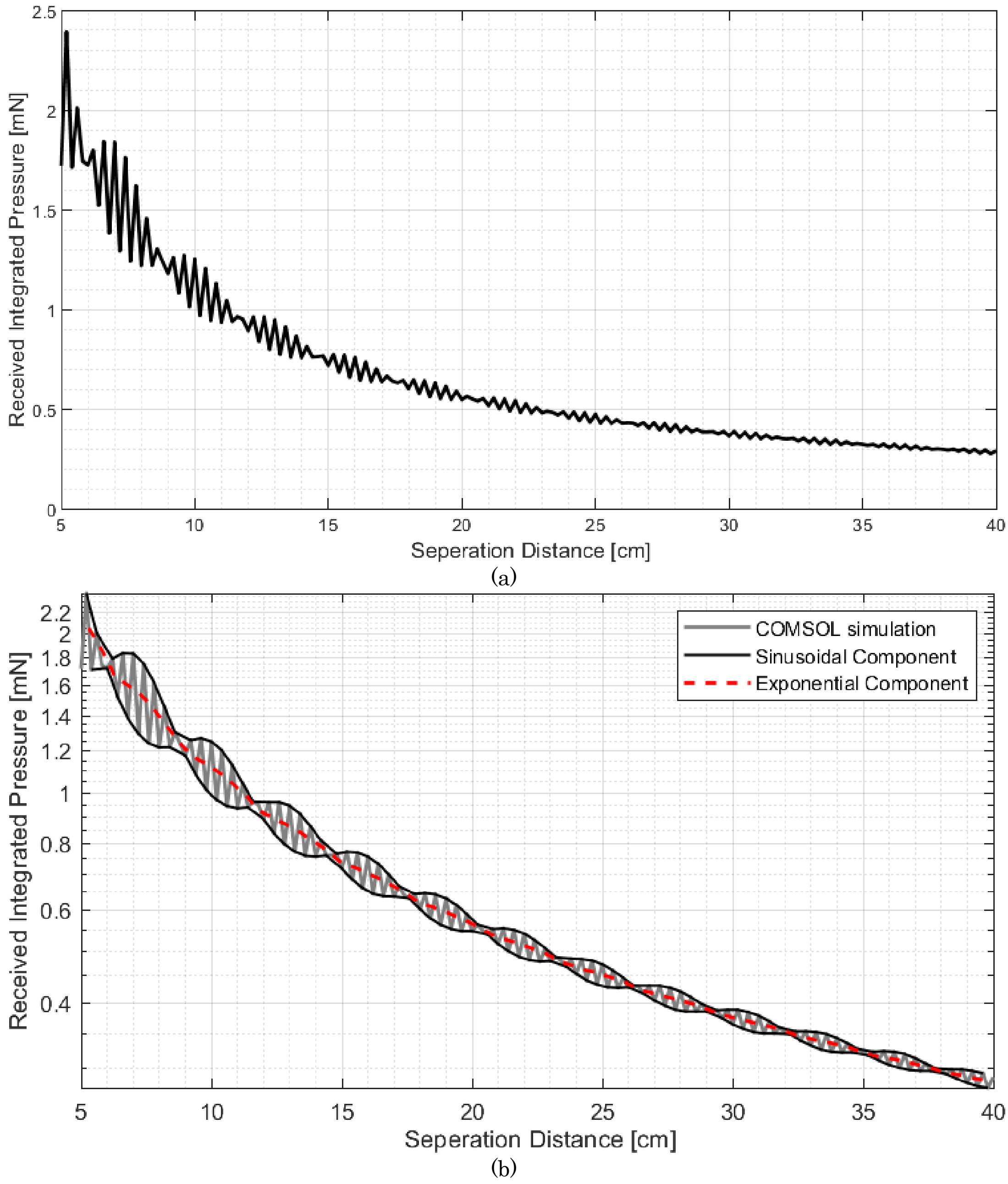

Figure 4.2: The received acoustic pressure integrated over the receiver's surface for varying separation distance at an operating frequency of 40 kHz. (a) Results from COMSOL simulation. (b) Processed COMSOL results to define the exponential and sinusoidal components.

Although this estimates the distance between the pressure peaks, it would not be possible to estimate the precise position to place the receiver to ensure that it operates at a pressure peak, causing uncertainty in the receiver's output power. However, as $\Delta\mathbb{Z}$ is a function of the transmitted wave frequency, the pressure peaks can be steered by controlling the frequency for a given separation distance between the transducers.

$$\Delta\mathbb{Z} = \frac{c}{2f} = \frac{\lambda}{2} \tag{4.1}$$

The results clearly show an exponential decrease in the received acoustic power due to beam divergence and signal absorption. However, the effect of the sinusoidal components is notable even at long separation distances ($> 30\ cm$), which suggests strong reflections in the APT system. The exponential component was fitted using MATLAB curve fitting tools to obtain the fitting parameters for an exponential fit. The model converged for the function $f(x) = ae^{bx}$ for parameters $a = 5.1$ and $b = -0.7$ with a R-Square error of 0.94, where x is the separation distance between the transducers. A better fit with R-Square error of 0.99 was obtained with an additional exponential term $f(x) = ae^{bx} + ce^{dx}$, where $a = 1.9e^{-5}$, $b = -2.4$, $c = 5e^{-4}$ and $d = -0.3$.

The highest intensity of SPL was observed at Rayleigh distance or the Near-field limit ($2.3\ cm$) for the transmitter operating at $40\ kHz$. Further investigations revealed that the received sound pressure intensity on the receiver's face is ununiform (as shown in Figure 4.3). In other words, at certain separation distances, reflection creates a high intensity at the centre of the receiver surface and low intensity around the edges. This leads to lower average received intensity compared to distances when the reflection does not significantly affect the transmitted centre lobe of the high-intensity beam. The received pressure pattern also depends on the alignment of the receiver with respect to the transmitter. Therefore, the sinusoidal component represents the fluctuation in the received acoustic pressure, shows a repetitive pattern of locally increasing and decreasing fluctuations.

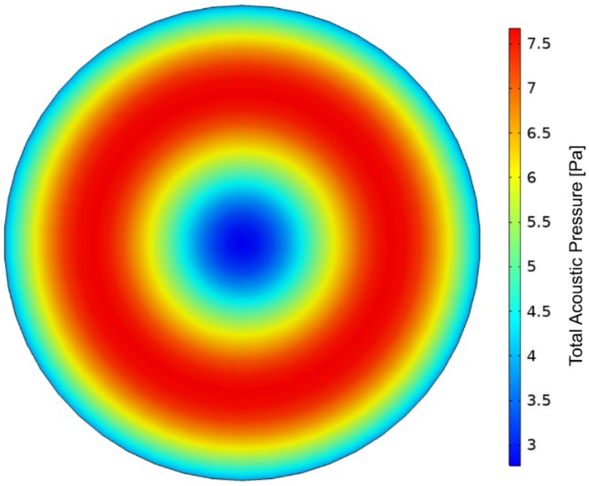

Figure 4.3: The total acoustic pressure pattern across the receiver surface when capturing a 40 kHz acoutic wave transmitted from 10 cm away from the transmitter with reflections.

4.1.2. Experimental Verification

The reflection in the air medium is experimentally evaluated by placing the transducers in an acoustic chamber and measuring the power yielded by the receiver for different ranges of separation distance in the far-field region. Figure 4.4 shows the improvised setup from Figure 3.9b, where a 2-axis position and angular stage are added to the receiver mount for precise position control.

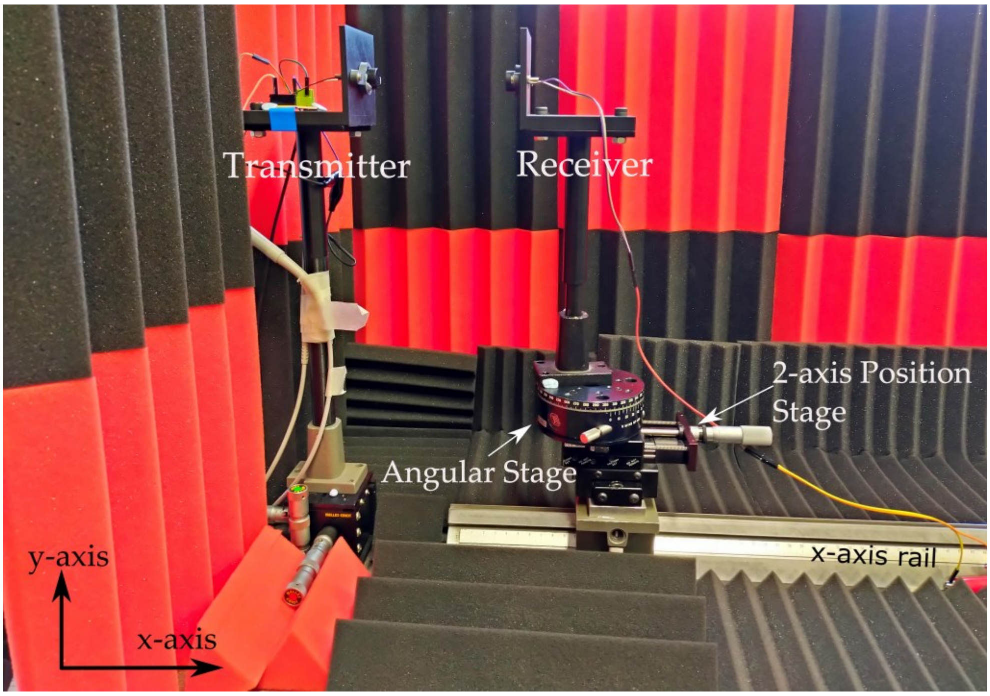

Figure 4.4: Experimental setup for evaluating the behaviour of the APT system for changing receiver position.

Firstly, the load voltage variations across the receiver for both resistive and complex load matching techniques were measured by incrementing the separation distance by 0.5 cm from 3 cm to 95 cm. The FUS-40E transmitter was operated at 40 kHz with 30 V_{p-p} square wave pulsing. The measured load voltage plotted in Figure 4.5 virtually validates the received pressure trend from COMSOL calculations. The voltage at the receiver is plotted as measured on a resistive and a complex matched load, in Figure 4.5 top and bottom respectively. The peaks and the valleys due to reflections are enveloped by solid lines, calculated by data analysis tools. The mean value of the fluctuation band is plotted as dashed lines for the respective graphs.

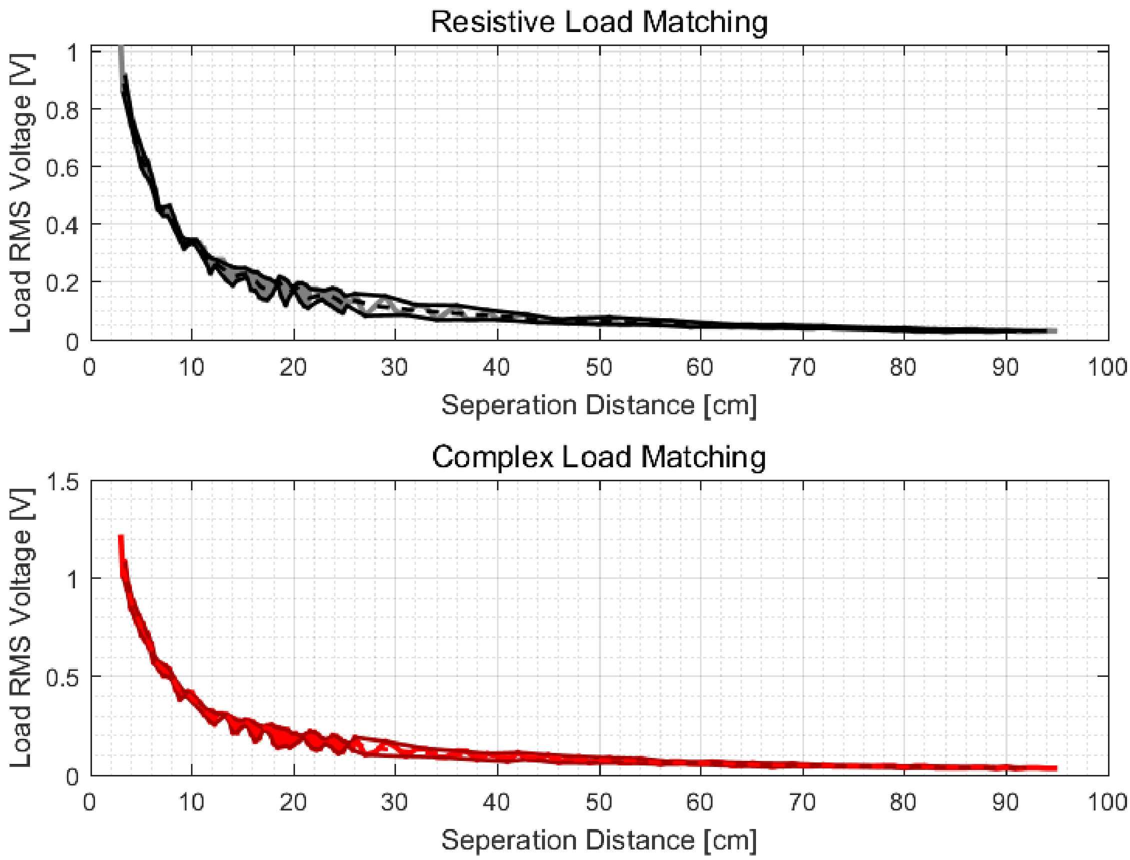

Figure 4.5: Measured output RMS load voltage for resistive and complex load matching techniques measured from 3 cm to 95 cm for a transmitter sourced by a 30 V_{p-p} square wave at 40 kHz operational frequency. The peaks and valleys of the measured voltage due to reflections are enveloped to determine the fluctuations.

The difference between the peak and valley envelopes of the received voltage's sinusoidal component is a measure of phase-related voltage fluctuation over distance. These fluctuations can be used to estimate the uncertainty of the received power at a given separation distance. The calculated fluctuation from the measure load voltage is plotted in Figure 4.6. As previously discussed, the local increase and decrease in the fluctuations are due to the ununiform distribution of sound intensity across the receiver's surface. It is also noticeable that a complex matched APT system is more sensitive to changes compared to resistive load matching, as tuning of the system is disturbed.

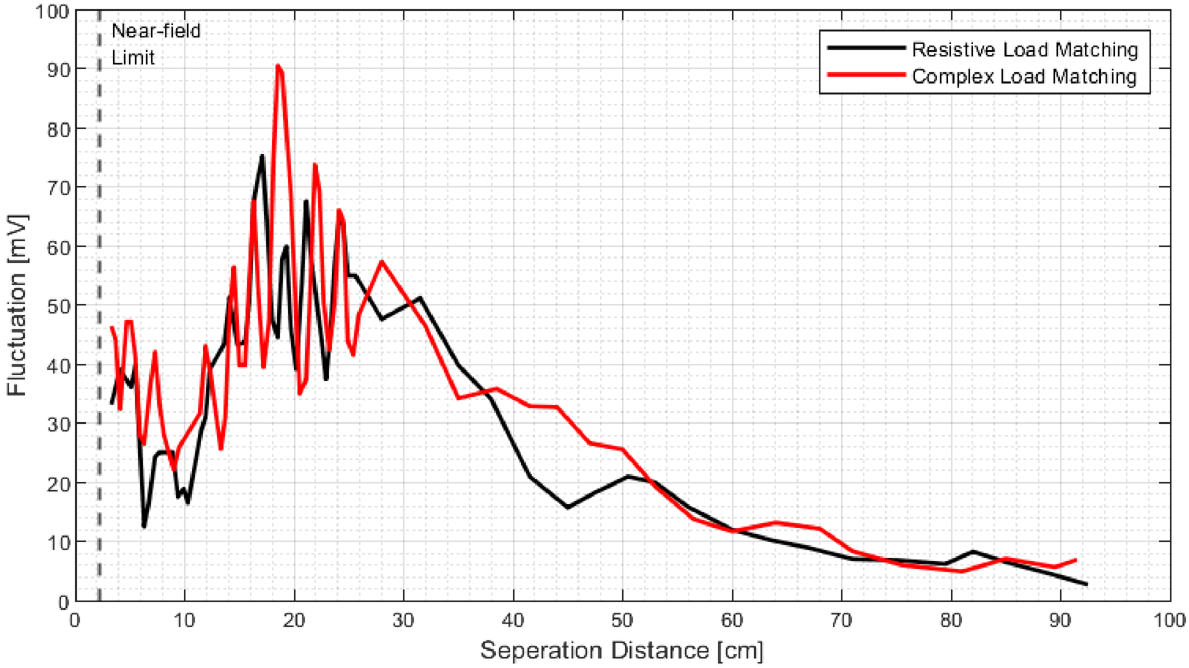

Figure 4.6: The AC component of the received voltage (fluctuation) calculated by taking the difference between the peak and valley envelopes.

Secondly, the behaviour of the APT for frequencies 39.5 kHz to 41 kHz was analysed by measuring the open-circuit voltage across the APT receiver with and without the matching inductance. This frequency range was selected for tuning the transmitter and receiver to reach the highest possible received power. Placing the receiver mount at 9.5 cm, 19.5 cm, and 29.5 cm, the separation distance was increased by 200 μm steps for 1 cm distance using the positioning stage. The open circuit (OC) voltage was measured across the terminals of the receiver with and without a matching inductor connected in parallel. The results for the transmitter operating at 39.5 kHz, 40 kHz, 40.5 kHz, and 41 kHz are plotted in Figure 4.7. It is noticeable that the reflections are significant even for large separation distances ($>$ 30 cm) from the fluctuations in the OC voltage across the receiver. Befitting the results from impedance matching, the received OC voltage for 40.5 kHz increased by 34 % and 41 kHz increased by 180 % after tuning the electrical impedance of the APT system. Correspondingly, the improvement in real power delivered to the receiver load is calculated by computing the voltage across the theoretical optimum load. The results showed that the output power delivered to the resistive load improved by approximately 4 times for 40.5 kHz and 16 times for 41 kHz. For instance, the power delivered to the receiver operating at 40.5 kHz placed 19.5 cm away from the receiver improved from 31 μW to 153 μW due to reactive compensation.

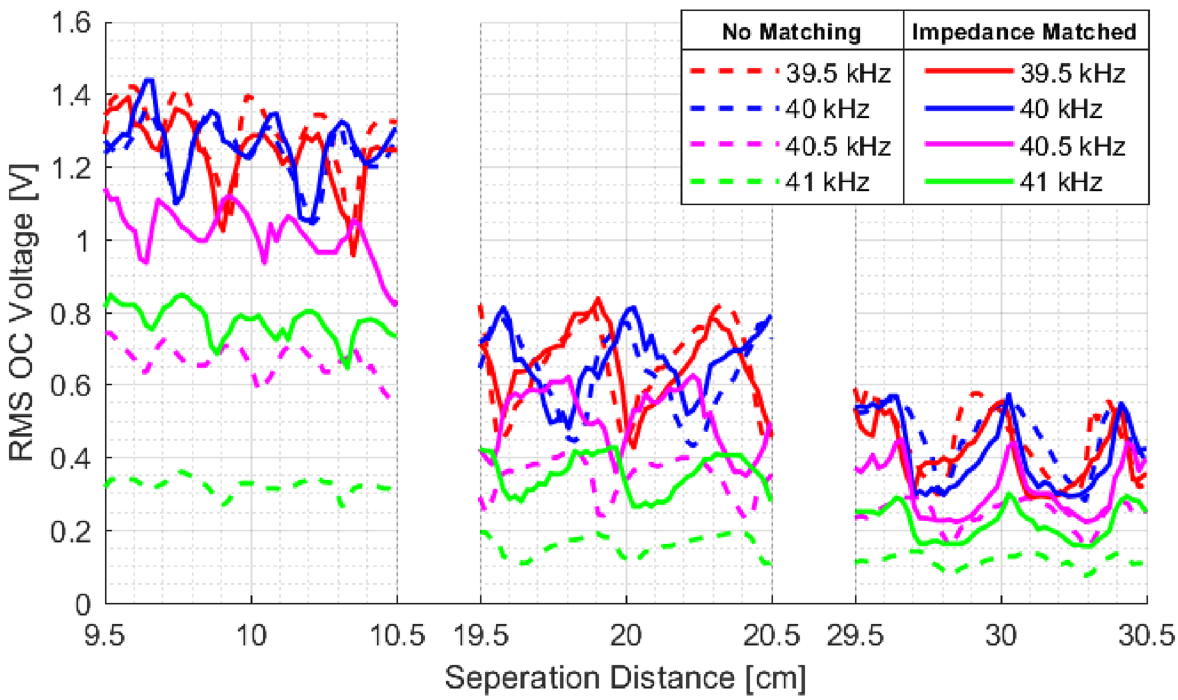

Figure 4.7: Standing waves profile for an APT system transmitting acoustic waves in air at an operating frequency of 40 kHz. Three range of separation distance were analysed across the far-field region and the open circuit (OC) voltage was measured across the receiver.

Given the dissimilarities in the acoustic impedance of the active element (PZT) and the transmission medium (air), the reflection of the transmitted waves is unavoidable. Due to reflections, peaks and valleys in the received power occur even at slight variations in receiver placements. For example, if the receiver position is changed by 1 mm, from 19.9 cm to 20 cm, the received power at resonance frequency is dropped by 17 μW from 23 μW to 6 μW. In addition, as the peaks are shifted based on the operating frequency (Eq. 4.1), similar power can be yielded by tuning the APT system off-resonance. For instance, when the separation distance between the transducer is 20 cm, the power delivered to the load at resonance is 6 μW. However, for the same separation distance, the receiver yields 16 μW when the APT system operates in 40 kHz.

4.1.3. Summary

In essence, the concluding points of this section can be summarised as follows:

- Due to the vast acoustic impedance mismatch between PZT and air, the transmitted acoustic waves are reflected between the transducers, forming standing waves.
- Due to standing waves, local peaks and valleys are formed that leads to uncertainty of the received power from the APT receiver. The effect of reflection is persistent even for long separation distances ($> 30\ cm$).
- The magnitude of the fluctuations was experimentally measured and it was observed that the sinusoidal component of the received power is modulated by both reflections and the average pressure received on the receiver's active surface.
- However, the peak and valleys of the standing waves also depend on the transmitted wave frequency. Therefore, the received power inconsistency due to reflection can be counterbalanced by adjusting the operating frequency and dynamic impedance matching.
- Moreover, adding an acoustic impedance matching layer at the medium-transducer boundary would reduce the reflected waves at the PZT-air boundary, reducing the fluctuations due to standing waves.

4.2. Impacts of Receiver Orientation

Until now, all the simulations and experiments discussed the behaviour of the APT system for a perfectly aligned system. Meaning, the faces of the transmitter and the receiver overlap with each other. This section presents the analysis of the load voltage and received power as a function of the receiver orientation in the yz-plane, where the receiver face does not overlap with the transmitter. It is noted that the x-axis corresponds to the power transmission direction (depth). The analysis provides an insight into the FUS-40E transducers and their behaviour in an APT system which is later expanded to study signal propagation for power delivery. They are analysed using the same experimental setup considered in Figure 4.4. This analysis aims to study the power uncertainty of the APT system due to disturbances in the orientation and alignment of the receiver concerning the transmitter.

4.2.1. Misalignment

Misalignment between the transducers is defined as the offset distance between the receiver and transmitter centres, as shown in Figure 4.8a. Since the same transducer is used as both transmitter and receiver, the transducers' centre and circumference overlap when perfectly aligned (Figure 4.8b). Additionally, the propagation axis of the sound wave aligns with the centre of the receiver. This is represented as 0-offset between the transducers. However, when the offset increases, as shown in Figure 4.8b (i) and (ii), the transducers become misaligned, therefore depending on the separation distance between the transducer, the receiver will receive less transmitted power.

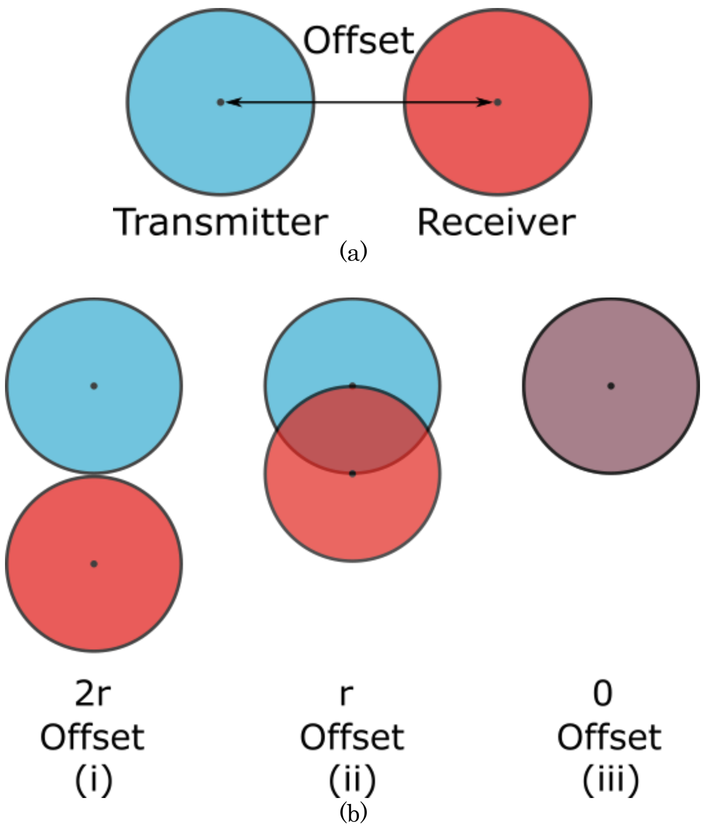

Figure 4.8: (a) Representation of the faces of the transducers when observed from the yz-plane during misalignment of the receiver with respect to the transmitter. displaying how offset between the transducers is measured (b) Examples of misalignment studied in this work showing the transducer overlap for offset less than $2r$.

Figure 4.9 shows the measured RMS voltage (open circuit) and power profile in the far-field region for varying offset from $-24\,mm$ to $24\,mm$. The separation distance was increased by $5\,mm$ from 3 to 30 cm between the transducers with an offset measured every $4\,mm$ on both sides of the transmitted wave's propagation axis. The transmitter was operated at 39.5 kHz with a source voltage of 33 V_{p-p}. Since the reactance of the transducers at resonant frequency is negligible, the complex and resistive loading at 39.5 kHz is indifferent. The main lobe of the transmitted wave prevails within 5 cm separation distance and 10 mm offset from the transmitter. Accordingly, the power reduces significantly for increasing offset in the transition field (2 cm to 5 cm). However, this decline in the received power is less affected for separation distance $> 5\ cm$ due to geometrical spreading of the transmitted wave. In other words, the transmitter acts as a point source in the transition field. Therefore, the transmitted waves have a spherical geometry, making the receiver highly sensitive to misalignment. However, the transmitted wave assumes a planar geometry in the far-field region where the separation distance is very large compared to the transmitter dimensions. Thus, the receiver becomes highly sensitive in the near-field region, whereas it is less affected by alignment in the far-field region.

In addition, minor reflection can be noted even for large offset values. To analyse the reflection profile from a narrower perspective, the misalignment profile for separation distance 9.5 cm to 10.5cm was measured for every 200 μm by setting the offset from 0 mm to 24 mm. The measured voltage (OC) is plotted in Figure 4.10. This figure is provided to clarify the reflection pattern for varying offset values in the far-field region. It is clear from the profile that the reflection pertains to the same pattern for all offsets. However, this could be a consequence of the 3D printed transducer mounts, which are 80 mm in width. Therefore, although there is an offset of 24 mm between the center of the transducers, the mount faces still overlap by 16 mm, causing reflection of the transmitted waves. Consequently, the APT receiver dimensions are a significant design parameter that play a crucial part in the system's reflection profile. Having a reflective architecture at the transmitter or the receiver can enhance the received power by increasing the standing waves in the system.

Additionally, it was also realised that the voltage and power are not always maximum at 0-offset. For example, Figure 4.9c shows a cross section of Figure 4.9a and Figure 4.9b at 8 cm separation distance. While the APT receivers are perfectly matched the peak power is obtained at 4 mm offset instead of 0-offset, operated at 40.5 kHz. This is due to constructive interference of the transmitted and reflected waves, forming local low-intensity fields in the propagation axis and symmetric high-intensity fields on both sides.

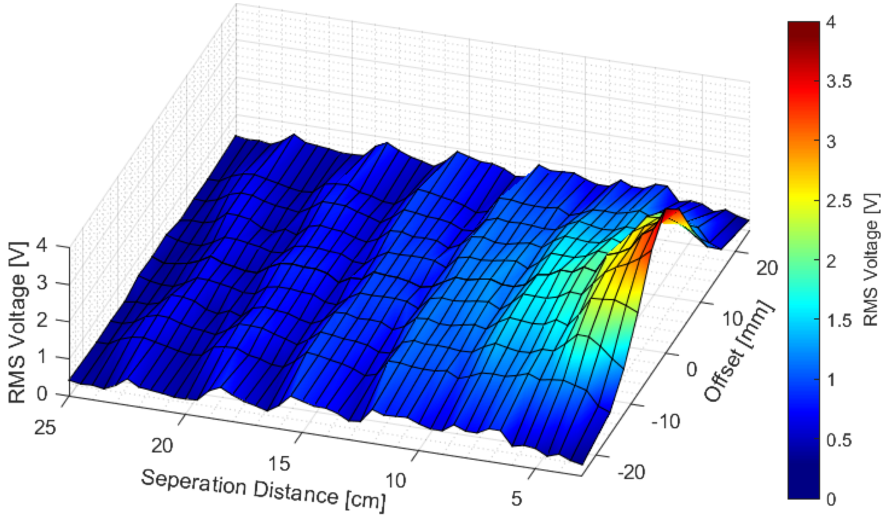

(a)

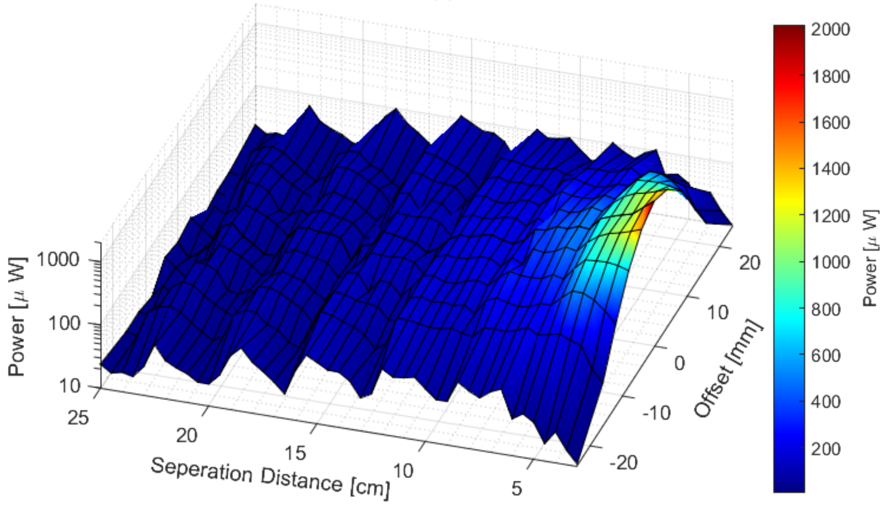

(b)

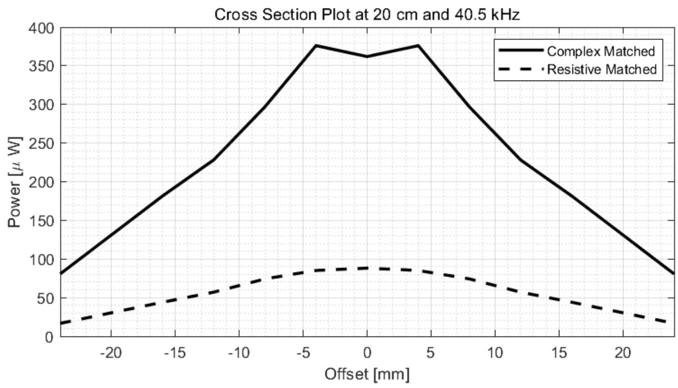

(c)

Figure 4.9: Measured open circuit RMS voltage and impedance-matched power obtained from a FUS-40RE APT system operated at 39.5 kHz for seperation distance varying from 3 cm to 25 cm. The measurements were made at an ambient condition of 25.5 ± 0.5°C and 20 % RH dry air. The power is obtained from measuring the voltage across the experimentally derived optimum load. (c) presents a cross section of the power obtained at 8 cm separation distance operated at 40.5 kHz.

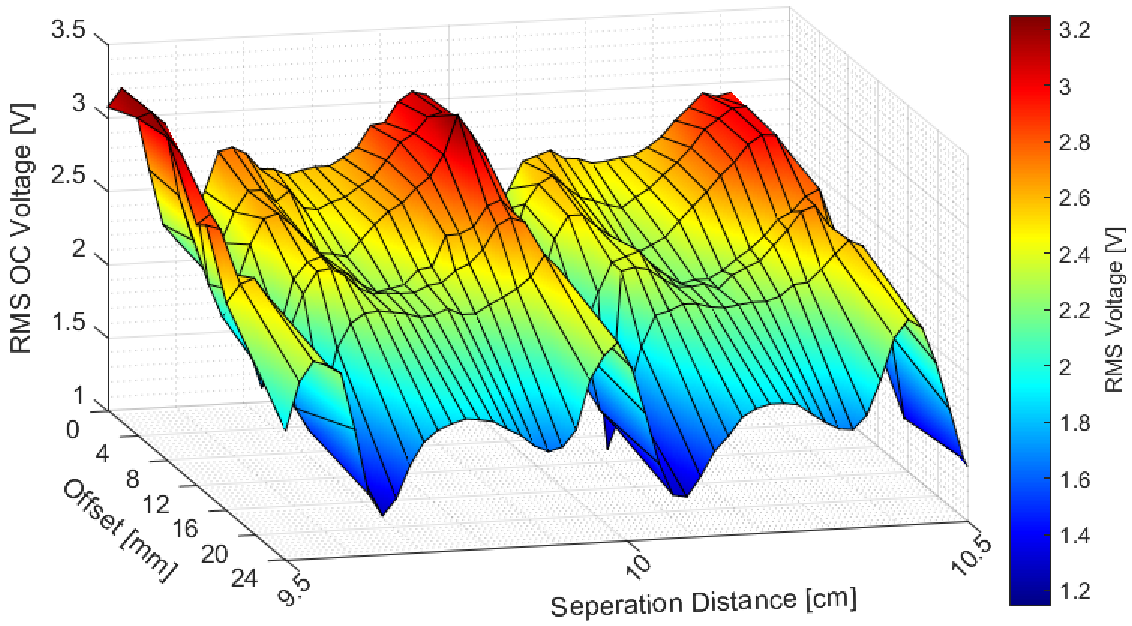

Figure 4.10: Detailed open circuit RMS voltage profile for a focused separation distance range to analyse the sensitivity of the APT system due to misalignment and reflection.

The system's vulnerability due to misalignment at different operating frequencies is further analysed using the same experiment for 40 kHz, 40.5 kHz, and 41 kHz. The measured RMS power with resistive and complex impedance matched load is summarised in Figure 4.11 and Figure 4.12, respectively. The colour map is limited to the same scale as Figure 4.9b for easy comparison. Similar to the resonance frequency, the received power is sensitive to the offset in the transition field. However, for separation distances more than 5 cm, the effect of misalignment on the received power is still minimal. Also, reflection is persistent in all the power profiles due to interference. Although similar effects of misalignment as discussed above can be observed for the tested frequency range, a clear interpretation of the power trends could not be achieved by comparing the individual profiles.

To better understand the power profile of the APT system for varying frequencies and impedance matching techniques, a design graph is demonstrated in Figure 4.13 that combines all the power profiles for the studied operating frequencies. This offset-frequency design graph gives the frequency at which the receiver can deliver maximum power to the load for a given separation distance and offset. For example, Figure 4.13a for resistive load power profile can be read as follows: when the receiver is placed at 13.5 cm away from the tranmitter with an 8 mm offset, maximum power can be harvested when the transmitter operates at 40 kHz. However, when the separation is

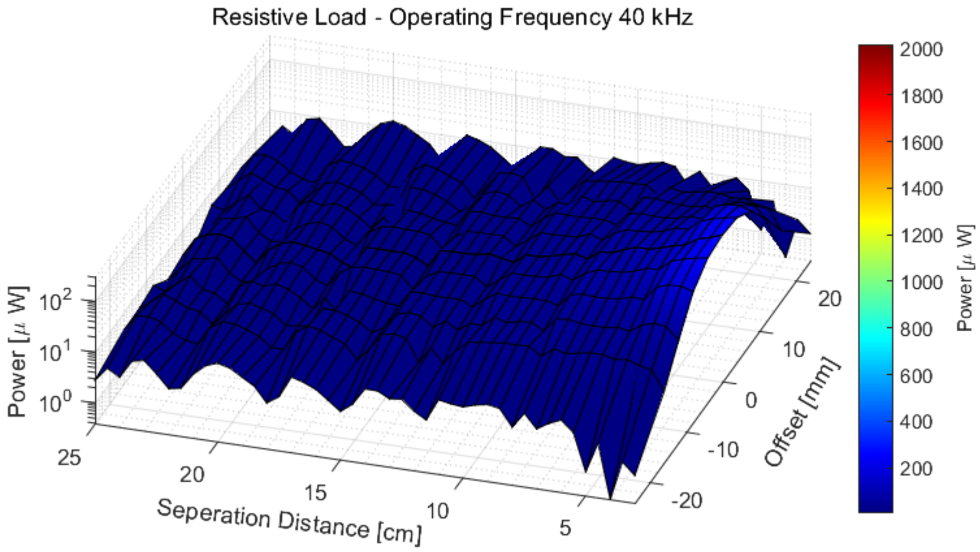

(a)

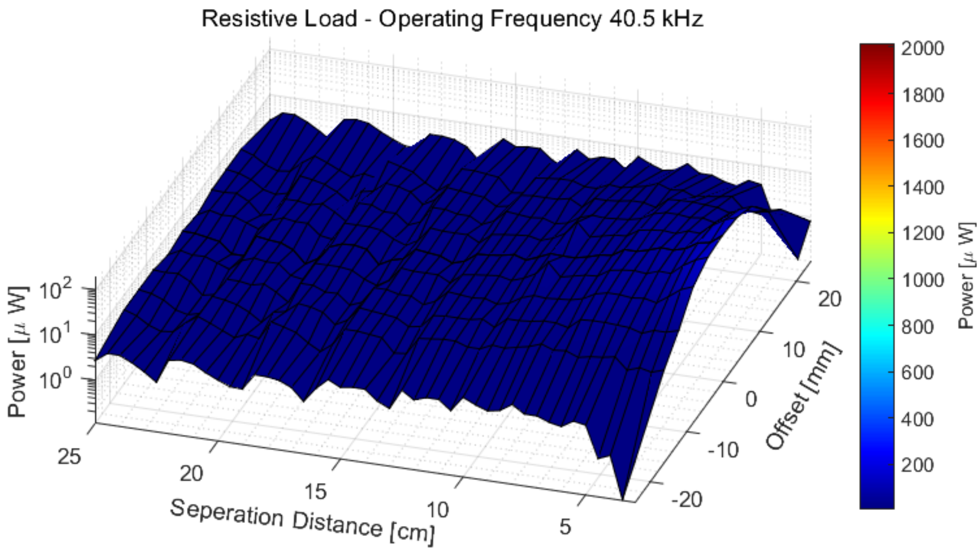

(b)

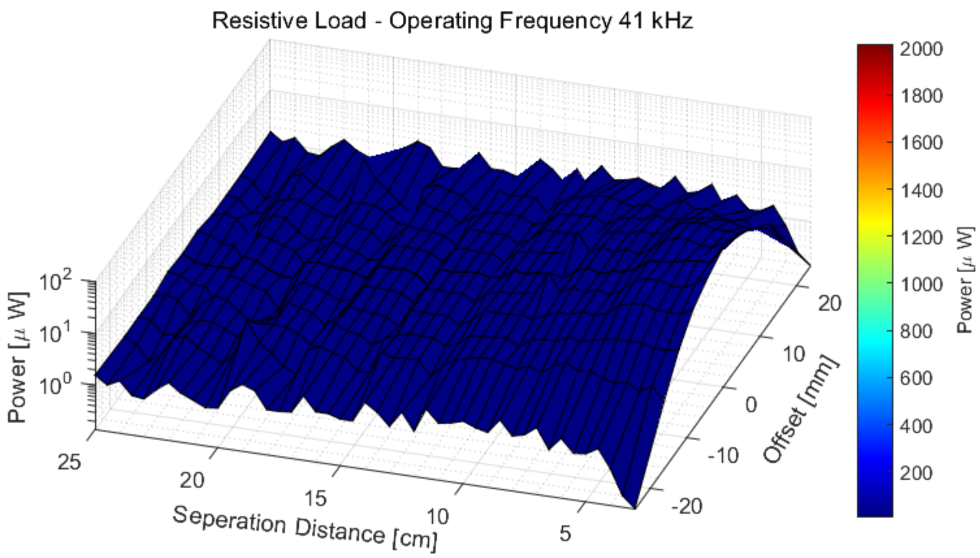

(c)

Figure 4.11: Measured RMS voltage profiles of an ATP system with resistive matched load for varying offset from $-24\ mm$ to $24\ mm$ operating at (a) 40 kHz (b) 40.5 kHz (c) 41 kHz.

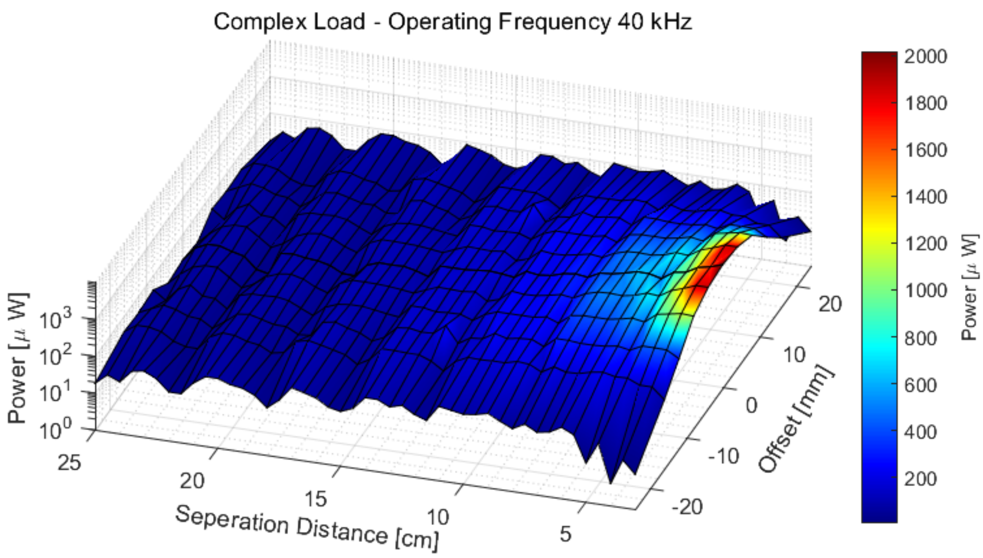

(a)

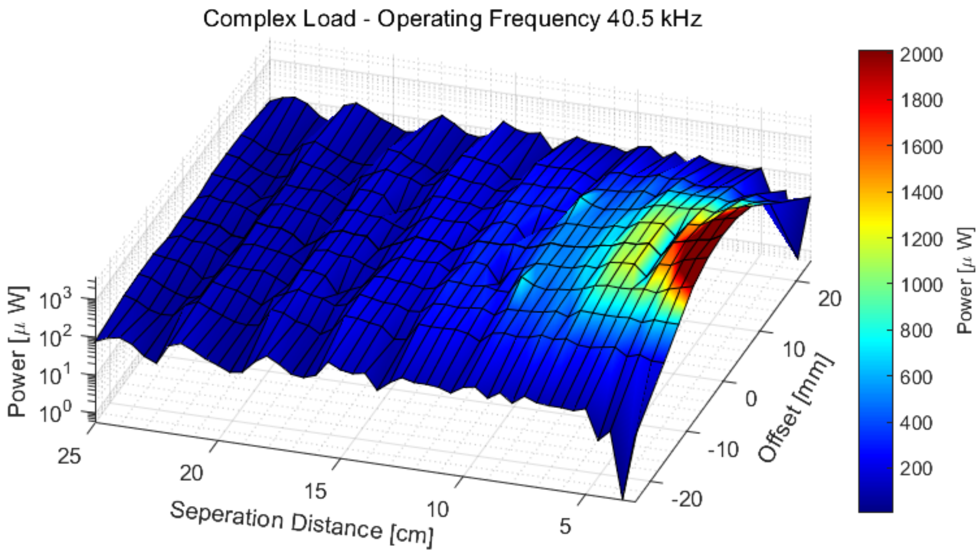

(b)

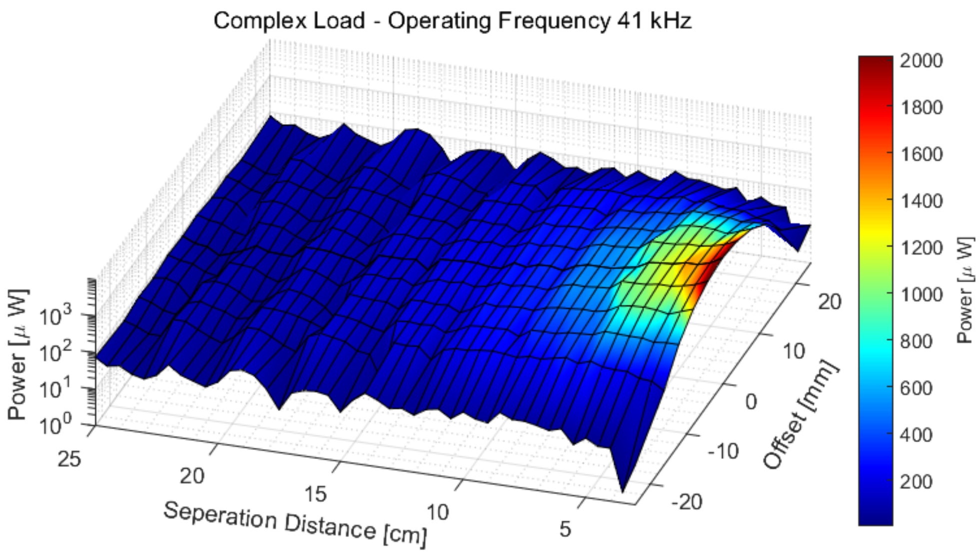

(c)

Figure 4.12: Measured RMS power profiles of an ATP system with complex matched load for varying offset from $-24\,mm$ to $24\,mm$ operating at (a) $40\,kHz$ (b) $40.5\,kHz$ (c) $41\,kHz$.

distance 12 cm with the same offset, 39.5 kHz yields the maximum power. Following the observations from Figure 3.18, when the transmitter is not tuned, and a resistive load is used with the receiver, operating the APT at the nominal frequency of the transducers (39.5kHz) would be sufficient to yield the maximum power throughout the targeted field for resistive loading conditions. Besides, higher output power can be achieved by employing complex loading techniques.

On the other hand, Figure 4.13b displays the power pattern for a tuned transmitter and a receiver with complex load matching. A mixture of all the tested frequencies is observed in the plot, with 40.5 kHz predominantly achieving maximum power. Accordingly, the plot can be read as follows: when the transducers are separated by 14 cm with an offset of 4 mm from their centers, maximum power can be received by operating the transducers at 41 kHz and tuning the transducers using complex impedance matching. However, when the separation distance is increased to 15 cm, the transducer muct be tuned and operated at 40.5 kHz to achieve maximum power.

A repeating pattern is also noticeable in both power profiles, where the maximum power alternates for approximately every 2 cm by frequencies 0.5 kHz apart. For instance, 40.5 kHz and 41 kHz produces the maximum power for complex impedance tuning, and 39.5 kHz and 40 kHz generates the maximum power for resistive loading. This occurs as the peak of one operating frequency coincides with the valley of the other. Therefore, operating the APT system off-resonance and tuning the transducers can minimise the effects of reflection and improve the system's reliability.

Further investigations of the power design graph revealed that the effect of increasing offset on the received power and reflection pattern is also dependant on the operating frequency of the APT system. For instance, the drop in received power due to increasing offset when operated at 39.5 kHz was insignificant for separation over 10 cm. However, when operated at 41 kHz, the decrease in received power for increasing offset was notable even at 25 cm separation distance. This could be owing to the directivity of the transmitter ($D(\theta)$) that was discussed in Eq. 2.31, which is reiterated in Eq. 4.2 for convenience. The divergence angle θ can be approximated in the far-field region for a receiver of dimensions negligible compared to the transmitter as:

$$D(\theta) = \frac{2J_1(kr_{TX}\sin(\theta))}{k\, r_{TX}\sin(\theta)} \tag{4.2}$$

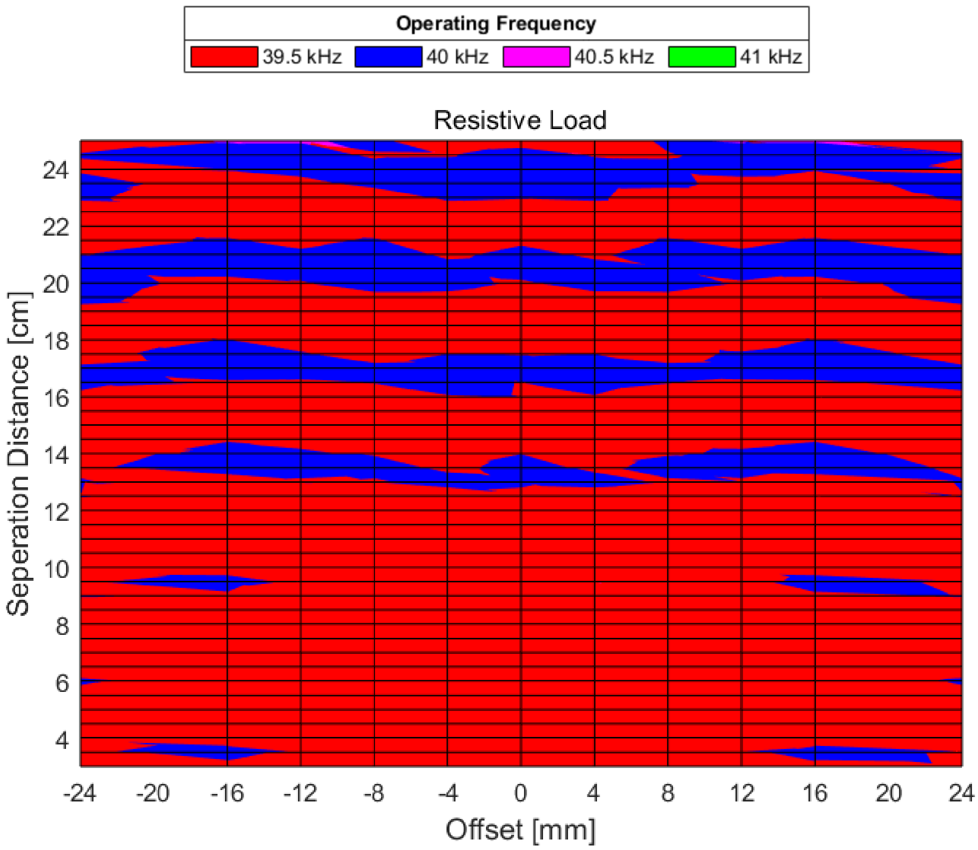

(a)

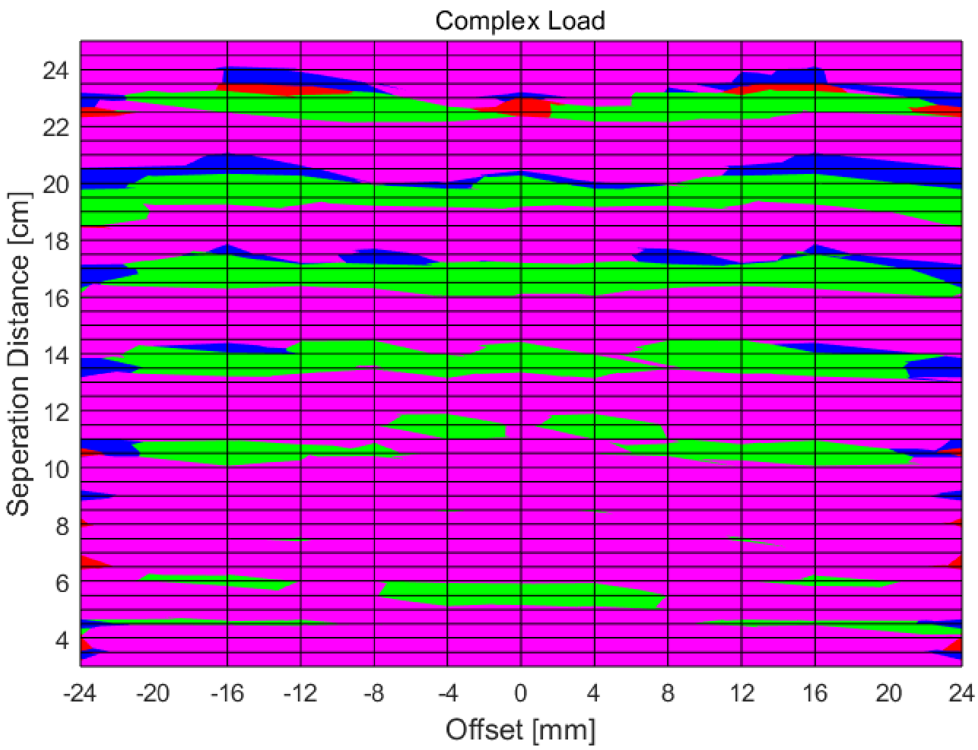

(b)

Figure 4.13: Design graph demonstrating the various operating frequencies to obtain the maximum power for a given offset and separation distance.

where, $J_1$is the first order Bessel function, k is the wave number, and r_{TX} is the receiver radius. The directivity of the transducer is dependent on the factor $k\, r_{TX} = (2\pi f\, r_{TX})/\, c$, where r_{TX} is the transmitter radius. Consequently, for a given r_{TX} and constant directivity, when the frequency increases, the divergence angle (θ) converges closer to the propagation axis. In other words, increasing the operating frequency the beam width of the transmitted wave decreases. This causes the receiver to be more sensitive to offset in the far-field region, reducing the effective aperture of the transmitter.

These observations were validated by studying the radiation pattern of the transducer using the COMSOL model, by assuming negligible attenuation losses in the medium. The radiation pattern was computed by evaluating the SPL at 25 cm from the transmitter for operating frequencies from 37 kHz to 42 kHz incremented by 0.5 kHz. The results are as plotted in Figure 4.14, where the frequency increases from the blue to the red line.

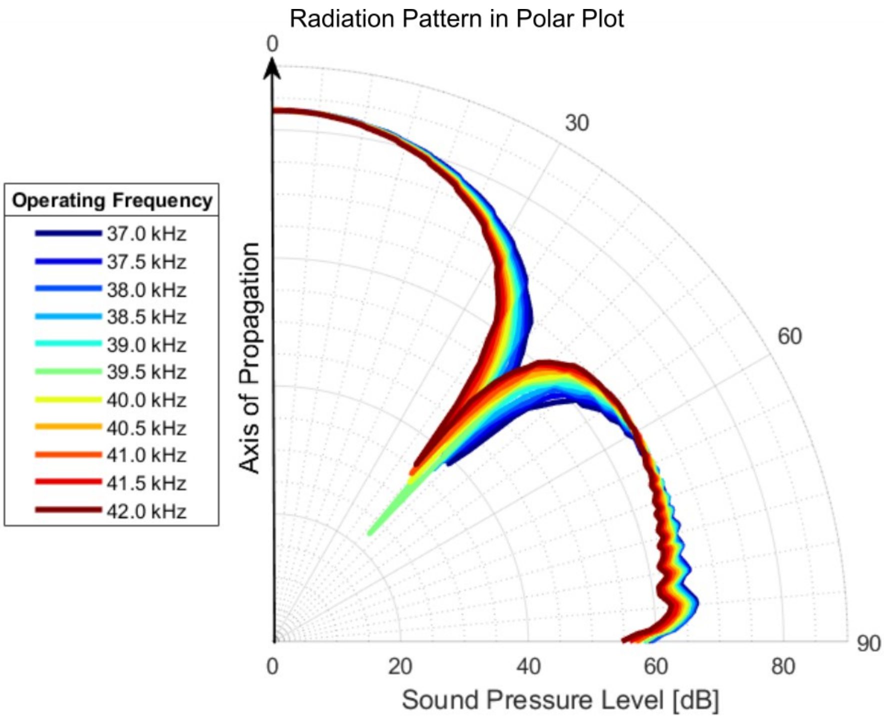

13

Figure 4.14: Simulated radiation pattern for a transmitter of the same dimension operating at different frequencies representated using a polar plot. The radiation demonstrated is half of a symmetric profile around the propagation axis, evaluated at 25 cm.

It can be noticed that the main lobe (in the direction of the propagation axis) gets narrower for increasing frequency, but the side lobe (normal to the propagation axis) gets wider. A decrease of approximately 1^o in the beam width was measured for every 0.5 kHz increase in operating frequency. For instance, a beam width of 75.5^o was calculated for 39.5 kHz operating frequency, that decreased to 74.5^o for 40 kHz. However, it is worth nothing that the variation in directivity of the transducer is negligible, since the difference among the subsequent frequencies is small.

To quantitatively analyse the improvement in the system performance due to off-resonance actuation of the transmitter, the difference in the measured power at the resonance frequency ($39.5\ kHz$) and the optimum frequency (obtained from Figure 4.13) is calculated. This evaluated power difference is plotted in Figure 4.15 for both resistive (Figure 4.15a) and complex loading (Figure 4.15b). It worth mentioning that as the reactance of the transducer is insignificant at resonant frequency, the transducers are only resistive matched at $39.5\ kHz$. Furthermore, it can be observed that the power difference in the transition field ($3\ cm$ - $5\ cm$) is much higher compared to the far-field region. Figure 4.15 only demonstrates the received power increase in the far-field region when the reflection and misalignment pattern of the different operating frequencies are prominent.

For resistive load matching, the APT system performs satisfactorily when operated at the resonance frequency, irrespective of the reflection throughout the far-field region. Therefore, changing the operating frequency barely improves the received power. The maximum power increase is $10.4\ \mu W$ when the transducers are separated by $17.5\ cm$ and $16\ mm$ offset. This is caused by the exact overlapping of the valley of the $39.5\ kHz$ and peak of $40\ kHz$ transmitted waves. Since the power transfer efficiency of the APT system operated at $40.5\ kHz$ and $41\ kHz$ with resistive loading is less than at the nominal frequency, operating at these off-resonance frequencies would be unavailing.

However, when both the transducers are tuned using a complex impedance matching technique, the received power improves significantly when operated in off-resonance frequencies. For instance, the power increased from $57\ \mu W$ to $263\ \mu W$ by operating the APT system at $40.5\ kHz$ instead of the nominal frequency when the receiver was placed $13\ cm$ away at $16\ mm$ offset. This improves the power by $206\ \mu W$, and consequently, the efficiency of the APT system is increased by 360%. The advantage of using a well-tuned APT system is substantially noticeable for considerable separation distance and offsets. For example, a power increase of $54\ \mu W$ is measured for a separation distance of $25\ cm$ and $24\ mm$ offset. In fact, the increase in the power transfer efficiency improves as the separation distance increases (Figure 4.16). Therefore, the importance of APT system tuning and complex impedance matching of the receiver becomes essential as the range of the APT system increases.

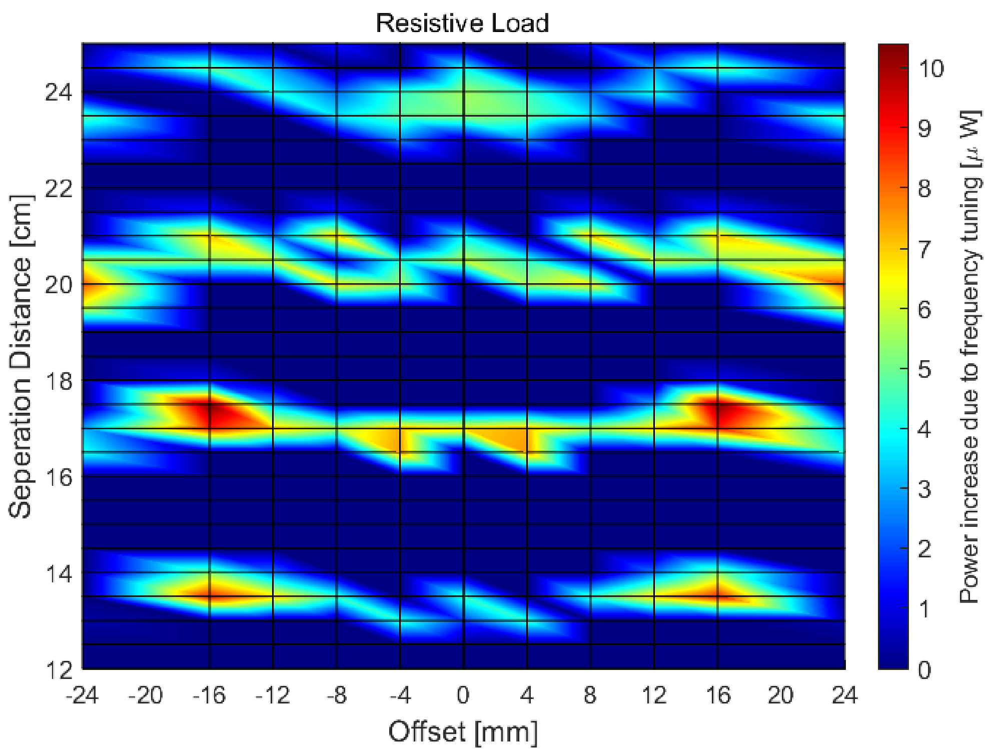

(a)

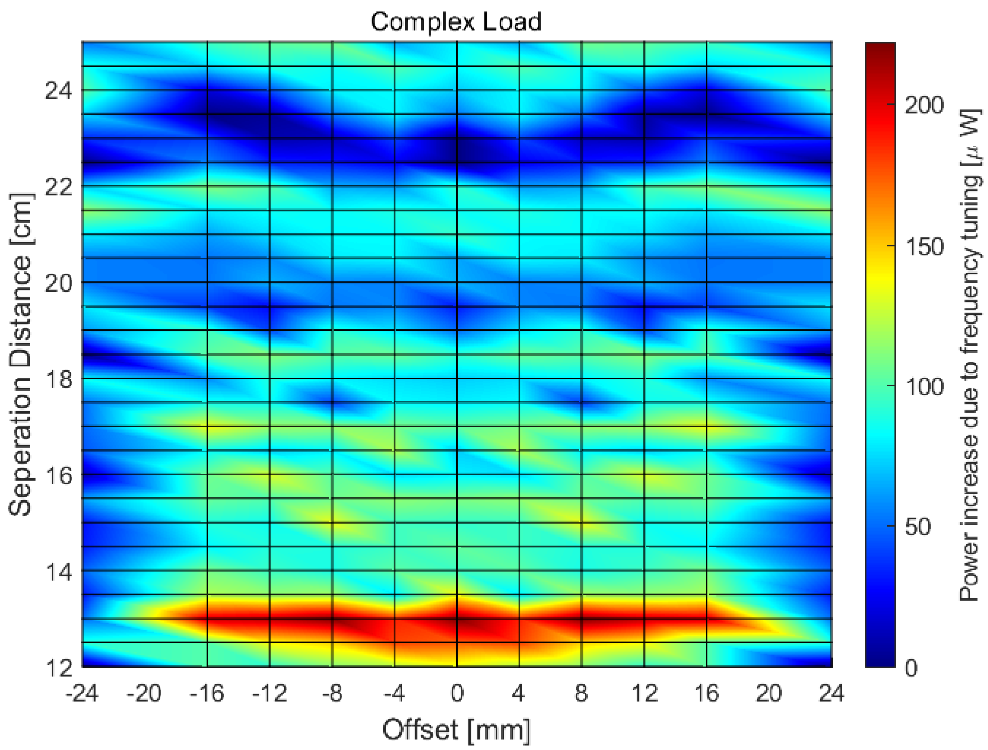

(b)

Figure 4.15: Quantitative design graph demonstrating the increase in power achieved by active tuning of the APT system when using (a) resistive and (b) complex loading methods and driving the transmitter off-resonance.

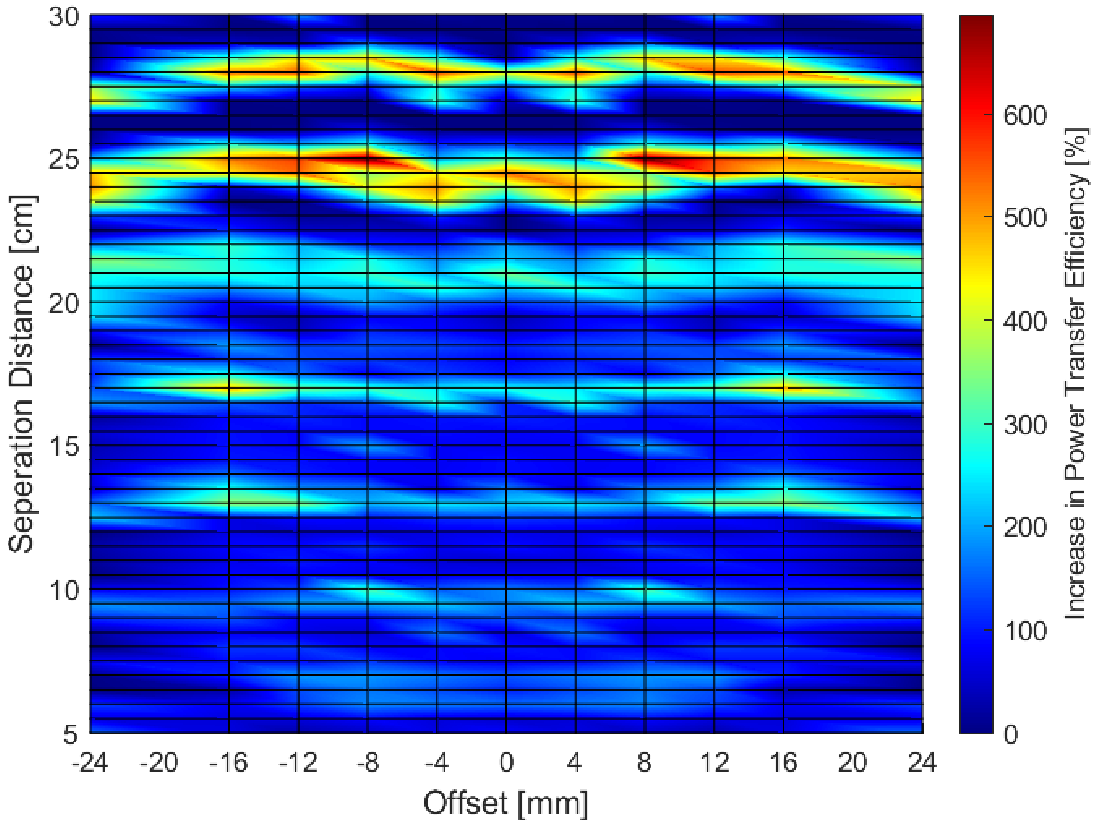

Figure 4.16: Measured improvement in the power transfer efficiency of the APT when operated at the optimised frequency and complex loading with respect to the nominal frequency.

4.2.1. Misorientation

Misorientation of the receiver can be characterized by the angle between the transmitter and receiver faces. In this work, the angle between the transducer faces is defined as the orientation angle and is represented by δ (as shown in Figure 4.17a). Figure 4.17b represents how misorientation alters the acoustic waves received on the receiver's surface.

Firstly, it can be noticed that the pressure profile on the receiver's surface changes as the angle between the transducers is increased. For instance, at 0^0 orientation angle, concentric bands of high- and low-pressure wave incidents on the receiver with decreasing pressure from the centre. However, as the angle increases, the receiver face will be exposed to vertical bands of varying pressure. An experimental assessment of the pressure pattern on the receiver surface can be complicated. Therefore, COMSOL simulations are used for computing the pressure pattern using the same setup shown in Figure 4.1. The simulations were performed by placing the receiver at a separation distance of 10 cm, 20 cm, and 30 cm from the transmitter with a orientation angle of 0^o, 10^o, 15^o, and 30^o.

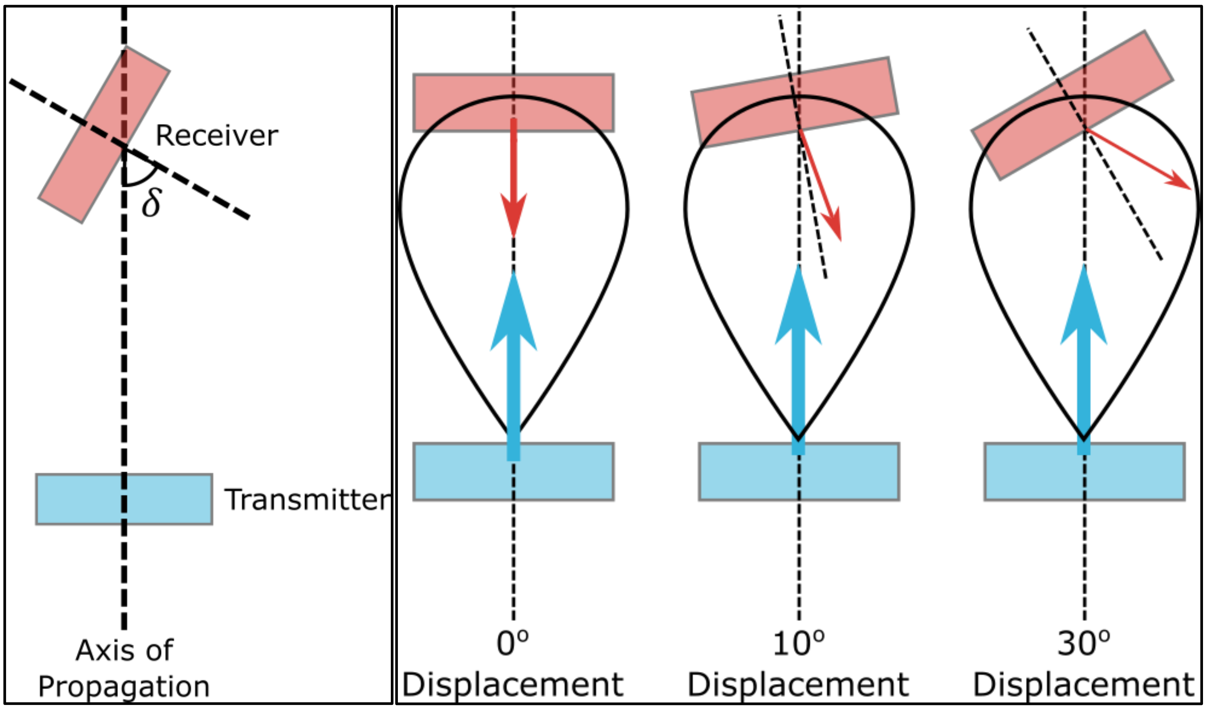

(a) (b)

Figure 4.17: Representation of the transducers in misorientation. (a) Demonstration of a receiver being displaced by an angle of δ from the propagation axis. (b) Demostration of the APT system when the receiver is rotated by 0^o, 10^o, and 30^o.

The total computed pressure along the diameter of the receiver is as shown in Figure 4.18. The figure is plotted like a table where each column represents an orientation angle, and each row represents one separation distance. For example, the pressure trend across the receiver's diameter when placed 20 cm away from the transmitter at a 15^oorientation angle is plotted in the second row - third column. It can be noticed that when the receiver is aligned with the transmitter, a symmetric pattern of pressure is computed across the diameter along the receiver's centre. The distance between the peaks of the pressure for 0^o orientation angle is the wavelength of the acoustic waves in the medium. These peaks appear in the same pattern irrespective of the separation distance. However, the received pressure is asymmetric when the orientation angle increases because the pressure bands overlap. This decreases the received integrated pressure, decreasing the power delivered to the load.

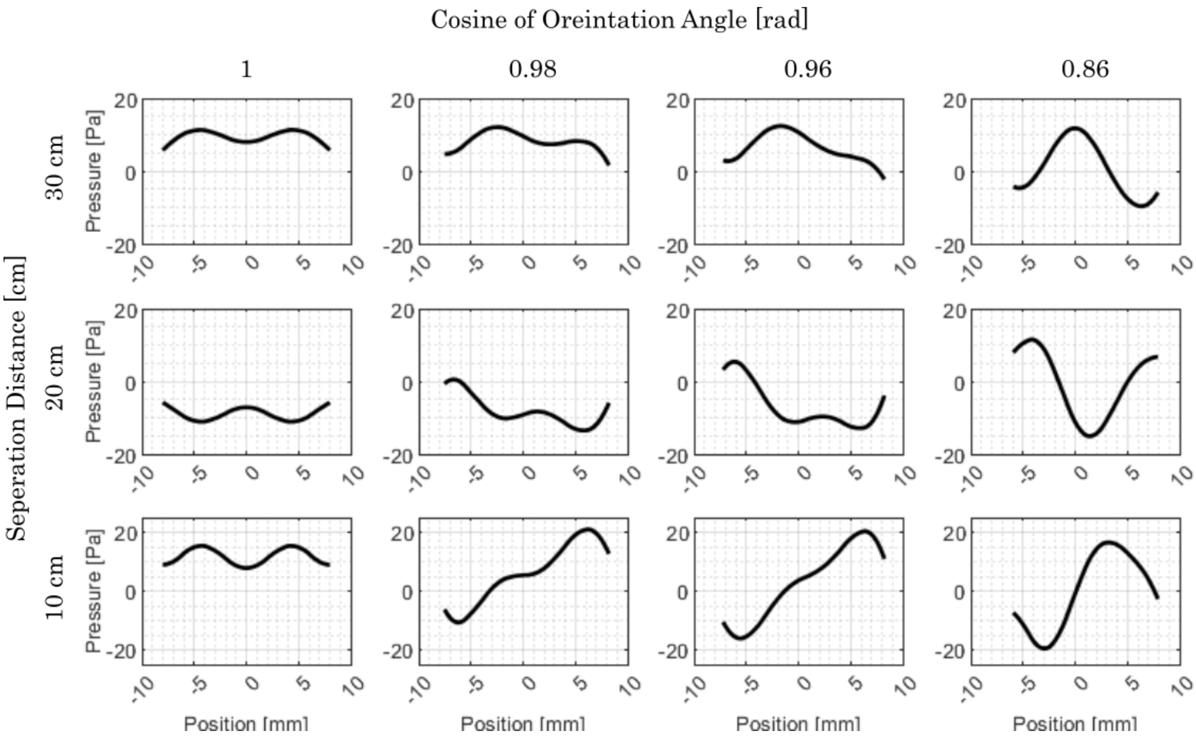

Figure 4.18: Calculated pressure along the diameter of the receiver for various separation distances and orientation angles.

Secondly, according to the law of reflection, the angle of the incident wave and the reflected wave from the normal is equal. Therefore, when the orientation angle is 0^o, the reflected wave travels back along the propagation axis, causing standing waves. When the orientation angle between the transducers increases, the reflected wave travels farther from the propagation angle, reducing the system's standing waves. The direction of the transmitted and the reflected waves are denoted as blue and red arrows in Figure 4.17b, respectively.

To experimentally validate the effects of orientation angle on reflection, the output power delivered to the load is measured for orientation angles between -30^o to 30^o, when operating the APT system at 39.5 kHz. The measurements were taken for every 50 mm separation distance from 3 cm to 30 cm, and the results are plotted in Figure 4.19. A decrease in the repeating peaks and valleys is easily notable when comparing the significant peaks and valleys at the centre (0^o orientation angle) with the flat surface at 30^oorientation angle. At around 15^o, the incident wave is reflected at 30^o away from propagation axis. This avoids the interference of the transmitted and reflected waves, consequently unable to form standing waves between the transducers.

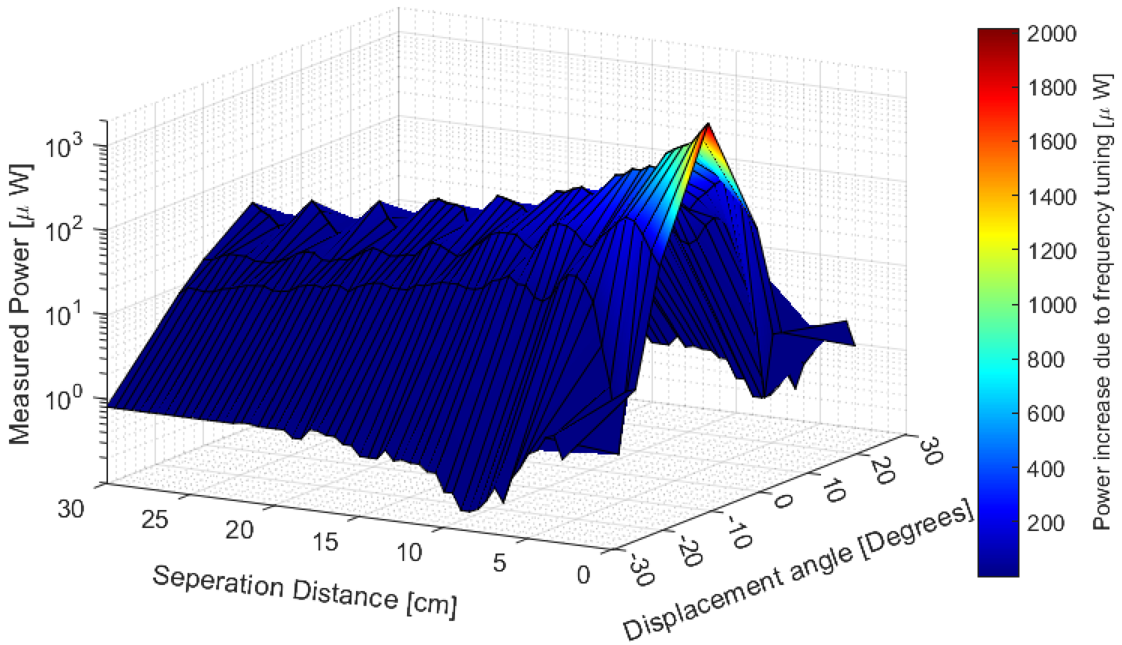

Figure 4.19: Experimentally measured power received by transmitting continuous 39.5 kHz acoustic waves to the receiver in the far field region. The power was measured for every 50 mm separation distance with the orientation angle ranging from -30^o to 30^o.

The change of the reflection coefficient concerning the orientation angle can be analytically computed using Snell's law and the formulation discussed in Eq. 2.36. For changing orientation angles, the angle of refraction (θ_R) can be computed by using Snell's law as follows:

$$\theta_R = \sin^{-1}\frac{v_{PZT}\sin(\delta)}{v_{air}} \tag{4.3}$$

where v_{PZT} and v_{air} is the speed of the acoustic wave in the transducer and air, respectively. Subsequently, the reflection coefficient of the transducer for varying δ is calculated, and the results are as shown in Figure 4.20.

Theoretically, the calculation shows a sharp incline in the transmitted angle for a slight increase in orientation angle. And the reflection coefficient is > 0.99 and reaches 1 for orientation angles around 6^o. In other words, all the incident acoustic waves are reflected into the medium when the receiver is misoriented by more than 6^o. However, the experimental results display acceptable received power even at $\delta = 15^o$. The difference in the calculations could be because of employing the values of v_{PZT} and Z_{PZT} from the PZT parameters. However, in practice, the transducers are structured with a porous impedance matching layer, reducing the reflection at the PZT-medium boundary. Nevertheless, it is essential to note that the reflection coefficient of an APT system is highly sensitive to the misorientation angle due to the significant difference between the acoustic impedance of the air and the piezoelectric material. Therefore, the impedance matching layer between the medium and the receiver is a crucial design parameter for air-based APT systems. In summary of the theoretical analysis, when the orientation angle of the receiver increases the following effects occurs, which together contributes to decreased received power:

1. The active area of the receiver facing the transmitted acoustic wave decreases, leading to irregular pressure pattern. This results in reduced integrated pressure due to the large phase difference of the absolute pressure received at different points along the receiver surface.
2. The angle of reflection of the transmitted wave is twice the misoreintation angle. Therefore, it is reflected away from the propagation axis at the PZT-air boundary. This reduced the standing waves between the transducers.
3. The reflection coefficient of APT system increases and approaches unity rapidly for slight changes in orientation angle.

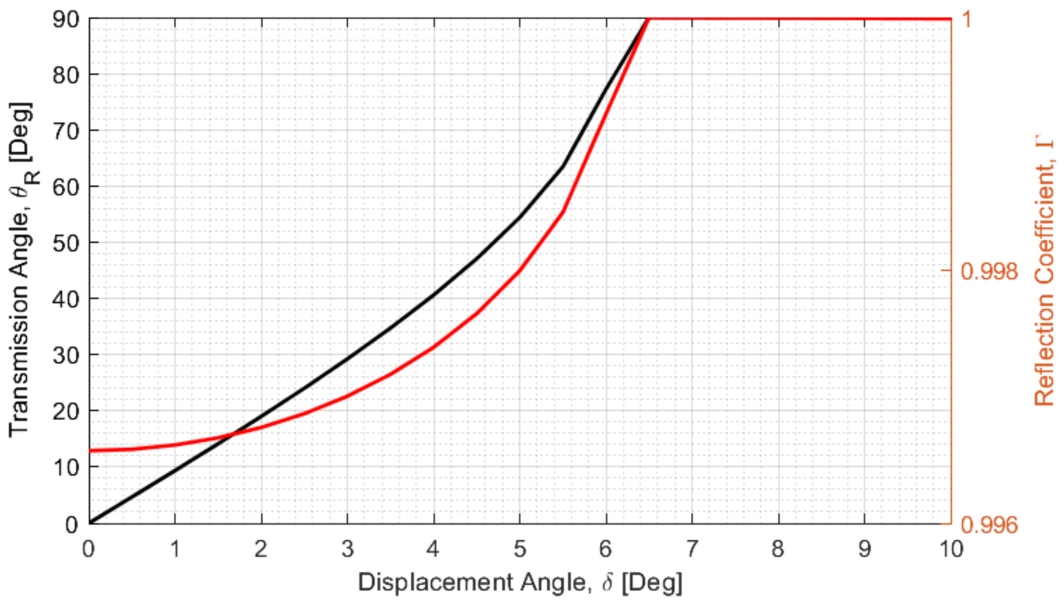

Figure 4.20: Analytically computed transmission angle and reflection coefficient for varying orientation angle between the piezoelectric transducers operating at 39.5 kHz in air.

As an effect of the changes in the received pressure, reflection pattern, and reflection coefficient, the load voltage and power declines when the orientation angle increases. Following these observations, the effect of operational frequency on the sensitivity of the received power due to misorientation is analysed by experimentally measuring the delivery power to the load for every 2^o of orientation angle from $0^o$to 35^o for 10 cm, 20 cm, and 30 cm separation distances. The results are mirrored for the negative misorientation angles to demonstrate a complete profile. Figure 4.21 and Figure 4.22 show the output power results for resistive and complex load matching, respectively. The transmitter was operated at 39.5 kHz, 40 kHz, 40.5 kHz, and 41 kHz in each case.

Initial examination of the results shows that the change in frequency unalters the reflection patterns due to misorientation. Instead, all the three effects studied earlier are observed. In agreement with chapter 3 observations, 39.5 kHz consistently provides the highest output power for resistive matching and operating at 40.5 kHz has higher efficiency for complex loading. In addition, tuning the reactance of the transducers results in a higher load voltage and power.

It is essential to notice that the effects of misalignment and misorientation are nonlinear. Unlike misalignment, frequency tuning does not enhance the lost output power due to misorientation. For instance, when a receiver is misaligned by 8 mm at a separation distance of 10 cm, changing the operating frequency from 40.5 kHz to 41 kHz will compensate the decrease in the output power by tuning the transducers (Figure 4.13). On the other hand, when there is a 8^o misorientation between the transducers separated by 10 cm operating at 40.5 kHz, the power is dropped by 2 mW. By changing the operating frequency to 41 kHz also results in a decline in power by 2.5 mW. This is because, when the receiver is offset, the pressure profile is no longer symmetrical, but the reflection is profile is persistent for increasing offset. In contrast, misorientation affects the reflection profile and the reflection coefficient of the APT receiver. Therefore, the power transfer efficiency will decrease irrespective of the operational frequency.

In addition, the losses due to angular misorientation and offset misalignment cannot be linearly superimposed. For example, a 4 mm offset at 11 cm separation distance operated at 39.5 kHz will cause a 11% power drop. and a 10^o orientation angle separately would cause a 62% power decrease. However, at a combined 4 mm offset and 10^o orientation angle will not correspond to a 73% reduction (deduced from experiments not included in this thesis) as the asymmetrical pressure profile due to misalignment is not accounted for in the reflection profile changes due to misorientation.

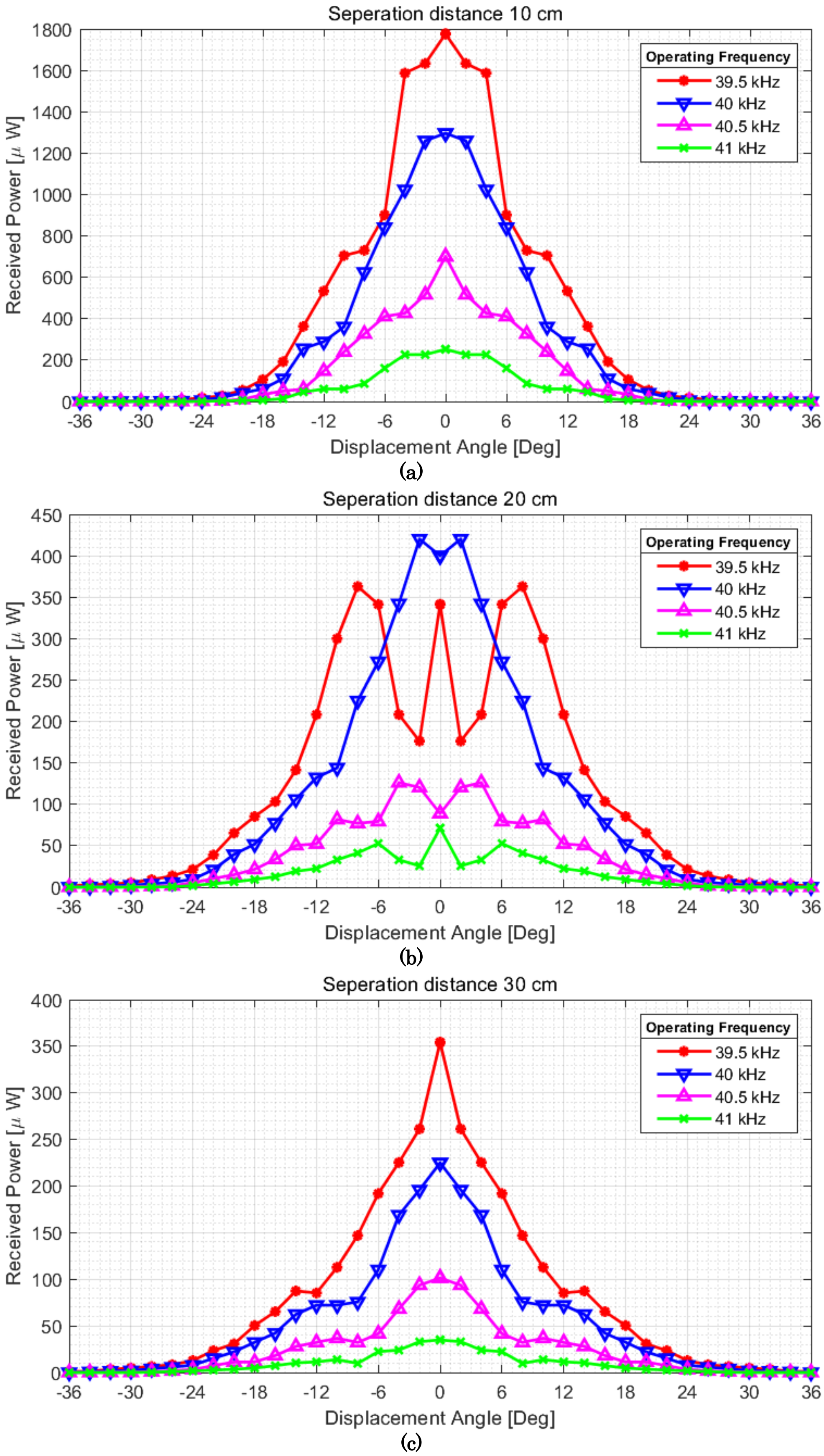

Figure 4.21: Measured output power across the resistive load for varying orientation angle and operating frequencies for (a) 10 cm (b) 20 cm and (c) 30 cm separation distance.

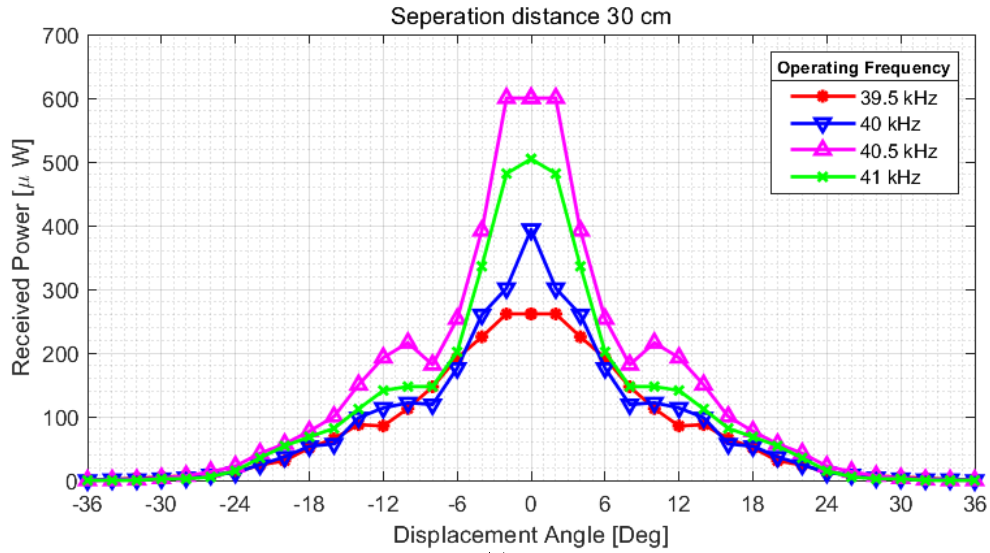

(a)

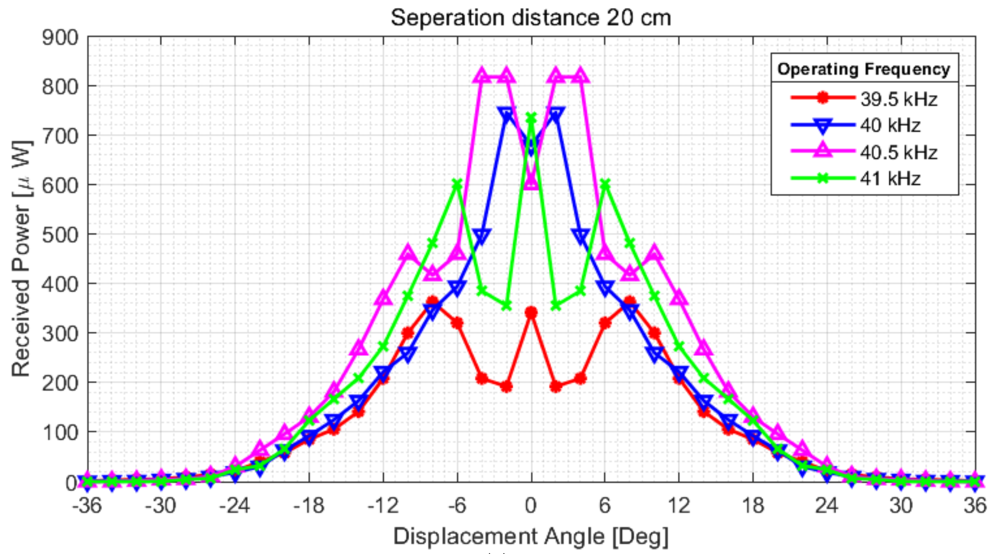

(b)

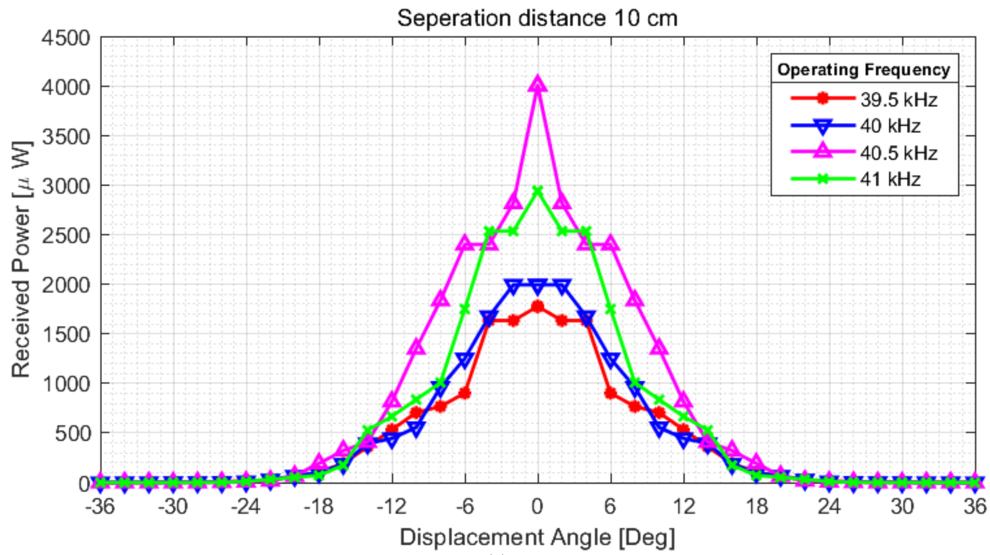

(c)

Figure 4.22: Measured output power across the complex load for varying orientation angle and operating frequencies for (a) 10 cm (b) 20 cm and (c) 30 cm separation distance.

4.3. Conclusion

The power transfer efficiency of an APT system is significantly affected by the standing waves caused by reflections, especially in air-based APT systems. Since the difference in acoustic impedance between air and PZT is vast, a large portion of the received wave is reflected into the medium at the receiver-medium boundary. This causes local peaks and valleys along the acoustic waves' propagation axis, making the system sensitive to the separation distance. Therefore, the reflections of the APT system using FUS-40E transducers are firstly studied using COMSOL modelling. The fluctuations observed in the simulations were then validated with experimental results. The extension of the APT system's reflections was also investigated based on the receiver load matching technique, transmitter tuning, and frequency of operation.

The effects of linear offset between the centres of the transducers were analysed using the misalignment design graphs. A 3D depth magnitude graph was developed by measuring the resistive and complex load-matched loads' output power. This provides a perception of the mean voltage and power as a function of offset and depth. It was observed that reflection was consistent even at a large offset ($> 20\ mm$). The APT system was also profiled to generate a design graph as a function of operating frequencies. Evaluating the design graph provided information about how changing the operating frequency by $0.5\ kHz$ could improve the efficiency of the APT system by shifting its operation from a valley point in the standing waves to a peak point.

A measured increase of up to 6 times the output power received at $39.5\ kHz$ was observed by utilizing the frequency tuning and complex impedance matching techniques. For instance, the received power at $12\ mm$ offset and $25\ cm$ separation distance, when operated at $39.5\ kHz$ increased from $18\ \mu W$ to $122\ \mu W$, if operated at $40.5\ kHz$. Therefore, combining tuning and impedance matching techniques can provide a reliable solution for condensing uncertainties in APT power transfer efficiency due to reflection and misalignment.

The misorientation experiments provide insight into the sensitivity of the output power for changes in angle between the faces of the transducers. As the angle between the transducers increases, three major impacts were observed: (1) the pressure pattern across the face of the receiver changes. (2) The fluctuation in the received power becomes minor due to decreased standing waves (3) The reflection coefficient of the APT system increases with receiver orientation angle. Consequently, these effects contribute to the declining output voltage and power for increasing orientation angle. Further analysis also shows that the effect of misorientation is identical to all operating frequencies. Therefore, frequency tuning cannot be exploited to evade losses due to misorientation.

The contributions of this chapter are to provide a detailed analysis of the load voltage and power sensitivity of an air-based APT system to changes in receiver position, orientation and alignment. Further analysis to define the system dependency on receiver loading, transmitter tuning, and the system operating frequency is also provided. The key findings of this chapter are as listed below:

1. The extend of the fluctuations caused due to standing waves is directly relatable to acoustic impedance mismatch between the sound source and the propagation medium.
2. The effects of misalignment and reflections can be compensated by combining complex impedance matching and off-resonance frequency tuning for optimum power transfer.
3. The advantage of using a well-tuned APT system and driving the transmitter at off-resonance frequencies is substantially noticeable for large separation distance and offsets.
4. Increasing orientation angle greatly affects the output power as it increases the reflection coefficient of the system, reduces the net received pressure and decreases the standing wave in the system.
5. Frequency tuning does not improve the performance of a misoriented receiver as the increased orientation angle reduces standing waves. Therefore, driving at off-resonance would not place the receiver at a more favourable wave position.
6. The effects of misalignment and misoreintation are nonlinear and the losses due to the respective effects can not be linearly superimposed.

The findings from this chapter can be further developed to implement acoustic impedance matching layers to improve the power transfer efficiency of APT systems.

5. Two-Stage Wireless Power Network

In this chapter, the findings of acoustic power transfer efficiency combined with inductive power transfer and autonomous vehicle technologies are applied to form the 'two-stage wireless power network'. Equipping inexpensive unmanned aerial vehicles and embedded devices with subsystems to facilitate wireless power transfer (WPT) allows them to become viable power delivery vehicles (PDV) and data collection agents. The potential of such a system to solve several residual problems concerning the maintenance and data collection from embedded devices is investigated in this work. Initially, the physical parameters modelling the power network and PDV are defined to understand the limitations of this powering strategy. The chapter then describes a novel dynamic recharge scheduling algorithm that combines weighted genetic clustering with nearest neighbour search to minimise PDV travel distance and WPT losses. Finally, the results from extensive simulations are discussed in detail, including significant design challenges to bring the simulation close to realistic values.

5.1. Power Distribution and Recharge Scheduling

The use of mobile chargers or power delivery vehicles (PDV), such as drones, for recharging remote network systems has been of recent interest [192, 193] as it provides certainty and proactive control to the spatial power distribution and easy assessment of the energy needs of the network. In practice, however, the PDV itself has limited energy, and visiting large numbers of nodes increases the fraction of carried energy that the PDV must expend for its propulsion, leading to frequent visits to the recharging station. Furthermore, some nodes may be buried in the ground or structures, limiting the efficiency in recharging them by WPT. Therefore, a key challenge is to ensure that a PDV can optimally schedule the power delivery across the network such that it is as reliable and resource-efficient as possible. A two-stage wireless power network (WPN) approach is proposed in this chapter to achieve this and outperform naive on-demand recharging strategies. In this recharge strategy, an extensive network of devices is grouped into small clusters, where packets of energy inductively delivered to each cluster by the PDV are acoustically distributed to devices within the cluster.

Recharge scheduling algorithms can be classified into deterministic and non-deterministic algorithms [194]. Non-deterministic algorithms, like Shortest-Job-Next with Preemption (SJNP), runs on a prompt-based scheme where a failing node sends a recharge request to the PDV to get energised. This, however, leads to inefficient use of the

PDV, and the charge schedule can be easily overlooked. Alternatively, deterministic algorithms, such as solutions to Traveling Salesman Problems (TSP) [195], work by constructing the shortest Hamiltonian cycle and using it as the path for the PDV. In this case, the node locations and energy consumption are recorded periodically at a base station and depending on whether we have a single-node [196] or a multi-node [195] scheme, the PDV periodically follows a pre-optimised path to recharge the nodes. To avoid enormous data-storage demands associated with tracking, Lin [194] proposed a heuristic "Temporal and Distantial Priority (TADP) algorithm", where a priority table is generated considering both charge time and PDV travel distance and conditioning the Shortest-Job-Next (SJN) algorithm into time slots. They also deduced the scheduling problem as Non-deterministic Polynomial hard (NP-hard), as the solution depends on optimising both time and distance. In other words, only a near-optimum solution can be obtained by considering soft computing rather than a specific analytic solution [197]. While these recharge schemes benefit the effective replenishment of the WSN nodes, the capacity of the PDV itself is assumed infinite. This assumption imposes an unfeasible load on the PDV, resulting in recharge failures.

To overcome this, Cheng [198] proposed using multiple charging vehicles. They optimised scheduling by including a genetic approach and studied the implications of the different combinations of SJN and TSP algorithms. The outline of their approach is to cluster the low energy nodes using K-means clustering for the available PDVs and calculate a fitness function based on the time and distance travelled by the PDV to recharge the nodes. This is reiterated until a near-optimal solution for each PDV is obtained. The use of multiple PDVs, however, may be infeasible to solve this problem for applications incorporating semi-accessible sensor nodes, which are the focus of this work.

Other studies consider the dual nature of a PDV to optimise both the problems of WSN recharge scheduling and data collection, hence simultaneously recharging a WSN node and collecting data from nearby nodes through multi-hop transmission [199, 200]. Although the work concentrates on the network topology configuration and adaptive tuning of data rates to reduce power consumption, they present a fast converging analytic algorithm and analyse the potential dual nature of PDV for further research.

Accordingly, in this article, a weighted genetic clustering algorithm [201, 202] is introduced for the multi-power distribution system to determine the optimised solution to schedule recharge paths for the PDV efficiently. A clustered WSN is composed of a collective group of nodes called a cluster. Each cluster consists of a set of nodes and one

CentreNode (CN). The CN is responsible for receiving the packets of energy from the PDV and distributing them to the cluster nodes. The CNs must be accessible to the PDV. To optimise both WPT systems, the proposed approach is an adapted unique combination of genetic clustering and TSP. This minimises the load on the PDV by finding the quickest route and maximising power distribution in both stages of WPT. The formation of the clusters is crucial as (a) it should not burden the cluster centre to transmit power to too many nodes, draining its energy and, (b) it should also transfer sufficient power to the node farthest from the centre. Since the separation distance largely determines the efficiency of the power transfer, the choice of cluster centre is vital. Furthermore, the energy management of the PDV is optimised through shortest path algorithms in order to avoid frequent recharging cycles. The proposed approach is then simulated and evaluated against performance metrics including throughput and computational time to understand the importance of sensor placement in a WSN to maximise the network lifetime.

In brief, the main contribution of this chapter is the designed scheduling algorithm for a two-stage WPN that maximises the energy distributed among the sensor nodes and minimises the transmission losses. When supported by our algorithm, our results also show that two-stage WPNs offer a practical and scalable solution for enabling large Industrial Internet of Things (IIOTs) networks with enhanced lifetime and self-management capabilities. The proposed system is evaluated in simulation using a 2D plane where the nodes are arbitrarily distributed, using realistic WPT parametric values. In doing so, this work firstly aims to understand the efficiency of a two-stage WPN for insufficiently accessible WSNs and, secondly, to study the reliability of such a system to deliver measurements at the expected frequency. Lastly, the C++ implementation of this work is published open-source for easy reference and further improvements[1].

5.2. System Model

Consider a network of N_S sensor nodes and a Base Station (BS) database located at the origin (0,0) administrating the wireless sensor network. The BS records the coordinate positions of all the nodes in the network and updates them as necessary whenever any changes occur. The initial position of the PDV is stored in the BS. The storage capacities of the sensor nodes (E_{max}^{SC}) and the PDV (E_{max}^{PDV}) are assumed to be finite but rechargeable

[1] https://github.com/achu6393/dynamicWeightedClustering.git

an infinite number of times. During each recharge cycle, the PDV starts from the BS visiting the nodes that triggered recharge requests through the first-stage power transfer and then flies back to the BS, where it is recharged to its maximum capacity (i.e. $E^{PDV} = E^{PDV}_{max}$). When initialising the algorithm, randomised positions and initial stored energies are appointed to the set of sensor nodes $S \in S_1, S_2, \ldots, S_{N_S}$ to generate a variety of scenarios.

Each Sensor Node S_i in the WSN is equipped with identical subsystems for wireless power transfer and conditioning circuitry. However, the storage capacity and sensing element can be modular depending on the purpose of the sensor. The nature of the WPT is characterised and designed based on its architecture and application. Therefore, the algorithm is designed to be versatile for any WPT system by changing a set of control parameters. In this work, the first power transfer stage is implemented inductively between the PDV and nodes, with energy subsequently distributed among the cluster acoustically. The system components of a wireless sensor node and the energy flow among the subsystems are as depicted in Figure 5.1.

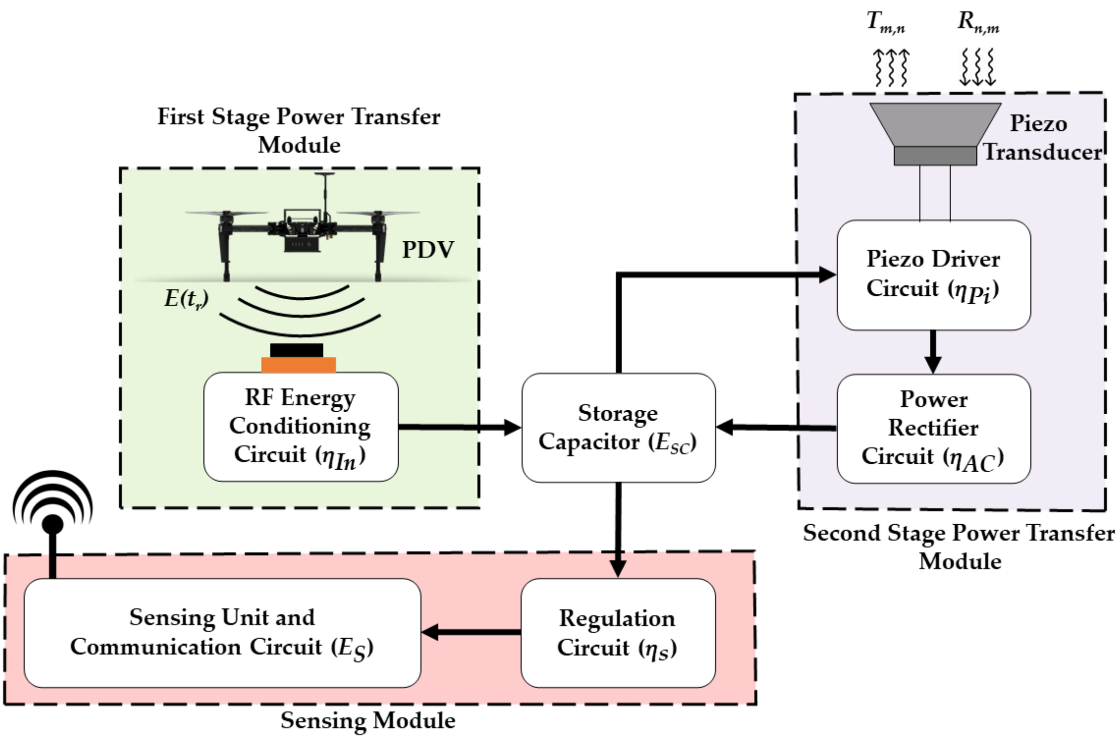

Figure 5.1: Process diagram of two-stage wireless power transfer representing the energy flow between the different subsystems and the modes of operation (cited from Pandiyan *et al.[69]*).

During time slot t_r, the PDV transfers $E(t_r)$ energy inductively to the sensor node at η_{In} efficiency. This charges the storage capacitor (SC) from its current state E^{SC} to E^{SC}_{max}.

For the secondary APT, the SC drives a piezoelectric transducer of efficiency η_{Pi}, through a driver of efficiency η_{AC}, to transmit $T_{n,m}$ energy from the sensor node S_n to S_m. The end nodes (S_m) receive attenuated energy of $R_{m,n}$ from S_n, which is then collected by the piezoelectric transducer and charges its own SC. During the sensing mode, the SC discharges to the sensing module to measure an attribute of the system using E^S energy with efficiency, η_S. All the modelling variables of the WPN are listed in Table 5.1. The use of storage capacitors for the sensor nodes introduces a small leakage current to the circuit due to the capacitor's internal conductance. To bring the system simulation close to reality, a leakage factor of μ is included in the fitness function. μ is a function of time that governs minuscule energy that outflows when the rated voltage continues to be applied to the storage unit.

Table 5.1: Modelling parameters used in the two-stage power transfer system.

Variable	Definition	Units
$x_{m,n}$	Distance between two sensor Nodes	[m]
x_{max}	Maximum distance for acoustic transfer	[m]
E^{PDV}	Energy of PDV	[J]
E^{PDV}_{max}	Maximum energy of PDV	[J]
E^{SC}	Energy stored in the sensor Node	[J]
E^{SC}_{max}	Maximum energy stored in the sensor Node	[J]
E^{S}	Energy utilised by the sensing unit	[J]
$g(f,x)$	Transmission gain of acoustic link	-
$E(t_r)$	Packet of energy delivered from PDV	[J]
N_S	No. of sensor nodes in the network	-
$R_{n,m}$	Energy received by node m from n	[J]
$T_{m,n}$	Energy transferred from node m to n	[J]
t_r	Time slot of the recharge cycle	[s]
α	Fitness function parameter for energy weight	[J^{-1}]
β	Fitness function parameter for PDV distance weight	[m^{-1}]
η_{In}	Efficiency of the inductive electronics	-
η_{AC}	Efficiency of the rectifier circuits	-
η_{Pi}	Efficiency of the Piezoelectric Transducer	-
η_{S}	Efficiency of the Sensing Module	-
μ	Leakage of SC	[%]

5.2.1. Power Delivery Vehicle

The PDV is modelled using the DJI Matrice 100 (M100) quad-copter drone, the specifications of which are summarised in Table 5.2. This drone model was employed due to familiarity with previous research projects, extending the possibility of evaluating the proposed recharge scheme experimentally in the future. The drone's flight is programmable by establishing a locally customised 2D/3D coordinate system by referencing the initial drone location mapped with respect to the BS at origin (0,0). The M100 onboard software comes with an open-source C++ library (GCC 4.8.1/5.3.1) for flight control development. The user can upload the compiled binary code of the C++ script by interfacing the onboard Software Development Kit (SDK) with serial communication ports (USART3) or through supported processors like STM32 or ARM (USART2 and USART3). Additional modular components for Wi-Fi and Bluetooth communication can also be connected for improved flight control. However, a balance between control precision and drone energy consumption must be planned for efficient power distribution.

The total time from the PDV take-off from the BS until its return is defined as the recharge cycle time, represented by t_r. An approximation of the PDV power dissipation per unit distance can be calculated from the maximum capacity and the flight time of the PDV. This model also accounts for the power surge during take-off. In addition, while transferring 'packets' of energy to the sensors, the inductive power transmitter will also lead to a fast discharge of the PDV battery.

Table 5.2: Power delivery vehicle specifications from DJI Matrice 100 datasheet [203].

Parameter	Specifications
Performance	
Hovering Time (with 2 TB48D Batteries)	40 min
Maximum Speed of Ascent	5 m/s
Maximum Speed of Descent	4 m/s
Maximum Flight Speed (GPS Mode)	17 m/s
Maximum power Consumption	350 W
Battery	
Battery Model	TB48D - Dual Battery
Capacity	5700 mAh
Energy	129.96 Wh
Max Charging Power	180 W
Flight Control System	
Model	N1
Flight Control	Programmable
Navigation	Custom local frame

5.2.2. Wireless Sensor Node

At any given time, a WSN node will either be in 'Sense Mode' or 'Power Distribution Mode'. In sense mode, the energy flows from the SC to the sensing unit as it measures and transmits data to the BS. When a node triggers a charge cycle, the algorithm is run to compute the 'Centre Nodes' (CN), which will receive a packet of energy inductively from the PDV. Following this, the CN will distribute a part of this energy to other 'End

Nodes' (EN) through acoustic power transfer. The nodes within the acoustic range of the CN operate in receiving mode, where the transmitted acoustic energy is transduced to electrical energy, recharging the SC through a power management unit. Considering the above network design, the energy level of the SC of each node in the network can be analytically derived and is explained as follows.

- **Sense Mode**

The sensing unit of a node includes the measuring element, data storage, central processing unit, and the RF communication port. The power consumption of a sensor depends on its mode of operation and the sampling rate. Two sensor nodes were included within the simulated system, and their specifications are summarised in Table 5.3. The highest energy consumption of the sensing unit would be during the transmission of the collected data to the neighbouring BS. The power consumption of each sensor is calculated for the active, stand-by and communication cycle. Consecutively, the average energy used per duty cycle is represented as E_S, can be evaluated for a given duty cycle. The power management unit of the node is assumed to have efficiency η_{AC}.

Table 5.3: Specifications of Sensing Unit Components [204-207].

Parameters		Temperature Node	Pressure Node
	Sensing Unit		
Model No.		LMT84	NPA300
Supply Voltage	Typ.	1.5 V	3.3 V
	Max.	5.5 V	5 V
Typical Current		5.4 μA	1.2 mA
Response Time		0.7 ms	0.5 ms
Sampling Frequency		0.01 Hz	0.1 Hz
On Time		2 ms	2 ms
	Storage Capacitor		
Model No.		HB1030-2R5106	PHB-5R0
Capacitance		10 F	3 F
Voltage		2.5 V	5 V
Leakage Current		20 μA	16 μA

- **Centre Node Mode**

In every recharge cycle, the proposed algorithm is initialised, and the network is evaluated for assigning centre nodes to receive a packet of energy $E(t_r)$ from the PDV for optimum power distribution. The inductive power electronics efficiency is represented as η_{In}. It is assumed that a CN is always fully recharged for every PDV visit before it drives the acoustic transmitter (i.e., $E^{SC} = E^{SC}_{Max}$). In this case, it will have sufficient energy to transmit acoustic waves with adequate SPL to account for the transmission loss in the medium.

Once the CN is fully charged, it drives the piezoelectric driver at its resonance frequency f, with an efficiency of η_{Pi} for secondary transmission of power to the surrounding end nodes. This driving sensor node can acoustically transmit energy to χ_T neighbouring nodes within the acoustic distance limits x_{max}. The energy that is transmitted for each end node is denoted by $T_{m,n}$, where m and n are the index numbers of the transmitting and receiving nodes, respectively. The amount of energy attenuated in the receiver node will depend on its distance from the transmitter and orientation.

- **End Node Mode**

End nodes are the set of nodes that can receive energy from the CN through the second stage acoustic power transfer. The nodes which can receive energy from one or more CN are clustered as χ_R. This aids the algorithm to classify the nodes by assessing their accessibility. Nodes that prompted multiple recharge requests but cannot be associated with a CN for acoustic power distribution are prioritised to act as CN for the next recharge cycle. In such circumstances, the node will be recharged inductively by the PDV. Therefore, the proposed recharge strategy would best apply to dense WSNs.

The amount of energy that is received from CN to node S_n separated by a distance x ($x < x_{max}$) during the recharge cycle t_r can be calculated with respect to the acoustic channel loss co-efficient $g(f, x)$. This is a function of the operating frequency of the transmitter f, distance x between the nodes, and the transfer medium properties. In this work, $g(f, x)$ is obtained from the experimental data from [58] and Section 4.1, which serves as a good approximation for the simulations of this work.

Further to the acoustic channel losses, the amount of received power will also depend on the coupling efficiency of the piezoelectric transducers η_{Pi} to transfer the acoustic vibrations into electric power. The received AC power is then rectified using a Schottky bridge rectifier of efficiency η_{AC} that charges the SC of the node. Cumulative losses are considered to calculate the received energy. To avoid abnormalities in the near field region of the acoustic WPT, $g(f, x)$ is also governed by the boundary condition that the χ_R includes nodes located between the near field limit (L) and $1\,m$, which is a practical acoustical limit for the transmitter system. Furthermore, the SC for the node is assumed to be imperfect, and a fraction of energy is lost to leakage (μ) for every recharge cycle t_r. The IPT and APT recharge the SC, increasing its stored energy and driving the piezoelectric transducer or the sensing modules extracts energy. Hence, the dynamics of the SC energy level of a given sensor node, after a recharge cycle t_r, can be computed as follows:

$$E^{SC}(t_r+1) = \min\begin{cases} \left(\left(E^{SC}(t_r) + \eta_{In}E(t_r) - \dfrac{T_{m,n}}{\eta_{Pi}} + \eta_{Pi}\eta_{AC}g(f,x)T_{m,n} - \dfrac{E^S}{\eta_S} \right) * \ 1-\mu \right. \\ E^{SC}_{max} \end{cases} \tag{5.1}$$

governed by the boundary conditions in the following equations (Eq. 5.2 - 5.4):

$$\mathrm{T_{m,n}(t_r)} > 0 \tag{5.2}$$

$$E^{SC}(t_r) > T_{m,n} > R_{n,m} \tag{5.3}$$

$$T_{m,n} + E^S > E^{SC}(t_r) \tag{5.4}$$

5.3. Recharge Scheduling Algorithm

The proposed algorithm for scheduling the two-stage WPT scheme, along with the design and assumptions of the genetic clustering algorithm, is discussed in detail in this section. The simulation is a two-layered combination of weighted genetic clustering and optimum path algorithm, executed in C++ programming language for easy integration with the system development software of DJI Matrice 100.

This work proposes a conceptually simple clustering and path optimisation algorithm that can be easily integrated for practical application in PDV rechargeable WSNs. Contrary to K-means algorithms, the suggested technique should always reach a near-optimal solution, even for large datasets. This is demonstrated by combining weighted clustering with a genetic algorithm. The results are further fed to a TSP solver to minimise the moving distance of the PDV.

5.3.1. Weighted Clustering

Two essential factors realise the goal to optimise the energy distribution in both stages of WPT to administer the order of recharge. Firstly, an accurate number of clusters (N_C) must be determined to enhance the first stage IPT. Otherwise, overwhelming the PDV with overestimated N_C will drain the PDV battery and result in an inefficient recharge cycle. Undervaluing the same can put more pressure on the CNs during the second acoustic energy distribution stage. However, estimating the recharge efficiency using a dynamic approach would eliminate the second energy distribution stage. Therefore, genetic clustering is selected over K-means clustering, where N_C is not pre-calculated but optimised based on the current energy demands of the WSN. This is a dynamic process that depends on the available acoustic connections, recharge requests and the PDV position during the recharge cycle.

Secondly, the choice of the CN is vital in employing an efficient APT. When clustering a WSN, transmitting energy packets to a dense cluster is preferred to a secluded CN with well-distributed ENs. This helps reduce acoustic channel losses. Additionally, some nodes in the WSN could be remotely located and therefore cannot be clustered with other nodes' acoustic distribution limits. In this case, they always receive less energy and lose energy quickly, resulting in frequent recharge triggering, measurement failures and reduced active lifespan. Therefore, it is critical to consider these trade-offs during clustering and change the CN according to the dynamic demand of energy. This is achieved by introducing a set of positive weight factors w for all nodes in the network ($w_i \in w_{S_1}, w_{S_2}, \dots, w_{S_{NS}}$) defined as the rounded ratio between the maximum charge of the SC to its current charge in the given t_r, expressed as follows:

$$\mathrm{w_i} = \mathrm{round}\left(\frac{\mathrm{E_{max}^{SC_i}}}{\mathrm{E^{SC_i}}}\right) \tag{5.5}$$

where i is the index of the sensor ($i = 1,2, \dots, N_S$).

To initiate a recharge cycle, the node automatically prompts a recharge request when its energy level is drained below a defined threshold. Two different threshold levels are defined for adaptability, first at 70 % of E_{Max}^{SC} and another at 50 % of E_{Max}^{SC}, below which the node might not have enough energy to measure or communicate with the BS. This strategy allows us to prioritise the clustering process for node(s) nearing the second threshold. Once sufficient information is gathered on the WSN state, all the nodes in the WSN are classified either into the non-charging or charging list. This data is fed into the genetic clustering algorithm to allocate the charging path to the PDV. Following the first stage of energy transfer, the CN distributes the energy to the nodes within range. It should be noted that a node located within the acoustic range of a CN is set to WPT mode, although it may not be in the charging list.

5.3.2. Dynamic Clustering using Genetic Algorithm

When initialising a genetic algorithm (GA), a vector of potential solutions is initialised as 'candidate population' where each candidate represents a distinctive set of clusters. The initialised population is iterated over a known number of times following the process of crossover, mutation and selection to evaluate the best candidates in that population. A set of control parameters is assigned to influence the quality of the search for the GA algorithm as listed below:

1: *Population* (Pop): defines the maximum number of candidate solutions allowed per population and affects execution speed.

2: *Crossover Ratio* (CR): defines the percentage of genes allowed to crossover between the two parents.

3: *Number of Generations* (Gen): defines the maximum number of iterations.

The choices of these parametric values are problem-dependent. The significance of these parameters, along with the steps involved in the algorithm, is explained as follows. An illustrative overview of the process is scripted as pseudocode in Algorithm 5.1.

Algorithm 5.1: Weighted Clustering using Genetic Algorithm

Input: Coordinates of Nodes; Energy level of Nodes; Position and Energy of PDV
Output: Optimized PDV Flight Path
Start
Set WPT model constants (x_{max} $g(f, x), x,$ η)
Set GA clustering constants (Pop, CR, Gen)
Evaluate maximum allowable clusters (K_{max})
Initialise Target Vector ($[X]_1$) for first generation
repeat
    Perform GA Crossover to generate Trial Vector ($[V]_{gen}$)
    Perform GA Mutation on $[V]_{gen}$
    Compute metric for $[X]_{gen}$ and $[V]_{gen}$
    Perform GA Selection
until : Optimized Fitness Function or maximum generation achieved
Store the vector of center node vertices in PDV_{path}
Perform TSP Algorithm to obtain PDV_{path}^{opt}
return PDV_{path}^{opt}

- **Initialisation**

The genetic algorithm commences by estimating the maximum number of clusters (K_{max}) for the given WSN. K_{max} is dependent on the charge capacity of the PDV and its approximate travel time across the WSN for the computed path in order to avoid exhausting its energy. In this work, K_{max} is set to the maximum number of nodes it can fully charge with 40 % of its battery capacity. In this way, enough energy is reserved for the flight itself. The value of K is then appropriately minimised during the iterations.

Assuming N_S^{RR} number of sensors out of N_s in the WSN prompted a recharge request, a vector of these nodes is onset, and K number of nodes are randomly selected as CNs for each cluster. The remaining nodes in the network are randomly assigned to one of the clusters if they are inside the acoustic limits of the CN (Figure 5.2a). In some cases, all the nodes in the network are not included in the cluster because either the node might not have called a recharge request, or it is out of the acoustic range from every other CN. This is repeated until Pop samples of a vector of clusters are formed (Figure 5.2b).

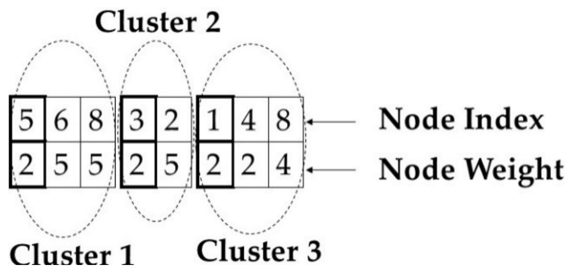

(a)

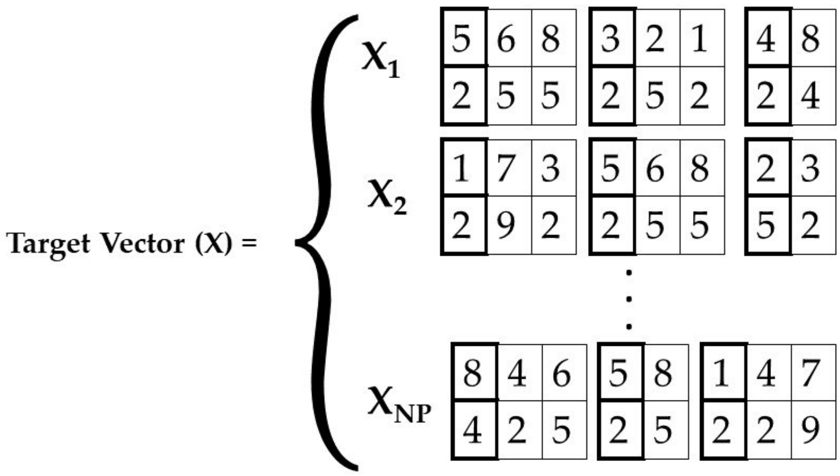

(b)

Figure 5.2: Representation of sample data of vectors during the initialisation process in GA clustering. (a) Structure of a candidate vector holding the index and weight of the nodes in the clusters. (b) Structure of a target vector is represented as a matrix of candidate vectors after the initialisation process. The bolded frames represent the CN of each cluster. (cited from Pandiyan *et al.* [69])

The resulting vector of samples is known as the Target Vector ($[X]$) and the first entity (highlighted by a bolded frame in Figure 5.2) is the CN of the respective cluster.

- **Fitness Function**

It is essential to define a fitness function that acts as a metric to evaluate the candidate solutions of each population when adopting a genetic algorithm. The goal of the GA to maximise the power distribution and minimise the travel distance of the PDV is approached as a multi-objective optimisation problem formulated as a weighted sum. Given N_C number of clusters distributed over an area of A, each containing a centre node CN_i ($i \in 1,2,\dots,N_C$ is the index of the cluster), the described optimisation problem can be formulated as:

$$\min_{CN\in A} \max_{i=1}^{N_C} \approx x(CN_i, CN_{i+1}) \cdot \sum_{\forall S_j \in N_C^i} w_j * E_j^{SC} \tag{5.6}$$

where w_j and E_j^{SC} are the positive weight factor and energy of the node S_j belonging to i^{th} cluster. The sum of $w_j E_j^{SC}$ represents the total energy of i^{th} cluster, and $x\big(CN_j, Cnj+1\big)$ is the distance between two cluster centres. Therefore, the optimisation is a MINIMAX problem to minimise the maximum expenditure of the PDV.

Using the system model described in Section 5.2, the cumulative increase in energy of WSN (ΔE^{WSN}) can be calculated for the assumed cluster formation from Eq. 5.1 - 5.4 and Eq. 5.6.

$$\Delta E_{WSN} = \sum_{i=1}^{N_S} E_i^{SC}(t+1) - E_i^{SC}(t) \tag{5.7}$$

The total distance travelled by the PDV can be calculated as follows:

$$x^{PDV} = x_{p_1}^{BS} + \sum_{i=1}^{k-1} x_{p_i,p_{i+1}} + x_{p_k}^{BS} \tag{5.8}$$

where x is the Euclidean distance between two points.

Flight duration should also be considered in addition to distance and the energy transfer, as listed in Table 5.2. Throughout the flight duration, a metric of charging delay and sensor downtime also accounts for the PDV energy evaluation. This is done by setting a tolerable threshold to this value, and if a candidate solution exceeds this, the fitness metric is immediately set to -1. A negative fitness value reduces the probability of the candidate being selected for the next generation. A similar condition is applied if the PDV runs out of power mid recharge cycle, thereby enforcing practical conditions in the simulations.

Accordingly, the metric can be summarised as Eq. 5.8, the inverse of which gives the fitness function:

$$M = \begin{cases} \alpha * \Delta \mathrm{E}^{\mathrm{WSN}} + \dfrac{\beta}{\mathrm{d_{PDV}}}, & if\ E^{PDV} > E^{flight} \\ -1, & otherwise \end{cases} \tag{5.9}$$

The constants α and β used in Eq. 5.8 are user-defined parameters to weigh the importance of one criterion over the other. For example, if the application is highly restricted by the travel distance of the PDV, β is set to a high value to manipulate the fitness metric. For the simulation performed in this work, α and β are set to $100\,J^{-1}$ and $0.1\,m^{-1}$ for imposing a preference of charging more nodes in the WSN over minimising PDV travel distance.

- **Crossover**

Crossover is a probabilistic process of selecting a substring from two samples of the target vector to produce two proto-samples, generating the *Trial Vector* ($[V]$). In this work, a *2-point crossover strategy* was implemented and controlled by the CR parameter. The steps involved with crossover are illustrated in Figure 5.3.

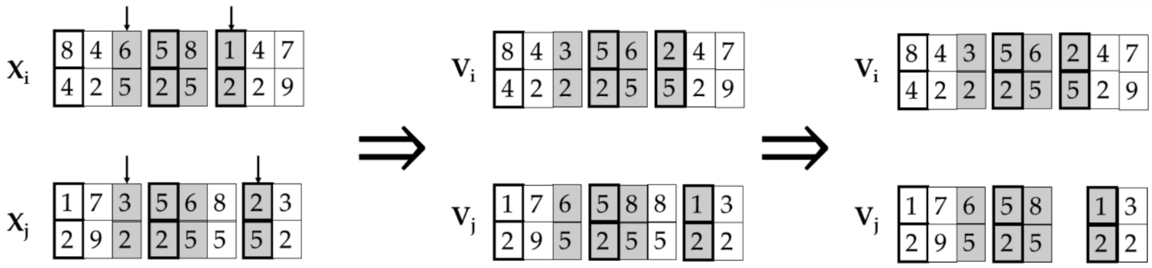

Figure 5.3: Illustration of the steps involved in the 2-point crossover strategy of GA clustering. The arrows represent the beginning and endpoints of crossover, and the shaded cells are exchanged among the clusters. Subsequently, the duplicates are removed. (cited from Pandiyan *et al.* [69])

Initially, two candidates X_i and X_j are chosen at random from the target vector. A substring of the same length in each cluster is then chosen based on the set CR. These substrings, indicated by grey cell shading in Figure 5.3, are then exchanged between the target vector candidates forming two trial candidates, as in Algorithm 5.2. In the illustrated example, one node from clusters 1 and 3 is exchanged as part of the sequence. However, there is a size mismatch for the second cluster. In such circumstances, the smallest size among them is chosen for generating the sequence, which is 2 in the shown example. The final step of the crossover is to remove any duplicates from each cluster, as shown in cluster 2 of V_i.

Algorithm 5.2: GA 2-point Crossover Scheme

Start

Initialise $V_i = X_I$ and $V_j = X_J$

Randomly select the starting point of the sequence

Repeat

    Swap the sequence $V_i = X_j$ and $V_j = X_i$

until $rand(0,100] < CR$ or end of the smallest cluster

for $i = pop\ to$ 1 do:

    if $V_i - 1 == V_i$ or $X_i - 1 == X_i$ then

        Remove Duplicates

    end if

end for

- ### Mutation

As the crossover process is fully randomised, some nodes inside the trial vector cluster could be outside the acoustic limits of the CN. Therefore, a further step of mutation is recommended to alter the trial vector candidate. Swap Mutation is designed for this work, where two indices are selected at random from two different clusters in the same candidate, and the corresponding nodes are swapped. Figure 5.4 demonstrates the swap mutation process. Each candidate in the trial vector undergoes mutation with equal probability.

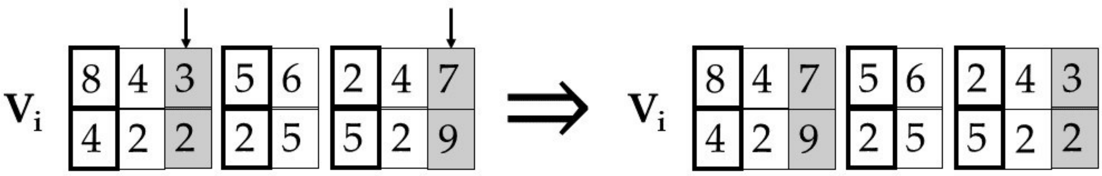

Figure 5.4: Illustration of the swap mutation process. (cited from Pandiyan *et al.* [69])

Supposing the node population is dense in specific regions, the GA initialisation may cluster more nodes into a single cluster exceeding the physical limits of the acoustic transmission. Consider the examples represented in Figure 5.5a. Since the distribution of the nodes are sparse, all the nodes within the acoustic range (x_{max}) can be included in the cluster. However, as demonstrated in Figure 5.5c, dense clusters must be segregated into smaller clusters to avoid overlapping sensor nodes in the path of the energy transfer. The overestimation of power distribution is eliminated by introducing a *penalty function* that has two functions:

1. To find the group of closest nodes concerning the CN and restrict a maximum node population per cluster. For each cluster, the end nodes are initially arranged by ascending distance from the CN, and a look-up table of displacement angle from the CN (origin) is calculated. Then, an angular scan from the nearest node is performed, and the closest nodes are clustered, as shown in Figure 5.5b.
2. A scan for any duplicates within a population is performed after mutation to avoid scenarios with overlapped sensors. The code implements this by using a linked list data structure vector, removing the sensor node references once assigned to a cluster.
3.

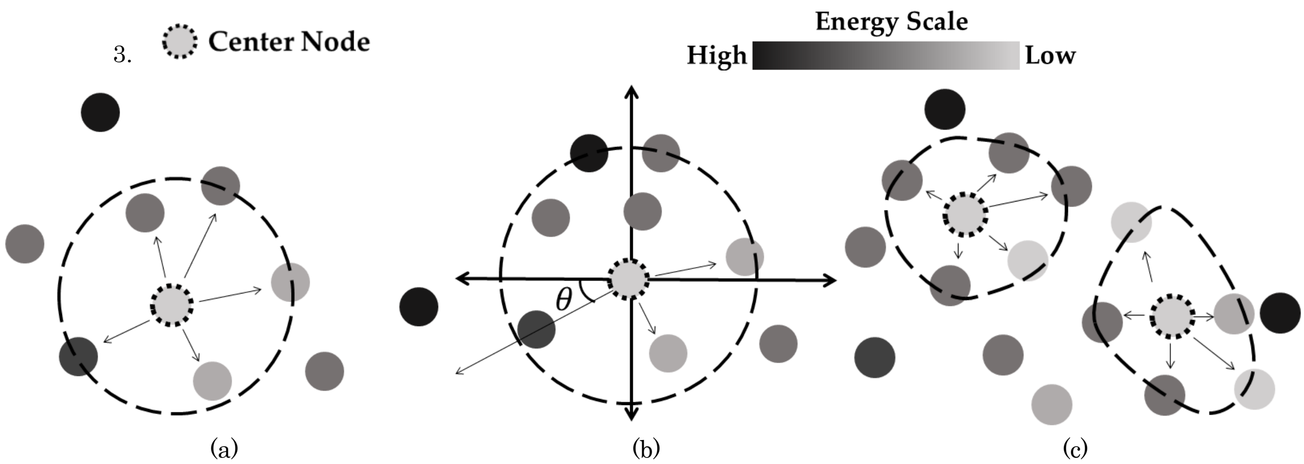

Figure 5.5: Representation of different cases of cluster formation for the given system (a) Single cluster with x_{max} as the cluster limit (b) Angle calculation for the EN from the CN (c) Multi-cluster formation in a dense WSN.

- ## Selection

The choice of the selection algorithm for the GA depends on the nature of the problem evaluated. For this work, the *survival-of-the-fittest* concept from the natural theory of evolution is adopted and is governed by Eq.5.10. A binary selection scheme is where the candidate with the higher metric value comparing the target and the trial vector is selected for the mating pool of the next generation. This selection method ensures that the candidate pool gets closer to the optimal solution or stays the same but never declines. Then, the selected candidates are initialised as the target vector for the next iteration, and the GA clustering is repeated until the maximum number of generations is reached or an optimal solution is found. Algorithm 5.3 illustrates the pseudocode for the survival of the fittest scheme.

$$X_{i,gen+1} = \begin{cases} X_{i,gen}, if M(X_{i,gen}) > M(V_{i,gen}) \\ V_{i,gen}, \quad otherwise \end{cases} \tag{5.10}$$

Algorithm 5.3: GA Survival-of-the-fittest Selection Scheme

Start
1: Compute the M(Xgen) and M(Vgen)
2: Initialise Xgen+1 = Xgen
3: if M(Xgen) < M(Vgen) then
4: Xgen+1 = Vgen
5: **end if**

5.3.3. Optimum Path Finder

An array of the sensor node coordinates is assembled for the PDV after generating the cluster centres for first stage power transfer. The array of coordinates is then loaded to the travelling salesman problem (TSP) algorithm to generate the optimised path. This is achieved by implementing a simple nearest node search algorithm generating a low-cost path for the PDV to traverse the WSN, stationing at the chosen points to transfer packets of energy. Therefore, an optimal power control scheme is obtained, where the PDV uses a dynamic clustering algorithm to minimise the acoustic and inductive channel losses and maximise the energy supplied to the sensor nodes in each PDV visit. Algorithm 5.4 describes the steps employed for optimising the UAV path.

Algorithm 5.4: Travelling Salesman Problem (TSP) Algorithm

Input: Vertices of the Center Nodes
Output: Optimized PDV Flight Path
Start
1: **Repeat**
2: Find u = nearest node from current PDV Position.
3: Calculate $temp$ = energy to travel to and recharge u and proceed back to BS.
4: **if** $E_{PDV} < temp$ then
5: Exit Loop
6: **else**
7: Add u to PDV_{path}^{opt}
8: Remove vertice u from PDV_{path}
9: **end if**
10: **until** PDV_{path} is Empty
11: **return** PDV_{path}^{opt}

5.4. Implementation and Results

This section presents results from the proposed algorithm simulations and evaluation of a two-stage power distributed WPN. The algorithm was coded in C++ 14 using standard libraries to ensure compatibility with PDV system software for future experiments. The binary codes were executed on a 64-bit Intel Core i5 CPU @ 2.20 GHz with 4 GB RAM to obtain results. All the presented results are the average of 100 simulations. The priorities of optimisation depend on the network and application specification. The following performance metrics are used in this work:

1. *Frequency of PDV Visit:* The total number of completed PDV recharge cycles over a specified period.
2. *Throughput [%]:* The percentage of sensor nodes that are successfully charged either inductively or acoustically to the total number of charge requests received by the BS.
3. *Computational speed [s]:* Defined as the time period between the received charge requests and when the GA deploys a recharge path.

5.4.1. Impact of Algorithm Parameters

Given the limited computation resources of the PDV, the computation of the charge scheduling algorithm needs to be fast and efficient while maintaining a level of complexity. A series of simulations were evaluated to understand their effects on algorithm performance for a network of 5000 sensor nodes distributed over a square area of 4 km^2 and a storage battery charged between 60 and 100 %. The values of Gen and Pop were varied within 50 and 100 to analyse their influence on the computational speed and the throughput. Based on the results, a suitable value for the GA parameters was concluded. The influence of the GA parameters on the computational speed and the effective charging are summarised in Figure 5.6.

Figure 5.6a shows that higher Gen or Pop values will significantly impact the computation time of the algorithm, signifying that the algorithm may have reached the optimum solution in fewer iterations. Also, it can be interpreted from Figure 5.6b that the increase of Gen and Pop has only a small impact on the GA performance metric from the overlapping throughput plots. This indicates that the algorithm converges to a near-optimum solution at all times.

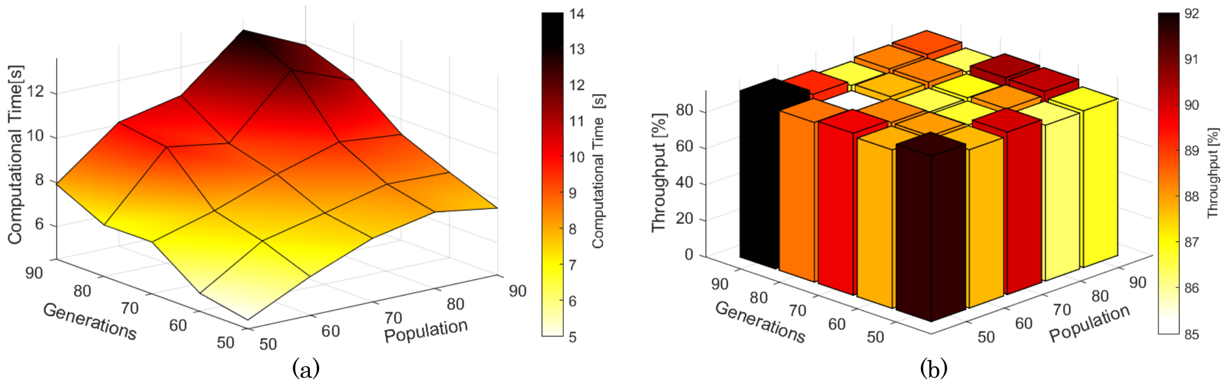

Figure 5.6: GA Parameter analysis for a network of 2000 sensors distributed over a 4 km^2network area. (a) Throughput analysis (b) Computational time analysis.

To analyse the correlation between the computational time and throughput of the algorithm, Figure 5.7 displays the analysis results for $Gen = 50$ and varying Pop. This trend follows the main graph and is offset by the computation time. It is concluded that throughput and computational time are independently influenced by Gen and Pop. Consequently, Gen and Pop are set to 50 for the following simulations to conserve resources.

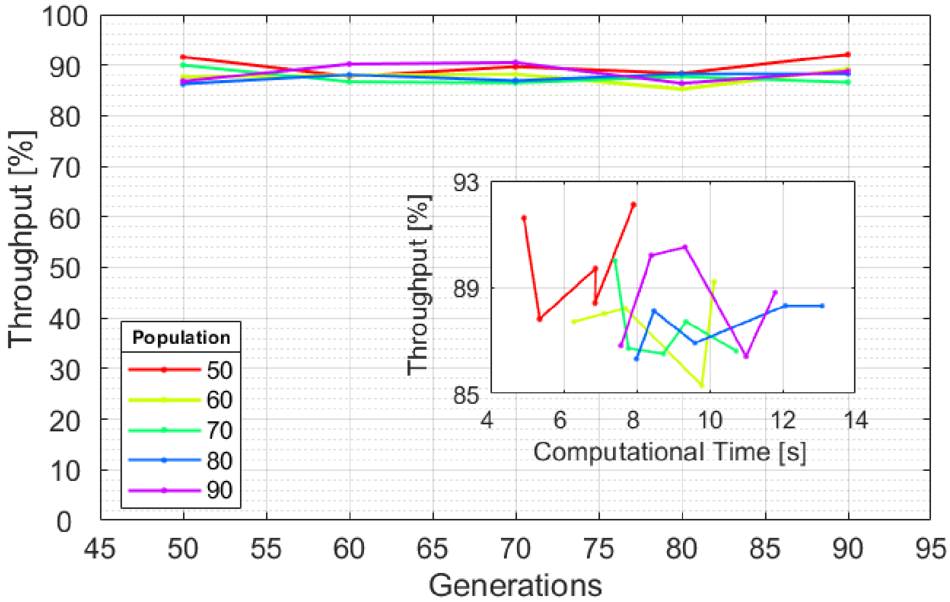

Figure 5.7: GA Parameter analysis to correlate the throughput and the computational time of the proposed algorithm. (cited from Pandiyan *et al.* [69])

5.4.2. Impact of PDV Parameters

As this work is focused on a specific WPN design, for comparing the performance of the proposed algorithm, we introduce a baseline design where the PDV charges all the nodes through IPT (i.e. no second stage of power distribution). This analysis demonstrates the performance gap between the proposed WPN and IPT recharged networks and helps understand both systems' limitations. Figure 5.8a illustrates the results from simulating a network containing 100 to 5000 sensor nodes distributed across a square area from $0.1\,km^2$ to $25\,km^2$. The PDV becomes overloaded for more extensive networks, and charging each node yields only ~ 10 % throughput. Two-stage WPN manages to satisfy at least 30% of the charge requests for WSN spread over $25\,km^2$. These results are also summarised in Table 5.4. However, the node placement and initial energy in these simulations are randomly initialised at the beginning of each recharge cycle. Meaning, the initial simulations only stabilises the network energy distribution. The simulation results plotted in Figure 5.8 represent the performance of the WPN response to a static network.

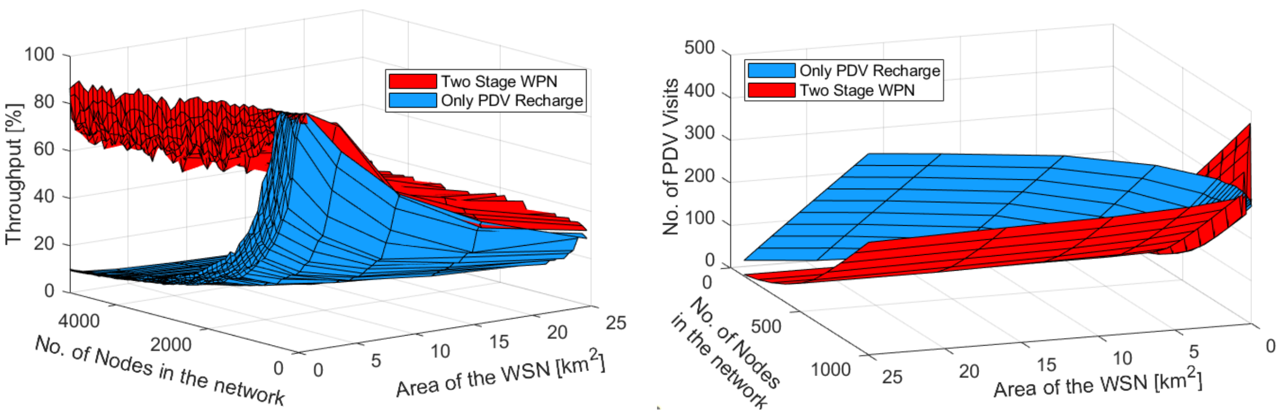

(a) (b)

Figure 5.8: Demonstration of variation in performance metrics for varying density of WSN. (a) Comparison of the overall throughput for the two-stage WPN and PDV recharge network for varying network size and density. (b) Total number of times that the PDV is fully recharged and takes-off for recharging the network for single-stage and two-stage WPN simulated continuously for seven days. (cited from Pandiyan *et al.* [69])

The system was continuously simulated to evaluate the algorithm's performance in a dynamic network when operated for seven days time period and for varying WSN densities. The average frequency of PDV recharge cycles was recorded for these simulations and is plotted in Figure 5.8b. It can be observed that for increasing the WSN area, the total PDV cost (in terms of number of PDV visits) increases non-linearly. This is because, in larger WSN, the PDV can fulfil the demands of only a few remote nodes through IPT. This results in very low throughput and hence persistent recharge requests from the SNs, which the PDV cannot meet. Thus, leading to an accumulation of unfulfilled requests. The two-Stage WPN scheme reduces this effect by increasing the throughput through secondary APT within clusters. In addition, the initial spikes in Figure 5.8b might be subject to random initiation of the WSN. In comparison, the two-stage WPN is superior in dense and large WSN. For sparsely distributed or smaller WSNs (in comparison to the PDV flight range,~ 6 km^2), a pure IPT recharge network would be an acceptable power distribution solution, given the reduced components.

Table 5.4: Throughput comparison by power distribution scheme

Area [km^2]	Number of Nodes	Throughput [%]	
		Two-Stage WPT	IPT Only
0.01	100	100.0	100.0
	1500	96.5	35.1
	3000	93.0	16.6
	5000	86.5	10.1
1	100	100.0	100.0
	1500	76.1	23.5
	3000	64.0	23.5
	5000	67.4	8.3
25	100	31.4	28
	1500	36.7	10.2
	3000	31.9	6.4
	5000	35.6	4.3

5.4.3. Impact of System Model Parameters

In the previous simulations, the WSN simulated was a heterogeneous network with a random mixture of two types of sensors, as mentioned in Table 5.3. In this section, we compare the algorithm's performance based on the heterogeneity or homogeneity of the WSN. In this work, a homogenous network represents a network of pressure sensors, and a heterogeneous network is a mixture of temperature and pressure sensors with varying sampling rates, energy consumption and energy storage units (as summarised in Table 5.3). The throughput of the PDV for the Two-Stage and IPT-Only networks are compared for both networks in Figure 5.9. This is simulated for networks of 100 to 1000 nodes spread over an area from 0.1 km^2 to 1 km^2.

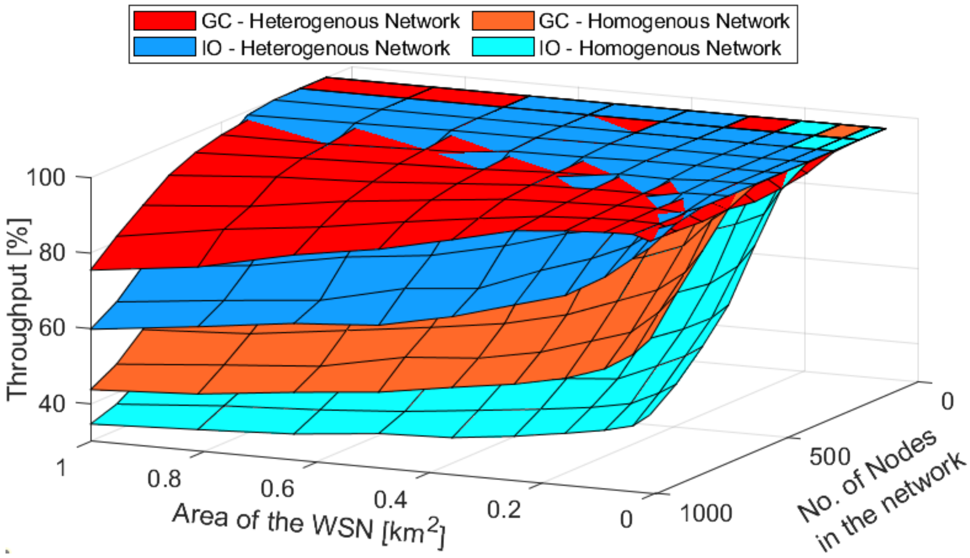

Figure 5.9: Comparison of PDV throughput for homogeneous (Only Pressure Sensor) and heterogeneous (both Pressure and Temperature Sensor) networks with Genetic Clustering (GC) Two-stage WPN and Inductive Only (IO) WPN.

Comparing the power distribution methods over the varying WSN density, the two-stage power transfer has a significantly higher throughput when compared to charging nodes through only inductive methods, maintaining the trend seen in Section 5.4.2. For network area $< 0.2\,km^2$ and < 300 nodes, all 4 cases yielded a $\sim 100\,\%$ throughput. However, there are apparent differences between the homogeneous and heterogeneous WSN. The throughput of heterogeneous WSN appears to be better than homogeneous WSN, mainly because of the difference in the energy demand of the networks. In other words, the overall power consumption and sampling frequency of the pressure sensor WSN are higher than for temperature sensors resulting in increased power demand in the homogeneous pressure sensor network.

In the heterogeneous network, this reduces the number of recharge requests that the PDV receives per recharge cycle, consequently reducing the load on the PDV. This suggests that the energy demand of a real-time network has a complex correlation with network architecture. Hence, having a dynamic scheduling algorithm is essential to optimise the costs involved in a WPN.

5.4.4. Algorithm Complexity Analysis

The input to the algorithm is the vector of sensor nodes in the network. Storing all the node data is unnecessary, and even in worst cases, the write memory is limited to only the flight path of the PDV. For visiting N_C cluster heads, the working memory can thus be deduced as $\Theta(N_C)$. Consider the worst-case scenario where the nodes are sparsely placed and therefore must be individually charged. Finding the cluster head would then require N_C iterations. The worst-case scenario for the optimisation loop is that each iteration results in minimum metric margins among the competing generations. As two vectors of size Pop are used in the algorithm, it takes $Gen * Pop^2$ iterations to find the cluster heads. Running the TSP algorithm has a complexity of $O\left({N_C}^2\right)$, where N_C is solely dependent on the battery capacity of the PDV. Therefore, in large WSNs, N_C is limited and has a fixed value (i.e. $N_C^2 \ll Gen * Pop^2$). Hence the total time complexity of the proposed genetic weighted clustering algorithm is $O(nm^2)$, where $n = Gen$ and $m = Pop$.

5.5. Conclusion

This chapter exploits recent advances in genetic computing to resolve a dynamic recharge scheduling problem for two-stage energy distribution systems, where power is distributed among the WSN using multiple WPT methods. The goal is to develop a sustainable and autonomous WPN for large scale industrial monitoring networks by forming clusters of nodes that can distribute the received power packets from a power delivery vehicle to the other nodes by a secondary WPT method.

In the studied system, inductive and acoustic WPT methods were considered. A novel dynamic optimisation algorithm was proposed by combining weighted genetic clustering and a TSP solution, thereby jointly minimising the PDV travel distance and losses during WPT. All parameters used in the system model simulation are practical values obtained from off-the-shelf components and experimental data. Extensive simulations of the proposed system and algorithm were evaluated against the case of a single-stage IPT recharge scheme, using the network charging state and the number of required vehicle recharge visits as two independent performance metrics. The throughput analysis gives insight into the correlation between the recharge demand and network specifications, signifying the importance of the two-stage WPT scheme to significantly improve the number of recharged nodes in large, dense networks. These results reveal the merits and limitations of the proposed model.

Furthermore, since the two-stage WPT scheme is based on clustering WSN nodes for APT, node placement is also a determining factor in enhancing the recharge performance. Therefore, this algorithm can be used as a novel planning tool to architect the placement of sensors in a network for optimised sensing data and power transfer. Furthermore, a complexity analysis of the algorithm was implemented to assess its compatibility with the generic onboard SDK. For future work, adapting the algorithm for multiple PDVs may be interesting to reduce charging delays in the network and help inform a comparative cost analysis. Implementing the scheme experimentally will be a critical next step to progress towards autonomous and sustainable monitoring systems successfully. Additionally, the PDV recharge scheme can be scheduled for recharging and communication purposes where it can acquire local data of the sensors to learn the system behaviour. The algorithm can evolve to a machine learning algorithm that could also predict the WPN requests using this data.

As the primary author of [69], my contributions to this work include conception, modelling and design, coding the software, data collection, analysis, and interpretation. David E Boyle supervised the software design and algorithm work, and the wireless power network design and implementation were supervised by Michail E Kiziroglou. Critical revision of the work and the final approval of the article was completed by Steven W Wright and Eric M Yeatman.

6. Conclusion

This final chapter briefly summarises the most important conclusion of this thesis and the contributions of this work. Furthermore, it lists several recommendations for future work on improving the power transfer efficiency of through-air APT systems and multi-stage wireless power networks. Since research in the through-air APT system is relatively recent, this leaves multiple opportunities and directions for further investigation of APT systems.

6.1. Thesis conclusion

This thesis focuses on the wireless power transfer from an electrical source to an electrical load, using acoustic waves as the energy carrier that propagates through the air at ultrasonic frequencies. Its primary purpose lies in providing an overview of the current technologies in wireless energy solutions for large networks, opportunities and limitations of the APT approach and presents an application and efficiency of APT systems through software simulations. In addition, this research explores several characteristics of the airborne APT system in pursuit of optimised system performance.

The study beings by understanding the first principles relating to the acoustic waves' propagation and acoustical source behaviour to understand the potential of using sound waves as energy carriers. The properties of acoustic waves from a circular piston sound source are evaluated to derive the acoustic intensity and pressure for a given separation distance and directivity of the source. As the scope of this research is to estimate the performance of the APT system in the far-field region, the relationship between the sound intensity and the medium of propagation were analytically computed to obtain the propagation losses for *cm*-range distance. Subsequently, the state-of-the-art acoustic wireless power transfer technologies were reviewed for different propagation media. Although only limited literature was available for airborne APT systems, the transducers technology, range, the power output of the existing systems was compared, and its limitations were recognized.

Comprehending these findings, a piezoelectric APT finite element model for the APT system using piezoelectric transducers was programmed using COMSOL Multiphysics software to understand the losses in the air due to diffraction, attenuation, and acoustic mismatch losses. Furthermore, an equivalent circuit model of the FUS-40E transducer was derived to find the optimal loading conditions, which indicates that complex impedance matching of both the transmitter and receiver would provide the maximum power output, especially for off-resonance frequencies. Finally, these results were experimentally validated using the FUS-40E piezoelectric transducers, complying with the safety standard for workspace sound exposure levels by limiting the transmitted sound power to $110\,dB$ and by restricting the operating frequency to the ultrasonic frequency range (above $40\ kHz$).

Additionally, a detailed 3D profiling of the acoustic system in the far-field region was provided, analysing the receiver sensitivity to disturbances in separation distance, receiver orientation and alignment. Reflections in the system have been successfully modelled by FEM analysis and verified experimentally. The misalignment and reflection experimental measurements are presented as a design graph describing the output voltage and power as a function of the separation distance, offset, loading method, and operating frequency. Although reflection was consistent in the system for considerable separation distance and offset, combining the impedance tuning and driving the APT system off-resonance was observed to improve the system's robustness by improving the output power in the far-field.

As an application scenario, a hybrid inductive and acoustic power transfer system for powering a distributed sensor node network was considered. A programmable power delivery vehicle was considered to distribute power among the wireless network, where quantised power packets are sent to a node via inductive power transfer, which is later distributed to the neighbouring nodes acoustically. Assuming certain conditions and corresponding values for power link efficiencies, a dynamic automated recharge scheduling algorithm was developed. This algorithm was used in simulation, to program power delivery vehicles to evaluate the recharge request of the sensor nodes in a network and compute the optimised path for recharging. The performance of the proposed algorithm was evaluated against single-stage inductive power transfer methods for various network and algorithm parameters.

6.2. Thesis Contributions

According to the contents of this thesis, the contribution of this work towards the acoustic wireless power transfer research are as listed below:

- *Presenting the applications of far-field through-air acoustic power transfer to a broader audience*: APT systems have gained attention for powering biomedical implants and through-wall applications due to their non-invasive properties. However, air based APT systems are less exploited with considerable potential for powering WSNs. This thesis, along with its publications and conference presentations, aims to help in bringing attention to airborne APT systems to a broader audience.

- *Modelling and experimental validation of impedance matching techniques for APT transducers*: The electrical equivalent model for the transducer loading condition is derived. The feasibility of the different impedance matching techniques is experimentally validated to identify the optimum method to deliver power to the receiver. The integration of complex matching enhanced the power transfer efficiency and reduced the load resistance.
- *Increasing APT operation bandwidth*: Complex impedance matching of the system's transducers provides an advantage to drive the transmitter off-resonance for cases where there is a resonance mismatch between the transducers due to make, defect or ambient conditions. Therefore, utilizing self-tuning techniques, similar power levels can be achieved for a 4 kHz bandwidth. In addition, combining the frequency tuning and impedance matching techniques allows powering receivers at varying positions from a single transmitter.
- *Optimization of output power and 3D profiling of reflection and misalignment*: Reflections measured in the APT system has been prominent and generate standing waves that restrict the placement of the receiver in specific locations for a given operating frequency. The measurements results achieved for different operational frequencies prove that the sensitivity of the APT system to reflection and offset can be considerably reduced by driving the receiver at off-resonance frequency. Design graphs were generated from the results to provide researchers with a tool to determine the operating frequency of the transmitter to deliver the optimised power at different loading conditions
- *Dynamic recharge scheduling software*: Equipping inexpensive unmanned vehicles and embedded devices with subsystems to facilitate WSNs allows such vehicles to become viable mobile power delivery vehicles and data collection agents. A two-stage power transfer network was proposed and studied in this thesis to achieve on-demand charging of sensor nodes. This recharge scheme is scheduled using a dynamic novel algorithm that combines a weighted genetic algorithm with the nearest neighbour search to jointly minimize vehicle travel

distance and power transfer losses. This software provides a general tool for network designers to evaluate and plan the sensor node positions in the most advantageous locations for optimised sensing data and power transfer.

6.3. Future Work

Given the limited research done in the far-field APT system using air as the propagation medium, there are serval aspects to investigate to improve the power transfer efficiency of APT systems. The essential recommendations that were discussed during the course of this research are summarised in this section.

- *Modelling:* The models presented in this thesis agreed with the experimental results, but the computational requirements of the models (especially for FEM analysis) are excessive. For acoustic calculations, the mesh size for the COMSOL simulations should be at least $1/5\ th$ the wavelength of the acoustic wave to obtain accurate results. Since the tested transducers are operated at an ultrasonic frequency, the mesh size is extremely fine, increasing the computational time and memory requirements for far-field calculations. Therefore, a trade-off between computing accuracy and speed is essential for FEM analysis. However, eliminating problematic factors from the system design can reduce the model requirements of APT systems. For instance, by using a very small receiver in the system, the diffraction and reflections in the APT system become negligible. Therefore, modelling the system using the transmission line and KLM models with accurately fit parameters can define the system output for perfectly aligned receivers. This greatly reduces the system's complexity but will probably underestimate the output power. Consequently, combining FEM analysis and equivalent circuit parameter fitting can aid bringing accurate modelling of APT system in future. This will allow researchers to understand the system from which the model can be optimised. Also, additional features such as waveguides and horns can be combined as separate components to the model, providing modularity for the users.
- *Transducer design*: This work's simulation and experimental work are based on off-the-shelf piezoelectric transducers, which are commercially manufactured for sensing or imaging purposes. Consequently, the power density of these transducers is very low. APT transducer design is a research field on its own and therefore was out of the scope of this thesis. However, recent advances in piezoelectric Micromachined Ultrasonic Transducers (pMUTs) have shown great potential for

ultrasonic APT in biomedical implantations [105, 123], which can be expanded to air-based APT systems.

Additionally, it can be realised from the results of Chapter 3 that electrical impedance matching is substantially more important for the transmitter than the receiver. This applies to both acoustic and electrical impedance. The electrical impedance allows the transmitter to operate at shifted frequencies, which is important only in combination with receiver position and alignment. A poorly matched transducer has a reflection coefficient close to one, implying that the transmitter primarily reflects the acoustic wave at the radiating face-medium boundary and only a minor portion of the wave is transmitted into the air.

When the directivity of the transmitter is significant, as long the transducer material is relatively lossless, the reflected wave will travel back and forth inside the transducer and return to the radiating surface. However, in cases of high diffraction (as seen for FUS-110A transducers), the efficiency of these transducers for far-field power transmission declines significantly due to the spreading of acoustic waves. Therefore, connecting waveguides to the radiating face of the transmitter can help guide the acoustic waves into the propagation medium. Also, employing different transducer architecture for the transmitter and the receiver would be beneficial, as the transmitter design should focus on high power transmission with minimal spreading and receiver design should attend to low sensitivity to misoreintation and impedance.

- *Self-tuneable Impedance Matching Circuit*: Chapter 3 and Chapter 4 discusses the advantages of a self-tuneable impedance matching circuit for the APT receiver and its enhancements to the robustness of the APT system. In this work, decade reactance and resistance boxes were utilised for demonstration purposes which manually tuned the transmitter and the receiver to the optimised impedance value. However, such an approach is not practical for real-world applications. However, existing research has demonstrated automatic impedance matching with feedback control and neural networks methods for additional energy and complexity cost [208, 209]. Since power consumption is a critical criterion for WSNs, low energy self-tuneable circuits using switching circuits [210], instead of costly computational algorithms, be helpful for APT systems.

  Additionally, frequency tuning of the transmitter depending on the separation distance between the transducer would optimise the output power of the APT systems. During this research, slight noise on the transmitter signal due to the reflected wave from the receiver was observed. This is evaluated in proximity sensors to calculate the distance between the source and the obstruction, such as the receiver). Considering the sufficient energy source available at the transmitter side, computational software can be employed to compute the position of the receiver and the optimum operating frequency for maximum power delivery.

- *Acoustic Meta-lens*: Acoustic lenses using metamaterial design is an expanding field of research for acoustical imaging and sensing. However, they can also be adapted for power transfer applications. An acoustic meta-lens is composed of lattice columns structures to maintain a 2D/3D shape. The width and height of the columns within the lattice can be adjusted to form meta units of characteristic acoustic impedance inside the lens structure. Research on acoustic lenses expanded to 3D due to the advancements in 3D printing technologies, facilitating the fabrication of complex lens designs. 3D lenses also provide an advantage of focusing incident acoustic waves in all directions, therefore producing a higher SPL level than 2D lenses. Consequently, when the APT receiver is placed at the focal point of the lens, higher output power can be delivered.

  Due to the vast difference between the acoustic impedance of air and solids, acoustic lenses should be designed with Gradient-Index (GRIN), where the refractive index of the lens's cross-section gradually increases from the surface to the centre [93, 97]. As a result, the thickness of the lattice columns should be smaller than a quarter of the wavelength for the desired bending of the acoustic waves. However, the wavelength is very small as far-field APT systems are operated at ultrasonic frequencies. Therefore, understanding the limitations of current 3D printing technologies and complex Computed Aided Designing (CAD) is required to develop GRIN acoustic lenses. In addition, the latest advancement in polyjet printing technologies has allowed printing two or more materials of different densities in the desired ratio to control the local density of the structure [211], at the cost of accuracy for μm-scale printing. While these tools currently have a number of shortcomings in terms of complexity and accuracy, it demonstrates a pathway towards broadband and beam steering for single transmitter – multi-receiver APT systems.

- *Multiple PDV recharge scheduling*: The recharge scheduling algorithm proposed and evaluated in this work programs a single PDV for recharging the WSN. However, employing multiple PDVs and base stations can help reduce the charging delays, and the constraints of the PDV can be minimised. Furthermore, integrating the data collection module while recharging the WSN can also optimise the sensor node performance as less energy will be used for communication. Also, acquiring local data can help learn the system behaviour utilised to develop machine learning algorithms to predict the recharge requests from the sensor nodes.

References

[1] I. F. Akyildiz and M. C. Vuran, *Wireless sensor networks*. John Wiley & Sons, 2010.

[2] I. F. Akyildiz, W. Su, Y. Sankarasubramaniam, and E. Cayirci, "Wireless sensor networks: a survey," *Computer networks,* vol. 38, no. 4, pp. 393-422, 2002.

[3] D. Estrin, L. Girod, G. Pottie, and M. Srivastava, "Instrumenting the world with wireless sensor networks," in *2001 IEEE International Conference on Acoustics, Speech, and Signal Processing. Proceedings (Cat. No. 01CH37221)*, 2001, vol. 4: IEEE, pp. 2033-2036.

[4] J. K. Gerrikagoitia, G. Unamuno, E. Urkia, and A. Serna, "Digital manufacturing platforms in the industry 4.0 from private and public perspectives," *Applied Sciences,* vol. 9, no. 14, p. 2934, 2019.

[5] W. Ding, "Study of smart warehouse management system based on the IOT," in *Intelligence computation and evolutionary computation*: Springer, 2013, pp. 203-207.

[6] M. Abdelhafidh, M. Fourati, L. C. Fourati, and A. Abidi, "Remote water pipeline monitoring system IoT-based architecture for new industrial era 4.0," in *2017 IEEE/ACS 14th International Conference on Computer Systems and Applications (AICCSA)*, 2017: IEEE, pp. 1184-1191.

[7] K. Patil and N. Kale, "A model for smart agriculture using IoT," in *2016 International Conference on Global Trends in Signal Processing, Information Computing and Communication (ICGTSPICC)*, 2016: IEEE, pp. 543-545.

[8] P. D. Mitcheson, E. M. Yeatman, G. K. Rao, A. S. Holmes, and T. C. Green, "Energy harvesting from human and machine motion for wireless electronic devices," *Proceedings of the IEEE,* vol. 96, no. 9, pp. 1457-1486, 2008.

[9] A. Nechibvute, A. Chawanda, and P. Luhanga, "Piezoelectric energy harvesting devices: an alternative energy source for wireless sensors," *Smart Materials Research,* 2012.

[10] M. S. Mahmoud and A. A. Mohamad, "A study of efficient power consumption wireless communication techniques/modules for internet of things (IoT) applications," *Advances in Internet of Things,* no. 6, pp. 19-29, 2016, doi: 10.4236/ait.2016.62002.

[11] A. Khaligh, P. Zeng, and C. Zheng, "Kinetic energy harvesting using piezoelectric and electromagnetic technologies—state of the art," *IEEE transactions on industrial electronics,* vol. 57, no. 3, pp. 850-860, 2009.

[12] M. Gorlatova, J. Sarik, G. Grebla, M. Cong, I. Kymissis, and G. Zussman, "Movers and shakers: Kinetic energy harvesting for the internet of things," *IEEE Journal on Selected Areas in Communications,* vol. 33, no. 8, pp. 1624-1639, 2015.

[13] A. Cuadras, M. Gasulla, and V. Ferrari, "Thermal energy harvesting through pyroelectricity," *Sensors Actuators A: Physical,* vol. 158, no. 1, pp. 132-139, 2010.

[14] M. Kang and E. M. Yeatman, "Coupling of piezo-and pyro-electric effects in miniature thermal energy harvesters," *J Applied Energy,* vol. 262, p. 114496, 2020.

[15] K. Xiao *et al.*, "Artificial light-driven ion pump for photoelectric energy conversion," *Nature communications,* vol. 10, no. 1, pp. 1-7, 2019.

[16] S. Roundy, P. K. Wright, and J. Rabaey, "A study of low level vibrations as a power source for wireless sensor nodes," *Computer communications,* vol. 26, no. 11, pp. 1131-1144, 2003.

[17] M. Safaei, H. A. Sodano, and S. R. Anton, "A review of energy harvesting using piezoelectric materials: state-of-the-art a decade later (2008–2018)," *Smart*

Materials and Structures, vol. 28, no. 11, p. 113001, 2019/10/22 2019, doi: 10.1088/1361-665x/ab36e4.
[18] J. Wang, L. Geng, L. Ding, H. Zhu, and D. Yurchenko, "The state-of-the-art review on energy harvesting from flow-induced vibrations," *Applied Energy,* vol. 267, p. 114902, 2020/06/01/ 2020, doi: https://doi.org/10.1016/j.apenergy.2020.114902.
[19] A. Thakre, A. Kumar, H.-C. Song, D.-Y. Jeong, and J. Ryu, "Pyroelectric Energy Conversion and Its Applications—Flexible Energy Harvesters and Sensors," *Sensors,* vol. 19, no. 9, 2019, doi: 10.3390/s19092170.
[20] M. Yuan, Z. Cao, J. Luo, and X. Chou, "Recent Developments of Acoustic Energy Harvesting: A Review," vol. 10, no. 1, p. 48, 2019. [Online]. Available: https://www.mdpi.com/2072-666X/10/1/48.
[21] M. Cansiz, D. Altinel, and G. K. Kurt, "Efficiency in RF energy harvesting systems: A comprehensive review," *Energy,* vol. 174, pp. 292-309, 2019/05/01/ 2019, doi: https://doi.org/10.1016/j.energy.2019.02.100.
[22] T. Wacharasindhu and J. Kwon, "A micromachined energy harvester from a keyboard using combined electromagnetic and piezoelectric conversion," *Journal of Micromechanics and Microengineering,* vol. 18, no. 10, p. 104016, 2008.
[23] H. Xia, R. Chen, and L. Ren, "Analysis of piezoelectric–electromagnetic hybrid vibration energy harvester under different electrical boundary conditions," *Sensors and Actuators A: Physical,* vol. 234, pp. 87-98, 2015/10/01/ 2015, doi: https://doi.org/10.1016/j.sna.2015.08.014.
[24] F. U. Khan and Izhar, "Hybrid acoustic energy harvesting using combined electromagnetic and piezoelectric conversion," *Review of Scientific Instruments,* vol. 87, no. 2, p. 025003, 2016, doi: 10.1063/1.4941840.
[25] R. K. Gupta, Q. Shi, L. Dhakar, T. Wang, C. H. Heng, and C. Lee, "Broadband Energy Harvester Using Non-linear Polymer Spring and Electromagnetic/Triboelectric Hybrid Mechanism," *Scientific Reports,* vol. 7, no. 1, p. 41396, 2017/01/25 2017, doi: 10.1038/srep41396.
[26] L.-C. Zhao *et al.*, "A water-proof magnetically coupled piezoelectric-electromagnetic hybrid wind energy harvester," *Applied Energy,* vol. 239, pp. 735-746, 2019.
[27] K. Fan, S. Liu, H. Liu, Y. Zhu, W. Wang, and D. Zhang, "Scavenging energy from ultra-low frequency mechanical excitations through a bi-directional hybrid energy harvester," *Applied Energy,* vol. 216, pp. 8-20, 2018.
[28] B. Yang, C. Lee, W. L. Kee, and S.-P. Lim, "Hybrid energy harvester based on piezoelectric and electromagnetic mechanisms," *Journal of Micro/Nanolithography, MEMS,MOEMS,* vol. 9, no. 2, p. 023002, 2010.
[29] P. Gambier, S. Anton, N. Kong, A. Erturk, and D. Inman, "Piezoelectric, solar and thermal energy harvesting for hybrid low-power generator systems with thin-film batteries," *Measurement science technology,* vol. 23, no. 1, p. 015101, 2011.
[30] P. Chatterjee and M. Bryant, "Aeroelastic-photovoltaic ribbons for integrated wind and solar energy harvesting," *Smart Materials and Structures,* vol. 27, no. 8, p. 08LT01, 2018/07/10 2018, doi: 10.1088/1361-665x/aacbbb.
[31] C. Bowen, H. Kim, P. Weaver, and S. Dunn, "Piezoelectric and ferroelectric materials and structures for energy harvesting applications," *Energy Environmental Science,* vol. 7, no. 1, pp. 25-44, 2014.
[32] A. Sabo, "Alignment independent and self aligning inductive power transfer system," 2004.
[33] E. Waffenschmidt and T. Staring, "Limitation of inductive power transfer for consumer applications," in *2009 13th European Conference on Power Electronics and Applications*, 2009: IEEE, pp. 1-10.

[34] Z.-H. Ye, Y. Sun, X. Dai, C.-S. Tang, Z.-H. Wang, and Y.-G. Su, "Energy efficiency analysis of U-coil wireless power transfer system," *IEEE Transactions on Power Electronics,* vol. 31, no. 7, pp. 4809-4817, 2015.

[35] W. Zhong, X. Liu, and S. R. Hui, "A novel single-layer winding array and receiver coil structure for contactless battery charging systems with free-positioning and localized charging features," *IEEE Transactions on Industrial Electronics,* vol. 58, no. 9, pp. 4136-4144, 2010.

[36] J. Lawson, M. Pinuela, D. C. Yates, S. Lucyszyn, and P. D. Mitcheson, "Long range inductive power transfer system," *Journal of Physics: Conference Series,* vol. 476, p. 012005, 2013/12/04 2013, doi: 10.1088/1742-6596/476/1/012005.

[37] J. Lawson, D. C. Yates, and P. D. Mitcheson, "High Q Coil Measurement for Inductive Power Transfer," *IEEE Transactions on Microwave Theory and Techniques,* vol. 67, no. 5, pp. 1962-1973, 2019, doi: 10.1109/TMTT.2019.2901442.

[38] C. Park, S. Lee, G.-H. Cho, and C. T. Rim, "Innovative 5-m-off-distance inductive power transfer systems with optimally shaped dipole coils," *IEEE transactions on power electronics,* vol. 30, no. 2, pp. 817-827, 2014.

[39] J. I. Agbinya and N. F. A. Mohamed, "Design and study of multi-dimensional wireless power transfer transmission systems and architectures," *International Journal of Electrical Power & Energy Systems,* vol. 63, pp. 1047-1056, 2014/12/01/ 2014, doi: https://doi.org/10.1016/j.ijepes.2014.06.071.

[40] M. P. Kazmierkowski and A. J. Moradewicz, "Unplugged but connected: Review of contactless energy transfer systems," *IEEE Industrial Electronics Magazine,* vol. 6, no. 4, pp. 47-55, 2012.

[41] A. W. S. Putra, M. Tanizawa, and T. Maruyama, "Optical wireless power transmission using Si photovoltaic through air, water, and skin," *IEEE Photonics Technology Letters,* vol. 31, no. 2, pp. 157-160, 2018.

[42] A. Dasgupta, M.-M. Mennemanteuil, M. Buret, N. Cazier, G. Colas-des-Francs, and A. Bouhelier, "Optical wireless link between a nanoscale antenna and a transducing rectenna," *Nature communications,* vol. 9, no. 1, pp. 1-7, 2018.

[43] R. M. Dickinson, "Wireless power transmission technology state of the art the first Bill Brown lecture," *Acta Astronautica,* vol. 53, no. 4-10, pp. 561-570, 2003.

[44] D. E. Raible, D. Dinca, and T. H. Nayfeh, "Optical frequency optimization of a high intensity laser power beaming system utilizing VMJ photovoltaic cells," in *2011 International Conference on Space Optical Systems and Applications (ICSOS)*, 2011: IEEE, pp. 232-238.

[45] R. L. Rosa, C. Dehollain, F. Pellitteri, R. Miceli, and P. Livreri, "A Battery-free Asset Monitoring System based on RF Wireless Power Transfer," in *2020 IEEE 20th Mediterranean Electrotechnical Conference (MELECON)*, 16-18 June 2020 2020, pp. 181-186, doi: 10.1109/MELECON48756.2020.9140484.

[46] A. Sample and J. R. Smith, "Experimental results with two wireless power transfer systems," in *2009 IEEE Radio and Wireless Symposium*, 18-22 Jan. 2009 2009, pp. 16-18, doi: 10.1109/RWS.2009.4957273.

[47] R. L. Rosa, C. Dehollain, F. Pellitteri, R. Miceli, and P. Livreri, "An RF Wireless Power Transfer system to power battery-free devices for asset tracking," in *2019 26th IEEE International Conference on Electronics, Circuits and Systems (ICECS)*, 27-29 Nov. 2019 2019, pp. 534-537, doi: 10.1109/ICECS46596.2019.8965070.

[48] L. Xie, Y. Shi, Y. T. Hou, and A. Lou, "Wireless power transfer and applications to sensor networks," *IEEE Wireless Communications,* vol. 20, no. 4, pp. 140-145, 2013, doi: 10.1109/MWC.2013.6590061.

[49] S. He, J. Chen, F. Jiang, D. K. Y. Yau, G. Xing, and Y. Sun, "Energy Provisioning in Wireless Rechargeable Sensor Networks," *IEEE Transactions on Mobile Computing,* vol. 12, no. 10, pp. 1931-1942, 2013, doi: 10.1109/TMC.2012.161.

[50] F. W. Vook, A. Ghosh, and T. A. Thomas, "MIMO and beamforming solutions for 5G technology," in *2014 IEEE MTT-S International Microwave Symposium (IMS2014)*, 1-6 June 2014 2014, pp. 1-4, doi: 10.1109/MWSYM.2014.6848613.

[51] P. S. Yedavalli, T. Riihonen, X. Wang, and J. M. Rabaey, "Far-Field RF Wireless Power Transfer with Blind Adaptive Beamforming for Internet of Things Devices," *IEEE Access,* vol. 5, pp. 1743-1752, 2017, doi: 10.1109/ACCESS.2017.2666299.

[52] G. V. B. Cochran, M. W. Johnson, M. P. Kadaba, F. Vosburgh, M. W. Ferguson-Pell, and V. R. Palmeiri, "Piezoelectric internal fixation devices: A new approach to electrical augmentation of osteogenesis," *Journal of Orthopaedic Research,* https://doi.org/10.1002/jor.1100030414 vol. 3, no. 4, pp. 508-513, 1985/01/01 1985, doi: https://doi.org/10.1002/jor.1100030414.

[53] P. J. Larson and B. C. Towe, "Miniature ultrasonically powered wireless nerve cuff stimulator," in *2011 5th International IEEE/EMBS Conference on Neural Engineering*, 27 April-1 May 2011 2011, pp. 265-268, doi: 10.1109/NER.2011.5910538.

[54] J. Charthad, M. J. Weber, T. C. Chang, and A. Arbabian, "A mm-Sized Implantable Medical Device (IMD) With Ultrasonic Power Transfer and a Hybrid Bi-Directional Data Link," *IEEE Journal of Solid-State Circuits,* vol. 50, no. 8, pp. 1741-1753, 2015, doi: 10.1109/JSSC.2015.2427336.

[55] M. Meng and M. Kiani, "Design and Optimization of Ultrasonic Wireless Power Transmission Links for Millimeter-Sized Biomedical Implants," *IEEE Transactions on Biomedical Circuits and Systems,* vol. 11, no. 1, pp. 98-107, 2017, doi: 10.1109/TBCAS.2016.2583783.

[56] S. Ozeri and D. Shmilovitz, "Ultrasonic transcutaneous energy transfer for powering implanted devices," *Ultrasonics,* vol. 50, no. 6, pp. 556-566, 2010/05/01/ 2010, doi: https://doi.org/10.1016/j.ultras.2009.11.004.

[57] S. Ozeri, D. Shmilovitz, S. Singer, and C.-C. Wang, "Ultrasonic transcutaneous energy transfer using a continuous wave 650kHz Gaussian shaded transmitter," *Ultrasonics,* vol. 50, no. 7, pp. 666-674, 2010/06/01/ 2010, doi: https://doi.org/10.1016/j.ultras.2010.01.004.

[58] M. E. Kiziroglou, D. E. Boyle, S. W. Wright, and E. M. Yeatman, "Acoustic energy transmission in cast iron pipelines," *Journal of Physics: Conference Series,* vol. 660, p. 012095, 2015/12/10 2015, doi: 10.1088/1742-6596/660/1/012095.

[59] H. Fu, J. Rao, M. S. Harb, and S. Theodossiades, "Ultrasonic Wireless Power Links for Battery-Free Condition Monitoring in Metallic Enclosures," *Ultrasonics,* p. 106395, 2021/03/06/ 2021, doi: https://doi.org/10.1016/j.ultras.2021.106395.

[60] S. Sherrit *et al.*, "KW Power Transmission using Wireless Acoustic-Electric Feed-through (WAEF)," 09/04 2008, doi: 10.1061/40988(323)120.

[61] B. Xiaoqi *et al.*, "High-power piezoelectric acoustic-electric power feedthru for metal walls," in *Proc.SPIE Industrial and Commercial Applications of Smart Structures Technologies 2008*, 19 March 2008 2008, vol. 6930, doi: 10.1117/12.776473. [Online]. Available: https://doi.org/10.1117/12.776473

[62] A. Denisov and E. Yeatman, "Ultrasonic vs. Inductive Power Delivery for Miniature Biomedical Implants," in *2010 International Conference on Body Sensor Networks*, 7-9 June 2010 2010, pp. 84-89, doi: 10.1109/BSN.2010.27.

[63] M. G. L. Roes, "Exploring the potential of acoustic energy transfer," Department of Electrical Engineering, Technische Universiteit Eindhoven, Technische Universiteit Eindhoven.

[64] A. Kurs, A. Karalis, R. Moffatt, J. D. Joannopoulos, P. Fisher, and M. Soljačić, "Wireless Power Transfer via Strongly Coupled Magnetic Resonances," *Science,* vol. 317, no. 5834, p. 83, 2007, doi: 10.1126/science.1143254.

[65] M. G. L. Roes, M. A. M. Hendrix, and J. L. Duarte, "Contactless energy transfer through air by means of ultrasound," in *IECON 2011 - 37th Annual Conference of the IEEE Industrial Electronics Society*, 7-10 Nov. 2011 2011, pp. 1238-1243, doi: 10.1109/IECON.2011.6119486.

[66] A. Y. Pandiyan, M. E. Kiziroglou, and E. M. Yeatman, "Complex Impedance Matching for Far-Field Acoustic Wireless Power Transfer," in *2021 IEEE 20th International Conference on Micro and Nanotechnology for Power Generation and Energy Conversion Applications (PowerMEMS)*, 6-8 Dec. 2021 2021, pp. 44-47, doi: 10.1109/PowerMEMS54003.2021.9658395.

[67] A. Y. S. Pandiyan, R. L. Rosa, M. E. Kiziroglou, and E. M. Yeatman, "Understanding Far Field Ultrasonic Power Transmission for Automobile Sensor Networks in Free Space," in *2019 19th International Conference on Micro and Nanotechnology for Power Generation and Energy Conversion Applications (PowerMEMS)*, 2-6 Dec. 2019 2019, pp. 1-4, doi: 10.1109/PowerMEMS49317.2019.71805308205.

[68] A. Y. S. Pandiyan, M. E. Kiziroglou, D. E. Boyle, S. W. Wright, and E. M. Yeatman, "Optimal Energy Management of Two Stage Energy Distribution Systems Using Clustering Algorithm," in *2019 19th International Conference on Micro and Nanotechnology for Power Generation and Energy Conversion Applications (PowerMEMS)*, 2-6 Dec. 2019 2019, pp. 1-4, doi: 10.1109/PowerMEMS49317.2019.82063210088.

[69] A. Y. S. Pandiyan, D. E. Boyle, M. E. Kiziroglou, S. W. Wright, and E. M. Yeatman, "Optimal Dynamic Recharge Scheduling for Two-Stage Wireless Power Transfer," *IEEE Transactions on Industrial Informatics,* vol. 17, no. 8, pp. 5719-5729, 2021, doi: 10.1109/tii.2020.3035645.

[70] G. W. Stewart and R. B. Lindsay, *Acoustics: A text on theory and applications*. D. Van Nostrand Company, Incorporated, 1930.

[71] P. M. Morse, *Vibration and sound*, 2nd ed. (International series in pure and applied physics). McGraw-HillBookCompany, Inc., 1948.

[72] H. Kuttruff, *Acoustics: An Introduction* 1st ed. ed. CRC Press, 2006.

[73] S. Horowitz and M. Sheplak, D. Briand, E. Yeatman, and S. Roundy, Eds. *Micromachined Acoustic Energy Harvesters* (Micro Energy Harvesting). Wiley-VCH, 2015.

[74] D. T. Blackstock, "Fundamentals of physical acoustics," ed: Acoustical Society of America, 2001.

[75] M. Alonso and E. J. Finn, *Fundamental university physics*, 2 ed. (Fields and waves). Addison-Wesley Publishing Company, 1967.

[76] S. P. Näsholm and S. Holm, "On a fractional Zener elastic wave equation," *Fractional Calculus and Applied Analysis,* vol. 16, no. 1, pp. 26-50, 2013/03/01 2013, doi: 10.2478/s13540-013-0003-1.

[77] H. Basaeri, D. B. Christensen, and S. Roundy, "A review of acoustic power transfer for bio-medical implants," *Smart Materials and Structures,* vol. 25, no. 12, p. 123001, 2016/11/10 2016, doi: 10.1088/0964-1726/25/12/123001.

[78] M. Tikander, "Model-based curvefitting for in-situ impedance measurements," 09/16 2002.

[79] L. E. Kinsler, A. R. Frey, A. B. Coppens, and J. V. Sanders, *Fundamentals of Acoustics*. Wiley, 1999.

[80] H. E. Bass, L. C. Sutherland, and A. J. Zuckerwar, "Atmospheric absorption of sound: Update," *The Journal of the Acoustical Society of America,* vol. 88, no. 4, pp. 2019-2021, 1990/10/01 1990, doi: 10.1121/1.400176.

[81] H. E. Bass, L. C. Sutherland, A. J. Zuckerwar, D. T. Blackstock, and D. M. Hester, "Atmospheric absorption of sound: Further developments," *The Journal of the Acoustical Society of America,* vol. 97, no. 1, pp. 680-683, 1995/01/01 1995, doi: 10.1121/1.412989.

[82] L. B. Evans, H. E. Bass, and L. C. Sutherland, "Atmospheric Absorption of Sound: Theoretical Predictions," *The Journal of the Acoustical Society of America,* vol. 51, no. 5B, pp. 1565-1575, 1972/05/01 1972, doi: 10.1121/1.1913000.

[83] T. Zaid, S. Saat, Y. Yusop, and N. Jamal, "Contactless energy transfer using acoustic approach - A review," in *2014 International Conference on Computer, Communications, and Control Technology (I4CT)*, 2-4 Sept. 2014 2014, pp. 376-381, doi: 10.1109/I4CT.2014.6914209.

[84] P. M. C. Morse and K. U. Ingard, *Theoretical Acoustics*. Princeton University Press, 1986.

[85] A. Arnau, *Piezoelectric transducers and applications*. Springer, 2004.

[86] P. C. Pedersen, O. Tretiak, and P. He, "Impedance-matching properties of an inhomogeneous matching layer with continuously changing acoustic impedance," *The Journal of the Acoustical Society of America,* vol. 72, no. 2, pp. 327-336, 1982.

[87] R. Hill and S. M. A. El-Dardiry, "A theory for optimization in the use of acoustic emission transducers," *The Journal of the Acoustical Society of America,* vol. 67, no. 2, pp. 673-682, 1980/02/01 1980, doi: 10.1121/1.383893.

[88] R. L. Goldberg and S. W. Smith, "Multilayer piezoelectric ceramics for two-dimensional array transducers," *IEEE Transactions on Ultrasonics, Ferroelectrics, and Frequency Control,* vol. 41, no. 5, pp. 761-771, 1994, doi: 10.1109/58.308512.

[89] D. Callens, C. Bruneel, and J. Assaad, "Matching ultrasonic transducer using two matching layers where one of them is glue," *NDT & E International,* vol. 37, no. 8, pp. 591-596, 2004/12/01/ 2004, doi: https://doi.org/10.1016/j.ndteint.2004.03.005.

[90] M. Toda and M. Thompson, "Novel multi-layer polymer-metal structures for use in ultrasonic transducer impedance matching and backing absorber applications," *IEEE Transactions on Ultrasonics, Ferroelectrics, and Frequency Control,* vol. 57, no. 12, pp. 2818-2827, 2010, doi: 10.1109/TUFFC.2010.1755.

[91] X. Yang *et al.*, "Multi-layer polymer-metal structures for acoustic impedance matching in high-frequency broadband ultrasonic transducers design," *Applied Acoustics,* vol. 160, p. 107123, 2020/03/01/ 2020, doi: https://doi.org/10.1016/j.apacoust.2019.107123.

[92] M. Bakhtiari-Nejad, M. R. Hajj, and S. Shahab, "Dynamics of acoustic impedance matching layers in contactless ultrasonic power transfer systems," *Smart Materials and Structures,* vol. 29, no. 3, p. 035037, 2020/02/19 2020, doi: 10.1088/1361-665x/ab6fe5.

[93] J.-W. Kim, S.-J. Lee, J.-Y. Jo, S. Wang, and S.-H. Kim, "Acoustic imaging by three-dimensional acoustic Luneburg meta-lens with lattice columns," *Applied Physics Letters,* vol. 118, no. 9, p. 091902, 2021, doi: 10.1063/5.0037600.

[94] D. R. Smith, S. Schultz, P. Markoš, and C. M. Soukoulis, "Determination of effective permittivity and permeability of metamaterials from reflection and transmission coefficients," *Physical Review B,* vol. 65, no. 19, p. 195104, 04/19/ 2002, doi: 10.1103/PhysRevB.65.195104.

[95] J. Zhang, Y. Liu, X. Li, L. Shi, M. Yang, and B. Bai, "2D simulation of the electromagnetic wave across the non-uniform reentry plasma sheath with COMSOL," *AIP Advances,* vol. 9, no. 5, p. 055316, 2019, doi: 10.1063/1.5085876.

[96] Y. Ruan *et al.*, "3-D underwater acoustic wave focusing by periodic structure," *Applied Physics Letters,* vol. 114, no. 8, p. 081908, 2019/02/25 2019, doi: 10.1063/1.5081661.
[97] S. Huang, L. Peng, H. Sun, Q. Wang, W. Zhao, and S. Wang, "Frequency response of an underwater acoustic focusing composite lens," *Applied Acoustics,* vol. 173, p. 107692, 2021/02/01/ 2021, doi: https://doi.org/10.1016/j.apacoust.2020.107692.
[98] S.-n. Suzuki, S. Kimura, T. Katane, H. Saotome, O. Saito, and K. Kobayashi, "Power and Interactive Information Transmission to Implanted Medical Device Using Ultrasonic," *Japanese Journal of Applied Physics,* vol. 41, no. Part 1, No. 5B, pp. 3600-3603, 2002/05/30 2002, doi: 10.1143/jjap.41.3600.
[99] W. B. Phillips, B. C. Towe, and P. J. Larson, "An ultrasonically-driven piezoelectric neural stimulator," in *Proceedings of the 25th Annual International Conference of the IEEE Engineering in Medicine and Biology Society (IEEE Cat. No.03CH37439)*, 17-21 Sept. 2003 2003, vol. 2, pp. 1983-1986 Vol.2, doi: 10.1109/IEMBS.2003.1279844.
[100] Y. Shigeta, Y. Hori, K. Fujimori, K. Tsuruta, and S. Nogi, "Development of highly efficient transducer for wireless power transmission system by ultrasonic," in *2011 IEEE MTT-S International Microwave Workshop Series on Innovative Wireless Power Transmission: Technologies, Systems, and Applications*, 12-13 May 2011 2011, pp. 171-174, doi: 10.1109/IMWS.2011.5877115.
[101] F. Mazzilli *et al.*, "In-vitro platform to study ultrasound as source for wireless energy transfer and communication for implanted medical devices," in *2010 Annual International Conference of the IEEE Engineering in Medicine and Biology*, 31 Aug.-4 Sept. 2010 2010, pp. 3751-3754, doi: 10.1109/IEMBS.2010.5627541.
[102] G. Wild and S. Hinckley, "Wireless acoustic communications and power supply for in vivo biomedical devices," in *2010 IEEE International Ultrasonics Symposium*, 11-14 Oct. 2010 2010, pp. 1169-1172, doi: 10.1109/ULTSYM.2010.5936017.
[103] A. Sanni, A. Vilches, and C. Toumazou, "Inductive and Ultrasonic Multi-Tier Interface for Low-Power, Deeply Implantable Medical Devices," *IEEE Transactions on Biomedical Circuits and Systems,* vol. 6, no. 4, pp. 297-308, 2012, doi: 10.1109/TBCAS.2011.2175390.
[104] G. E. Santagati, N. Dave, and T. Melodia, "Design and Performance Evaluation of an Implantable Ultrasonic Networking Platform for the Internet of Medical Things," *IEEE/ACM Transactions on Networking,* vol. 28, no. 1, pp. 29-42, 2020, doi: 10.1109/TNET.2019.2949805.
[105] H. Basaeri, Y. Yu, D. Young, and S. Roundy, "Acoustic power transfer for biomedical implants using piezoelectric receivers: effects of misalignment and misorientation," *Journal of Micromechanics and Microengineering,* vol. 29, no. 8, p. 084004, 2019/06/13 2019, doi: 10.1088/1361-6439/ab257f.
[106] T. C. Chang, M. L. Wang, J. Charthad, M. J. Weber, and A. Arbabian, "27.7 A 30.5mm3 fully packaged implantable device with duplex ultrasonic data and power links achieving 95kb/s with <10−4 BER at 8.5cm depth," in *2017 IEEE International Solid-State Circuits Conference (ISSCC)*, 5-9 Feb. 2017 2017, pp. 460-461, doi: 10.1109/ISSCC.2017.7870460.
[107] M. Haerinia and R. Shadid, "Wireless Power Transfer Approaches for Medical Implants: A Review," *Signals,* vol. 1, no. 2, 2020, doi: 10.3390/signals1020012.
[108] O. Shaul, S. Boaz, and S. Doron, "Non-invasive sensing of the electrical energy harvested by medical implants powered by an ultrasonic transcutaneous energy transfer link," in *2012 IEEE International Symposium on Industrial Electronics*, 28-31 May 2012 2012, pp. 1153-1157, doi: 10.1109/ISIE.2012.6237251.

[109] Y. Shigeta, T. Yamamoto, K. Fujimori, M. Sanagi, S. Nogi, and T. Tsukagoshi, "Development of ultrasonic wireless power transmission system for implantable electronic devices," in *2009 European Wireless Technology Conference*, 28-29 Sept. 2009 2009, pp. 49-52.
[110] A. Denisov and E. M. Yeatman, "Micromechanical Actuators Driven by Ultrasonic Power Transfer," *Journal of Microelectromechanical Systems,* vol. 23, no. 3, pp. 750-759, 2014, doi: 10.1109/JMEMS.2013.2281596.
[111] F. Mazzilli, C. Lafon, and C. Dehollain, "A 10.5 cm Ultrasound Link for Deep Implanted Medical Devices," *IEEE Transactions on Biomedical Circuits and Systems,* vol. 8, no. 5, pp. 738-750, 2014, doi: 10.1109/TBCAS.2013.2295403.
[112] P. Sprawls, *Physical principles of medical imaging*. Aspen Gaithersburg, 1993.
[113] S. Arra, J. Leskinen, J. Heikkila, and J. Vanhala, "Ultrasonic Power and Data Link for Wireless Implantable Applications," in *2007 2nd International Symposium on Wireless Pervasive Computing*, 5-7 Feb. 2007 2007, p. 1, doi: 10.1109/ISWPC.2007.342668.
[114] S. Q. Lee, W. Youm, and G. Hwang, "Biocompatible wireless power transferring based on ultrasonic resonance devices," *Proceedings of Meetings on Acoustics,* vol. 19, no. 1, p. 030030, 2013/06/02 2013, doi: 10.1121/1.4800386.
[115] M. Changki, H. Scott, and J. R. Leon, "Effect of misalignment between ultrasound piezoelectric transducers on transcutaneous energy transfer," in *Proc.SPIE*, 2013, vol. 8688, doi: 10.1117/12.2009895. [Online]. Available: https://doi.org/10.1117/12.2009895
[116] Q. He, J. Liu, B. Yang, X. Wang, X. Chen, and C. Yang, "MEMS-based ultrasonic transducer as the receiver for wireless power supply of the implantable microdevices," *Sensors and Actuators A: Physical,* vol. 219, pp. 65-72, 2014/11/01/ 2014, doi: https://doi.org/10.1016/j.sna.2014.07.008.
[117] Q. L. Sung, Y. Woosub, H. Gunn, S. M. Kee, and O. Yusuf, "Resonant ultrasonic wireless power transmission for bio-implants," in *Proc.SPIE*, 2014, vol. 9057, doi: 10.1117/12.2046600. [Online]. Available: https://doi.org/10.1117/12.2046600
[118] S. H. Song, A. Kim, and B. Ziaie, "Omnidirectional Ultrasonic Powering for Millimeter-Scale Implantable Devices," *IEEE Transactions on Biomedical Engineering,* vol. 62, no. 11, pp. 2717-2723, 2015, doi: 10.1109/TBME.2015.2444854.
[119] L. Radziemski and I. R. S. Makin, "In vivo demonstration of ultrasound power delivery to charge implanted medical devices via acute and survival porcine studies," (in eng), *Ultrasonics,* vol. 64, pp. 1-9, 2016, doi: 10.1016/j.ultras.2015.07.012.
[120] D. B. Christensen and S. Roundy, "Non-dimensional analysis of depth, orientation, and alignment in acoustic power transfer systems," *Smart Materials and Structures,* vol. 27, no. 12, p. 125013, 2018/11/13 2018, doi: 10.1088/1361-665x/aab575.
[121] Q. Shi, T. Wang, and C. Lee, "MEMS Based Broadband Piezoelectric Ultrasonic Energy Harvester (PUEH) for Enabling Self-Powered Implantable Biomedical Devices," *Scientific Reports,* vol. 6, no. 1, p. 24946, 2016/04/26 2016, doi: 10.1038/srep24946.
[122] D. Gong, S. Ma, Y. Chiu, H. Lee, and Y. Jin, "Study of the Properties of AlN PMUT used as a Wireless Power Receiver," in *2019 IEEE 69th Electronic Components and Technology Conference (ECTC)*, 28-31 May 2019 2019, pp. 1503-1508, doi: 10.1109/ECTC.2019.00231.
[123] B. Herrera, F. Pop, C. Cassella, and M. Rinaldi, "AlN PMUT-based Ultrasonic Power Transfer Links for Implantable Electronics," in *2019 20th International Conference on Solid-State Sensors, Actuators and Microsystems & Eurosensors*

XXXIII (TRANSDUCERS & EUROSENSORS XXXIII), 23-27 June 2019 2019, pp. 861-864, doi: 10.1109/TRANSDUCERS.2019.8808320.
[124] H. Basaeri, Y. Yu, D. Young, and S. Roundy, "A MEMS-Scale Ultrasonic Power Receiver for Biomedical Implants," *IEEE Sensors Letters,* vol. 3, no. 4, pp. 1-4, 2019, doi: 10.1109/LSENS.2019.2904194.
[125] F. Narvaez, S. Hosseini, H. Farkhani, and F. Moradi, "Analysis and Design of a PMUT-based transducer for Powering Brain Implants," *arXiv preprint arXiv:.04443,* 2021.
[126] E. Mehdizadeh and G. Piazza, "AlN on SOI pMUTs for ultrasonic power transfer," in *2017 IEEE International Ultrasonics Symposium (IUS)*, 6-9 Sept. 2017 2017, pp. 1-4, doi: 10.1109/ULTSYM.2017.8092630.
[127] E. Mehdizadeh and G. Piazza, "Through-package wireless powering via piezoelectric micromachined ultrasonic transducers," in *2018 IEEE Micro Electro Mechanical Systems (MEMS)*, 21-25 Jan. 2018 2018, pp. 1076-1079, doi: 10.1109/MEMSYS.2018.8346746.
[128] A. Bhargava and S. Shahab, "Acoustic-electroelastic modeling of piezoelectric disks in high-intensity focused ultrasound power transfer systems," *Journal of Intelligent Material Systems and Structures,* p. 1045389X20975478, 2020, doi: 10.1177/1045389X20975478.
[129] S. Delvecchio, P. Bonfiglio, and F. Pompoli, "Vibro-acoustic condition monitoring of Internal Combustion Engines: A critical review of existing techniques," *Mechanical Systems and Signal Processing,* vol. 99, pp. 661-683, 2018, doi: 10.1016/j.ymssp.2017.06.033.
[130] C. Paraskevoulakos *et al.*, "Monitoring the degradation of nuclear waste packages induced by interior metallic corrosion using synchrotron X-ray tomography," *Construction and Building Materials,* vol. 215, pp. 90-103, 2019/08/10/ 2019, doi: https://doi.org/10.1016/j.conbuildmat.2019.04.178.
[131] R. P. Welle, "Ultrasonic power communication system," 2000.
[132] Y. T. Hu, X. S. Zhang, J. S. Yang, and Q. Jiang, "Transmitting Electric Energy Through a Metal Wall by Acoustic Waves Using Piezoelectric Transducers," *Ultrasonics, Ferroelectrics and Frequency Control, IEEE Transactions on,* vol. 50, pp. 773-781, 08/01 2003, doi: 10.1109/TUFFC.2003.1214497.
[133] Z. Yang, J. Yang, and Y. Hu, "Energy trapping in power transmission through an elastic plate by finite piezoelectric transducers," *IEEE Transactions on Ultrasonics, Ferroelectrics, and Frequency Control,* vol. 55, no. 11, pp. 2493-2501, 2008, doi: 10.1109/TUFFC.957.
[134] Z. T. Yang and S. H. Guo, "Energy trapping in power transmission through a circular cylindrical elastic shell by finite piezoelectric transducers," *Ultrasonics,* vol. 48, no. 8, pp. 716-723, 2008/12/01/ 2008, doi: https://doi.org/10.1016/j.ultras.2008.04.001.
[135] C. F. Lü, J. S. Yang, J. Wang, and W. Q. Chen, "Power transmission through a hollow cylinder by acoustic waves and piezoelectric transducers with radial polarization," *Journal of Sound and Vibration,* vol. 325, no. 4, pp. 989-999, 2009/09/11/ 2009, doi: https://doi.org/10.1016/j.jsv.2009.04.002.
[136] R. P. Welle, "Ultrasonic data communication system," 1999.
[137] M. Kluge, T. Becker, J. Schalk, and T. Otterpohl, "Remote acoustic powering and data transmission for sensors inside of conductive envelopes," in *SENSORS, 2008 IEEE*, 26-29 Oct. 2008 2008, pp. 41-44, doi: 10.1109/ICSENS.2008.4716378.
[138] M. Kluge, J. Sabater, J. Schalk, L. V. Ngo, H. Seidel, and U. Schmid, "Wireless Sensing of Physical Parameters Inside Hermetically Enclosed Conductive Envelopes," 2007. [Online]. Available: https://doi.org/10.1115/DETC2007-35481.

[139] L. v. Ngo, M. Kluge, J. Sabater, J. Schalk, H. Seidel, and U. Schmid, "Long-Term Performance of Ultrasonic Transducers Used for Energy and Data Transmission," in *2nd European Conference & Exhibition on Integration Issues of Miniaturized Systems - MOMS, MOEMS, ICS and Electronic Components*, 9-10 April 2008 2008, pp. 1-6.
[140] S. Stewart *et al.*, "Studies of acoustic-electric feed-throughs for power transmission through structures," in *Proc.SPIE*, 2006, vol. 6171, doi: 10.1117/12.657736. [Online]. Available: https://doi.org/10.1117/12.657736
[141] S. Stewart, B. Mircea, B. Xiaoqi, B.-C. Yoseph, and C. Zensheu, "Efficient electromechanical network model for wireless acoustic-electric feed-throughs," in *Proc.SPIE*, 2005, vol. 5758, doi: 10.1117/12.598300. [Online]. Available: https://doi.org/10.1117/12.598300
[142] C. Zensheu *et al.*, "Power loss consideration in wireless piezoelectric acoustic-electric power feedthru," in *Proc.SPIE*, 2007, vol. 6529, doi: 10.1117/12.716433. [Online]. Available: https://doi.org/10.1117/12.716433
[143] B. Xiaoqi *et al.*, "Wireless piezoelectric acoustic-electric power feedthru," in *Proc.SPIE*, 2007, vol. 6529, doi: 10.1117/12.716429. [Online]. Available: https://doi.org/10.1117/12.716429
[144] B. Xiaoqi *et al.*, "High-power piezoelectric acoustic-electric power feedthru for metal walls," in *Proc.SPIE*, 2008, vol. 6930, doi: 10.1117/12.776473. [Online]. Available: https://doi.org/10.1117/12.776473
[145] S. Moss *et al.*, "Modelling and Experimental Validation of the Acoustic Electric Feedthrough Technique," 2008.
[146] S. Moss, M. Konak, C. Phoumsavanh, K. Tsoi, and I. Powlesland, "Acoustic Electric Feedthrough Demonstrator Mk-I," 2009.
[147] S. Moss *et al.*, "Design of the acoustic electric feedthrough demonstrator mk-II," in "Mater. Forum," Citeseer, 2009, vol. 33.
[148] S. Moss, J. Skippen, M. Konak, and I. Powlesland, "Footprint Reduction for the Acoustic Electric Feedthrough Technique," 2010.
[149] M. Scott, S. Jeremy, K. Michael, P. Ian, and G. Steve, "Detachable acoustic electric feedthrough," in *Proc.SPIE*, 2010, vol. 7647, doi: 10.1117/12.848901. [Online]. Available: https://doi.org/10.1117/12.848901
[150] T. L. Murphy, "Ultrasonic digital communication system for a steel wall multipath channel: Methods and results," Knolls Atomic Power Laboratory (KAPL), Niskayuna, NY (United States), 2005.
[151] G. J. Saulnier *et al.*, "P1G-4 Through-Wall Communication of Low-Rate Digital Data Using Ultrasound," in *2006 IEEE Ultrasonics Symposium*, 2-6 Oct. 2006 2006, pp. 1385-1389, doi: 10.1109/ULTSYM.2006.358.
[152] T. J. Lawry, K. R. Wilt, J. D. Ashdown, H. A. Scarton, and G. J. Saulnier, "A high-performance ultrasonic system for the simultaneous transmission of data and power through solid metal barriers," *IEEE Transactions on Ultrasonics, Ferroelectrics, and Frequency Control,* vol. 60, no. 1, pp. 194-203, 2013, doi: 10.1109/TUFFC.2013.2550.
[153] J. D. Ashdown, L. Liu, G. J. Saulnier, and K. R. Wilt, "High-Rate Ultrasonic Through-Wall Communications Using MIMO-OFDM," *IEEE Transactions on Communications,* vol. 66, no. 8, pp. 3381-3393, 2018, doi: 10.1109/TCOMM.2018.2805848.
[154] S. Roa-Prada *et al.*, "An Ultrasonic Through-Wall Communication (UTWC) System Model," *Journal of Vibration and Acoustics,* vol. 135, no. 1, 2013, doi: 10.1115/1.4007565.

[155] D. A. Shoudy *et al.*, "P3F-5 An Ultrasonic Through-Wall Communication System with Power Harvesting," in *2007 IEEE Ultrasonics Symposium Proceedings*, 28-31 Oct. 2007 2007, pp. 1848-1853, doi: 10.1109/ULTSYM.2007.465.
[156] D.-X. Yang, Z. Hu, H. Zhao, H.-F. Hu, Y.-Z. Sun, and B.-J. Hou, "Through-Metal-Wall Power Delivery and Data Transmission for Enclosed Sensors: A Review," (in eng), *Sensors (Basel),* vol. 15, no. 12, pp. 31581-31605, 2015, doi: 10.3390/s151229870.
[157] M. R. Awal, M. Jusoh, T. Sabapathy, M. R. Kamarudin, and R. A. Rahim, "State-of-the-Art Developments of Acoustic Energy Transfer," *International Journal of Antennas and Propagation,* vol. 2016, p. 3072528, 2016/09/06 2016, doi: 10.1155/2016/3072528.
[158] T. Ishiyama, Y. Kanai, J. Ohwaki, and M. Mino, "Wireless Power Transmission System using Ultrasonic Air Transducer for Mobile Applications," *The proceedings of the JSME annual meeting,* vol. 2003.5, pp. 273-274, 08/05 2003, doi: 10.1299/jsmemecjo.2003.5.0_273.
[159] M. G. L. Roes, J. L. Duarte, M. A. M. Hendrix, and E. A. Lomonova, "Acoustic Energy Transfer: A Review," *IEEE Transactions on Industrial Electronics,* vol. 60, no. 1, pp. 242-248, 2013, doi: 10.1109/TIE.2012.2202362.
[160] M. G. L. Roes, M. A. M. Hendrix, and J. L. Duarte, "The effect of reflections on the performance of an acoustic energy transfer system," in *2012 IEEE Energy Conversion Congress and Exposition (ECCE)*, 15-20 Sept. 2012 2012, pp. 388-393, doi: 10.1109/ECCE.2012.6342796.
[161] M. G. L. Roes, J. L. Duarte, and M. A. M. Hendrix, "Design of stepped exponential horns for acoustic energy transfer systems," in *2013 IEEE International Ultrasonics Symposium (IUS)*, 21-25 July 2013 2013, pp. 306-309, doi: 10.1109/ULTSYM.2013.0079.
[162] "SonicEnergy Homepage." https://sonicenergy.com/ (accessed.
[163] M. Perry, "Receiver controller for wireless power transfer," 2015.
[164] M. Perry, "Sender controller for wireless power transfer," 2015.
[165] M. Perry, "Receiver communications for wireless power transfer," 2015.
[166] M. Perry, "Sender transducer for wireless power transfer," 2015.
[167] M. Perry, "Receiver transducer for wireless power transfer," 2015.
[168] M. Perry, "Sender communications for wireless power transfer," ed: Google Patents, 2012.
[169] M. Perry, "Coordinated wireless power transfer," ed: Google Patents, 2019.
[170] M. Perry, P. Reynolds, S. Taffler, and A. Joyce, "Power density control for wireless power transfer," ed: Google Patents, 2018.
[171] M. Perry, P. Reynolds, S. Taffler, and A. Joyce, "Beam interaction control for wireless power transfer," ed: Google Patents, 2017.
[172] A. Joyce and P. Reynolds, "Beamforming for wireless power transfer," ed: Google Patents, 2021.
[173] V. Klymko, M. Roes, J. v. Duivenbode, and E. Lomonova, "Phased transducer array for acoustic energy harvesting inside an MRI machine," in *2013 IEEE International Ultrasonics Symposium (IUS)*, 21-25 July 2013 2013, pp. 1979-1982, doi: 10.1109/ULTSYM.2013.0505.
[174] S. Surappa and F. L. Degertekin, "Characterization of a parametric resonance based capacitive ultrasonic transducer in air for acoustic power transfer and sensing," *Sensors and Actuators A: Physical,* vol. 303, p. 111863, 2020/03/01/ 2020, doi: https://doi.org/10.1016/j.sna.2020.111863.
[175] A. Erturk and D. J. Inman, "An experimentally validated bimorph cantilever model for piezoelectric energy harvesting from base excitations," *Smart Materials*

and Structures, vol. 18, no. 2, p. 025009, 2009/01/13 2009, doi: 10.1088/0964-1726/18/2/025009.
[176] A. Erturk and D. J. Inman, "A Distributed Parameter Electromechanical Model for Cantilevered Piezoelectric Energy Harvesters," *Journal of Vibration and Acoustics,* vol. 130, no. 4, 2008, doi: 10.1115/1.2890402.
[177] W. P. Mason, "Piezoelectric or Electrostrictive Effect in Barium Titanate Ceramics," *Physical Review,* vol. 73, no. 11, pp. 1398-1399, 06/01/ 1948, doi: 10.1103/PhysRev.73.1398.2.
[178] C. B. Williams and R. B. Yates, "Analysis of a micro-electric generator for microsystems," *Sensors and Actuators A: Physical,* vol. 52, no. 1, pp. 8-11, 1996/03/01/ 1996, doi: https://doi.org/10.1016/0924-4247(96)80118-X.
[179] Y. Yang and L. Tang, "Equivalent Circuit Modeling of Piezoelectric Energy Harvesters," vol. 20, no. 18, pp. 2223-2235, 2009, doi: 10.1177/1045389x09351757.
[180] W. P. Mason, *Electromechanical transducers and wave filters*, 2nd ed. ed. New York (N.Y.) : Van Nostrand (in und), 1948.
[181] A. Denisov and E. Yeatman, "Stepwise Microactuators Powered by Ultrasonic Transfer," *Procedia Engineering,* vol. 25, pp. 685-688, 2011/01/01/ 2011, doi: https://doi.org/10.1016/j.proeng.2011.12.169.
[182] S. Cochran, C. E. M. Démoré, and C. R. P. Courtney, "6 - Modelling ultrasonic-transducer performance: one-dimensional models," in *Ultrasonic Transducers*, K. Nakamura Ed.: Woodhead Publishing, 2012, pp. 187-219.
[183] R. Krimholtz, D. A. Leedom, and G. J. E. L. Matthaei, "New equivalent circuits for elementary piezoelectric transducers," vol. 6, pp. 398-399, 1970.
[184] S. Sherrit, S. P. Leary, B. P. Dolgin, and Y. Bar-Cohen, "Comparison of the Mason and KLM equivalent circuits for piezoelectric resonators in the thickness mode," in *1999 IEEE Ultrasonics Symposium. Proceedings. International Symposium (Cat. No.99CH37027)*, 17-20 Oct. 1999 1999, vol. 2, pp. 921-926 vol.2, doi: 10.1109/ULTSYM.1999.849139.
[185] S. Sherrit and B. K. Mukherjee, "Characterization of piezoelectric materials for transducers," *arXiv preprint arXiv:.04443,* 2007.
[186] J. O. Kim, J. G. Lee, and H. Y. Chun, "Radial vibration characteristics of spherical piezoelectric transducers," *Ultrasonics,* vol. 43, no. 7, pp. 531-537, 2005/06/01/ 2005, doi: https://doi.org/10.1016/j.ultras.2005.01.004.
[187] S. Lin, Z. Fu, X. Zhang, Y. Wang, and J. Hu, "Radially sandwiched cylindrical piezoelectric transducer," *Smart Materials and Structures,* vol. 22, no. 1, p. 015005, 2012/11/30 2012, doi: 10.1088/0964-1726/22/1/015005.
[188] M. Redwood, "Transient Performance of a Piezoelectric Transducer," *The Journal of the Acoustical Society of America,* vol. 33, no. 4, pp. 527-536, 1961/04/01 1961, doi: 10.1121/1.1908709.
[189] N. Kong, D. S. Ha, A. Erturk, and D. J. Inman, "Resistive Impedance Matching Circuit for Piezoelectric Energy Harvesting," *Journal of Intelligent Material Systems and Structures,* vol. 21, no. 13, pp. 1293-1302, 2010/09/01 2010, doi: 10.1177/1045389X09357971.
[190] (2003). *ISO 226:2003 Acoustics — Normal equal-loudness-level contours*. [Online] Available: https://www.iso.org/standard/34222.html
[191] (2008). *Guidance for Industry and FDA—Staff Information for Manufacturers Seeking Marketing Clearance of Diagnostic Ultrasound Systems and Transducers.*
[192] Y. Peng, Z. Li, W. Zhang, and D. Qiao, "Prolonging Sensor Network Lifetime Through Wireless Charging," in *2010 31st IEEE Real-Time Systems Symposium*, 30 Nov.-3 Dec. 2010 2010, pp. 129-139, doi: 10.1109/RTSS.2010.35.

[193] P. D. Mitcheson *et al.*, "Energy-autonomous sensing systems using drones," in *2017 IEEE SENSORS*, 29 Oct.-1 Nov. 2017 2017, pp. 1-3, doi: 10.1109/ICSENS.2017.8234092.
[194] C. Lin, Z. Wang, D. Han, Y. Wu, C. W. Yu, and G. Wu, "TADP: Enabling temporal and distantial priority scheduling for on-demand charging architecture in wireless rechargeable sensor Networks," *Journal of Systems Architecture,* vol. 70, pp. 26-38, 2016/10/01/ 2016, doi: https://doi.org/10.1016/j.sysarc.2016.04.005.
[195] L. Xie, Y. Shi, Y. T. Hou, W. Lou, H. D. Sherali, and S. F. Midkiff, "On renewable sensor networks with wireless energy transfer: The multi-node case," in *2012 9th Annual IEEE Communications Society Conference on Sensor, Mesh and Ad Hoc Communications and Networks (SECON)*, 18-21 June 2012 2012, pp. 10-18, doi: 10.1109/SECON.2012.6275766. [Online]. Available: https://ieeexplore.ieee.org/ielx5/6265425/6275759/06275766.pdf?tp=&arnumber=6275766&isnumber=6275759&ref=
[196] L. Xie, Y. Shi, Y. T. Hou, and H. D. Sherali, "Making Sensor Networks Immortal: An Energy-Renewal Approach With Wireless Power Transfer," *IEEE/ACM Transactions on Networking,* vol. 20, no. 6, pp. 1748-1761, 2012, doi: 10.1109/TNET.2012.2185831.
[197] W. Xu, W. Liang, X. Jia, H. Kan, Y. Xu, and X. Zhang, "Minimizing the Maximum Charging Delay of Multiple Mobile Chargers Under the Multi-Node Energy Charging Scheme," *IEEE Transactions on Mobile Computing,* vol. 20, no. 5, pp. 1846-1861, 2021, doi: 10.1109/TMC.2020.2973979.
[198] R.-H. Cheng, C. Xu, and T.-K. Wu, "A Genetic Approach to Solve the Emergent Charging Scheduling Problem Using Multiple Charging Vehicles for Wireless Rechargeable Sensor Networks," *Energies,* vol. 12, no. 2, 2019, doi: 10.3390/en12020287.
[199] S. Guo, C. Wang, and Y. Yang, "Joint Mobile Data Gathering and Energy Provisioning in Wireless Rechargeable Sensor Networks," *IEEE Transactions on Mobile Computing,* vol. 13, no. 12, pp. 2836-2852, 2014, doi: 10.1109/TMC.2014.2307332.
[200] Z. Chen and H. Shen, "Joint Mobile Data Collection and Energy Supply Scheme for Rechargeable Wireless Sensor Networks," in *2019 20th International Conference on Parallel and Distributed Computing, Applications and Technologies (PDCAT)*, 5-7 Dec. 2019 2019, pp. 496-500, doi: 10.1109/PDCAT46702.2019.00098.
[201] U. Maulik and S. Bandyopadhyay, "Genetic algorithm-based clustering technique," *Pattern Recognition,* vol. 33, no. 9, pp. 1455-1465, 2000/09/01/ 2000, doi: https://doi.org/10.1016/S0031-3203(99)00137-5.
[202] D. W. Hearn and J. Vijay, "Efficient Algorithms for the (Weighted) Minimum Circle Problem," *Operations Research,* vol. 30, no. 4, pp. 777-795, 1981.
[203] "DJI Matrice 100 User Manual," Datasheet from DJI Mar 2016. Accessed: 21/01/2020. [Online]. Available: https://www.dji.com/uk/matrice100/info
[204] "LMT84 1.5-V, SC70/TO-92/TO-92S, Analog Temperature Sensors," Datasheet from EATON, 2011.
[205] "HB Supercapacitors cylindrical cells (Technical Data 4375)," Data sheet from Texas Instruments, 2017. [Online]. Available: www.ti.com/lit/ds/symlink/lmt84.pdf
[206] "PowerStor: Supercapacitors PHB Series Technical Sheet 4402," Data sheet from Cooper Bussmman, Data Sheet 2011.
[207] "NovaSensor NPA | Surface Mount Pressure Sensors," Datasheet from Amphenol Advanced Sensors, 2019. [Online]. Available: https://www.amphenol-sensors.com/en/novasensor/pressure-sensors/3161-npa-series

[208] Y. Li, W. Dong, Q. Yang, S. Jiang, X. Ni, and J. Liu, "Automatic impedance matching method with adaptive network based fuzzy inference system for WPT," *IEEE Transactions on Industrial Informatics,* vol. 16, no. 2, pp. 1076-1085, 2019.

[209] Y. Li, W. Dong, Q. Yang, J. Zhao, L. Liu, and S. Feng, "An automatic impedance matching method based on the feedforward-backpropagation neural network for a WPT system," *IEEE Transactions on Industrial Electronics,* vol. 66, no. 5, pp. 3963-3972, 2018.

[210] Y. Cai and Y. Manoli, "A piezoelectric energy-harvesting interface circuit with fully autonomous conjugate impedance matching, 156% extended bandwidth, and 0.38μW power consumption," in *2018 IEEE International Solid - State Circuits Conference - (ISSCC)*, 11-15 Feb. 2018 2018, pp. 148-150, doi: 10.1109/ISSCC.2018.8310227.

[211] O. Rungrojwittayakul *et al.*, "Accuracy of 3D Printed Models Created by Two Technologies of Printers with Different Designs of Model Base," *Journal of Prosthodontics,* vol. 29, no. 2, pp. 124-128, 2020, doi: https://doi.org/10.1111/jopr.13107.